Liposomal formulations of Metallophthalocyanines-Nanoparticle conjugates for hypoxic photodynamic therapy and Photoelectrocatalysis

A thesis submitted in fulfillment of the requirement for the degree of

DOCTOR OF PHILOSOPHY

of

RHODES UNIVERSITY

By

NNAMDI NWAHARA

https://orcid.org/0000-0002-0533-8209

JANUARY 2023

DEDICATION

This work is dedicated to my family.

ACKNOWLEDGEMENTS

"Our soul waiteth for the LORD: he is our help and our shield. For our heart shall rejoice in him, because we have trusted in his holy name." Psalms 33:20-21.

I would like to express my sincere gratitude to my supervisor; Distinguished Prof Nyokong. Thank you for the encouragement and guidance throughout my PhD studies. Thank you for the travelling opportunities and research ideas. Your patience has made me believe in the validity of my dreams. I would also like to appreciate Prof Earl Prinsloo. Thank you for your guidance and patience throughout my PhD study.

I would also like to appreciate the team at the Institute for Nanotechnology Innovation (INI), Prof Philani Mashazi, Prof John Mack, Dr. Jonathan Britton and Ms. Gail Cobus for the assistance afforded to me during my PhD Study. I also extend my gratitude to Marvin Randall for his assistance with TEM and SEM at the Electron Microscopy Unit (EMU).

To all my S22 and F3 colleagues and friends, thank you for the pleasant working environment and memories. Mojahi Motaung, Dr. Tayo Adeniyi, Dr. Robin Nxele, Chipo Simbi, Azole Sindelo, Prof Pinar Sen, Prof. Ngoy and Neil Kramm, I appreciate you guys, thank you for your individual roles in making my journey beautiful.

Lastly, I would like to acknowledge The National Research Foundation and the Department of Science and Technology/Mintek for funding my studies.

TABLE OF CONTENTS

List of abbreviations

AOPs	**Advanced oxidation processes**
DBU	**1,8-diazabicyclo[5.4.0]undec-7-ene**
$CDCl_3$	**Deuterated chloroform**
DMSO-d6	**Deuterated dimethyl sulfoxide**
DCC	**Dicyclohexylcarbodiimide**
DMF	**Dimethylformamide**
DMSO	**Dimethyl sulfoxide**
DPBF	**Diphenylisobenzofuran**
EDS	**Energy dispersive X-ray spectroscopy**
EPR	**Enhanced permeability and retention**
FA	**Folic acid**
FT-IR	**Fourier Transform Infrared**
GSH	**Glutathione**
GQDs	**Graphene quantum dots**
HOMO	**Highest occupied molecular orbital**
ISC	**Intersystem crossing**
LUMO	**Lowest unoccupied molecular orbital**
MS	**Mass Spectrometer**
MPc	**Metallophthalocyanine**
MALDI	**Matrix–Assisted Laser Desorption/Ionization**
NPs	**Nanoparticles**

Nd–YAG	**Neodymium–doped Yttrium Aluminum Garnet**
NHS	**N-hydroxysuccinimide**
PBS	**Phosphate buffer saline**
PDT	**Photodynamic therapy**
Pc	**Phthalocyanine**
^{1}H NMR	**Proton nuclear magnetic resonance**
ROS	**Reactive oxygen species**
Std	**Standard**
THF	**Tetrahydrofuran**
TCSPC	**Time-correlated single photon counting**
TEM	**Transmission electron microscope**
UV/Vis	**Ultraviolet/ visible spectroscopy**

Abstract

This thesis investigates new strategies to enhance the efficacy of photodynamic therapy (PDT) under hypoxic conditions using *in-vitro* cancer cell models. Phthalocyanines are chosen as viable photosensitizer complexes owing to the favourable absorption properties. To this end, this thesis reports on the synthesis and photophysicochemical properties of various zinc and silicon phthalocyanines (Pcs). To afford better photophysicochemical properties, the reported Pcs were conjugated to different nanoparticles (NPs) through chemisorption as well as amide bond formation to yield Pc-NP conjugates.

All the studied Pcs showed relatively high triplet and singlet oxygen quantum yields corresponding to their low fluorescence quantum yields. The various mechanisms for hypoxic response include (i) Type I PDT, (ii) PDT coupled with oxygen-independent therapy and (iii) *in-situ* oxygen generation using catalase-mimicking nanoparticles which serve to supplement *in-vitro* oxygen concentrations using MPcs or MPc-NPs conjugates. The mechanisms were assessed using electrochemical, computational techniques and catalase mimicking experiments.

The as-synthesised Pcs or Pc-NPs were subjected to liposomal loading before PDT studies which led to enhanced biocompatibility and aqueous dispersity. The *in-vitro* dark cytotoxicity tests and photodynamic therapy activities of the fabricated Pc-liposomes and Pc-NPs-liposomes on either Henrietta Lacks (HeLa) or Michigan Cancer Foundation-7 (MCF-7) breast cancer cells are presented herein. This work further showed that folic acid (FA) functionalization of liposomes could be exploited for active drug delivery and herein led to an almost 3-fold increase in drug uptake vs non-FA functionalised liposomes in accordance with folate receptor (FR) expression levels between HeLa and MCF-7 cells.

The *in-vitro* dark cytotoxicity and photodynamic therapy of selected Pc complexes and conjugates were accessed using MCF-7 and HeLa cell lines. The various mechanisms; (i) Type I PDT, (ii) PDT coupled with oxygen -independent therapy and (iii) *in-situ* oxygen generation using catalase-mimicking nanoparticles were shown to adequately compensate for the otherwise attenuation of PDT activity under hypoxia.

Preamble

Photodynamic therapy (PDT) is an anti-cancer treatment modality that employs an otherwise inactive chemical (photosensitizer) that is activated by light to produce cytotoxic reactive oxygen species (ROS) including singlet oxygen. Since oxygen is critical to PDT, the endogenous hypoxic microenvironment that characterizes most tumors presents a significant bottleneck to the clinical adoption of PDT. Moreover, intratumoral hypoxia is further aggravated by oxygen consumption during the administration of PDT, resulting in suboptimal treatment outcomes. Therefore, there is an urgent need to develop new strategies to sensitize cancer cells to photodynamic damage.

This thesis investigates new strategies to enhance the efficacy of photodynamic therapy (PDT) under hypoxic conditions using *in-vitro* cancer cell models. It was hypothesized that the efficacy of PDT could be substantially improved by (1) utilizing metallophthalocyanines (MPcs) as near-infrared (NIR) active photosensitizers, which have the potential for applications targeting deeper-seated tissues, (2) utilizing targeted phthalocyanines to pharmacologically relevant sites within the tumor using liposomal drug delivery systems, and these MPcs were used either alone or in the presence of various metallic nanoparticles (NPs) to positively modulate their photophysical and photochemical properties and afford them responsiveness to hypoxia within tumor tissue. This thesis, therefore, describes the synthesis of symmetrical and asymmetrical metallophthalocyanines as photosensitizers in the presence of various metallic nanoparticles. Liposomes are used as effective drug delivery systems. The thesis addresses hypoxia and multiple strategies are explored for improving the efficacy of PDT towards hypoxia tumor environment. A small section of this work explored the use of MPcs as photocatalysts in photoelectrocatalysis.

Chapter 1:

Introduction and literature review

Introduction

This chapter describes the basis of the thesis. It gives background on metallophthalocyanines, nanoparticles employed, and how these nanomaterials can be conjugated to form visible light active photodynamic hybrids responsive to tumor hypoxia. A section of this chapter focuses on the application of metallophthalocyanine-nanoparticle (MPcs-NPs) conjugates as effective photoelectrochemical hybrids.

1.1 Metallophthalocyanines (MPcs)

Phthalocyanines (Pcs) and their metalated derivatives are two-dimensional 18 π-electron aromatic macrocycles that consist of four isoindole units linked through nitrogen atoms, **Figure 1.1**. Phthalocyanines enjoy exclusive properties such as high thermal and chemical stability, as well as acute photo-responsiveness to near-infrared (NIR) radiation. Phthalocyanines are architecturally flexible. The phthalocyanine ring can allow for the incorporation of a variety of substituents either at the non-peripheral (α) or peripheral (β) positions, modulating a varied number of important properties such as solubility, stability, and biocompatibility [1]. They have a similar (although larger) core structure to the naturally occurring porphyrin complexes such as heme, and as such, over 70 different metals or metalloids can be introduced into their inner core to form metallophthalocyanines (MPcs) via a coordinate-covalent bond between the nitrogen atoms and metal ions [2]. The various metals also help to modulate the physical, electronic, and optical properties of MPc complexes. Pcs have found applications in several fields such as optical limiting [3-5], electro-catalysis [6,7], photosensitizers in photodynamic therapy (PDT) [8-10] and in solar cell technology [11].

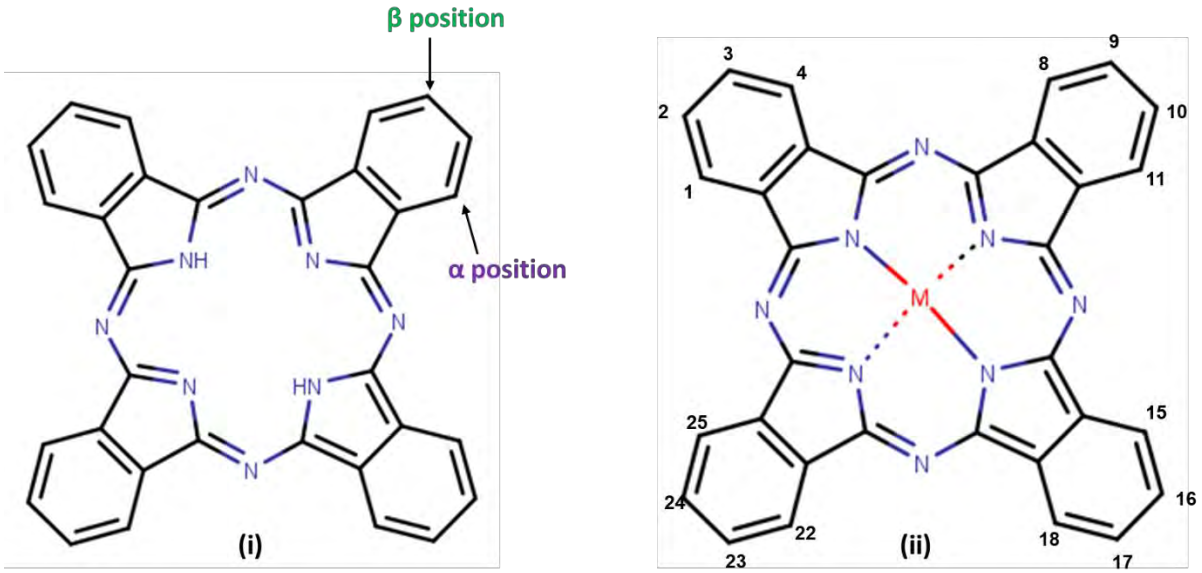

Figure 1.1: The molecular structures of (i) an unmetallated phthalocyanine (H_2Pc) and (ii) a metallophthalocyanine (MPc).

1.1.1 Synthesis of Metallophthalocyanines (MPcs)

A wide variety of ortho-disubstituted benzene derivatives such as phthalonitrile, phthalimide, phthalic anhydride, and 1,3-diiminoisoindoline have been applied as starting materials for Pc synthesis, depending on the particular application (**Scheme 1.1**). Phthalic anhydride is usually the starting material of choice for synthesis on an industrial scale since phthalic anhydride is a relatively cheaper starting material [12]. However, in a laboratory setting, a suitable phthalonitrile is often preferred because it leads to a higher purity product.

The synthesis of MPcs via the phthalonitrile route generally involves the cyclotetramerization of the desired phthalonitrile (or dicyanobenzene) derivative in the presence of a metal salt of choice, a high boiling point solvent and a catalyst (commonly 1,8-diazabicyclo [5.4.0] undec-7-ene (DBU)) with sufficient heating. MPc complexes containing metals in the +3 or +4 oxidation states (such as In^{3+}, Rh^{3+}; Sn^{3+} and Si^{4+}, etc.) are routinely reported in the literature. They can bind one

or two axial ligands. Such MPc complexes have drawn significant interest since axial ligation helps to prevent aggregation through the steric hindrance of the macrocycle.

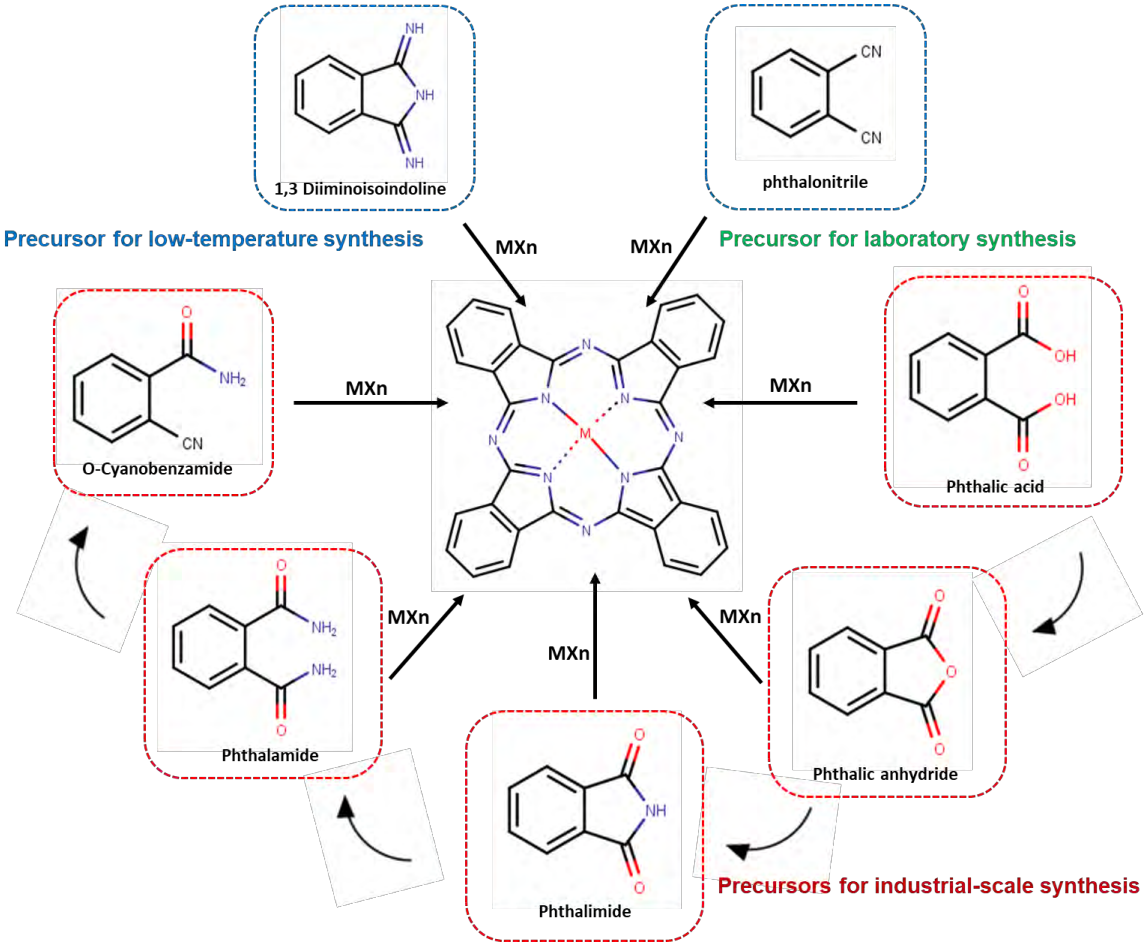

Scheme 1.1: Phthalocyanine ring showing potential sites for substitution (peripheral and non-peripheral positions) and synthesis from varied starting materials. MXn = Appropriate metal salt.

Amidst all MPcs, silicon phthalocyanines (SiPcs) have received particular interest owing to their hexacoordinated silicon (IV) [13]. Besides, the presence of two axial positions renders SiPcs unique among Pcs. Axial ligands serve to modulate the properties of SiPcs as desired. Moreover, bulky axial substituents perturb planarity and significantly help to improve solubility [14-16].

In this work, silicon phthalocyanines with axial phenolic substituents are of interest. Silicon phthalocyanine dichloride (Cl_2SiPc) was employed as a precursor molecule. In the synthesis, the axial Si–Cl bonds undergo substitution reactions with phenolic substituents to generate the corresponding symmetrically substituted bis-alkoxy derivatives.

Symmetrically substituted Pcs are synthesized by cyclo-condensation of mono-substituted phthalonitrile precursors to obtain tetra-substituted Pcs. For the synthesis of non-peripherally (α) and peripherally (β) substituted Pcs, phthalonitrile precursors substituted at the 3 and 4 positions are used, respectively. Asymmetric MPcs are often preferred where specific binding or coordination with other molecules are needed. As a result, there has been much interest in the design of asymmetrical Pcs. Besides, such Pcs exhibit better organization capabilities and exhibit unique properties, which are necessary for many applications such as photodynamic therapy, optical limiting, and catalysis.

Amongst the numerous methods employed in the synthesis of asymmetric Pcs, statistical mixed condensation of two differently substituted phthalonitriles is the most common. The resulting Pcs bear one (B) isoindole sub-unit and three identical (A) sub-units (or vice versa) (AB_3 or A_3B). The condensation of A and B isoindole subunits often results in a mixture of six compounds labeled ABBB, AABB, ABAB, BBBB, AAAB, and AAAA (**Scheme 1.2**).

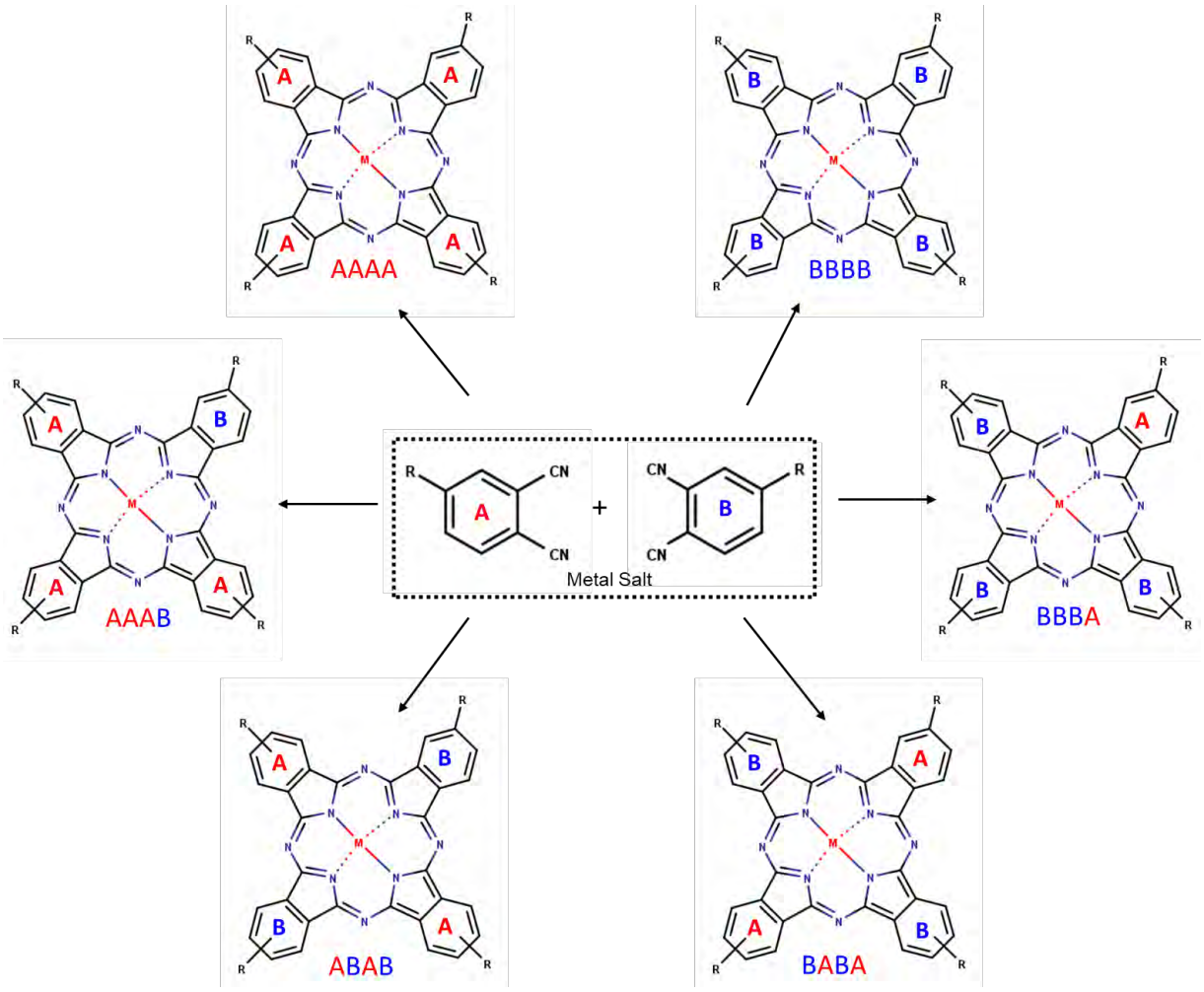

Scheme 1.2: possible outcomes from a mixed condensation reaction using the statistical condensation of phthalonitriles A and B. R = Subsituent.

High yields of asymmetrically substituted Pcs can be obtained in a ratio of A and B of 3:1. Larger mole ratios of 9:1 or higher could be employed in accordance with the reactivity of the substituents. The desired asymmetrical structure is then obtained by separating the different fractions formed via chromatographic methods. Both symmetrical (tetra-substituted) and asymmetrical (AB_3 or A_3B) MPcs complexes were employed in this work.

1.1.2 Electronic absorption spectra of MPcs

The absorption spectra of phthalocyanines are significantly influenced by whether they are metalated or not, the number, position, and nature of substituents, amongst other factors [1,17,18]. A typical electronic absorption spectrum of a metallated phthalocyanine is shown in **Figure 1.2**. The UV-vis spectrum of MPcs is characterized by a sharp absorption band in the red region of the electromagnetic spectrum called the Q band and a less intense B band (which consists of two bands) appearing between 300 – 400 nm [19,20]. Gouterman's four orbital model sufficiently describes the spectral features of phthalocyanines [21,22]. According to Gouterman's four orbital model, the Q band absorbance is due to electron transitions from the ground state (a_{1u}) highest occupied molecular orbital (HOMO) to the e_g lowest unoccupied molecular orbital (LUMO), **Figure 1.2 (insert)**. The less intense B band absorbance results from transitions from the a_{2u} to e_g and b_{2u} to e_g transitions. A single Q band characterizes metallated symmetrical Pcs, while unmetallated Pcs and asymmetrically substituted MPcs may exhibit a split Q band subject to solvent effects [23].

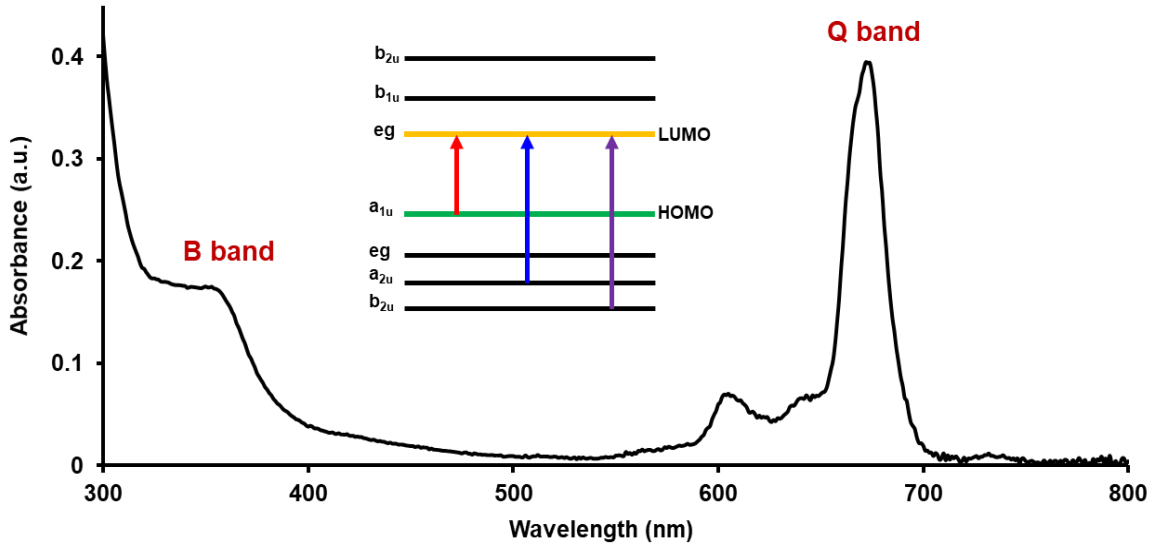

Figure 1.2: Example of ground state UV-vis spectrum of Pcs extrapolated from unpublished work. Insert = molecular orbital representation of electronic transition).

Phthalocyanines are an important sub-class of porphyrin-type molecules whose applications have been vital in several research areas. Two such important categories are the subject of this thesis, which employed the photosensitization of the Pc complex for the generation of ROS for photodynamic therapy (PDT) and in the degradation of pollutants. The following section introduces PDT.

1.2 PHOTODYNAMIC THERAPY

Photodynamic therapy (PDT) is a non-invasive cancer treatment modality that has received considerable interest owing to its merits over conventional therapies. It is noninvasive and thus presents lower risks of complications or patient scarring. PDT has been applied for the treatment of a large variety of tumors, including skin lesions [24], esophageal malignancies [25], and early central stage lung tumors [26], amongst others. In principle, PDT involves three specific

components: (i) a photosensitizer (PS) drug, (ii) molecular oxygen, and (iii) light of a specific wavelength.

Figure 1.3 shows the photochemical mechanisms (Type I and Type II) that occur following the photoexcitation of MPcs. During the photosensitization process, MPcs (initially in their ground state, S_0) absorb light. The absorbed light sensitizes MPcs from the S_0 to an excited singlet state (S_n), which converts to the S_1 state through internal conversion, **Figure 1.3**. Since the S_1 state is short-lived (10^{-9} - 10^{-6} s), it may be readily deactivated through radiative (such as fluorescence), **Figure 1.3**. Alternatively, it may undergo intersystem crossing (ISC) for the S_1 state to populate the triplet state (T_1), (a spin inversion) [27]. The T_1 state is a longer-lived state (10^{-3} - 1 s), allowing for electron transfer reactions with proximal cell components (Type I reaction) or energy transfer to molecular oxygen (Type II reaction). The Type I photochemical reaction often leads to the formation of various radicals such as hydroxyl radicals ($^{\bullet}OH$) or superoxide radicals ($O_2^{\bullet-}$). Another product of Type I photochemical reaction is the interaction of nitric oxide ($NO\cdot$) (which may be formed from nitric oxide photodonors) and superoxide radicals to form peroxynitrite ions ($ONOO^-$) as reactive nitrogen species (RNS). The Type II photochemical process leads to the generation of singlet oxygen ($^1O_2$) as the chief photogenerated product. Singlet oxygen is highly toxic and is the most important ROS in PDT [28,29].

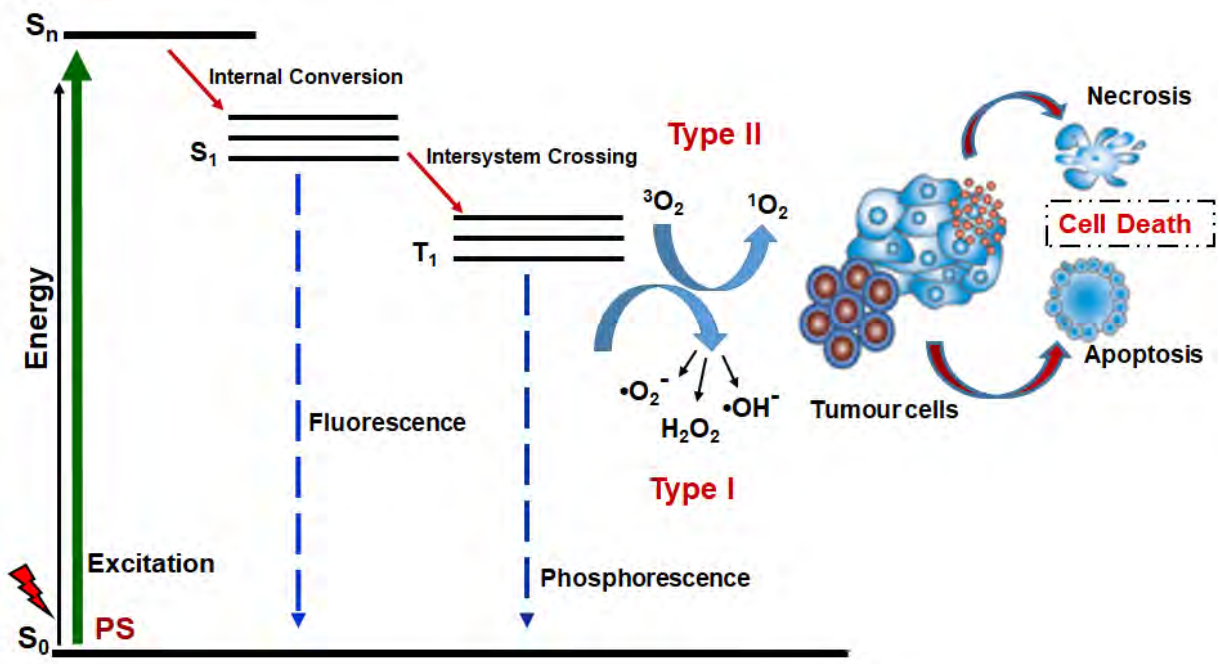

Figure 1.3: A modified Jablonski diagram showing the transition between ground state (S_0) and electronically excited states (S_1 and T_1). Abs = absorption, F = fluorescence, VR = vibrational relaxation, IC = internal conversion, intersystem crossing, Phosphorescence, S_1 = singlet excited state, T_1 = first triplet state.

Despite the promise of PDT, its full clinical translation is yet to be realized because of several reasons. These include:

(1) Suboptimal photosensitizers

(2) Poor bio-distributive properties and delivery of photosensitizer

(3) The tendency of tumor cells to survive PDT and adapt to post-therapeutic conditions owing to inadequate oxygen concentrations (Hypoxia).

This work aimed to develop approaches to enhance PDT efficacy. This involved the synthesis and evaluation of various photosensitizers. This work also evaluated the properties of PS when conjugated to nanomaterials as delivery vehicles for photodynamic therapy. As such it explored

various strategies for hypoxic alleviation/response for improved photodynamic therapy. The following sections will introduce these applications of MPcs.

1.2.1 Metallophthalocyanines as photosensitizers in Photodynamic therapy

Based on extensive biological data, an ideal photosensitizer should exhibit minimal dark toxicity with a large extinction coefficient in the optical therapeutic window (600-800 nm), which is the the spectral range of visible and NIR light (650–850 nm) characterized by a high penetration depth into human tissues [30,31]. These desired properties have served as important guidelines for designing new photosensitizers for PDT.

MPcs with central metals such as zinc (II), aluminum (III), and silicon (IV) are particularly interesting for PDT due to their highly efficient ROS generation. Many such MPcs are known photosensitizers for PDT, many of which are at various stages of clinical trials [32-36]. Some examples are shown in **Figure 1.4**.

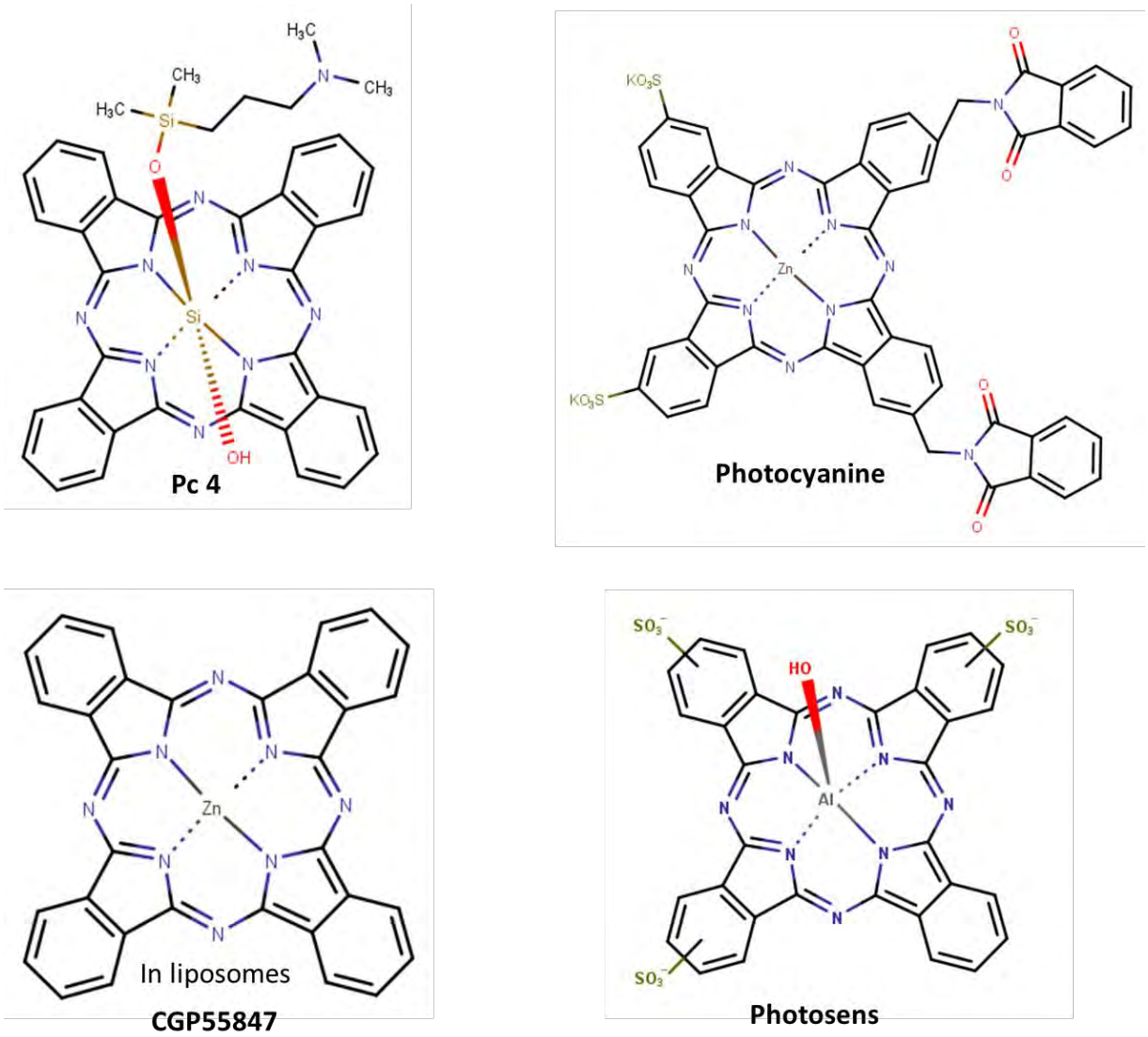

Figure 1.4: Some MPcs in clinical trials as PS for PDT.

This thesis focuses on the synthesis of various symmetric and asymmetric substituted zinc phthalocyanines and axially substituted silicon phthalocyanines for the primary purpose of developing potential photosensitizers for PDT. The efficiency of ROS generation by the employed MPcs is often indicative of their efficacy for PDT application and is examined herein.

1.2.2 Targeted delivery of the photosensitizer towards tumor tissue

The indiscriminate localization of photosensitizers in both normal and tumor tissue greatly hampers PDT success [37]. This is aggravated by the poor water-solubility and unfavorable pharmacokinetic properties of many PSs. Consequently, therapeutic performance is compromised as undesirable side effects are unavoidable [38]. PS localization is therefore crucial in PDT.

Conventionally, passive PDT targeting is facilitated by the leaky intratumoral blood vessels that characterises most tumors. Various nanomaterials have been linked to PSs, which allow their passive delivery to tumor tissue via the enhanced permeability and retention (EPR) effect [39, 40]. Additionally, many metal-based nanomaterials (particles with dimensions in the 1- 100 nm range) are known to improve the photosensitizing properties of PSs molecules by enhancing ISC through an external heavy atom effect. Nanomaterials such as graphene quantum dots [41-43] or metal-based nanoparticles such as platinum, gold, and silver nanoparticles [44-47] have been used previously as nanocarriers for PS agents. Biodegradable polymeric particles, oil dispersions, liposomes, and hydrophilic polymer-PS conjugates are also important passive targeting systems. Nanoparticle (NP) based systems therefore represent a viable method for the delivery of PSs. An ideal drug delivery system should facilitate selective delivery and accumulation of therapeutic concentrations of the PS without loss or alteration of PS activity.

In this work, liposomes were employed as the primary drug transport vehicles for the delivery of the as-synthesized MPcs. Both MPcs and MPcs-nanoparticle conjugates were subjected to liposomal loading alone or liposomes functionalized with folic acid as a targeting moiety. The PDT activity of the resultant nanocomposites were investigated herein. The following sections give a brief outline of liposomes for intratumoral PS delivery.

1.2.2.1 Liposomes

Liposomes are spherical nanostructures with one or more concentric lipid bilayers [48]. Liposomes effectively carry hydrophilic drugs within their aqueous inner core and hydrophobic components within lipophilic regions between the polar head groups of their lipid bilayer [49]. Importantly, liposomal incorporation does not adversely affect the photosensitizing ability of the encapsulated PS [50-52]. Liposomes are also highly biocompatible. Since most liposomes are made of naturally occurring phospholipids, they are non-immunogenic and non-toxic at pharmacological concentrations [53]. Liposomes are already Federal Drug Administration-approved drug delivery vehicles for Daunorubicin and Doxorubicin, and several other anti-cancer formulations [54,55].

Active drug targeting may be achieved by modifying liposomes with targeting ligands to afford cancer-specific receptor-mediated uptake. Active targeting greatly minimizes undesired side-effects associated with non-specific PS uptake and is based on targeting overexpressed or uniquely expressed molecules on cancer cell surfaces. The serum half-life of liposomes can be prolonged by the incorporation of polyethylene glycol (PEG) units. Such long-circulating liposomes allow for prolonged interaction time between the target and targeted liposome and hence afford better delivery outcomes [56]. Various targeting ligands such as carbohydrates, folic acid, antibodies, aptamers, peptides, and oligonucleotides have been used as affinity ligands [57,58]. Folic acid is used to modify liposomes in this work.

1.2.2.2 Folic Acid and Targeted Liposomes

Folic acid constitutes a distinct subclass of receptor-targeting moieties among a growing class of targeting ligands. Folic acid, a well-known water-soluble B-complex vitamin [59], selectively binds to and delivers attached drugs into any cell that expresses cell surface folate receptors (FRs). FRs are significantly up-regulated in numerous epithelial cancer cells, including ovarian, breast, brain, lung, renal, and colorectal cancer, as opposed to normal epithelia [60-62]. Normal tissues with low FR levels are consequently spared the toxicity that commonly limits non-targeted therapies. Folic acid can therefore be exploited towards folate-receptor-positive cancer cells allowing drug endocytosis via the FR [53].

Folic acid is a particularly appealing ligand for drug targeting due to its small molecular size, low immunogenicity, high binding affinity FRs on cell surfaces, and well-defined conjugation chemistry [63]. Also, the ability of FA to bind its receptor to allow endocytosis is not altered by covalent conjugation to other molecules and its applicability has been successfully demonstrated by various researchers [64,65].

In this work, FA was used as the active targeting agent to deliver phthalocyanines to cancer cells. This work further explored the differential uptake of folate targeted liposomes against hypoxic MCF-7 and HeLa cells as *in-vitro* cellular models for the first time.

1.2.3 Hypoxia

The aberrant proliferation as well as distorted blood vasculature in most tumours result in both fast consumption of oxygen and insufficient blood supply to the tumor microenvironment (TME). As a consequence, TME is characteristically hypoxic. Hypoxia is characterised by both low oxygen concentrations and acidulated tumor environments [66,67]. Hypoxia is an essential consideration in any cancer-related therapy. Hypoxia is particularly important in PDT since oxygen is a limiting factor. Since the fundamental mechanisms of PDT necessitate the presence of oxygen, it is reasonable to expect that PDT would be greatly limited by insufficient tissue oxygenation. Compounding on this, hypoxic tumor cells are much more invasive and metastatic [68] and as a result, hypoxic tumor tissues are considered the most important factor impacting patient prognosis.

In addition to low oxygen, the effectiveness of PDT is also limited by the hypoxia-induced overexpression of glutathione (GSH), which consumes ROS, further limiting PDT effectiveness [69]. Therefore, there is a clear and urgent need to develop PS candidates sensitive to the hypoxic microenvironments of tumors. This work hypothesizes that using intelligent PS candidates that are either responsive to and/or modulate tumor hypoxia could result in enhanced PDT efficacy.

Table 1.1 lists previously reported MPcs either used alone or conjugated to various nanoparticulate delivery systems for application in PDT using different cancer cell lines [52,70-81]. Although the table is not exhaustive, it is evident that most studies in PDT only seek to address either solubility issues associated with the use of metallophthalocyanines or the use of nanomaterials to improve the photophysical and photochemical properties of the various employed MPcs.

With the above in mind, this thesis aims to devise new strategies to improve PDT. NIR responsive MPcs are synthesised herein, and their PDT activity is explored. The effect of nanoparticle

conjugation on the photophysical and photochemical properties of the employed MPcs are evaluated herein. To limit PDT hypoxia-induced adaptation mechanisms within cells, this work reports on the design and synthesis of novel MPcs and MPcs-conjugates that are either responsive to hypoxia or help modulate the hypoxic microenvironment. All PSs employed in this work were subjected to liposomal loading to achieve physiological biocompatibility and improve PS delivery within tumor cells.

Table 1.1: Pcs with NPs alone or loaded in liposomes for PDT.

Phthalocyanines	Nanoparticles	Application	Reference
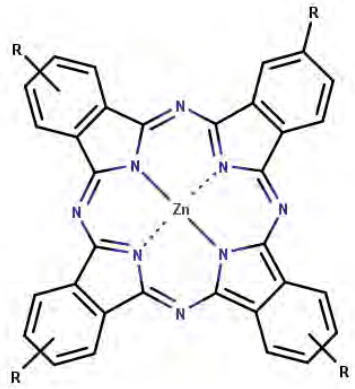 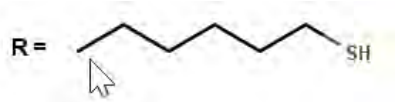	AuNPs	PDT on MCF-7 human breast cells under normoxia	[71]
	AuNPs	Photophysics and Photochemistry	[72]
	Liposomes	*In-vitro* PDT against glioblastoma cells under normoxia	[73]
	Liposomes	PDT against MDA-MB 231 breast cancer cells under normoxia	[74]

	Liposomes	*In-vitro* PDT against Human non-small cell lung cancer cells (A549) under normoxia	[75]
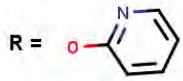	Bimetallic Pt and Fe NPs	Photophysics and Photochemistry	[76]
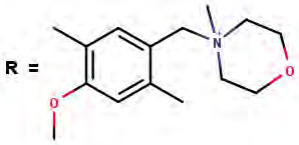	π-π stacked biotinylated graphene quantum	*In-vitro* PDT against MCF-7 cells under normoxia	[77]
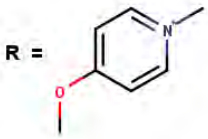	π-π stacked graphene quantum dots	*In-vitro* PDT against MCF-7 cells under normoxia	[78]
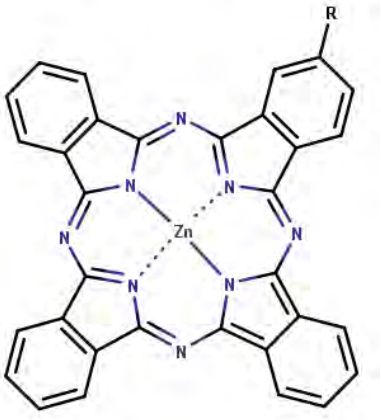	AgNPs and AuNPs	PDT on MCF-7 human breast cells under normoxia	[79]

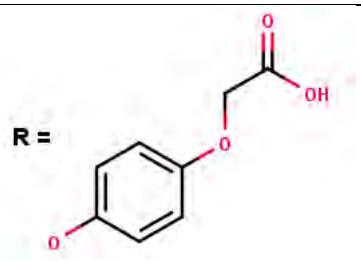 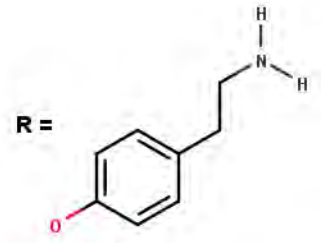	Liposomes	*In-vitro* PDT against MCF-7 cells under normoxia	[80]
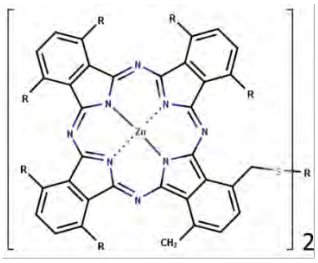 R = *n*-C_6H_{13}	AuNPs	*In-vitro* PDT against B78H1 cell line (amelanotic clone of murine melanoma) under normoxia	[70]
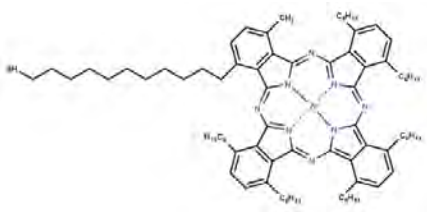	Lactose linked to AuNPs	PDT MDA-MB-231 human breast adenocarcinoma and MCF-10A human mammary epithelial cells under normoxia	[81]

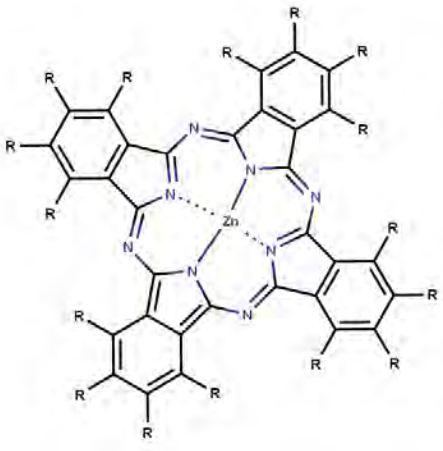 ZnPc (R = H) and $ZnF_{16}Pc$ (R = F)	Liposomes	*In-vitro* PDT against HeLa cells under normoxia	[52]

NPs = Nanoparticles

MDA-MB-231 = M.D. Anderson - Metastatic Breast 231

Besides work by Wang *et al.* [82] and Broekgaarden and co-workers [83-85], which sort to tackle the limitations of hypoxia on PDT using ZnPc and Prussian blue, there are no known studies on the use of substituted MPcs for hypoxic PDT, either alone or within liposomes. The liposomes enabled improved water solubility and potentially improved biocompatibility for photodynamic activity on both human cervical carcinoma (HeLa) and human breast adenocarcinoma (MCF-7) cell lines as *in-vitro* cancer models. The effects of symmetry on the photophysical and photochemical properties of MPcs and their PDT activity on MCF-7 and Hela cells are also investigated. This work further highlights the synergistic advantages of folate targeting and hypoxic response using MPcs-loaded liposomes for PDT for the first time.

1.3 Metallophthalocyanines conjugates employed in this work

This work focuses on the synthesis and application of various ZnPc and SiPc derivatives. ZnPc and SiPc are particularly desirable for PDT owing to their closed shell nature of the central metal which results in favorable photophysical and photochemical properties [86-88]. Moreover, being a heavy atom, Zn promotes intersystem crossing (ISC) to the triplet state, leading to complexes with high singlet oxygen generating abilities. The structures of phthalocyanines and conjugates used in this work are shown in **Table 1.2**. Complex **4** (zinc (II) 2-(carboxyethyl-4-phenyl) phthalocyanine) has been previously reported [89]. The other complexes (**1**, **2**, **3**, **5**, and **6**) are reported for the first time in this work.

In this work, MPcs and MPcs conjugates were designed to modulate hypoxia. Three general strategies were developed and explored herein; (**A**) new PSs focusing on Type I PDT or combination therapy (complex **1**), (**B**) strategies that are O_2-independent (complex **2**) and (**C**) oxygen-replenishing strategies that directly or indirectly elevate O_2 concentrations for PDT

(complexes **3** and **4**). The following sections highlight the particular mechanisms employed. Complexes **5** and **6** were not targeted.

Table 1.2: MPcs and MPc conjugates employed in this work

Pc structure and name	NPs employed	Application
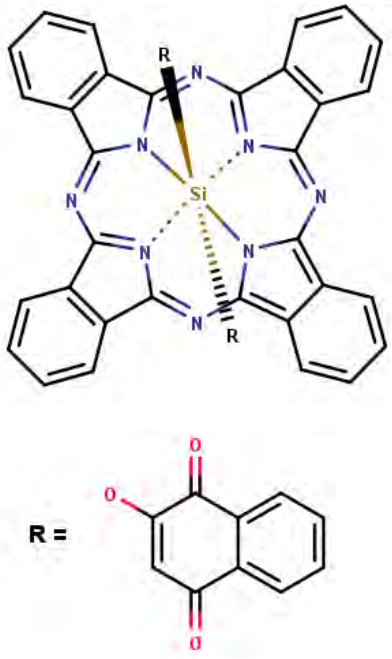 Complex **1** [**NEW**] Silicon (IV) 1,4 naphthoquinone phthalocyanine	Liposomes	Photodynamic therapy on hypoxic MCF-7 and HeLa cells
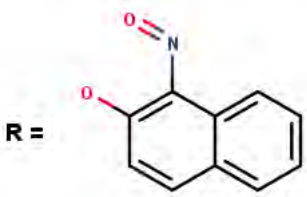 Complex **2** [**NEW**] Silicon (IV) 1-nitrosonathoquinone phthalocyanine	Liposomes	Photodynamic therapy on hypoxic MCF-7 and HeLa cells

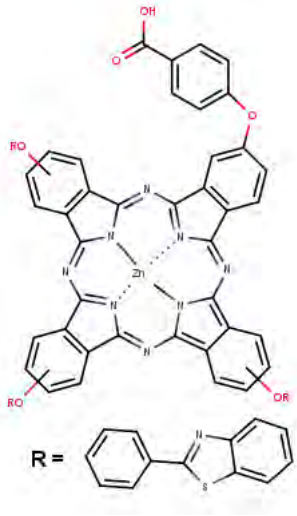 Complex **3** [**NEW**] Zinc (II) tris [(4-benzo[d]thiazol-2-ylphenoxy)-2-carboxyphenoxy phthalocyanine	Amine-functionalized GQDs – amide bonded to Pc MnO_2@AgNPs and MnO_2@AuNPs grown on the Pc-GQDs conjugate The conjugates were loaded into liposomes	Photodynamic therapy on hypoxic MCF-7 and HeLa cells
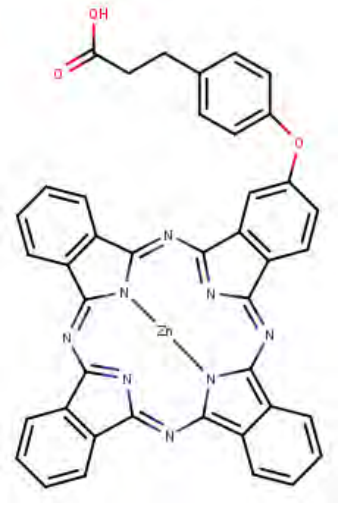 Complex **4** [89] Zinc (II) 2-(carboxyethyl-4-phenyl) phthalocyanine	Amine-functionalized graphene quantum dots (GQDs) – amide bonded to Pc MnO_2@PtNPs adsorbed onto the Pc-GQDs conjugate via Pt-N, Mn-N bonds. The conjugates were loaded into liposomes. The conjugates were also loaded into folic acid-functionalised liposomes	Photodynamic therapy on hypoxic MCF-7 and HeLa cells As a side application, complex **4** was also applied in photoelectrocatalysis with GONS and TiO_2

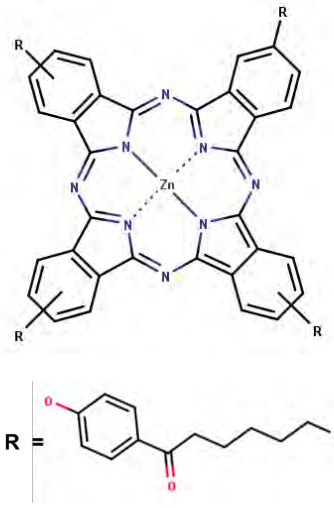 Complex **5** [**NEW**] Zinc (II) tetra (4-heptanoylphenoxy) phthalocyanine	Both Pcs were loaded into liposomes Photodynamic therapy on MCF-7 and HeLa cells as *in-vitro* models
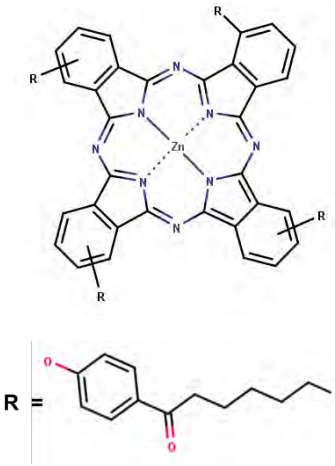 Complex **6** [**NEW**] Zinc (II) tetra (3-heptanoylphenoxy) phthalocyanine	

NPs = Nanoparticles

GQDs = Graphene quantum dots

GONS = Graphene oxide nanosheets

In this work, two hypoxic models were used: $CoCl_2$ and Oxyrase pretreatment. $CoCl_2$ is a well-documented hypoxia mimicking molecule for both *in vivo* [90] and *in-vitro* applications [91,92]. $CoCl_2$ stabilizes the hypoxia-inducible factor (HIF-1α), the central signaling factor governing hypoxia. EC-Oxyrase is a commercially available oxidase mixture that specifically removes oxygen from the micro-environment but does not generate any other gas [93,94]. The employed cells were subjected to pretreatment with $CoCl_2$ or EC-Oxyrase as *in-vitro* hypoxic cell models.

1.3.1 Group A: Type I PDT

In recent years, there has been increased research interest in using hypoxia-responsive prodrugs (HAPs). HAPs take advantage of the inherent oxygen gradient between tumor and normal tissues and are selectively activated via reductive metabolisms in sufficiently hypoxic environments. However, to date HAPs alone have only shown sub-optimal anticancer effects [95]. The combination of HAPs with PDT is an attractive alternative. This is because PDT-potentiated O_2 consumption could further enhance the effects of the HAPs with enhanced antitumor responses. Despite the potential for PDT and HAPs combinational therapy, few studies have investigated the feasibility and efficacy of this strategy. The PS is typically co-delivered with prodrug-loaded nanoparticle delivery systems such as liposomes and silica-shelled nanoparticles [96-99].

This work sort to fabricate a photosensitizer complex that integrates a hypoxic response. A prodrug-like quinone moiety was utilized in this case. Many HAPs possess the quinoid structure due to their propensity to undergo a one-electron or two-electron reduction mediated by various reductive enzymes to the active radical anions in cancer cells through Type I mechanism which destroy cancer cells.

A novel naphthoquinone-substituted SiPc (SiPc-Prodrug, complex **1**) is presented herein for use in hypoxic-tumor environments for the first time. This work reports on the direct attachment of the prodrug moiety onto the Pc structure and subsequently evaluates the PDT efficacy of the resulting complex against normoxic and hypoxic cancer cells. Such an arrangement combines the near-infrared (NIR) responsiveness and singlet oxygen generation of the SiPc with the hypoxia-responsive naphthoquinone moiety for synergistic therapy. In effect, complex **1** is employed for combinatory therapy incorporating both hypoxic response and Type I PDT. Although Type I photosensitizers have been previously reported, this work constitutes the first account of combining Type I and hypoxic response within a PS system for PDT.

1.3.2 Group B: PDT coupled with O_2-Independent Therapy

Nitric oxide (•NO) is a ubiquitous gaseous messenger with vital functions in neurotransmission and vasodilation [100]. Recently, •NO has received research interest as an intriguing therapeutic species showing excellent anticancer and antimicrobial activity. •NO has been shown to be a suitable active radical that can effectively overcome the hypoxia gradient [101,102] and its release is independent of O_2 availability. Moreover, •NO readily reacts with the superoxide anion (O_2•-) at a faster rate than with oxygen to form highly reactive peroxynitrite (OONO)[101,103,104]. This then results in the formation of •OH and •NO_2 radicals leading to impaired cellular function and, ultimately, cell apoptosis [105]. To this effect, various •NO delivery agents have been reported [106]. The engineering of novel nitric oxide (•NO) photo donors (NOPD) broaden the horizon for new and underexplored anticancer treatment modalities.

The combination of PDT with nitric oxide (NO) photo donors represents a novel and underexplored approach for multimodal phototherapy. This work hypothesized that the anti-tumor efficacy of PDT may be augmented by using an exogenous NO donor-coupled phthalocyanine. In

this work, a novel nitroso-substituted silicon phthalocyanine (NO-SiPc, complex **2**), obtained by directly attaching a NO reservoir moiety to SiPc, is presented. Combining $^1O_2$ and •NO is appealing since such systems benefit from the multitargeted activity. The efficacy of the as-synthesized complex **2** as a dual red-light responsive singlet oxygen and nitric oxide generating PDT agent is herein investigated in normoxic and hypoxic-tumor cell environments. There are limited accounts of ruthenium phthalocyanine NO donors [107]. However, to date this work constitutes the first account of a dual red-light responsive singlet oxygen and nitric oxide generating SiPc PDT agents.

1.3.3 Group C: *In-situ* oxygen generation

Elevated H_2O_2 levels are a typical feature of hypoxic tumor microenvironments. Such elevated H_2O_2 levels (50–100 μM) are a consequence of the aberrant metabolism and proliferation characteristic of tumour tissue [108-110]. H_2O_2 levels are often closely related to a tumor's occurrence and development [111]. In both normal and cancer cells, catalase is an important enzyme that protects cells from oxidative damage by catalyzing the decomposition of hydrogen peroxide (H_2O_2) to form O_2 and water. In effect, the decomposition of H_2O_2 into oxygen in tumor tissue can be exploited to improve local oxygen levels necessary for hypoxic PDT [112-116]. Despite the promise of catalase, some key inherent limitations impede its clinical adoption in PDT. These include their relatively high cost for preparation, purification, and storage, poor stability, and narrow operational pH ranges [117,118].

To overcome these shortcomings, research has focused on developing more stable alternatives. Nanozymes are inorganic materials that effectively mimic biological enzymes. With advantages such as low cost, easy large-scale production, high stability, and tunable activities, these artificial enzymes show superiority over natural enzymes [118]. Nanozymes are effective enzyme mimics

demonstrating oxidase [119], horseradish peroxidase [120,121], as well as catalase activity [122,123]. Nanozymes are therefore potential substitutes for natural enzymes. Among nanozymes, catalase-like nanozymes consisting of Prussian Blue (PB) or metals or metal oxides such as Au, MnO_2, mesoporous CeO_2, and Pt nanoparticles (NPs) have been shown to readily catalyze the breakdown of H_2O_2 to O_2 [124,125].

Motivated by the successful application of MnO_2 for hypoxic PDT, this work sort to develop novel nanozyme systems by coupling MnO_2 with other metal nanoparticles with reported catalase-like activities. In essence, this work sort to fabricate nanozyme hybrids with superior catalytic activities that are not achievable when the constituting nanomaterials are used on their own. Bimetallic nanoparticles, owing to their multifunctionality, have the possibility for a unique combination of properties that are often not realizable using pure metal components [126]. Such bimetallic catalase mimics are reported here for the first time for PDT and are outlined below.

The presence of amine groups on the GQDs permitted the conjugation of complex **3** or **4** (which possess carboxylic acid functional groups) via amide coupling to form **3**@GQDs and **4**@GQDs, respectively and MnO_2 is combined with PtNPs, Au/Ag NPs. The MnO_2 NPs are grown *in-situ* on preformed PtNPs followed by linking to **4**@GQDs to form **4**@GQDs-MnO_2@PtNPs. Ag/Au NPs and MnO_2 NPs are also grown *in-situ* in the presence of **3**@GQDs to form **3**@GQDs-MnO_2-AuNPs and **3**@GQDs-MnO_2-AgNPs. The amine-functionality of the GQDs and nitrogen and sulphur presence on **3** enabled the *in-situ* growth of AuNPs/AgNPs- MnO_2 nanozymes onto **3**@GQDs via metal-nitrogen or sulfur interactions. The PDT effect of the resulting composites were assessed herein on hypoxic tumor cell models for the first time.

This work also explores the catalase-mimicking properties of the bimetallic MnO_2 and Pt nanoparticles (MnO_2@PtNPs) over its constituent NPs for the breakdown of H_2O_2 to oxygen. This work, therefore, investigates the integration of catalase-mimicking nanozymes (the above-mentioned bimetallic MnO_2@PtNPs) with **4**@GQDs for hypoxic PDT. The PDT effect of the resulting composites were assessed herein on hypoxic tumor cell models for the first time.

1.4 Metallophthalocyanines as photocalysts for organic pollutants

As a side application of ROS, complex **4** in this work was applied in the photocatalytic degradation of organic pollutants. The need for facile catalysts for the photodegradation of common recalcitrant water pollutants has attracted research interest. Among pollutants, industrial dyes such as azo dyes containing a single or plurality of azo (–N = N-) groups are particularly important since they are not easily oxidized and, as such, persist in the environment. Moreover, their aminated biodegradation products are known carcinogens [127]. Therefore, azo dyes are an important category of pollutants, and the development of efficient methods for the degradation of organic dyes in industrial wastewater is essential and urgent. In response, research methods (physical, chemical, or biological) have been devoted towards effective water treatment methods and protocols. Physical methods such as flocculation, coagulation, adsorption, and membrane-filtration, have only shown limited success [128,129]. Fouling and secondary pollution are often major challenges of physical methods, necessitating alternative routes.

Recently, advanced oxidation processes (AOPs), particularly photoelectrocatalytic (PEC) oxidation, have been applied for water treatment. PEC synergistically incorporates both photocatalytic technology and electrochemistry for sustained ROS generation [130]. In photoelectrocatalysis, the inherent limitations of archetypal photocatalysis (such as fast recombination of electron-hole pairs) are largely resolved. Additionally, compared to electrochemical degradation, a lower anodic potential is required in a typical photoelectrocatalytic cell [131]. Several semiconductors (ZnS, ZnO, TiO_2, Fe_2O_3, CdS) have demonstrated photocatalytic properties for PEC, with TiO_2 being the most notable. Despite the interest in TiO_2, low photocatalytic rates owing to fast recombination rates of photogenerated electron-hole pairs are common. Moreover, the wide bandgap (3.2–3.4 eV) of TiO_2 confines its utilization to only UV

irradiation, with limited exploitation of solar irradiance (less than 5 %) [132,133]. Different methodologies such as doping with metal or non-metal elements have been explored to confer visible-light response to TiO_2 [134-137]. However, these have only yielded suboptimal results. Alternatively, metallophthalocyanines (MPcs), owing to their excellent visible light absorption, can confer visible light response to TiO_2, effectively sensitizing TiO_2 [138-140].

The current work eliminates the limitations of TiO_2 photocatalysts by developing an efficient-visible light responsive PEC system. This was achieved by compositing a ZnPc (complex **4**), TiO_2, and graphene oxide nanosheets (GONS) (the latter as a support material) to fabricate an efficient photo-electrocatalyst for the degradation of Orange G azo dye. A zinc (II) phthalocyanine is chosen since ZnPcs are especially visible light responsive, well over their Cu, Ni, and Fe-based counterparts [141,142]. Although photocatalyst systems employing MPcs and TiO_2 or graphene-based nanomaterials are known, PEC systems employing Pcs are limited (**Table 1.3**) [139, 143-151], hence the aim of this work. Therefore, this work builds on visible-light responsive PEC work using MPcs.

Table 1.3: Photoelectrocatalytic systems employing MPcs with GQDs/graphene or TiO_2.

Phthalocyanines	Nanoparticles	Application	Reference
	TiO_2	Photocatalysis	[143]
 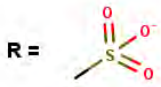	TiO_2	Photocatalysis	[144]
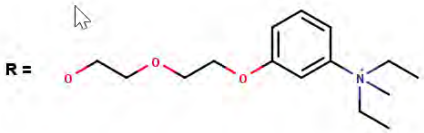	TiO_2	Photocatalysis	[145]

 **M = Zn**	TiO_2	Photocatalysis	[139]
M = Fe	TiO_2	Photoelectrocatalysis	[146]
M = Zn	carbon nitride	Photoelectrocatalysis	[147]
M = H_2	C60	Photoelectrocatalysis	[148]
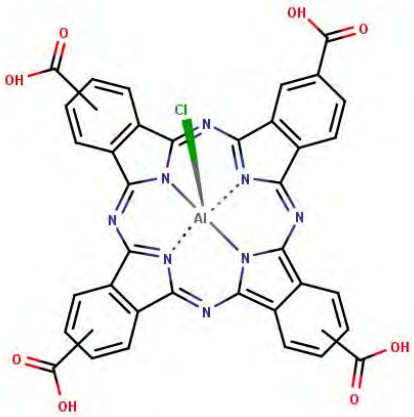	TiO_2	Photocatalysis	[149]

	-	Photoelectrocatalysis	[150]
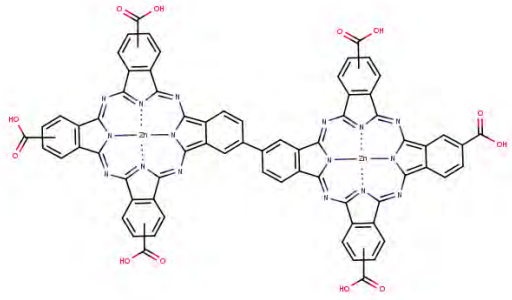 Binuclear cobalt phthalocyanine	-	Photoelectrocatalysis	[151]

1.5 Nanomaterials employed in this work

In this work, MPcs were conjugated to various nanoparticles (particles in a size range of 1–100 nm [152]. Nanomaterials can effectively modulate the photophysical and photochemical properties of MPcs. The nanoparticles of interest in this work are the carbon-based nanomaterials graphene oxide nanosheets (GONS) and graphene quantum dots (GQDs). Metal-based materials such as Pt, Au, and Ag nanoparticles, manganese oxide, and titanium dioxide nanoparticles were also used conjugated to MPcs and used to improve the photosensitizing behaviours of the employed phthalocyanines. The introduction to these nanoparticles therefore follows.

1.5.1 Graphene quantum dots (GQDs) and Graphene oxide nanosheets (GONS)

Graphene quantum dots (GQDs) are zero-dimensional, oxygen-rich (epoxy, hydroxyl, and carboxyl-containing) graphene segments with lateral dimensions less than 10 nm [153]. Research interest in GQDs can be attributed to properties such as good aqueous dispersity, pH stability, chemical inertness, and photostability which have allowed their application in a wide variety of fields [154-159].

The GQDs employed in this work possessed amine functional groups to facilitate conjugation to the employed MPcs, complex **3** and **4** (**Table 1.2**). **Table 1.1** shows some examples of MPcs with GQDs for PDT (conjugated via π-π stacking), this work constitutes the first description of the covalent conjugation of asymmetric MPcs to GQDs for PDT. Moreover, this work focuses on the application of MPcs-GQDs conjugates for hypoxic PDT for the first time.

Graphene oxide nanosheets (GONS), are ultra-thin, two-dimensional sheets of carbon atoms in a two-dimensional honeycomb lattice characterized by basal oxygen species that distort their aromaticity [160]. Their large surface area and unique electrical, catalytic, optical, and mechanical

properties have enabled them to be employed in a wide variety of applications, including photovoltaics [161] and catalysis [162]. In this work, composites of GONS, TiO_2, and MPcs are explored for PEC applicability. GONS are envisaged to act as attractive support material owing to their large surface area and they aid charge transport due to their excellent electron mobility.

1.5.2 Manganese oxide nanoparticles (MnO_2 NPs)

Transition metal oxides such as MnO_2 NPs, have received substantial research attention due to their distinct structure-property relationships in multiple fields, such as energy storage [163] and catalysis [164,165]. Recently, MnO_2 nanostructures have attracted considerable attention in biological application. Specifically, their pH sensitivity and reactivity with H_2O_2 under acidic environments can be exploited for continuous oxygen production in PDT [166,167].

The MnO_2 NPs employed in this work was synthesized primarily via the template method on preformed PtNPs. The template method was chosen because of its relative ease of synthesis, minimal use of harmful materials, and short reaction times [168]. MnO_2 NPs are also coupled with either AuNPs or AgNPs, and this work explored the resultant catalase-like properties of their MPc conjugates for PDT application for the first time. There are no reports on the coupling of MnO_2 NPs to MPcs (**Table 1.1**). This work constitutes the first report of coupling MnO_2 NPs with MPcs, and the resulting conjugates are applied for hypoxic PDT.

1.5.3 Gold and silver nanoparticles (AuNPs and AgNPs)

Among the diverse noble metal-based nanoparticles, gold nanoparticles (AuNPs) and silver nanoparticles (AgNPs) are among the most widely explored nanoparticles. Properties such as minimal cytotoxicity, chemical inertness, large-surface-area-to-volume ratios, and ease of structural and surface modifications have allowed applications in drug delivery [169,170].

Most reports of MPc conjugates with AuNPs or AgNPs focussed on symmetric Pcs. This work however, sort to explore the synthesis of conjugates involving asymmetric MPcs, complex **3** (**Table 1.2**). This work reports on the *in-situ* synthesis of bimetallic AgNPs-MnO_2 and AuNPs-MnO_2 localized on the GQDs-Pc complex (complex **3**) as support. This report investigates the effect of conjugating these hybrid nanoparticles on the photophysical and photochemical properties of the employed MPc (complex **3**). The affinity of metals for nitrogen/sulphur was exploited for the coupling of complex **3** with either AgNPs-MnO_2 or AuNPs-MnO_2. The catalase-mimicking properties of the resulting bimetallic hybrids are explored. The respective conjugates were subjected to liposomal loading and were subsequently employed for PDT against hypoxic MCF-7 breast cancer cells.

1.5.4 Platinum nanoparticles (PtNPs)

Platinum nanoparticles (PtNPs) have unique structural, catalytic, and optical properties, which have proved useful in many areas including biological applications [171-173]. Despite the utility PtNPs, the low stability of nano-scaled Pt has hampered their use in biological fields [174,175].

There are no reports on the MPcs-PtNPs conjugates (**Table 1.1**). This work represents the first report of MPcs (complex **4**) conjugates with PtNPs. To address the instability of nano-scaled Pt, this thesis reports on the use of MnO_2 NPs as surface-covering over PtNPs via *in-situ* formation over the PtNPs and herein explores the catalase mimicking ability of the resultant bimetallic MnO_2@PtNPs for the first time. This work also investigates the effect of the resulting MnO_2@PtNPs on the photophysicochemical properties of MPcs (complex **4**) (**Table 1.2**). This is done with the aim of enhancing the PDT efficacy of the employed MPcs-nanoparticle hybrids which were subsequently employed for hypoxic PDT. The as-synthesized MnO_2@PtNPs are herein adsorbed onto conjugates of complex **4** and amine-functionalized GQDs. The affinity of

metals for nitrogen was exploited for the coupling of complex **4**-GQDs conjugates with MnO_2@PtNPs.

1.5.5 Titanium dioxide (TiO_2)

Commercial forms of TiO_2 contain different ratios of anatase to rutile in order incorporate the merits of both phases. P-25 (Aeroxide), a mixture of 80% anatase and 20% rutile, is one of the most common. TiO_2 is the most widely used photocatalyst in energy and environmental applications since it is non-toxic, stable to photocorrosion, and cheap to produce [176]. Despite the wide adoption of transition metal oxides-based photocatalysts such as TiO_2, their large bandgap values and severe electron/hole recombination rates significantly hamper their efficiency to required practical levels. **Table 1.3** shows literature accounts of TiO_2-MPcs conjugates for photocatalytic and photoelectrocatalytic applications which have been limited to the use of symmetric MPcs. This work employed an asymmetric MPc (complex **4**). Asymmetric MPcs have better photophysical and photochemical properties over their symmetric counterparts. This work reports on the successful fabrication of a visible light-responsive TiO_2-graphene oxide nanosheet – complex **4** (TiO_2@GONS@**4**) ternary photocatalyst system for the photoelectrocatalytic degradation of Orange G azo dye.

1.6 PHOTOPHYSICAL AND PHOTOCHEMICAL PARAMETERS.

The photophysical and photochemical properties of phthalocyanines determine their feasibility for application in various areas such as photodynamic therapy. In effect, these properties measure changes in the electronic states of Pcs following interaction with light of appropriate wavelength. The Jablonski diagram (**Figure 1.3**) illustrates these changes, which include both radiative processes (fluorescence (F) and phosphorescence (P)) and non-radiative processes (vibrational relaxation (VR) and internal conversion (IC), vibrational relaxation (VR), and intersystem crossing (ISC) [177].

1.6.1 Fluorescence quantum yield (Φ_F) and lifetime (τ_F)

Fluorescence quantum yields (Φ_F) can be defined as the ratio of the number of fluorescing molecules to the number of photons absorbed, while fluorescence lifetime (τ_F) measures the average time spent by a fluorophore in its excited singlet state. These properties are influenced by several factors, including the solvent type, temperature, the nature of the central metal, and various energy transfer mechanisms [178]. For phthalocyanines, τ_F are usually in the nanosecond range.

In this work, fluorescence quantum yields were determined using comparative methods employing a suitable standard using Equation **1.1**.

$$\Phi_F = \Phi_{F(std)} \frac{F.A_{std}.n^2}{F_{std}.A.n^2_{std}} \qquad \textbf{1.1}$$

where F and $F_{(std)}$ are the areas under the fluorescence emission curves of the samples and the employed standard, respectively. A and A_{std} the respective absorbances of the sample and the standard at the excitation wavelength, and n and n_{std} are the respective refractive indices of solvents used for the sample and the standard. In this work, unsubstituted ZnPc in dimethylsulfoxide

(DMSO) ($\Phi_F = 0.20$) [1] was used as a standard to determine the standard for the MPcs, and quinine sulfate in H_2SO_4 (0.05 M, HCl) ($\Phi_F = 0.52$) [179] for the graphene quantum dots (GQDs).

The fluorescence lifetimes (τ_F) were determined using the time-correlated single photon counting (TCSPC) technique.

1.6.2 Triplet quantum yield (Φ_T) and lifetime (τ_T)

An optically excited molecule may either return to its ground state or undergo intersystem crossing (ISC) to its triplet state. Laser flash photolysis allows for the determination of the triplet properties of molecules by measuring the transient absorption molecules generated by short, intense light pulses [180]. The triplet quantum yield (Φ_T) measures the fraction of molecules that undergo intersystem crossing (ISC) from the first excited singlet state, S_1, to the triplet state T_1 (**Figure 1.3**). The triplet lifetime (τ_T) is the average time taken in the excited triplet state. Triplet state parameters are particularly important, especially in visible-light-driven processes such as photosensitization, since the triplet state is a prerequisite for singlet oxygen generation.

In this work, the triplet state parameters were determined experimentally using a comparative method [180] using **Equation 1.2**.

$$\Phi_T = \Phi_T^{std} . \frac{\Delta A_T . \varepsilon_T^{std}}{\Delta A_T^{std} . \varepsilon_T} \qquad \textbf{1.2}$$

where ΔA_T and ΔA_T^{std} represent changes in the triplet state absorbances of the sample and the standard, respectively. Φ_T^{std} represents the triplet state quantum yield for standard, and in this case the unsubstituted ZnPc which was employed ($\Phi_T = 0.65$ for ZnPc in DMSO) [181]. ε_T and ε_T^{std} represent the triplet state extinction coefficients of the sample and the standard, respectively. The

triplet state extinction coefficients were calculated from ground state molar extinction coefficients of the sample and standard, ε_s and ε_s^{std}, respectively, using equations **1.3a** and **1.3b**, respectively.

$$\varepsilon_T = \varepsilon_s \frac{\Delta A_T}{\Delta A_s} \quad \textbf{1.3a}$$

$$\varepsilon_T^{std} = \varepsilon_s^{std} \frac{\Delta A_T^{std}}{\Delta A_s^{std}} \quad \textbf{1.3b}$$

where ΔA_s and ΔA_s^{std} represent the changes in the ground state absorbances of the sample and the standard, respectively. The triplet lifetimes were obtained by fitting the triplet decay curves obtained from laser flash photolysis measurements using OriginPro® 8 software.

1.6.3 Singlet oxygen quantum yields (Φ_Δ)

The efficiency of singlet oxygen generation is represented by the singlet oxygen quantum yield (Φ_Δ), which is defined as the number of singlet oxygen molecules produced per quanta of light absorbed. In this study, Φ_Δ was determined using comparative photochemical methods requiring chemical scavengers with suitable standards with known singlet oxygen quantum yields. This is the most common method for quantifying singlet oxygen in laboratory settings owing mainly to its simplicity. In this work, the singlet oxygen scavenger, 1,3-diphenylisobenzofuran (DPBF) was used, and the respective quantum yields were calculated using **Equation 1.4**.

$$\Phi_\Delta = \Phi_\Delta^{std} . \frac{R^{sample} . I^{std}}{R^{std} . I^{sample}} \quad \textbf{1.4}$$

Where Φ_Δ^{std} represents the singlet oxygen quantum yield of the standard (in this case unsubstituted ZnPc with 0.67 in DMSO [1]. R^{sample} and R^{std} represent DPBF photobleaching rates in the

presence of the sample and standard, respectively. I^{sample} and I^{std} are the rates of light absorption by the sample and the standard, respectively.

1.7 Summary of Aims

This thesis work focuses on the design and synthesis MPcs-type photosensitizers for PDT. Various strategies such as coupling the as-synthesized MPcs with *in-situ* oxygen generating nanozyme hybrids, hypoxia activated prodrugs, and NO donor moieties are explored herein. The employed composites were subjected to liposomal loading to improve biocompatibility and folic acid functionalized liposomes afforded tumour specific delivery. The *in-vitro* PDT efficacy of the resultant PS systems are herein investigated using MCF-7 and Hela cell cancer cell models. This work, therefore, seeks to evaluate and validate phthalocyanine PS systems as potential hypoxia-responsive PDT agents. As a side application of ROS, some Pcs in this work were applied in the photoelectrocatalytic degradation of Orange G azo dye.

Thesis Objectives:

1. Synthesis and characterization of novel symmetrical and asymmetrical metallophthalocyanines bearing zinc or silicon central metal.
2. Fabrication of GONS, PtNPs and MnO_2@PtNPs nanoparticles.
3. Conjugation of synthesized metallophthalocyanines to the synthesized nanoparticles.
4. Investigation of the catalase-mimicking properties of various metal nanoparticles and their hybrids.
5. Spectroscopic (ground state electronic absorption and fluorescence), photophysical and photochemical evaluation of the synthesized MPs and their nanoparticle conjugates.
6. Encapsulation of the metallophthalocyanines and metallophthalocyanine conjugates into liposomes and the characterization of their nanoliposomal hybrids.

7. Cytotoxicity and photodynamic effects of liposome-encapsulated zinc phthalocyanine and silicon phthalocyanine derivatives either alone or in the presence of nanoparticles against hypoxic MCF-7 and HeLa cell lines as *in-vitro* cancer models.
8. Evaluation and comparison of photoelectrocatalytic efficiencies of the zinc phthalocyanine (complex **4**) modified with TiO_2 and GONS.

Chapter II

This chapter provides information on the materials, instrumentation, synthetic procedures, and protocols for characterization, as well as cytotoxicity and photodynamic therapy determinations of the synthesized complexes.

Experimental Section

2.1 Materials

2.1.1 General reagents and solvents

Deuterated dimethyl sulfoxide (DMSO-d_6), spectroscopic dimethyl sulfoxide (DMSO) and trifluoroacetic acid (TFA) were purchased from Merck. N, N-dimethylformamide (DMF), tetrahydrofuran (THF), chloroform and methanol were purchased from SAARChem. H_2O_2 was purchased from MONEMA. All aqueous solutions were prepared using ultrapure water obtained from ELGA, Veolia water PURELAB, chorus 2 (RO/DI) system (Marlow, UK). All other reagents and solvents were purchased from commercial suppliers and were of analytical grade and used as received.

2.1.2 Synthesis of Pcs, NPs, and their conjugates

Zinc acetate dihydrate, 1, 8-diazabicyclo [5.4.0] undec-7-ene (DBU), graphite flakes, potassium carbonate, N, N'-dicyclohexylcarbodiimide (DCC), N-hydroxysuccinimide (NHS), $KMnO_4$, gold (III) chloride hydrate, 1-pentanol, silver nitrate, hexachloroplatinic acid (H_2PtCl_6), trisodium citrate dihydrate ($Na_3C_6H_9O_9$), $NaBH_4$, 2-(*N*-morpholino) ethanesulfonic (MES) acid hydrate, 1-nitroso-2-naphthol, 2-hydroxy-1,4-naphthoquinone and $NaNO_3$ were purchased from Sigma-Aldrich. 1-Ethyl-3-(-3-dimethylaminopropyl) carbodiimide hydrochloride (EDC) was purchased from Merck. 2-Di-(9Z-octadecenoyl)-*sn*-glycero-3-phosphocholine (DOPC) and 1,2-distearoyl-*sn*-glycero-3-phosphoethanolamine-N-[amino(polyethylene glycol)-2000] (DSPE-PEG) employed for the synthesis of liposomes were sourced from Avanti Lipids (USA). Folic acid (FA) was purchased from SAARChem®. Phosphate buffered saline (PBS) was obtained from ThermoFisher.

2.1.3 Photophysicochemical studies

Anthracene-9,10-bis-methylmalonate (ADMA) and 1,3-diphenylisobenzofuran (DPBF) were purchased from Sigma Aldrich®. 2,2,6,6-Tetramethylpiperidine (TEMP) and 5,5-dimethyl-1-pyrroline N-oxide (DMPO) were obtained from Sigma-Aldrich. Unsubstituted ZnPc was synthesized from dicyanobenzene and was used as a standard for photochemical and photophysical studies of complexes in DMSO.

2.1.4 Photoelectrocatalysis

Titanium (IV) oxide (P25-TiO_2), orange G, and potassium persulfate were purchased from Sigma-Aldrich.

2.1.5 Cell studies and *in-vitro* PDT

Cultures of MCF-7 cells and HeLa cells were obtained from Cellonex®. Mouse Epithelial Fibroblasts (MEFs) were a generous gift from Prof Adrienne Edkins. 4′,6-Diamidino-2-phenylindole (DAPI), Dulbecco's Modified Eagle Medium (DMEM) cell culture media and 4-amino-5-methylamino-2',7'-dichlorofluorescein diacetate (DAF-FM DA) were obtained from ThermoFisher. Heat-inactivated fetal bovine serum (FBS) and 100 unit/mL penicillin-100 µg/mL streptomycin-amphotericin B were obtained from Biowest®. WST-1 cell proliferation neutral red reagent (Roche®), 7-dichlorofluorescin diacetate (DCFH-DA), cobalt chloride and EC-Oxyrase (EC = *E. coli*) were purchased from Sigma-Aldrich.

2.2 Equipment

1. Ground-state electronic absorption spectra were recorded on a Shimadzu UV-2550 spectrophotometer.
2. Fluorescence emission and excitation spectra were obtained on a Varian Eclipse spectrofluorometer using a 1 cm pathlength quartz cuvette. The excitation spectra were all recorded at the wavelength of the emission spectra.
3. Fluorescence lifetimes were measured using a time-correlated single photon counting setup (TCSPC), as depicted in **Figure. 2.1**. This was achieved using the Fluo Time 300, Picoquant GMbH with a diode laser as excitation source (LDH-P-670 driven by PDL 800-B, 670 nm, 20 MHz repetition rate, Picoquant GmbH). Fluorescence was detected under the magic angle with a Peltier-cooled photomultiplier tube (PMT) (PMA-C 192-N-M, Picoquant GmbH) and integrated electronics (PicoHarp 300E, Picoquant GmbH). A monochromator with a spectra width of about 4 nm was used to select the required emission wavelength. The response function of the system, which was with a scattering Ludox solution (DuPont), had a full width at half-maximum (FWHM) of about 300 ns. The ratio of stop to start pulses was kept low (below 0.05) to ensure good statistics. All fluorescence decay curves were measured at the maximum emission peak. The data were analyzed with the program FluoFit (Picoquant GmbH).

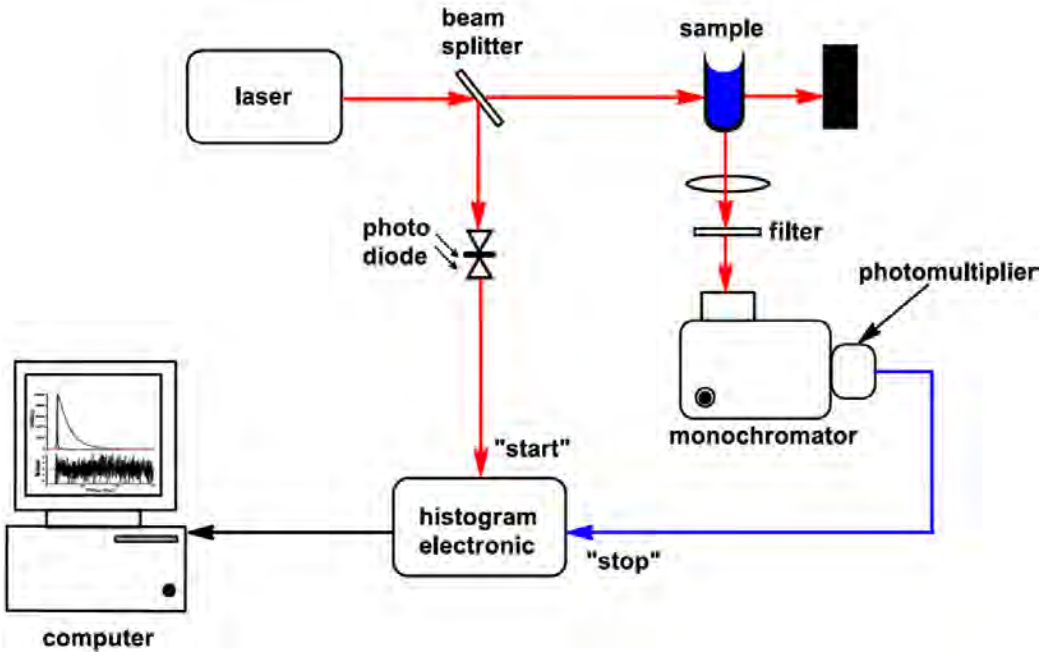

Figure 2.1: Schematic representation of a typical TCSPC setup.

4. Mass spectra data were collected with a Bruker AutoFLEX III Smart beam TOF/TOF mass spectrometer. The spectra were acquired using α-cyano-4-hydroxycinnamic acid as the MALDI matrix, and a 355 nm Nd:YAG laser as the ionizing source.
5. Elemental analyses were carried out on a Vario EL III MicroCube CHNS instrument analyzer.
6. FT-IR spectra were obtained on a Perkin-Elmer spectrum 100 with universal attenuated total reflectance (ATR) sampling accessory.
7. Zeta potential and dynamic light scattering (DLS) experiments were performed on a Malvern Zetasizer nanoseries, Nano-ZS90.
8. Atomic force microscopy (AFM) measurements in tapping mode were carried out with MFP-3D Origin supplied by Asylum research (Oxford instruments company, USA).
9. Cyclic voltammetry (CV) experiments were performed using Autolab potentiostat PGSTAT 302 electrochemical workstation (driven by GPES software version 4.9). A three-

electrode setup, where the glassy carbon electrode (GCE, 3 mm diameter) served as the working electrode, a platinum wire as the counter electrode and a silver/silver chloride (in 3.0 M KCl) wire as the reference electrode. The glassy carbon electrode (GCE) was polished to a silver mirror on a Buehler-felt pad, using alumina (< 10 μm) and then washed with Millipore water. The electrode was then sonicated for 5 min in Millipore water. In between each polishing step, the electrode was washed with Millipore water to remove impurities. The electrochemical experiments using MPcs were carried out under nitrogen in an electrochemical cell.

10. Proton-nuclear magnetic resonance spectra (^{1}H NMR) were recorded in deuterated solvent (DMSO-d_6) using either Bruker EMX400 MHz NMR spectrometer or a Bruker ADVANCE II 600 MHz spectrometer using tetramethylsilane (TMS) as an internal reference
11. Thermal gravimetric analysis (TGA) measurements were recorded over a temperature range of 50 - 800 ºC on a Perkin Elmer TGA 8000 Thermogravimetric Analyzer, operated under a nitrogen atmosphere.
12. Transmission electron microscopy (TEM) images were obtained using a Zeiss Libra TEM 120 model operated at 90 kV.
13. The scanning electron microscope (SEM) images were obtained using a JOEL JSM 840 scanning electron microscope.
14. Energy-dispersive X-ray spectroscopy (EDS) was done on an INCA PENTA FET coupled to the VAGA TESCAM using 20 kV accelerating voltage.
15. 7. X-ray diffraction (XRD) patterns were recorded using a Cu kα radiation (λ = 1.5405 Å, nickel filter), on a Bruker D8 Discover equipped with a proportional counter. Scanning was

at 10 min-1 with a filter time constant of 2.5 s per step and a slit width of 6.0 nm. The data were obtained in the range from 2θ = 10° to 100°. A zero-background silicon wafer slide was used for sample placement. The data analysis was carried out using Eva (evaluation curve fitting) software. Subtraction of spline fitted to the curved background

16. Raman spectra were obtained with a Bruker Vertex 70- Ram II spectrometer (equipped with a 1064 nm Nd:YAG laser and liquid nitrogen cooled germanium detector). For Raman experiments, a long wavelength laser (1064 nm) was employed since it allows for minimal sample fluorescence, maximising scattering efficiencies.
17. Triplet state quantum yields were determined using a laser flash photolysis system consisting of an LP980 spectrometer with a PMT-LP detector and an ICCD camera (Andor DH320T-25F03). The signal from a PMT detector was recorded on a Tektronix TDS3012C digital storage oscilloscope. The excitation pulses were produced using a tunable laser system consisting of an Nd:YAG laser (355 nm, 135 mJ/4–6 ns) pumping an optical parametric oscillator (OPO, 30 mJ/3–5 ns) with a wavelength range of 420–2300 nm (NT-342B, Ekspla). The schematic representation of the setup is shown in **Figure 2.2**. The solutions were prepared such that the sample and standard absorbance values were ~1.5 at the Q band in 1 cm path length quartz cells. The solutions were deaerated using argon and then sealed. Lastly, the solutions were illuminated using an appropriate excitation wavelength at the crossover wavelength of the sample and the standard at the Q band region is used.

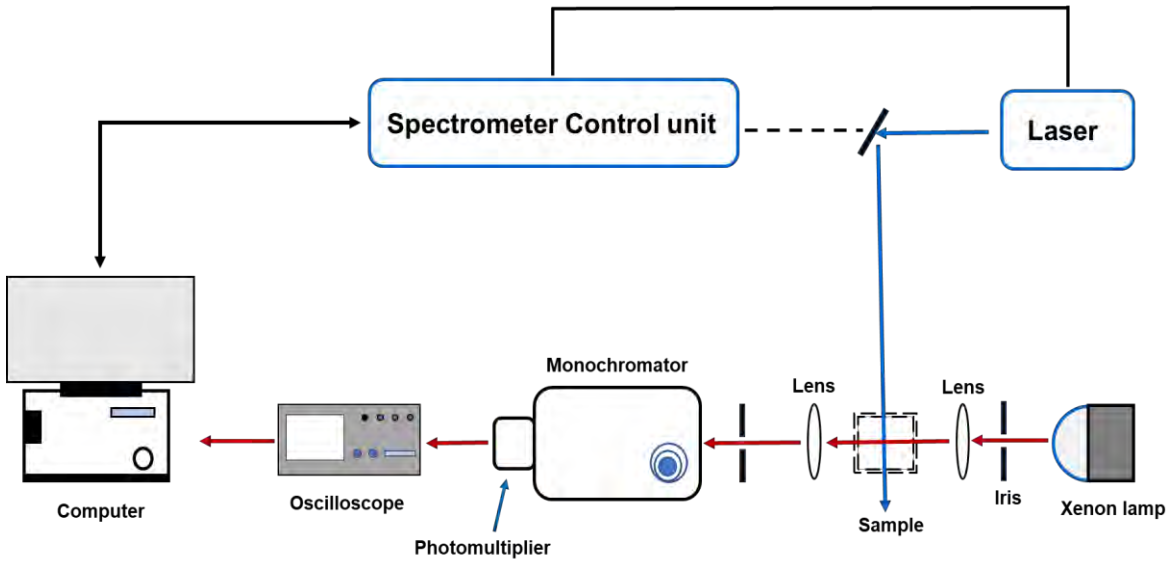

Figure 2.2: Schematic diagram of the laser flash photolysis setup.

18. The triplet lifetimes were obtained by exponential fitting of the kinetic curves using OriginPro 8 software.
19. Electron paramagnetic resonance (EPR) spectra were recorded on a Bruker EPR 300E X-band (10 GHz) spectrometer equipped with a TM probe with a flat quartz cell. The spin Hamiltonian parameters were obtained by simulation of the spectra. The static field (3000–4000 G), center field (3488–3495 G), the modulation amplitude (6.25–6.38 G), the time constant (10.24 ms), the conversion time (5.12 ms), the resolution (1024 pts), power (2.00 mW) and the modulation frequency (100 kHz) were used as the experimental parameters at 298 K with one scan. EPR spectroscopy was used to assess the generation of singlet oxygen. TEMP was used as a singlet oxygen-specific scavenger. In the presence of singlet oxygen, TEMP is oxidized to 2,2,6,6- tetramethyl piperidinyl oxy (TEMPO), which is observed as three hyperfine splitting signals of equal intensities. 5,5-Dimethyl-1-pyrroline N-oxide (DMPO) was used to probe the existence of hydroxyl radicals or superoxide radicals.

20. Irradiation for singlet oxygen quantum yield and PDT studies were performed the Modulight® Medical Laser system (ML) 7710-680 channel Turnkey laser system coupled with a 2 × 3 W channel at 680 nm, cylindrical output channels, aiming beam, integrated calibration module, foot/hand switch pedal, fiber sensors (subminiature version A) connectors and safety interlocks. Solutions of photosensitizer containing DPBF in DMSO or ADMA in aqueous media were prepared in the dark and irradiated in the Q-band region. DPBF and ADMA degradation at 417 nm and 380 respectively, was monitored during irradiation to quantify the singlet oxygen quantum yield with reference to a standard. The layout of the set-up is shown in **Figure 2.3**.
21. A Metrohm Swiss 827 pH meter was used for all pH measurements.
22. X-ray photoelectron spectroscopy (XPS) analysis was done using a Kratos AXIS Ultra DLD, with Al (monochromatic) anode equipped with a charge neutraliser, supplied by Kratos Analytical. The following parameters were used: the emission was 10 mA, the anode (HT) was 15 kV and the operating pressure below 5 x 10^{-9} torr. A hybrid lens was used and resolution to acquire scans was at 160 eV pass energy in slot mode. The centre used for the scans was at 520 eV with a width of 1205 eV, with steps at 1 eV and dwell time at 100 ms. High-resolution scans were acquired using 80 eV pass energy in slot mode.
23. Time-of-flight-secondary ion mass spectrometer (TOF-SIMS) data were recorded with an ION TOF GmbH TOF SIMS 5–100 run in micro-raster mode. The raster area was 3000 µm × 3000 µm, and the sample was run in both positive and negative ion modes. The analyzer was set to a standard operating mode with a cycle time of 100 µs; the primary beam was a Bi_3 ion cluster gun with a current of 0.4 pA and an energy of 3000 eV (also termed as spectrometry mode). The Bi_3 cluster and electron flood gun were used to get a

better ion signal from the sample. Charge compensation was used to account for the electron flood gun. The raw data were processed using the Surface Lab 6.5 software provided by ION TOF. Glassy carbon plates (Goodfellow, UK) of 1 × 1 cm and 2 mm thick were used as substrates for TOF-SIMS.

24. Light-triggered liposomal release experiments were conducted using a General Electric Quartz line projector lamp (300 W). A 600 nm glass cut off filter (Schott), and a water filter was used to filter off ultraviolet and infrared radiations, respectively. An interference filter (Intor, 670 nm with a bandwidth of 40 nm) was placed in the light path before the sample.

Figure 2.3: The Modulight® Medical Laser System used for PDT studies.

25. The various cells (MCF-7 and HeLa cells) were cultured in a humidified atmosphere incubator with ~5% CO_2 and temperature at 37 °C (Heal Force).
26. An oxygen probe (JPBJ-608 Portable Dissolved Oxygen Meter) was used to record the dissolved O_2 in H_2O_2 solutions.
27. *In-vitro* fluorescence and phase contrast imaging were performed using an Evos fluorescence microscope.
28. The *in-vitro* dark and post-treatment cell viability was measured using the cell proliferation neutral red reagent (WST-1 assay) on a Synergy 2 multi-mode microplate reader (BioTek®) at a wavelength of 450 nm.

2.3 Synthesis

Five MPcs complexes are reported here for the first time and their synthetic details are provided in this section. Details for the already known phthalonitriles: 4-(4-(benzo[d]thiazol-2-yl)phenoxy) phthalonitrile (**a**) [182], 4-(4-carboxyphenoxy)-phthalonitrile (**b**) [183], and 4-(4-(heptanoylphenoxy) phthalonitriles (**c**) [184], and Pcs: zinc(II) mono-[3-(4-phenoxy) (propanoic acid) phthalocyanine [89] and silicon phthalocyanine dichloride (Cl_2SiPc) [13] are as reported in literature. The amine -functionalized GQDs were synthesized according to reported methods [185,186].

2.3.1 Synthesis of Complex 1 (Scheme 3.1)

The synthesis of the employed complex **1** was carried out according to reported methods for axial ligand exchange in SiPcs, with slight modifications [187]. A mixture of silicon phthalocyanine dichloride, Cl_2SiPc (100 mg, 0.16 mmol), and lawsone (2-hydroxy-1,4-naphthoquinone, 142 mg, 0.81 mmol) was stirred in dimethylformamide (DMF, 20 mL) under argon for 20 min. Anhydrous K_2CO_3 was added to the solution, and the mixture was kept stirring for a further 24 h. The desired complex **1** was isolated by column chromatography using $CHCl_3$:methanol (99:1), Yield 14 %. FT-IR (UATR-TWO™) ν max/cm^{-1}: 3065, 3006 (Ar, C–H), 1650, (C = O), 1668, 1525 (C = N, C = C), 1233, 978 (Si-O-C), 809 (O-Si-O), 723 – 782 (C-H). λ_{max} (nm) (DMSO) 672 nm (log ε) 672 (4.67), 356 (4.35). ^{1}H NMR (400 MHz, DMSO-d_6) δ 9.71 – 9.44 (m, 8H), 8.54 – 8.30 (m, J = 38.2, 6.0 Hz, 8H), 7.93 – 7.72 (m, 8H), 5.84 (s, 2H). Anal. Calc. for ($C_{52}H_{26}N_8O_6Si$): C, 70.42; H, 2.29; N, 12.63. Found: C, 69.28, H, 1.88, 11.36. MALDI-TOF-MS m/z: Calculated: 886.92; Found: $[M\text{-lawsone} + H_2O]^+$ = 730.85.

2.3.2 Synthesis of Complex 2 (Scheme 3.1)

A mixture of Cl_2SiPc (100 mg, 0.16 mmol), and 1-nitroso-2-naphthol (142 mg, 0.81 mmol) was stirred in dimethylformamide (DMF, 10 ml) under argon for 20 min. Following this, K_2CO_3 was added to the solution, and the mixture was stirred for 24 h. After 24 h, the DMF was evaporated to dryness under reduced pressure. The desired NO-SiPc was isolated by column chromatography using $CHCl_3$:MeOH (98:2), Yield 16 %. FT-IR (UATR-TWO™) ν max/cm^{-1}: 3044, 3006 (Ar, C–H), 1600-1665 (C=N, C=C), 1560 (N-O), 1472-1331 (C-C), 1289 (tert, C-N), 1161 (C-N), 1235, 1072 (Si-O-C), 809 (O-Si-O), 723 – 782 (C-H). λ_{max} (nm) (DMSO) (log ε) 675 (4.96), 612 (3.68) 356 (4.35). ^{1}H NMR (400 MHz, DMSO-d_6) δ 9.64 (d, J = 27.8 Hz, 4H), 8.47 (d, J = 40.0 Hz, 6H), 7.45 – 7.29 (m, 12H), 7.23 (dd, J = 8.6, 2.1 Hz, 6H). Anal. Calc. for ($C_{52}H_{28}N_{10}O_4Si$): C, 70.58; H, 3.19; N, 15.83. Found: C, 69.52, H, 2.74, N, 15.06. MALDI-TOF-MS m/z: Calculated: 884.95; Found: [M-NO]+ = 854.90.

2.3.3 Synthesis of complex 3 (Scheme 3.2)

A mixture of 4-(4-(benzo[d]thiazol-2-yl) phenoxy) phthalonitrile (**a**) (0.6 g, 1.70 mmol), 4-(4-carboxyphenoxy)-phthalonitrile (**b**) (0.11 g, 0.42 mmol), zinc acetate (0.4 g, 2.19 mmol) dissolved in dry 1-pentanol (3 mL) was refluxed at 180 °C with constant stirring, in the presence of 1,8-diazobicylo[5.4.0]undec-7-ene (DBU, 2 drops) for 24 h under nitrogen atmosphere. Methanol was employed to precipitate the product which was collected through centrifugation. The product was purified using a silica packed column. A solvent mixture of methanol:tetrahydrofuran (3:97), and then DMF was used as eluents to give a blue powder as pure product. The purified product was dried in an enclosed fume hood, 24 % yield. FT-IR (ATR): ν (cm^{-1}): 3280 (OH), 3073 (Ar-CH), 2920 (CH), 1719 (CO), 1467 (Ar-CN). λ_{max} (nm) (DMSO) (log Ɛ): 680 (5.17), 614 (4.28), 340 (4.68). ^{1}H NMR (600 MHz, DMSO-d_6) δ 10.36 (s, 1H, COOH proton), 9.18 – 8.78 (m, 11H, Ar-

H), 8.42 – 8.08 (m, 13H, Ar-H), 7.64 – 7.46 (m, 16H, Ar-H). Anal. Calc. for ($C_{78}H_{41}N_{11}O_6S_3Zn$): C, 67.41; H, 2.97; N, 11.09; S, 6.92. Found: C, 66.54; H, 3.52; N, 10.76; S, 5.90. MALDI-TOF MS (m/z): calcd 1389.81: found 1390.21 $[M + H]^+$.

2.3.4 Synthesis of complex 5 (Scheme 3.3)

Zinc acetate $(Zn(OAc))_2$ (50.1 mg, 0.300 mmol), 4-(4-heptanoylphenoxy) phthalonitrile (**c**) (200 mg, 0.602 mmol), and DBU (0.2 mL) were mixed in 1-pentanol (5 mL) and the mixture was heated under reflux at 160 °C for 8 h. The product was cooled to room temperature, precipitated in with methanol to obtain pure product. FT-IR (ATR): ν (cm^{-1}): 3077 (Ar-H), 2929-2860 (Aliph. C-H), 1670-1587 (C=O), 1471 (C=C), 1226 (Ar-O-Ar). λ_{max} (nm) (DMSO) (log ε): 678 (4.76), 612 (4.28), 351 (4.41). ^{1}H NMR (400 MHz, DMSO-d_6) δ 8.27 – 7.70 (m, 16H), 7.48 – 7.19 (m, 12H), 1.63 (t, J = 7.1 Hz, 8H), 1.53 – 1.47 (m, 8H), 0.93 – 0.86 (m, 24H), 0.77 (t, 12H). Anal. Calc. for ($C_{84}H_{80}N_8O_8Zn$): C, 72.32; H, 5.78; N, 8.03. Found: C, 71.74; H, 5.05; N, 7.64. MALDI-TOF MS (m/z): calcd 1394.68: found 1398.14 $[M + 3H]^+$.

2.3.5 Synthesis of 3-(4-heptanoylphenoxy) phthalonitrile (d) and complex 6 (Scheme 3.3)

The 3-(4-heptanoylphenoxy) phthalonitrile (**d**) was obtained using 3-nitrophthalonitrile (503 mg, 2.91 mmol) and 1-(4-hydroxyphenyl)heptan-1-one (600 mg, 2.91 mmol), K_2CO_3 (668 mg, 4.84 mmol) in DMF (60 mL) under nitrogen atmosphere with stirring for 24 h at 60 °C. The product was isolated in ice-water, filtered and allowed to dry in the fume hood. Thereafter, the resultant solid was washed with hot methanol, and purified with ethanol to obtain compound d. Yield: 624.21 mg. ^{1}H-NMR (80 MHz, DMSO-d_6), (δ:ppm): 8.29 – 7.66 (m, 4H), 7.62 – 6.84 (m, 3H), 3.08 – 2.75 (m, 2H), 1.91 – 1.06 (m, 8H), 0.98 – 0.66 (m, 3H).

Zinc acetate $(Zn(OAc))_2$ (68.8 mg, 0.376 mmol), (3-(4-heptanoylphenoxy) phthalonitrile (**d**) (250 mg, 0.752 mmol), and DBU (0.2 mL) were mixed in 1-pentanol (5 mL) and the mixture was heated under reflux for 8 h. The product was cooled to room temperature, precipitated in with methanol to obtain pure product. FT-IR (ATR): ν (cm^{-1}): 3063 (Ar-H), 2919-2854 (Aliph. C-H), 1671-1577 (C=O), 1471 (C=C), 1235 (Ar-O-Ar). λmax (nm) (DMSO) (log ε): 694 (5.13), 621 (4.08), 342 (4.13). ^{1}H NMR (400 MHz, DMSO-d_6) δ 8.30 – 7.72 (m, 16H), 7.55 – 7.13 (m, 12H), 3.02 (t, J = 6.8 Hz, 8H), 1.35 – 1.27 (m, 32H), 0.90 (t, J = 2.3 Hz, 12H). Anal. Calc. for ($C_{84}H_{80}N_8O_8Zn$): C, 72.32; H, 5.78; N, 8.03. Found: C, 71.52; H, 5.21; N, 7.61.MALDI-TOF MS (m/z): calcd 1394.68: found 1396.28 $[M + H]^+$.

2.3.6 Nanomaterials and Pc-nanomaterials conjugates

Amine-functionalised GQDs employed in this work were synthesized using pyrolysis or the hydrothermal method according to literature specifications [188, 189].

2.3.6.1 Graphene oxide nanosheets (GONS)

The graphene oxide nanosheets (GONS) employed in this work were synthesised using the modified Hummer's method according to details from literature using graphite flakes [190]. Briefly, graphite flakes (1.5 g) were irradiated in a microwave oven at 700 W for 60 s to produce exfoliated graphite flakes (EG). Concentrated H_2SO_4 (98 %, 100 mL) was added to a mixture of EG (2.0 g) and $NaNO_3$ (2.0 g) and stirred in an ice bath for 30 min. $KMnO_4$ (3.5 g) was added, and the solution was slowly stirred for 4 h. The temperature of the reaction mixture was raised to 90 °C and left for 6 h. The reaction mixture was cooled to room temperature. Then, 100 mL of ice-cold water and 100 mL of H_2O_2 (30 %) were added followed by stirring for 2 h. The reaction mixture was centrifuged to obtain the graphene oxide nanosheets (GONS). The GONS were washed three times with 100 mL of HCl (1.0 M) to remove metal impurities and repeatedly washed with 100 mL of deionized H_2O until the pH became neutral (pH 7.0). The GONS were dried at 50 °C for 24 h.

2.3.6.2 Conjugation of complexes (3 and 4) to GQDs (Scheme 3.4)

The mixture of complex **3** (30 mg, 0.022 mmol), or complex **4** (30 mg, 0.032 mmol), DCC (0.025 g, 0.12 mmol) and NHS (15 mg, 0.130 mmol) in DMF (3 mL) was gently stirred at room temperature for 48 h to activate the carboxylic groups of the phthalocyanine complexes. Following this, amine-functionalised GQDs (15 mg) in 1:3 (v:v) water: DMF (1.5 mL) were added. The reaction mixture was subjected to further stirring for 72 h at room temperature. The product was

then collected and successively washed with deionized water, ethyl acetate, and then with ethanol by centrifugation and then dried in the fume hood to obtain **3**@GQDs and **4**@GQDs as products.

2.3.6.3 *In-situ* synthesis of 3@GQDs-MnO_2, 3@GQDs-MnO_2-AgNPs, and 3@GQDs-MnO_2-AuNPs (Scheme 3.5)

The syntheses of **3**@GQDs-MnO_2-AuNPs and **3**@GQDs-MnO_2-AuNPs involved the addition of gold (III) chloride (1 mg, 3.2 mmol) or Ag nitrate (1 mg, 5.88 mmol)) and $KMnO_4$ solutions to a solution of **3**@GQDs, followed by dropwise addition of $NaBH_4$ (0.05M) solutions. The resulting solutions were stirred vigorously for 2 min. The formed precipitates were then repeatedly washed with water, centrifuged and dried in a fume hood to obtain the respective conjugates. Similarly, the *in-situ* synthesis of MnO_2 on **3**@GQDs nanoplatforms was as follows: **3**@GQDs (10 mg) and $KMnO_4$ (2 mg, 0.0315 mmol) in 3 mL DMF:water (2:1), were sonicated together followed by dropwise addition of $NaBH_4$ (0.05M) solutions. The solution gradually changed from purple to brown. The resulting conjugate (**3**@GQDs-MnO_2) began to precipitate out of solution. The GQDs served as support layer to stabilize the as-formed NPs.

2.3.6.4 Synthesis of PtNPs, MnO_2 and MnO_2@PtNPs

MnO_2@PtNPs were synthesized by growing MnO_2 from $KMnO_4$ on the surface of pre-formed PtNPs under sonication. The small sized PtNPs (2 nm, from TEM) were synthesised using a solution of hexachloroplatinic acid as follows: aqueous solutions of H_2PtCl_6 (1 mL, 5 mM) and trisodium citrate (1 mL, 15 mM) were mixed in 20 mL water and stirred for 30 min at room temperature. Subsequently, $NaBH_4$ (200 µL, 50 mM) was added dropwise into the mixture which was separated by centrifugation and washed several times with water to remove excess salts. The formed PtNPs were then resuspended in water following which an aqueous $KMnO_4$ solution (1 mL, 0.03 M) and an aqueous 2-(*N*-morpholino) ethanesulfonic acid (MES)) solution (1 mL, 0.1

M, pH 6.0) were mixed with the PtNPs solution. The resulting mixture was subjected to sonication for 30 min until a brown precipitate was formed. The reaction mixture was centrifuged for 30 min, centrifuged, and then washed with water to remove any excess salts. MnO_2 alone was formed from $KMnO_4$ solution (1 mL, 0.03 M) and an aqueous 2-(*N*-morpholino) ethanesulfonic acid (MES)) solution (1 mL, 0.1 M, pH 6.0). The product was collected by centrifugation in water.

2.3.6.5 Synthesis of 4@GQDs-MnO_2@PtNPs (Scheme 3.6)

4@GQDs (5 mg) was solubilized in 2 mL DMSO. To this solution, MnO_2@PtNPs (5 mg) were added, and the mixture was sonicated for 12 h and then allowed to stir for further 48 h to allow for the immobilisation of the MnO_2@PtNPs onto the **4**@GQDs through the affinity of the MnO_2@PtNPs to the nitrogen of **4**@GQDs. The conjugate was precipitated out of solution using 1:1 (v:v) chloroform: ethanol mixture and dried using an in-house fume hood to obtain **4**-GQDs-MnO_2@PtNPs as product.

2.4 Liposomal loading

2.4.1 Non-targeted liposomes (Scheme 4.1)

For liposomal loading, a general procedure was followed using a conventional thin-film hydration method [191]. Generally (3 mg) of either MPc complex or conjugates with DOPC alone (0.127 mmol) or DOPC (0.127 mmol) and DSPE-PEG-NH_2 moiety (1mg/mL) were dissolved THF or in 2:1 (v:v) chloroform: ethanol (5 mL) depending on solubility. The resulting mixtures were then subjected to rotary evaporation at 40 °C to form a uniform lipid thin film, and an in-house vacuum was used overnight to remove the residual solvent. The different mixtures were then hydrated with PBS and sonicated to reduce the size of liposomes. This was followed by centrifuging to remove the unloaded components. The filtrate was freeze-dried to obtain its solid forms.

2.4.2 FA-functionalized liposomes (Scheme 4.1)

FA-functionalised liposomes were synthesised via EDC/NHS amide coupling reaction. The carboxylate group of folic acid (FA) was activated by NHS and EDC as follows; FA (0.4 mg, 0.9 mmol) was dissolved in PBS (pH 6.5, 0.5 mL). To the solution, non-targeted liposomes containing the DOPC (0.127 mmol) and DSPE-PEG-NH_2 moiety were added (1mg/mL) and the mixture was subjected to a shaker in the dark for 24 h. The resultant mixture was dialyzed against deionized waster three times using a dialysis membrane (MWCO 1000 DA) and fried dried. The product was stored at 4 °C.

The encapsulation efficiency (%EE) of PS agents encapsulated in the liposomes was determined using **Equation 2.1**:

$$Encapsulation\ Efficiency\ \ (EE) = \frac{Initial\ drug\ amount - Final\ drug\ amount}{Initial\ drug\ amount} \times 100 \qquad \textbf{2.1}$$

In each case, the final drug amount was determined by subtracting the unencapsulated drug weight from the initial drug weight. The unencapsulated drug was determined from the dried filtrate. The apparent hydrodynamic size and stability of the liposome formulations during storage was determined after a three-week storage period at 4 °C in a darkened room and undiluted.

2.5 Photodynamic therapy studies

2.5.1 Cell cultures

Michigan Cancer Foundation (MCF-7), Henrietta Lacks (HeLa), and Mouse Epithelial fibroblasts (MEF) were cultured using Dulbecco's modified Eagle's medium (DMEM) containing 4.5 g/L glucose with L-glutamine and phenol red. The medium was supplemented with 100 unit/mL penicillin-100 µg/ml streptomycin-amphotericin B and 10% (v/v) heat-inactivated fetal bovine serum (FBS) to obtain the cultured medium (supplemented DMEM). All experiments were conducted in triplicates. The cells were grown in T25 cm^2 vented flasks (Porvair®) and incubated at 37 °C and 5% CO_2. The cells were seeded into 96-well tissue culture plates (Porvair®) (1×10^4 cells per well) in cultured/supplemented DMEM containing phenol red.

2.5.2 *In-vitro* cellular uptake and imaging

The *in-vitro* cellular uptake of the employed MPcs complexes or conjugates (at 100 µg/mL each) was carried out in 96 well plates (5×10^3 cells per well). Following 24 h incubation, the cells were washed with phosphate-buffered saline (PBS) three times. After incubation at 12 h intervals at 37 °C, the cells were rinsed with PBS three times. Afterward, the cells were subjected to a Synergy 2 multi-mode microplate reader (BioTek®), and the fluorescence intensities for each sample were determined following excitation at 680 nm (owing to the presence of the Pc component). Cells with no drug treatment were used as appropriate negative controls.

A similar procedure was followed for visualizing the intracellular drug localization using HeLa cells (as an example of cancer cells) and mouse epithelial fibroblasts (MEF) in 6-well plates. To achieve this, the cells were also stained using DAPI, further incubated for 20 min, and then visualized using an Evos fluorescence microscope.

2.5.3 Measurement of intracellular NO release by DAF-FM DA

Released NO in cells was observed using the fluorescent probe DAF-FM DA (λex/ λem = 495 nm/515 nm). Typically, the employed cells were seeded in 96-well plates at a density of 5×10^3 cells per well and incubated for 24 h. After that, the medium was replaced by fresh DMEM medium containing PBS, Cl_2SiPc-liposomes or **2**-liposomes (100 μg/mL) and cells were incubated for another 12 h. After this incubation, the cells were stained with DAF-FM DA (10 μM) for 20 min. After the removal of residual DAF-FM DA by washing, the cells were resuspended in PBS. The DAF fluorescence was then determined at 515 nm using a microplate reader following excitation at 495 nm. Cells treated with DAF-FM DA alone were used as negative control.

2.5.4 Measurement of intracellular ROS by DCFH-DA

The *in-vitro* reactive oxygen species (ROS) generation by the MPc complexes was assessed using 2′,7′-dichlorofluorescein diacetate (DCFH-DA) as follows. Cells were seeded in 96-well plates were incubated overnight at 37 °C and allowed to adhere overnight. The cells were then loaded with the respective samples (100 μg/mL). After that, the medium was replaced with a fresh medium containing DCFH-DA (2 μM) and incubated at 37 °C for 20 min before treating with laser irradiation (0.28 $W{\cdot}cm^{-2}$). DCF fluorescence was measured in a multi-plate reader at excitation and emission wavelengths of 485 and 535 nm, respectively, on a Synergy 2 multi-mode microplate reader (BioTek®). Cells treated with DCFH-DA alone were used as a negative control, and those treated with H_2O_2 were used as a positive control.

2.5.5 Cytotoxicity

The dark cytotoxicity and PDT effects of the employed MPcs and conjugates (in DMEM) on MCF-7 cells were further verified by WST-assay. MCF-7 cells (1×10^4 cells) were seeded in 96-well plates and incubated overnight at 37 °C in a humidified 5% CO_2 atmosphere. The cells were then

washed twice with PBS, followed by drug administration. The drug formulations comprised 100 µL supplemented DMEM containing the as-synthesized Pcs or Pc-nanoparticle composites at a range of different concentrations and exposed to laser treatment for 10 min. The cells were then washed with PBS and re-incubated in fresh culture media for a further 24 h. Blank control wells containing the same volume of culture medium were included in each assay. Post-treatment cell viability was measured using the cell proliferation WST-1 assay on a Synergy 2 multi-mode microplate reader (BioTek®) at a wavelength of 450 nm, **Scheme 2.1**. WST-1 assay is based on measuring the overall activity of mitochondrial dehydrogenases in the sample where an expansion in the number of viable cells results in increases in the amount of formazan from cleaved tetrazolium by cellular enzymes, **Scheme 2.1**.

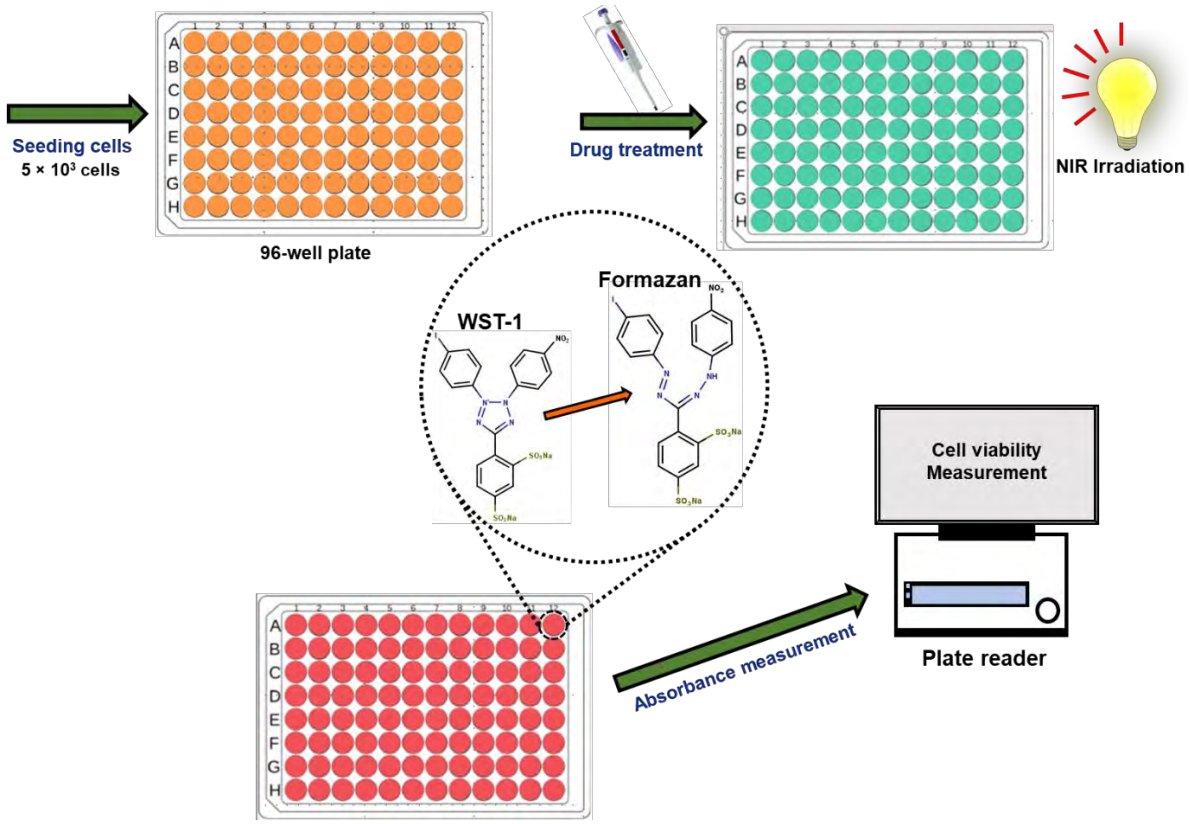

Scheme 2.1: Schematic diagram complete WST-1 cytotoxicity assay.

The percentage cell viability was determined as a function of absorbance of the sample, using **Equation 2.2**:

$$\%\ Cell\ Viability = \frac{Absorbance\ of\ the\ sample\ at\ 450\ nm}{Absorbance\ of\ the\ control\ at\ 450\ nm} \times 100 \qquad \textbf{2.2}$$

Morphological changes were examined in all controls (without irradiation) and at 24 h post-irradiation. A Zeiss® Axiovert. A1 Fluorescence LED (FL-LED) inverted microscope was used to view the cells under phase contrast.

2.6 Photoelectrocatalysis and degradation experiments

The photoelectrochemical measurements were carried out using an in-house assembled photoelectrochemical setup consisting of a 300 W Halogen lamp (OSRAM) as the light source and an AUTOLAB Potentiostat / Galvanostat PGSTAT302 N electrochemical workstation equipped with NOVA 1.10 software and FRA32 M for impedance measurement and analysis. The photocurrent measurement and degradation experiments were performed using the ITO/TiO_2@GONS@**4** as the working electrode, silver wire (Ag|AgCl) as the pseudo reference electrode, and a platinum wire as the counter electrode. The persulfate assisted degradation experiments were performed using aqueous solution of orange G (30 mL, 30 μM) and different concentrations of potassium persulfate. Sodium sulfate (0.5 M) was used as the supporting electrolyte. The degradation experiment was performed at an applied potential of 1.5 V vs. Ag|AgCl since this produced the highest photocurrent response (discussed later). An aliquot (10 mL) of the orange G solution was withdrawn every 10 min, and the change in Orange G concentration was determined by measurement of the absorption spectra. The degradation efficiency of the Orange G was calculated using **Equation 2.3**.

$$\%\, Degradation = {(A_0 - A_t)}/{A_0} \times 100 \qquad \textbf{2.3}$$

where A_0 and A_t are the absorbance values at time t = 0 and t = t, respectively. For comparison, photocatalysis (PC) and electrocatalysis (EC) degradation experiments were performed under the same conditions as PEC. The effect of the experimental conditions was optimized using the same procedure.

Results and Discussion

Chapter III: Synthesis and Characterization of Pcs, NPs, and conjugates

Chapter IV: Fabrication and Characterization of fabricated Liposomes

Chapter V: Modulation/Response to the Hypoxic Microenvironment

Chapter VI: Photophysical and photochemical parameters

Chapter VII: Photodynamic therapy

Chapter VIII: Photoelectrocatalytic degradation of orange G pollutant

Publications

The results discussed in the following chapters have been presented in the articles listed below, that have been published or submitted for publication in peer-reviewed journals. These articles have not been referenced in this thesis:

1. **Nnamdi Nwahara**, Mojahi Motaung, Garth Abrahams, Philani Mashazi, John Mack, Earl Prinsloo, Tebello Nyokong. Dual singlet oxygen and nitric oxide-releasing silicon phthalocyanine for augmented photodynamic therapy. **Materials Today Chemistry**. 26, 2022, 101201.
2. **Nnamdi Nwahara**, Garth Abrahams, John Mack, Earl Prinsloo, Tebello Nyokong. A hypoxia-responsive silicon phthalocyanine containing naphthoquinone axial ligands for photodynamic therapy activity. **Journal of Inorganic Biochemistry**. 239, 2023, 112078.
3. **Nnamdi Nwahara**, Garth Abrahams, Earl Prinsloo, Tebello Nyokong. Folic acid-modified phthalocyanine-nanozyme loaded liposomes for targeted photodynamic therapy. **Photodiagnosis and Photodynamic Therapy**. 36, 2021, 102527.
4. **Nwahara, Nnamdi**; Managa, Muthumuni; Stoffels, Mihlali; Britton, Jonathan; Prinsloo, Earl; Nyokong, Tebello. Synthesis of a near infrared-actuated phthalocyanine-lipid vesicle system for augmented photodynamic therapy. **Synthetic Metals**. 278, 2021, 116811.
5. **Nwahara, Nnamdi**; Adeniyi, Omotayo; Mashazi, Philani; Nyokong, Tebello. Visible light responsive TiO_2 - graphene oxide nanosheets - Zn phthalocyanine ternary heterojunction assisted photoelectrocatalytic degradation of Orange G. **Journal of Photochemistry and Photobiology, A: Chemistry**, 414, 2021, 113291.

6. **Nwahara, Nnamdi**; Managa, Muthumuni; Prinsloo, Earl; Nyokong, Tebello. Design of Phthalocyanine-Nanoparticle Hybrids for Photodynamic Therapy Applications in Oxygen-deficient Tumour Environment. **ChemistrySelect**, 4, 2019, 9084-9095.

Side Publications

1. Omotayo Adeniyi, **Nnamdi Nwahara**, Daniel Mwanza, Tebello Nyokong, Philani Mashazi. High-performance non-enzymatic glucose sensing on nanocomposite electrocatalysts of nickel phthalocyanine nanorods and nitrogen doped-reduced graphene oxide nanosheets. **Applied Surface Science**. 609, 2023, 155234.
2. Sivuyisiwe Mapukata, Jonathan Britton, **Nnamdi Nwahara** and Tebello Nyokong. The photocatalytic properties of zinc phthalocyanines supported on hematite nanofibers for use against methyl orange and Staphylococcus aureus. **Journal of Photochemistry and Photobiology A: Chemistry**. 424, 2022, 113637.
3. Omotayo Adeniyi; **Nnamdi Nwahara**; Daniel Mwanza; Tebello Nyokong, Philani Mashazi. Nanohybrid electrocatalyst based on cobalt phthalocyanine-carbon nanotube-reduced graphene oxide for ultrasensitive detection of glucose in human saliva. **Sensors and Actuators B: Chemical**, 348, 2021, 130723.
4. Pinar Sen, **Nnamdi Nwahara**, Tebello Nyokong. Photodynamic antimicrobial activity of benzimidazole substituted phthalocyanine when conjugated to Nitrogen Doped Graphene Quantum Dots against Staphylococcus aureus. **Main Group Chemistry**, 20, 2021, 175-191.
5. Sithi Mgidlana, **Nnamdi Nwahara**, Tebello Nyokong. Photocatalytic desulfurization of dibenzothiophene using methoxy substituted asymmetrical zinc(II) phthalocyanines conjugated to metal tungstate nanomaterials. **Polyhedron**, 197, 2021, 115053.

6. Sivuyisiwe Mapukata, **Nnamdi Nwahara**, Tebello Nyokong. The photodynamic antimicrobial chemotherapy of Staphylococcus aureus using an asymmetrical zinc phthalocyanine conjugated to silver and iron oxide-based nanoparticles. **Journal of Photochemistry and Photobiology A: Chemistry**. 402, 2020, 112813.
7. Lekgowa Collen Makola, **Nnamdi Nwahara**, Muthumuni Managa, Tebello Nyokong. Photodynamic therapy activity of 5, 10, 15-tris (5-bromo-2-thienyl), 20 (phenylcarboxy) porphyrin-conjugated to graphene quantum dot against MCF-7 breast cancer cells. Journal of Coordination Chemistry. 75, 2022, 1112-1128.

Chapter III

SYNTHESIS AND CHARACTERIZATION

This chapter describes the synthesis and characterizations of novel phthalocyanines, nanoparticles and the covalent linkage of MPcs to the different nanoparticles employed.

3 Synthesis and characterization

3.1 Metallophthalocyanines

The syntheses of complex **4** [89] and the parent dichloro silicon Pc (Cl_2SiPc) used in the synthesis of complexes **1** and **2** have been previously reported [13], and as such their syntheses and characterizations will not be discussed. Discussions on the syntheses and characterization of the new complexes (**1, 2, 3, 5,** and **6**) are elaborated below.

Complexes **1** and **2** originate from the parent dichloro silicon Pc (Cl_2SiPc). As a result, discussions on their syntheses and characterizations are combined herein for comparative reasons.

Complexes **5** and **6** only differ based on the position of the substituent groups (whether the alpha or beta positions), hence their characterization is also combined for comparative studies.

3.1.1 1,4 Naphthoquinone (lawsone) silicon (IV) phthalocyanine (1) and 1-nitrosonathoquinone silicon (IV) phthalocyanine (2), Scheme 3.1.

Both complexes **1** and **2** (Scheme 3.1) were synthesized by a base-catalyzed displacement reaction between the two chloride substituents from the parent Cl_2SiPc with either 2-hydroxy-1,4-naphthoquinone or 1-nitroso-2-naphthol in dried DMF in the presence of K_2CO_3 at room temperature. Various spectroscopic techniques were used to characterize and confirm the successful synthesis of the respective novel Pcs (complexes **1** and **2**).

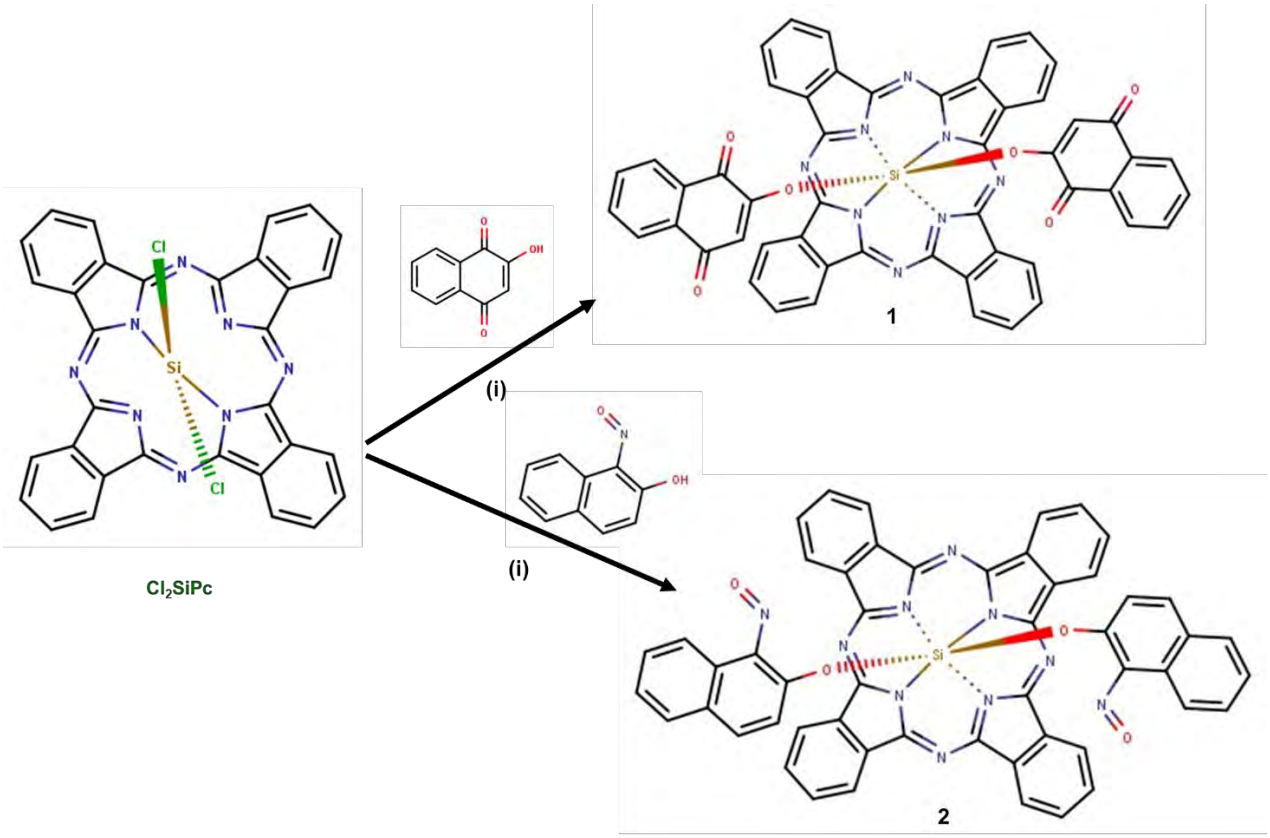

Scheme 3.1: Schematic illustration of the preparation of complexes **1** and **2** (i: DMF, K_2CO_3).

The FT-IR spectrum of complexes **1** (as an example) is shown in **Figure 3.1**, together with that of the parent Cl_2SiPc. The most striking features in the FT-IR spectrum of **1** are highlighted in black and green and include the disappearance of the Si-Cl vibration band (centered at 528 cm^{-1}) and the subsequent appearance of the characteristic Si-O-C vibrations (*ca.* 1233 and 978 cm^{-1}). For complex **1** the carbonyl stretching vibration (C=O) stemming from the naphthoquinone ring was observed at 1650 cm^{-1}. A similar spectrum was observed for complex **2**, with the asymmetric N-O stretching vibration observed at 1560 cm^{-1}. The disappearance of the Si-Cl vibration and the appearance of characteristic carbonyl and N-O stretching vibrations were decisive in confirming the successful introduction of the naphthoquinone or nitroso moieties and hence the successful synthesis of the desired complexes **1** and **2**.

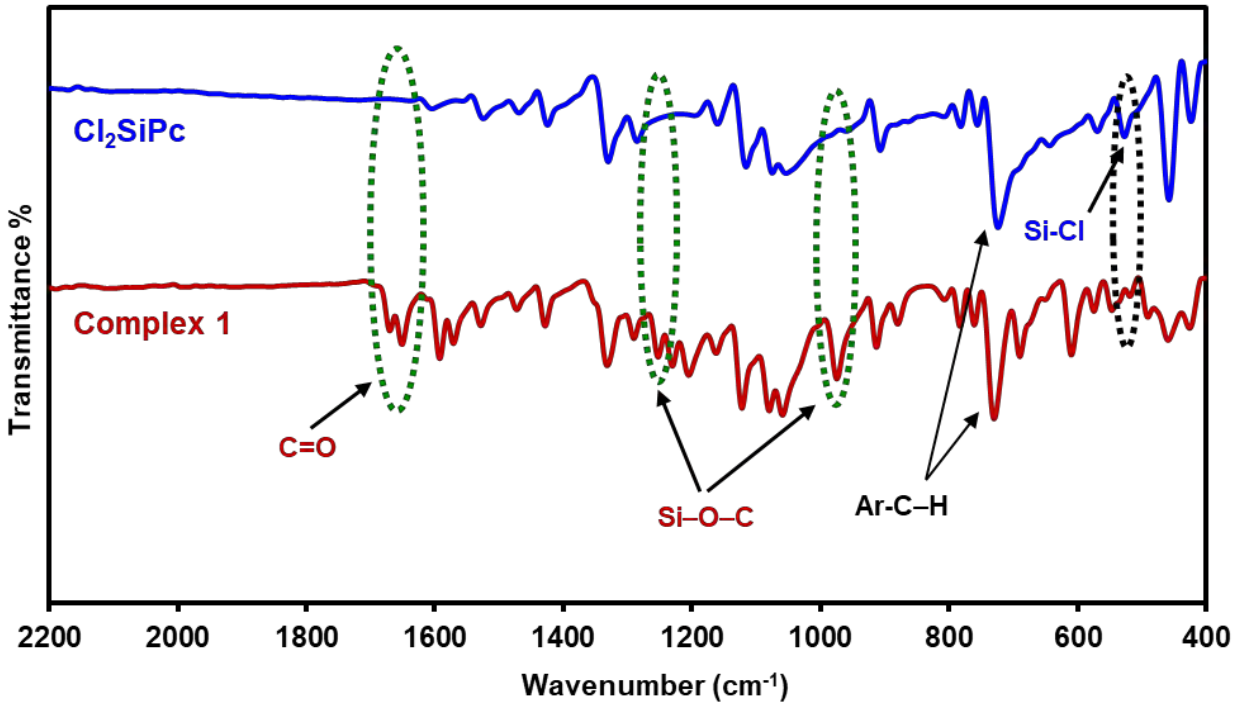

Figure 3.1: FT-IR spectra of Cl_2SiPc (blue) and complex **1** (red).

The mass spectrum for complex **1** gave an m/z peak at 730.29 which corresponds to [M-lawsone, $+H_2O$] $^+$, while that of complex **2** gave an m/z peak at 854.90 corresponding to the $[M - NO]^+$ molecular ionic peak (complex **2** used as an example, **Figure S1**). The elemental analysis values obtained corresponded with the expected values which suggested compound purities.

The ^{1}H NMR spectrum of complex **1** and **2** (complex **1** used as example, **Figure S2**) shows signals that integrate to give the expected number of protons in the expected regions. Only aromatic protons were observed. The phthalocyanine ring ^{1}H resonances appear as two downfield-shifted multiplets integrating each as 8 H at around 9.71 – 9.44 and 8.54 – 8.30 ppm, for the α and β protons, respectively for complex **1**. The singlet at 5.84 was ascribed the proton of the axial naphthoquinone, shifted compared to lawsone alone at 6.2 ppm in DMSO [192]. The singlet ^{1}H resonance of the axial substituent was observed strongly shifted upfield since it experiences a large

diamagnetic ring-current shielding effect induced by the macrocyclic ring. Peak integration gave the anticipated total number of protons, confirming the successful synthesis of **1**. Only aromatic protons were observed in the ^{1}H NMR spectrum of **2** with peaks located between 9.64 and 7.23 ppm. Peak integration gave the anticipated total number of protons, confirming the successful synthesis of **2**.

The elemental composition of the as-synthesized complexes **1** and **2** were confirmed using X-ray photoelectron spectroscopy (XPS) as an effective surface analysis technique (complex **2** shown as an example). **Figure 3.2** shows the survey scan of **2** and Cl_2SiPc for comparison. The XPS survey scan spectrum of **2** shows peaks at 102.1, 153.1, 283.8, 397.6, and 530.2 eV corresponding to the electronic states of Si 2p, Si 1s, C 1s, N 1s, and O 1s, respectively. The XPS survey spectrum of Cl_2SiPc shows the presence of various elements at their respective binding energies attributed to silicon (Si 2s and Si 2p), carbon (C 1s), oxygen (O 1s), nitrogen (N 1s) and chlorine (Cl 2p) chemical components. The disappearance of the Cl 2p peak in the spectrum of the complex **2** implies the successful axial ligand exchange and hence the successful synthesis of the desired complex **2**.

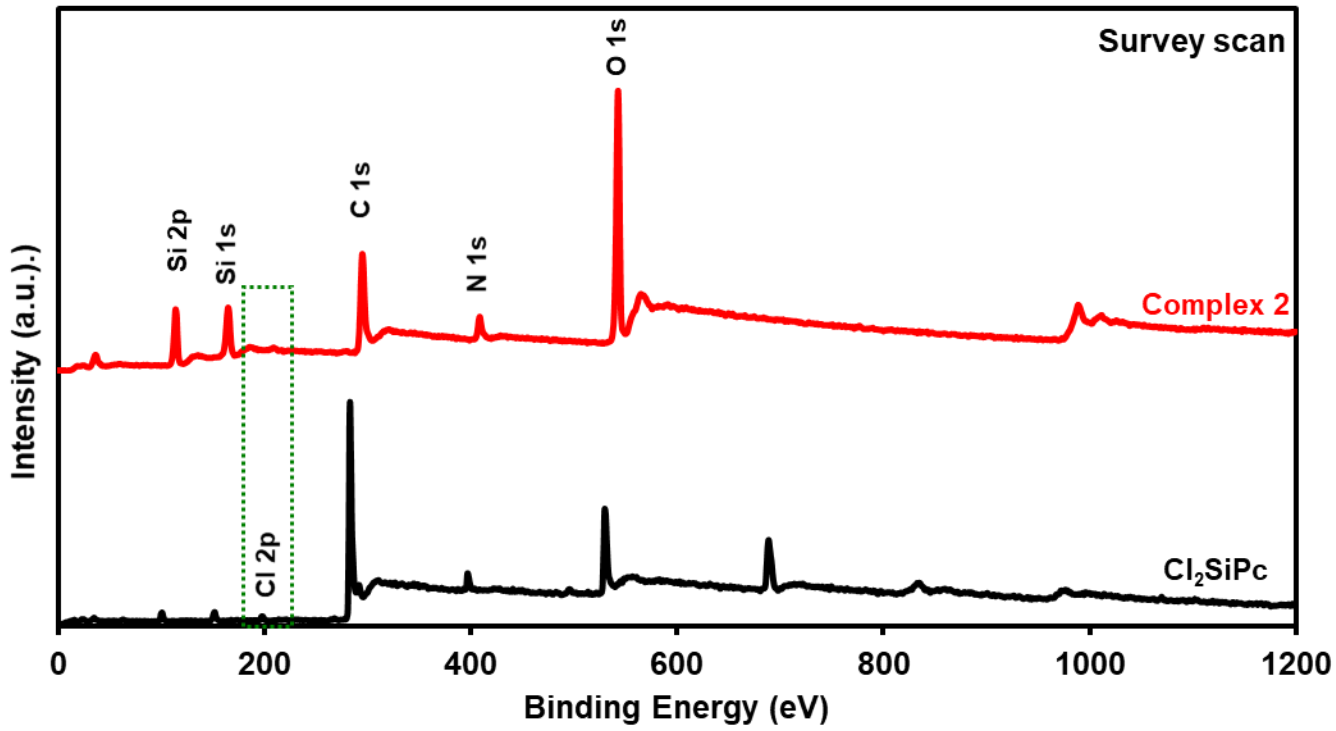

Figure 3.2: XPS survey spectra of complex **2** and Cl_2SiPc.

The deconvoluted high-resolution core level C 1s, N 1s, O 1s, and Si 2p XPS spectra of **2** are shown in **Figure 3.3**. The O 1s core-level spectrum was deconvoluted, and three chemically distinct peaks resulted. The resultant peaks at 532.4 eV, 535.7 eV, and 536.2 eV were attributed to the O–Si, O–C, and O=N, respectively. The presence of the O-Si peak signifies the successful attachment of the nitroso moiety to the Pc-core structure and hence successful synthesis of the desired complex **2**. The three peaks of the deconvoluted high-resolution N1s core-level spectrum were assigned to the N–Si (401.6 eV), N–C (404.5 eV), and the N=C or nitroso N=O (407.4 eV) [193]. The C 1s core-level spectrum could be fitted into three chemically distinct components centered at 286.4 eV, 288.6 eV, and 290 eV, which were attributed to C=C, C–O/C–N, and C=N [194]. The high-resolution Si 2p spectrum was deconvoluted to two peaks assigned to Si–N (103.8 eV) and Si–O–C (105.2 eV).

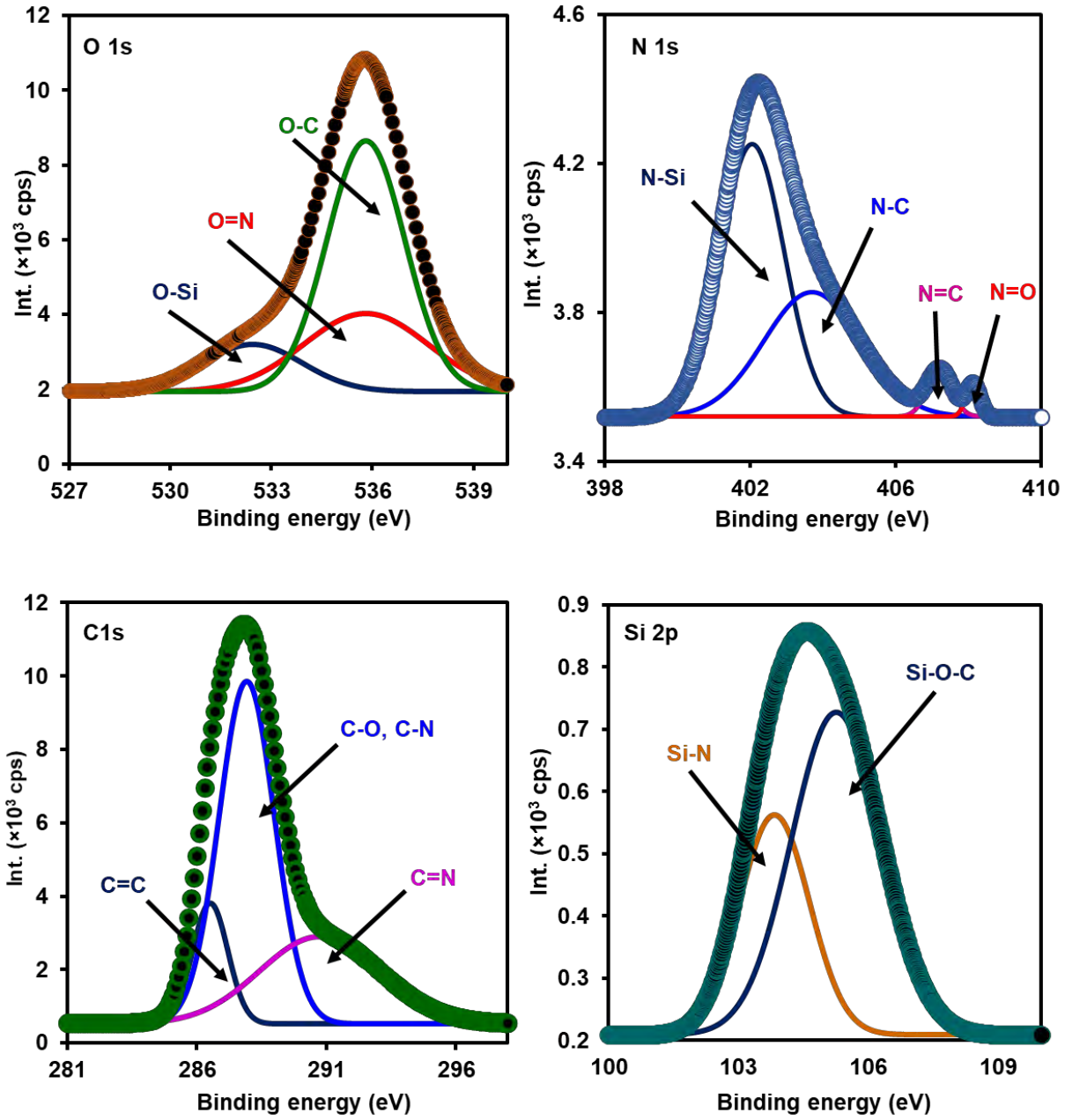

Figure 3.3: High-resolution O 1s, N 1s, C 1s, and Si 2p spectra of the as-synthesized complex **2**.

Figure S3 shows the C 1s core-level spectrum for **1**, which could be deconvoluted into four chemically distinct components centered at 283.5, 284.1, 285.7, and 292.8 eV. The components at 283.5 eV and 292.8 eV were attributed to the phenyl aromatic sp^2 carbon of the Pc-core as well as the axial naphthoquinone moiety (C=C) and the core isoindole units (C=N), respectively [195]. The components at 284.1 and 285.7 eV were attributed to the axial C-O and C=O bonds stemming from the naphthoquinone axial ligand, respectively. The core-level O 1s spectrum was deconvoluted into three distinct chemical environments at 530.6, 532.2, and 537.5 eV corresponding to O-Si, O-C, and O=C, respectively [196]. The presence of the O-Si peak signifies successful ligand exchange and hence synthesis of complex **1**. The component at high binding energy (537.5 eV) results from the carbonyl (O=C) of the axial naphthoquinone moiety. The two peaks of the deconvoluted core-level N 1s spectrum were assigned to the N-Si and N=C chemical environments at 397.8 and 399.7 eV, respectively. Likewise, the Si 2p core-level spectrum was deconvoluted into two chemically distinct components at 100.7 and 101.6 eV and assigned to Si-N and Si-O, respectively. The Si-N can be explained from the structure of complex **1** since the silicon metal core is bound to the phthalocyanine core by coordinate bonds to nitrogen.

For both complex **1** and **2**, the observations from XPS corroborate with FT-IR results with the presence of the C=O, C-O, N=O and Si-O groups. Taken together, these observations imply successful ligand exchange and hence successful synthesis of the desired complexes, **1** and **2**.

3.1.2 Synthesis of zinc (II) tris [(4-benzo[d]thiazol-2-ylphenoxy)-2-carboxyphenoxy phthalocyanine (3), Scheme 3.2

Mass spectral data agreed with the proposed structure for complex **3** (**Figure S4**). The mass spectrum of **3** gave an m/z peak at 1390.2, which corresponds to the $[M+1]^+$ molecular ionic peak. ^{1}H NMR spectrum for complex **3** gave aromatic protons between 9.18 - 7.46 ppm (figure not shown). The aliphatic proton attributable to the carboxyl group was observed at 10.36 ppm. Peak integration gave the expected total number of protons, confirming the relative purity of complex **3**. Elemental analysis values corresponded with expected values and suggest purity of the synthesized complex.

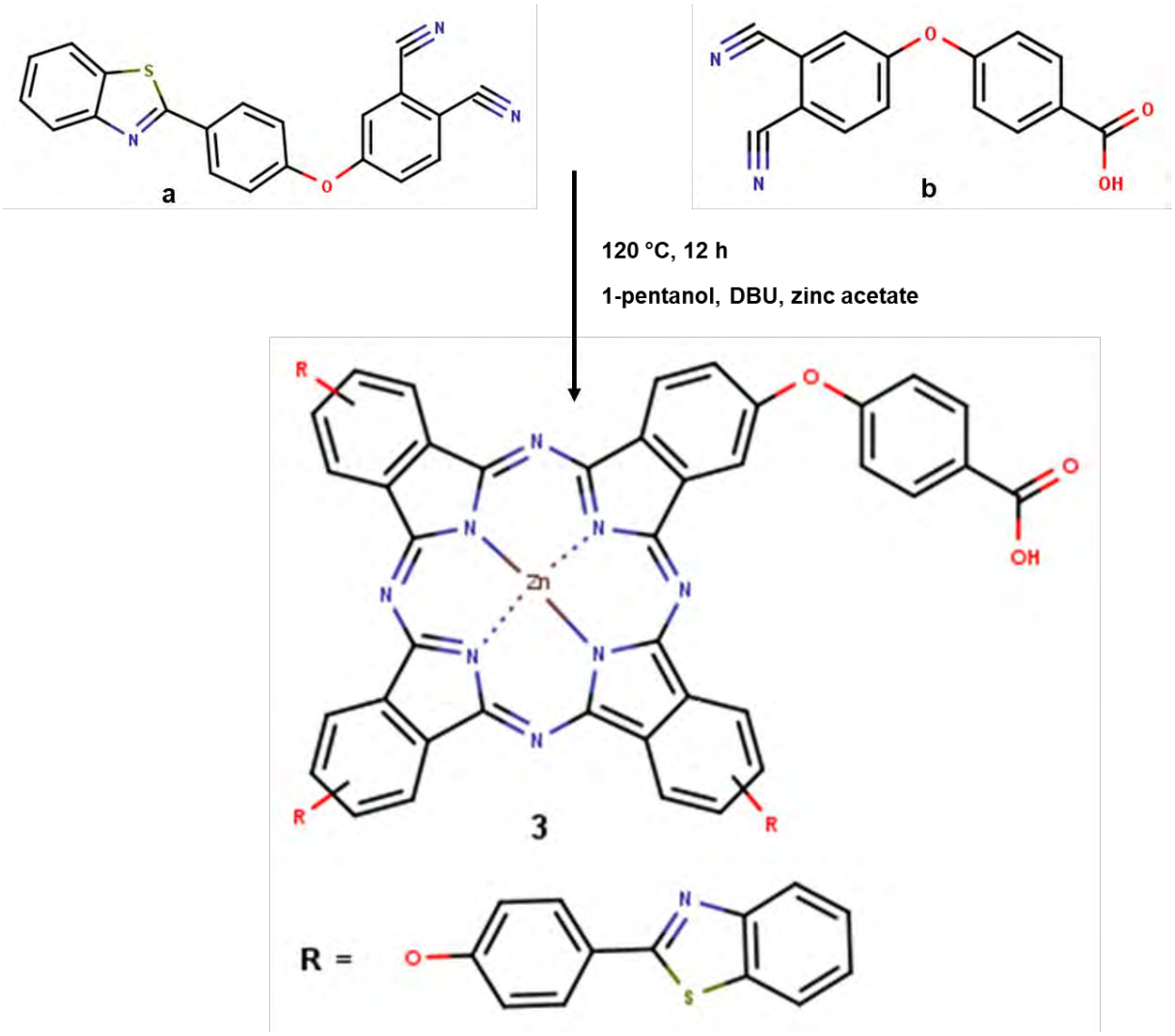

Scheme 3.2: Schematic illustration of the synthesis of complexes **3**.

3.1.3 3-(4-heptanoylphenoxy) phthalonitrile (d), tetra (4-heptanoylphenoxy) phthalocyanato zinc (II) (5) and Tetra (3-heptanoylphenoxy) phthalocyanato zinc (II) (6), Scheme 3.3.

The 3-(4-heptanoylphenoxy) phthalonitrile (**d**) was obtained by nucleophilic substitution reaction between 3-nitrophthalonitrile and 1-(4-hydroxyphenyl) heptan-1-one with K_2CO_3 as base. ^1H NMR peak integration gave the expected total number of protons, confirming the relative purity of 3-(4-heptanoylphenoxy) phthalonitrile (**d**). Mass spectral data agreed with their proposed structures (only **5** shown in **Figure S5**). The mass spectrum of **5** and **6** gave an m/z peak at 1398.14 and 1396.28, which corresponds to the $[M+3H]^+$ and $[M+H]^+$ molecular ionic peaks respectively. Both **5** and **6** were adequately confirmed using elemental analysis. ^1H NMR peak integration gave the expected total number of protons, confirming the relative purity of complexes **5** and **6**.

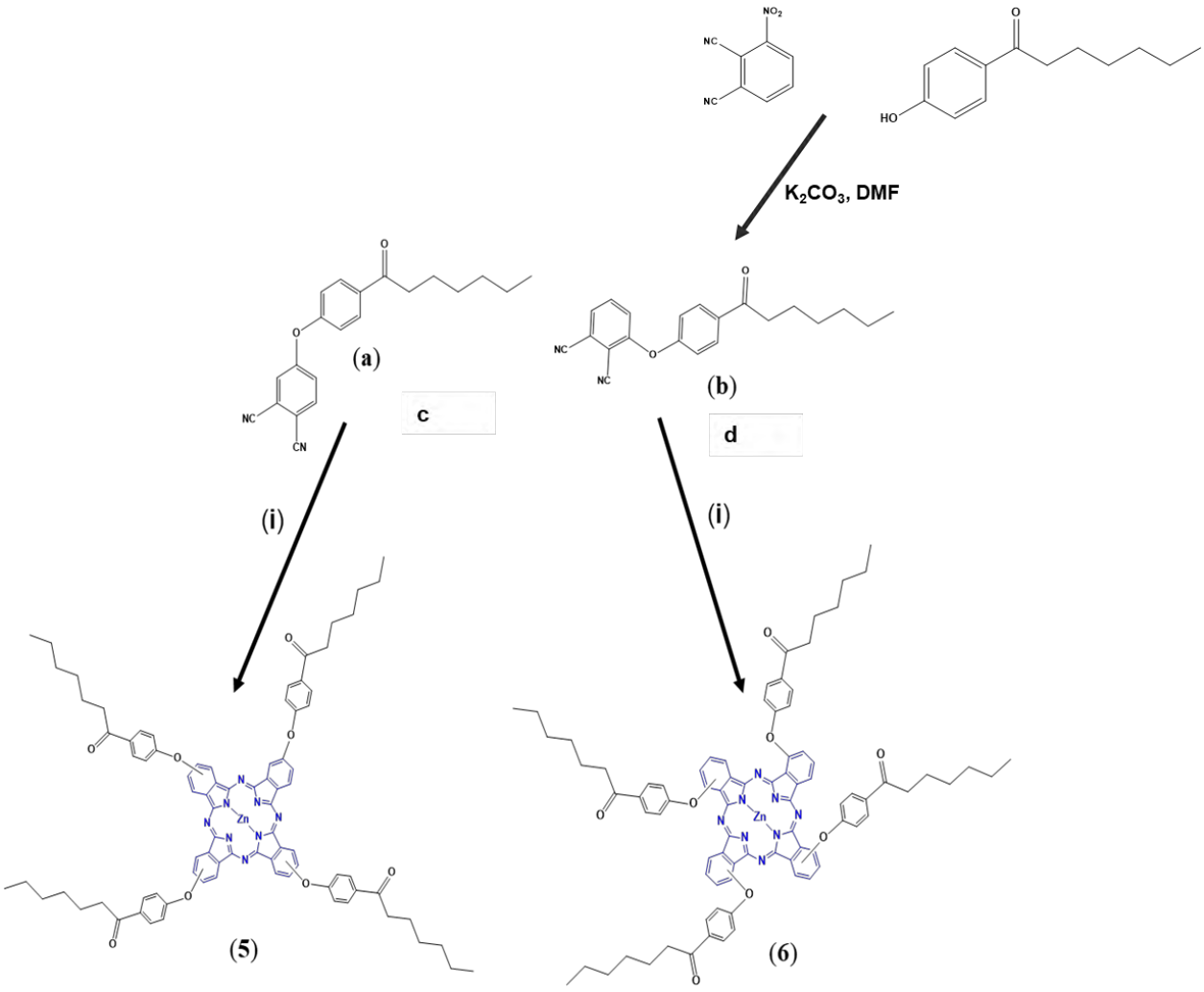

Scheme 3.3: Schematic illustration of the preparation of complexes **5** and **6** (i: *n*-pentanol, DBU, anhydrous zinc acetate [($Zn(CH_3COO)_2$,]).

3.1.4 UV-Vis Spectra

The UV-Vis spectra of **1**, **2**, **3**, **5** and **6** were recorded in DMSO and the Q band maxima are listed in **Table 3.1**, together with the known complex **4**. The electronic absorption spectra of the as synthesised phthalocyanines show the characteristic Q band and B band absorbances. The UV-Vis spectra of **1** and **2** are shown in **Figure 3.4**. The Q band absorption peak of **1** was observed at 672 nm, **Table 3.1**. The Q band absorption maximum of **2** was observed at 675 nm, with a 3 nm bathochromic shift compared to that in the electronic absorption spectrum of the parent Cl_2SiPc. The shift in the Q band absorbance of **2** compared to that of the parent Cl_2SiPc (at 672 nm) to higher wavelengths is attributed to strong electronic interaction between nitroso-naphthalene moiety and SiPc derivative. Changes in Q band absorbances owing to axial ligand contributions have also been reported for other MPc complexes [197]. For both **1** and **2**, the introductions of the naphthalene-type axial ligands were accompanied by an enhanced B band absorption intensity (< 400 nm) and was attributed to the presence of naphthalene-ring-associated electronic transitions.

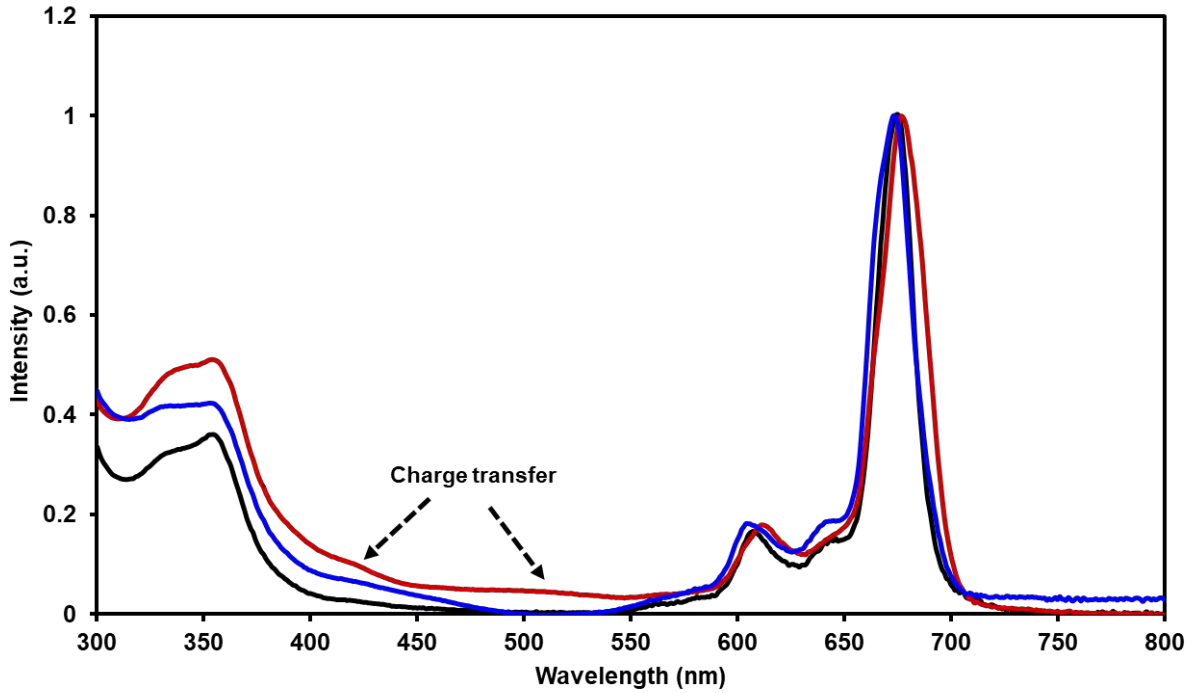

Figure 3.4: UV-Vis electronic absorption spectra of Cl_2SiPc (black), complex **1** (blue) and complex **2** (red), in DMSO.

The UV-Vis of complex **3** in DMSO shows a narrow Q band absorbance at 680 nm (Table 3.1). The Q band maxima of complex **3** is red-shifted compared to complexes **1** and **2** due to the presence sulfur which results in red-shifting in phthalocyanines [198].

The ground state absorption spectra for complexes **5** and **6** (**Figure 3.5**) showed monomeric behaviour of the complexes as evidenced by a single narrow Q band at 678 nm and 694 nm respectively (**Table 3.1**), as is typically observed for metalated phthalocyanines with degenerate D_{4h} symmetry [199]. The non-peripherally tetra-substituted zinc phthalocyanine (complex **6**) was red shifted by 16 nm compared to the peripherally substituted counterpart (complex **5**). The red spectral shift observed in the absorption spectrum of **6** results from greater linear combination of

the atomic orbitals coefficients at the non-peripheral positions of the highest molecular orbital (HOMO) as opposed to those at the peripheral positions [200].

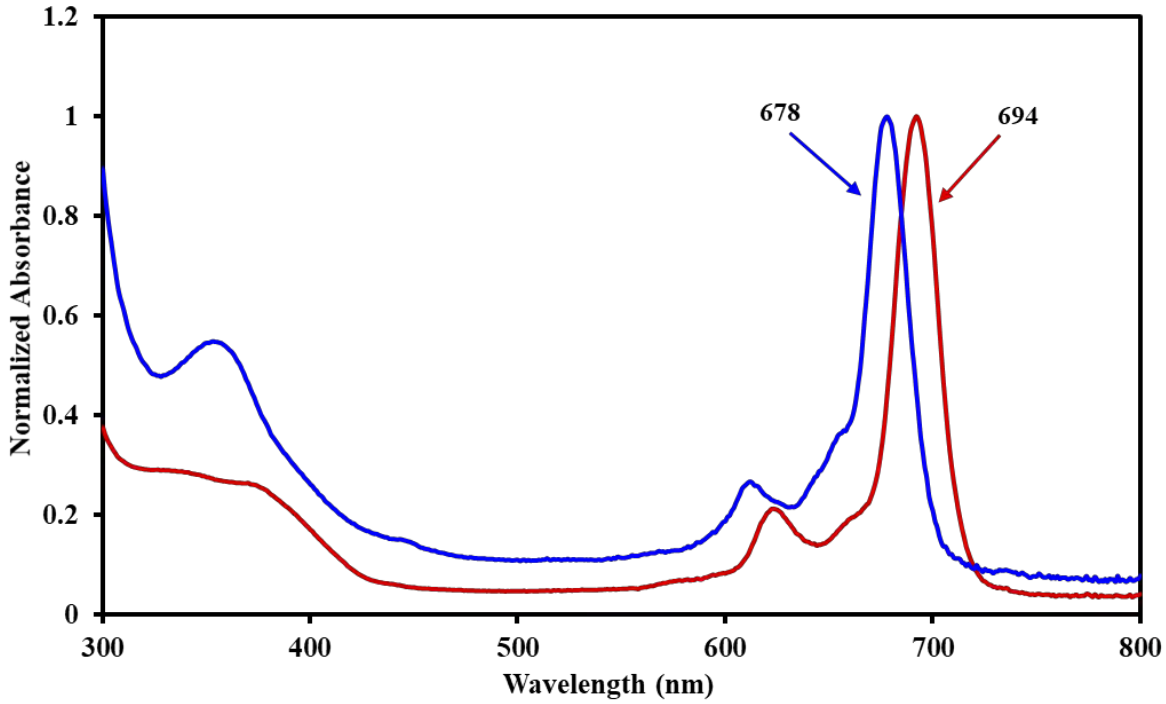

Figure 3.5: Ground state UV-vis spectra of complexes **5** (**blue**) and **6** (**red**) in DMSO.

Table 3.1: TEM sizes as well as Q band absorbance values of the Pc complexes employed in this work and their conjugates in DMSO.

Photosensitizer	TEM sizes (nm)	Q band absorbance (nm)[ab]
Complex **1**		672
Complex **2**		675
Complex **3**		680
3@GQDS	5	680 (360)
3@GQDs-MnO_2	12	680
3@GQDs-MnO_2-AgNPs	15	680
3@GQDs-MnO_2-AuNPs	18	680
Complex **4**		674
4@GQDs	4	675 (360)
4@GQDs-MnO_2@PtNPs	8	675 (326)
4@GONS@TiO_2	46	674 (385)
Complex **5**		678
Complex **6**		694

[a]Values in brackets are for nanoparticles alone. [b]The UV-vis spectra of GQDs were measured in water.

3.2 Nanoparticles and their MPc conjugates

This section outlines the synthesis and characterisation of the nanoparticles (NPs) and their MPc conjugates used in this work. Various NPs were synthesized and conjugated to MPcs complexes

to enhance the photophysical and photochemical properties of the latter. The various conjugates were characterized using spectroscopic and microscopic techniques and are outlined below. The lists of MPcs and MPc-NPs conjugates reported in this work are listed in **Table 3.1**. Commercial TiO_2 was used as obtained from manufacturers. The characterization of GONS will be presented in chapter 8.

3.2.1 MnO_2@PtNPs

MnO_2@PtNPs were synthesized by growing MnO_2 from $KMnO_4$ on the surface of pre-formed PtNPs under sonication. The synthesis of MnO_2@PtNPs was confirmed by X-ray photoelectron spectroscopy (XPS). **Figure 3.6** shows the XPS survey spectra of the MnO_2@PtNPs, as well as the high-resolution Mn 2p and Pt 4f core-level spectra of the MnO_2 and PtNPs within the bimetallic MnO_2@PtNPs. The survey spectrum of MnO_2@PtNPs shows elements present in the sample at 72 eV (Pt 4f), 283 eV (C 1s), 530 eV (O 1s), and 650 eV (Mn 2p). The appearance of the C 1s peak is mainly from residual citrate used as a capping agent in the synthesis of the PtNPs. The high-resolution core-level XPS spectra of Mn 2p of MnO_2@PtNPs, as well as the Pt 4f of PtNPs (for the latter both alone and in the MnO_2@PtNPs), were analysed to determine the oxidation state of Mn and Pt within the bimetallic MnO_2@PtNPs. In the high-resolution spectrum of the Mn 2p core-level region (**Figure 3.6**), peaks associated with Mn $2p_{3/2}$ and Mn $2p_{1/2}$ were observed at 641.8 and 653.4 eV, respectively, with a spin-orbit coupling of 11.6 eV, which is characteristic of MnO_2 in the Mn^{4+} oxidation state [201]. A satellite peak beside the Mn $2p_{3/2}$ peak was also observed. This peak was attributed to the presence of Mn^{2+} in the form of MnO [201,202]. The Pt 4f spectrum of the bimetallic MnO_2@PtNPs contains two main peaks at 74.17 and 70.88 eV with a difference of 3.3 eV, which are characteristic peaks of $4f_{5/2}$ and $4f_{7/2}$, respectively (**Figure 3.6**), implying the zero-valent nature of Pt. Meanwhile, the Pt $4f_{5/2}$ and Pt $4f_{7/2}$ peaks in the PtNPs prior to forming a

composite with MnO_2 were observed at 74.72 and 71.10 eV, respectively, (**Figure 3.6**). The Pt $4f_{5/2}$ and Pt $4f_{7/2}$ of the PtNPs without MnO_2 were found to be centered at higher binding energies than those in the MnO_2@PtNPs. The introduction of MnO_2 therefore led to significant shifts to lower binding energies. A peak at 71.86 eV was also observed in the core-level Pt 4f of PtNPs without MnO_2 and was assigned to the Pt^{2+} oxidation state. However, this peak was not observed in the core-level Pt 4f of MnO_2@PtNPs. The disappearance of the Pt^{2+} peak as well as shifts to lower binding energies suggest that there is a strong electronic interaction between Pt and MnO_2 in the MnO_2@PtNPs [202-205]. Moreover, such shifts have also been associated with synergistic effects, which are associated with enhanced catalytic activity [204]. Further, it is noted that the introduction of the MnO_2 layer significantly attenuated the intensity of the PtNPs within the bimetallic MnO_2@PtNPs.

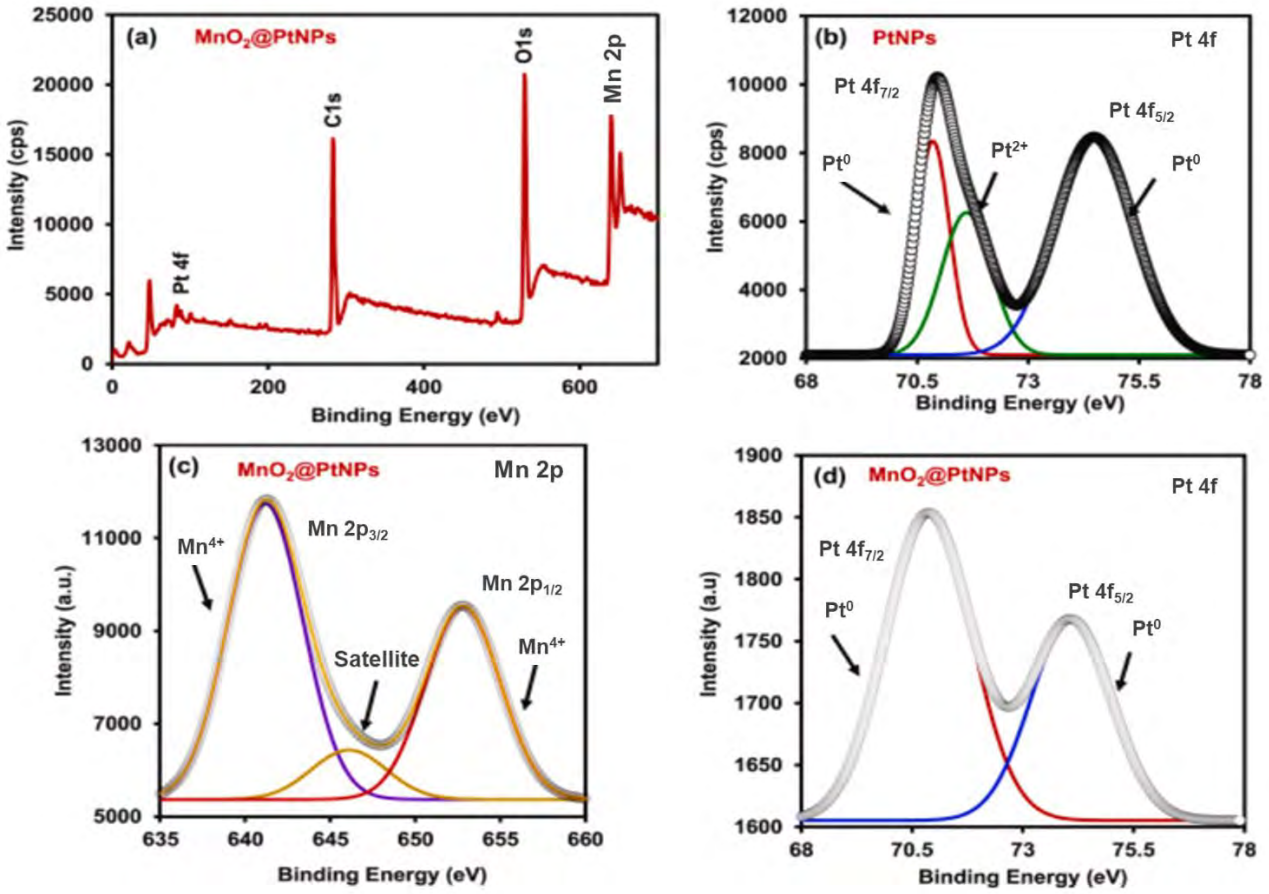

Figure 3.6: XPS survey spectra of (a) MnO_2@PtNPs. High-resolution core-level Pt 4f spectra of (b) PtNPs. High-resolution core-level Mn 2p spectra of (c) MnO_2@PtNPs, and the core level Pt 4f spectra of (d) MnO_2@PtNPs.

Time-of-flight secondary ion mass spectrometry (TOF-SIMS) analysis of MnO_2@PtNPs gave an RGB (red, green, and blue) plot (**Figure 3.7**). TOF-SIMS allows the determination of isotopic, elemental and molecular information from the surface of solid samples. The RGB plot of the TOF-SIMS image of MnO_2@PtNPs shows the mass locations of Pt in red colour, MnO_2 in green, and Mn in blue. As can be seen in **Figure 3.7**, the TOF-SIMS shows the Mn and Pt species within the MnO_2@PtNPs and imply a hybrid-type bimetallic structure. Taken together, TOF-SIMS, and XPS results suggest the successful synthesis of MnO_2@PtNPs.

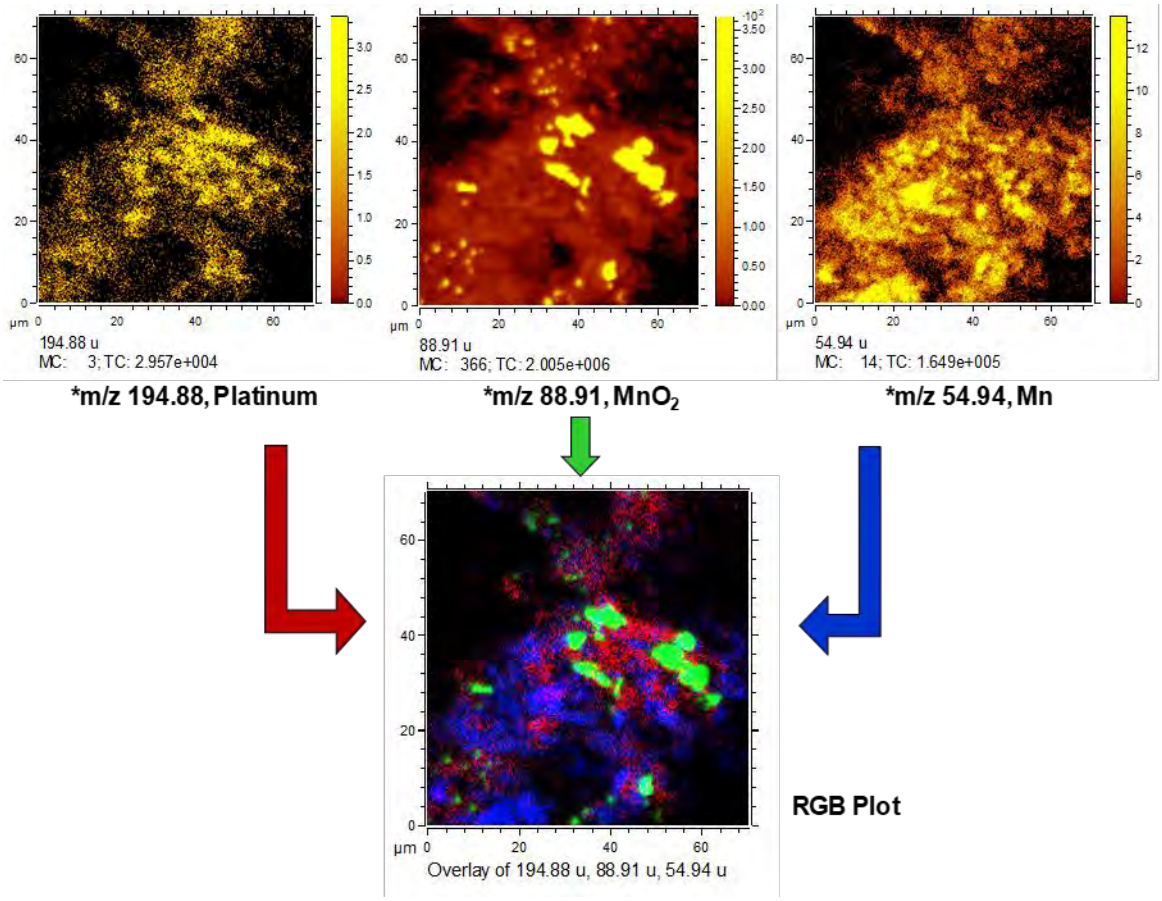

Figure 3.7: TOF-SIMS positive ion mode images of MnO_2@PtNPs. RGB = red, green, and blue.

3.2.2 Conjugates of complex 3 and complex 4 with NPs

NH_2-functionalised GQDs were conjugated to complex **3** and **4** (asymmetric MPcs) which allow for site specific binding or coordination. This was achieved via amide bond formation between the primary amine groups on the GQDs and the carboxylic acid group on either complex **3** or **4** (details are provided in chapter II). The synthesis of **3**@GQDs and **4**@GQDs was achieved using DCC and NHS assisted amide coupling of **3** or **4** to GQDs. It is important to note that π-π stacking is also possible between the complexes and GQDs. A general representation for the synthesis of **4**@GQDs (as an example) is shown in **Scheme 3.4**. **3**@GQDs-MnO_2-AgNPs and **3**@GQDs-MnO_2-AuNPs were formed by the simultaneous growth of AgNPs/AuNPs and MnO_2 NPs on **3**@GQDs (**Scheme 3.5**). Likewise, taking advantage of the abundance of amino groups on the GQDs (in **4**@GQDs), the as-synthesized MnO_2@PtNPs were adsorbed onto GQDs in **4**@GQDs (**Scheme 3.6**). Complex **4**, was used in this work particularly due to its simple structure. The list of conjugates is listed in **Table 3.1**.

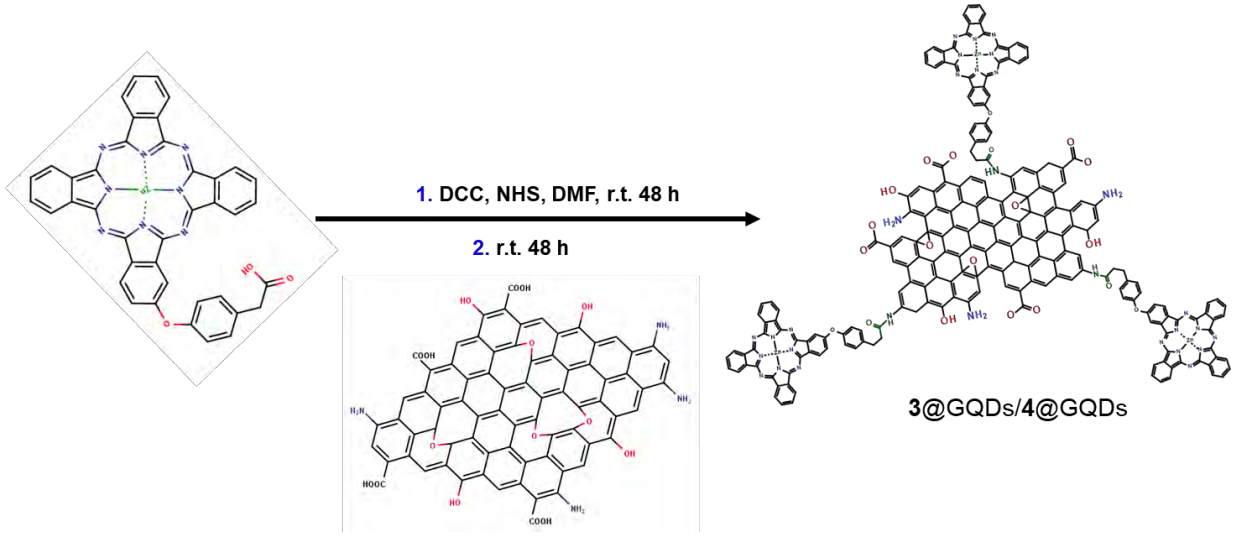

Scheme 3.4: Synthetic route for **3**@GQDs or **4**@GQDs.

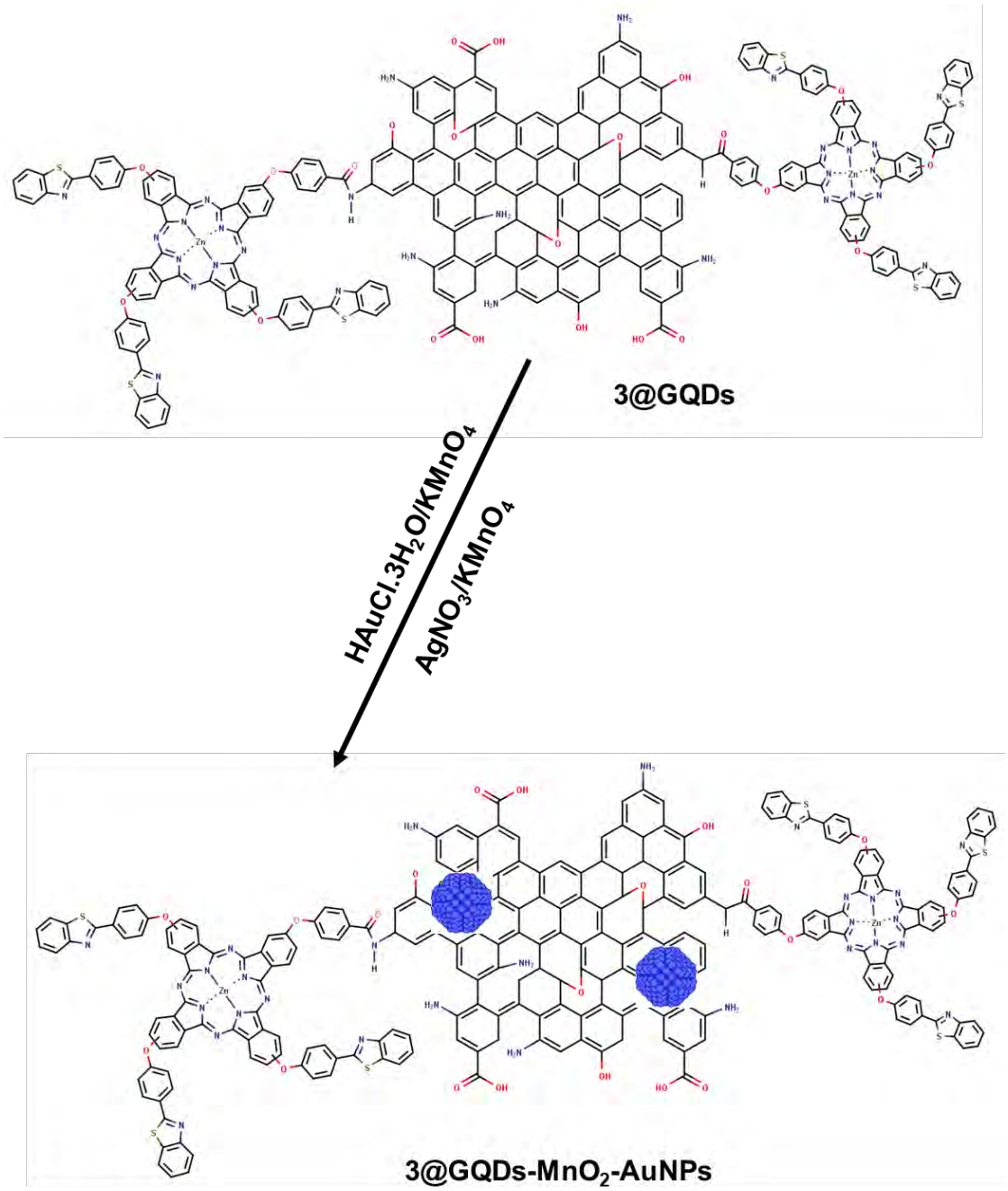

Scheme 3.5: Schematic for the preparation of **3**@GQDs-MnO_2-AuNPs (as an example) with an illustration of covalent interaction of GQDs and complex **3**, and the assembly of MnO_2 and AuNPs onto the Pcs/GQDs surface.

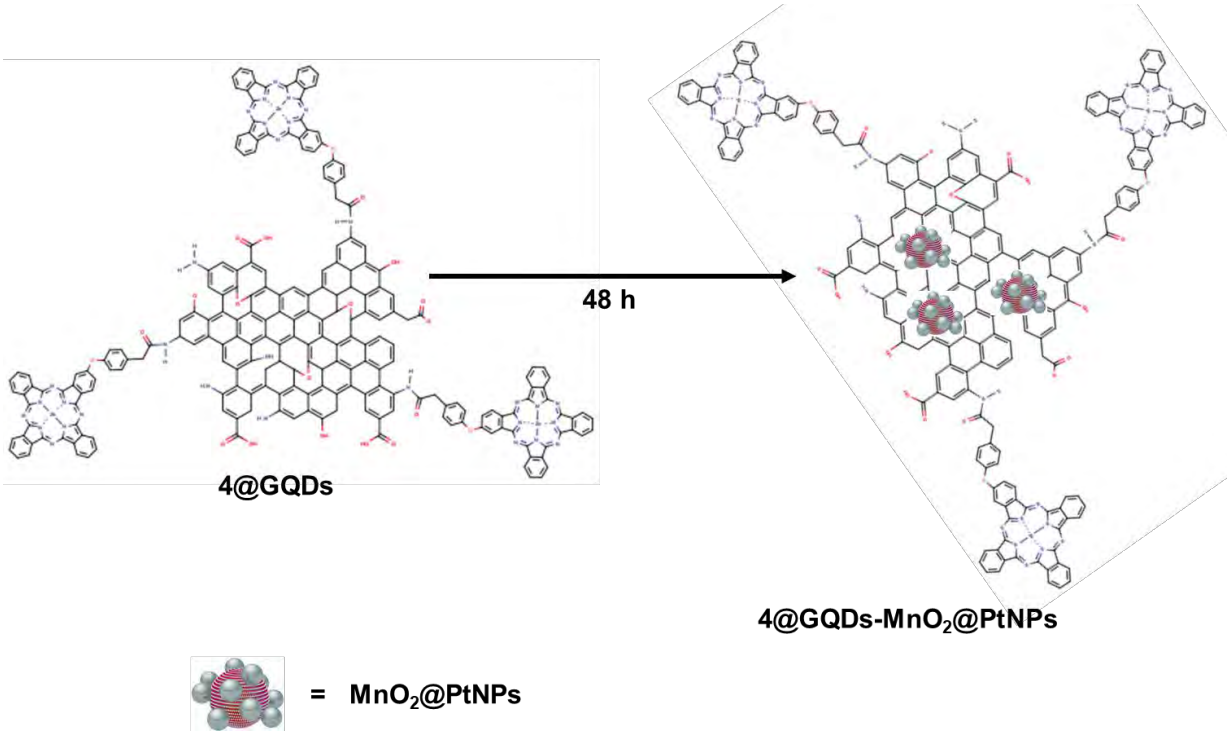

Scheme 3.6: Schematic for the preparation of **4**@GQDs-MnO_2@PtNPs with an illustration of covalent interaction of GQDs and complex **4**, and the assembly of MnO_2@PtNPs onto the Pcs/GQDs surface.

3.2.2.1 FT-IR

The successful amide conjugation of GQDs to **3** or **4** was confirmed using Fourier Transform Infrared spectroscopy. As can be observed in **Figure 3.8** (using **3**@GQDs as an example), two "fangs" attributable to the primary amines (NH_2) on the GQDs were observed at 3342 and 3246 cm^{-1}. The FT-IR spectrum of the **3**@GQDs (**Figure 3.8**) on the other hand, shows the presence of a single amide peak around 3325 cm^{-1}. The disappearance of the two peaks (N−H) and subsequent emergence of a new single peak at 3325 cm^{-1} confirms the successful conjugation and hence formation of the resultant **3**@GQDs. The presence of tracer peaks at 1526 and 1487 cm^{-1} owing to the presence of C=N vibrations in the FT-IR spectra of complex **3** in the **3**@GQDs conjugates confirms the presence of the MPc as an integration in the GQDs. Similar FT-IR spectra were observed for **4** and conjugates with GQDs.

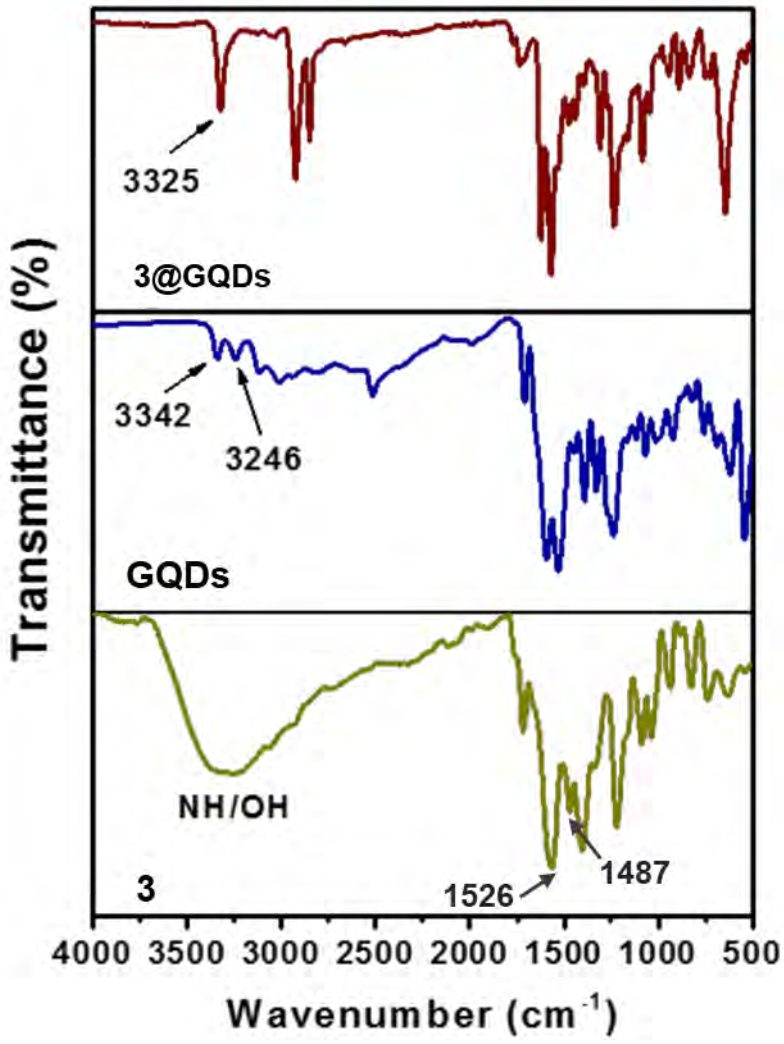

Figure 3.8: FT-IR spectra for GQDs, complex **3**, **3**@GQDs.

3.2.2.2 TEM

The relative morphologies and average diameters of the synthesised nanocomposites were confirmed by electron microscopy imaging. Amine-functionalised GQDs are presented as quasi-spherical nanoparticles with a uniform size of ≈ 4 nm (**Figure 3.9**). The particle sizes remained unchanged for **4**@GQDs or increased only slightly for **3**@GQDs to complex **3** (**Table 3.1**). A size increase was observed following attachments of MnO_2 alone, or MnO_2-AuNPs, or MnO_2-AgNPs in accordance with level of modification of **3**@GQDs, with sizes of 12, 15 and 18 nm for **3**@GQDs-MnO_2, **3**@GQDs-MnO_2-AgNPs and **3**@GQDs-MnO_2-AuNPs, respectively (**Table 3.1**) (**3**@GQDs-MnO_2-AuNPs and **3**@GQDs-MnO_2-AgNPs are used as examples, **Figure 3.10**). Scanning electron and X-ray energy dispersive spectroscopies (SEM-EDS) were utilized for the qualitative elemental mapping of the resultant nanocomposites of **3**. **Figure 3.10** presents the SEM image and the corresponding element mapping of **3**@GQDs-MnO_2-AgNPs and **3**@GQDs-MnO_2-AuNPs. As shown in **Figure 3.10**, the coexistence of Mn and Ag or Mn and Au elements (distributed within the composites) suggest the successful fabrication of **3**@GQDs-MnO_2-AgNPs and **3**@GQDs-MnO_2-AuNPs, respectively.

Figure 3.9 shows monodispersed spherical PtNPs with an average size of 2 nm. Upon compositing of the MnO_2 and PtNPs to the subsequent MnO_2@PtNPs, evidence of aggregation and hence size increases were observed. The MnO_2@PtNPs had a size average of 4 nm, which was greater than the size of the core PtNPs (2 nm). The spherical morphology of the MnO_2@PtNPs may be indicative of MnO_2 adhering to the surface of the PtNPs, maintaining a 3-dimensional morphology. In the TEM image of **4**@GQDs-MnO_2@PtNPs, the presence of individual GQDs, or PtNPs could not be distinguished, however, an increase in the size of the **4**@GQDs-MnO_2@PtNPs was observed (**Table 3.1**).

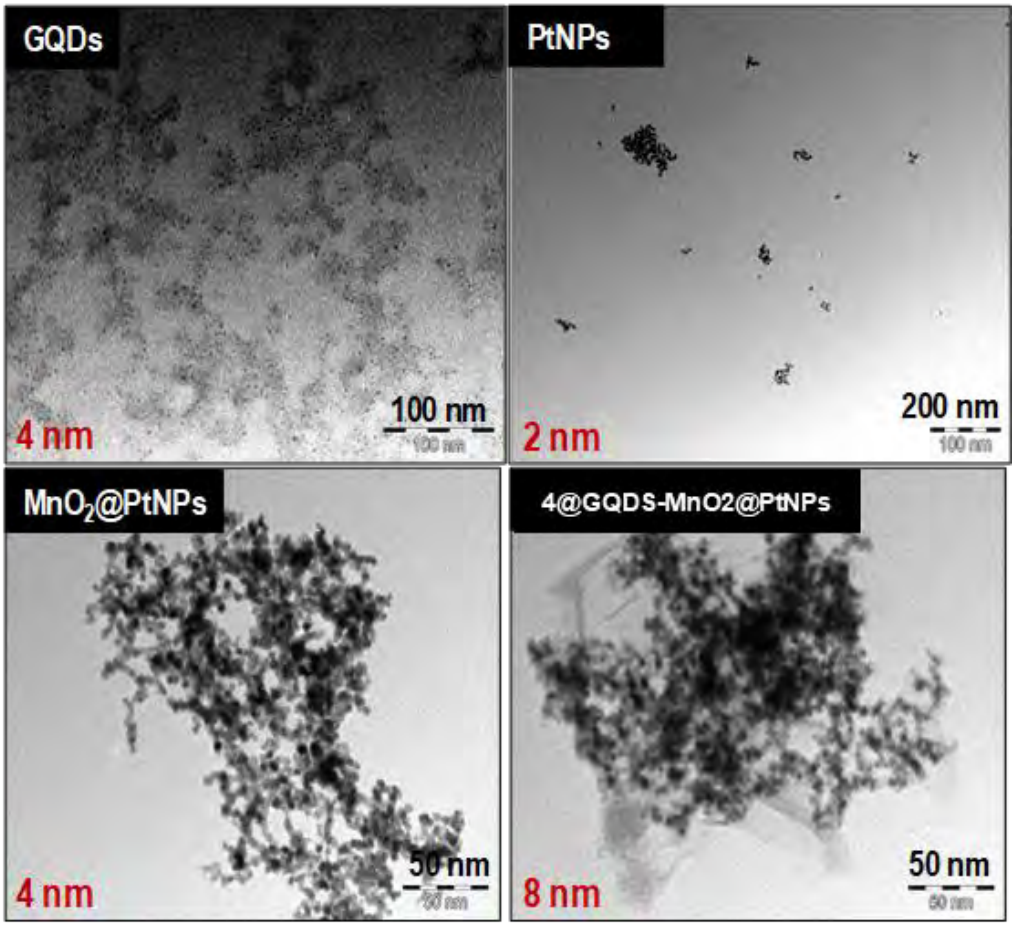

Figure 3.9: Transmission electron images of GQDs, MnO_2@PtNPs, PtNPs, and **4**@GQDs-MnO_2@PtNPs.

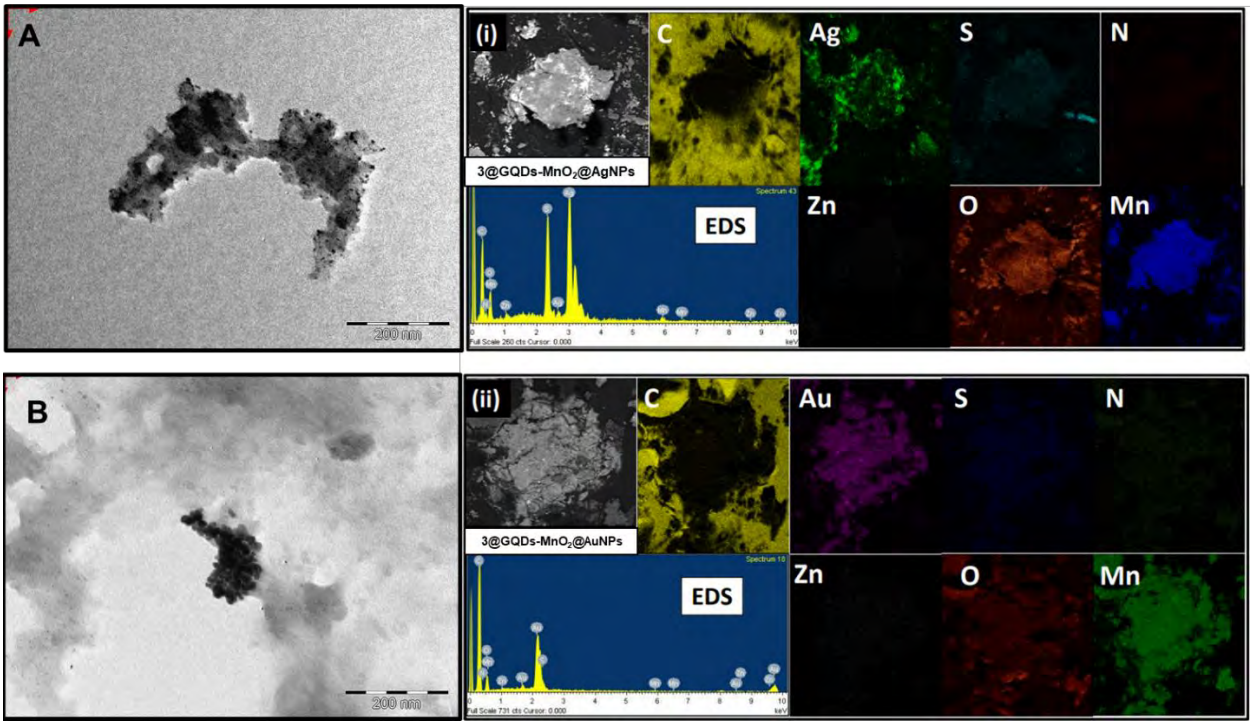

Figure 3.10: TEM images of (A) **3**@GQDs-MnO_2-AgNPs, and (B) **3**@GQDs-MnO_2-AuNPs and their respective SEM-EDS elemental mappings.

3.2.2.3 UV-Vis spectra

The UV-Vis spectrum of the GQDs showed an absorption maximum at 360 which is associated with the n–π* transition of C=O groups (**Figure 3.11A**) [189]. Upon conjugation of either **3** or **4** to the GQDs, no significant shifts in the Q band were observed (**Table 3.1** and **Figure 3.11A**). However, a consequence of the presence of GQDs was the enhancement in the Soret band region of the spectrum.

The UV-Vis spectrum of MnO_2@PtNPs showed no distinct peaks (**Figure 3.11A**). The Q band absorption due to the presence of **4** was evident in **4**@GQDs-MnO_2@PtNPs. There were no shifts in the Q band absorbance of **4**@GQDs-MnO_2@PtNPs compared to **4**@GQDs. However, **4**@GQDs-MnO_2@PtNPs showed enhanced absorbance below 500 nm, attributable to the presence of MnO_2@PtNPs within the composite, strongly suggesting the successful synthesis of **4**@GQDs-MnO_2@PtNPs and some aggregation.

Figure 3.11B shows the UV-Vis spectra of the conjugates of complex **3**. The surface plasmon resonance (SPR) bands attributable to the presence of Ag and Au in the conjugates were not clearly defined in the spectra of **3**@GQDs-MnO_2-AgNPs and **3**@GQDs-MnO_2-AuNPs (not shown), but there was broadening between 400 and 600 nm signaling the presence of these nanoparticles and some aggregation.

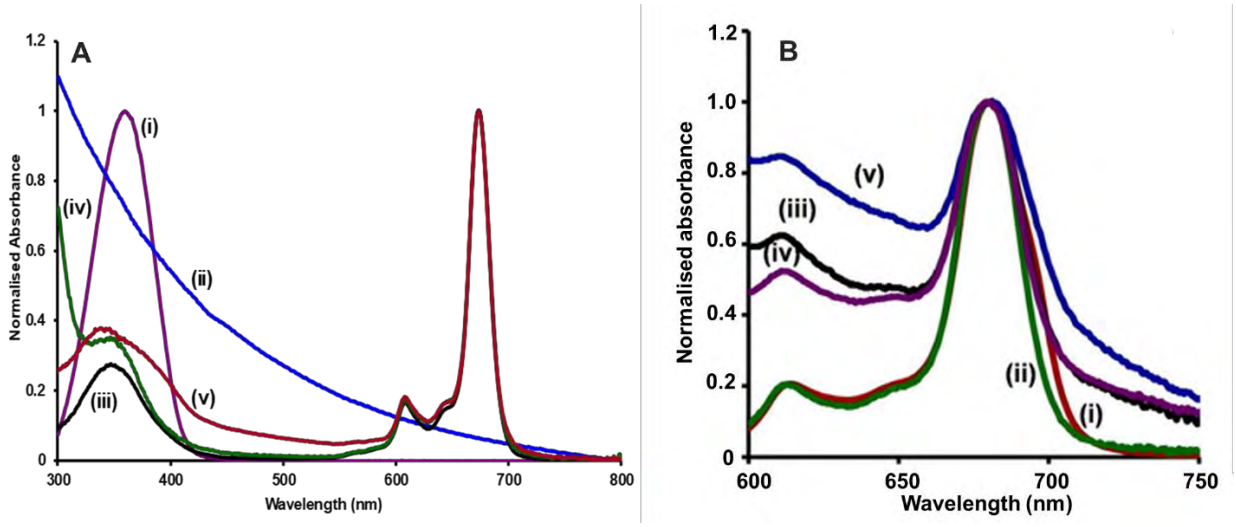

Figure 3.11: (A) Ground state absorption spectra of GQDs (i), MnO_2@PtNPs (ii), **4** alone (iii), **4**@GQDs (iv), and **4**@GQDs-MnO_2@PtNPs (v). (B) Ground state absorption spectra of complex **3** (i), **3**@GQDs (ii), **3**@GQDs-MnO_2(iii), **3**@GQDs-MnO_2-AuNPs (iv), and **3**@GQDs-MnO_2-AgNPs (v). All measurements were taken in DMSO.

3.2.2.4 Raman/EPR

GQDs display two characteristic Raman peaks termed the G-band (sp^2) (tangential mode) and the D-disorder band (breathing mode, sp^3). The Raman spectrum of the as-synthesised showed characteristic G and D bands centred at 1593 and 1301 cm^{-1}, respectively (**Figure 3.12A**). Shifts in the D-band position were observed post conjugation of complex **3** to the GQDs surface from 1301 cm^{-1} to 1418 cm^{-1} (**Figure 3.12A**). Likewise, the G-band was affected, with slight shifts from 1593 cm^{-1} for GQDs and **3**@GQDs to 1651 cm^{-1} for **3**@GQDs-MnO_2 and **3**@GQDs-MnO_2-AgNPs (the G band is very weak for the latter). Shifts in the Raman frequencies are often indicative of strong π-electron interactions in hybrid materials. The presence of defects on GQDs is quantified by the ratio of the intensity of the D over G band (D/G). The I_D/I_G (integrated intensity) ratios of D to G bands for the GQDs alone, **3**@GQDs, **3**@GQDs-MnO_2 and **3**@GQDs-MnO_2-AgNPs/**3**@GQDs-MnO_2-AuNPs were calculated to be 0.12, 0.20, 4.88 and 13.1, respectively.

For all conjugates, the observed increases in the I_D/I_G is associated with the introduction of defects to the basal planes and the edges of carbon structures [206], and signify increases in the structural disorder of the GQDs post-modification and hence, the successful synthesis of the respective Pc-nanoparticle hybrids. Besides, Raman spectroscopy also allows for the identification of metal oxide NPs (owing to their electron-phonon coupling). Raman spectrum of **3**@GQDs-MnO_2-AuNPs (used as an example) (**Figure 3.12B**) shows a peak at 605 cm^{-1} which may be attributed to the deformation modes of the Mn–O–Mn chain of MnO_2, and adjacent peaks at 496 cm^{-1} and 677 cm^{-1} are attributable to the Mn–O stretching modes [207]. The appearance of a new peak at 308 cm^{-1} (which is absent in GQDs alone) was attributed to the S−Au bond [208], and further confirms the successful assembly of MnO_2-AuNPs on the **3**@GQDs platform to form **3**@GQDs-MnO_2-AuNPs. For **4**@GQDs-MnO_2@PtNPs, peaks at 494 cm^{-1} and 677 cm^{-1}, were attributed to

the Mn-O stretching modes, characteristics peaks of MnO_2 [209], and further supports its successful synthesis.

The as-prepared composites were further characterised by electron paramagnetic resonance (EPR) spectroscopy at 298 K to confirm the presence of MnO_2 (with Mn in the +4-oxidation state) in the composites. **Figure 3.13** (**3**@GQDs-MnO_2-AuNPs is used as an example) shows the EPR spectrum **3**@GQDs-MnO_2-AuNPs. The spectrum shows the presence of six well-resolved hyperfine splitting characteristic of manganese [210]. Mn^{+4} ions possess paramagnetic nature at either low or high spin. Therefore, EPR experiments further substantiate the presence of MnO_2 in the composites and hence their successful synthesis.

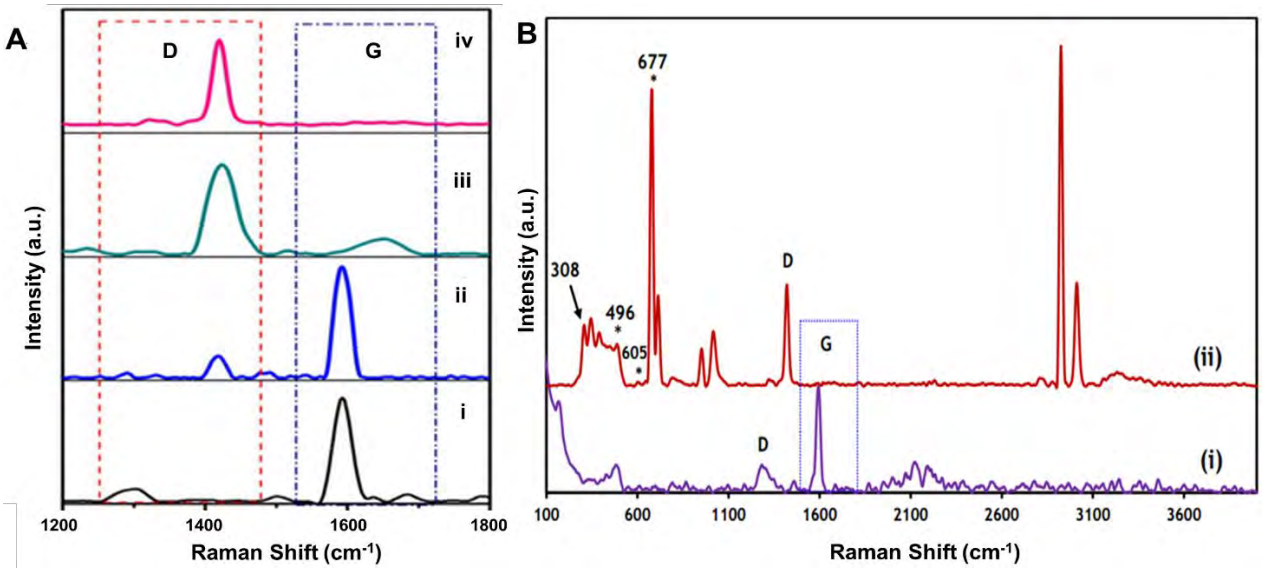

Figure 3.12: (A) Raman spectra of GQDs (i), **3**@GQDs (ii), **3**@GQDs-MnO_2 (iii), and **3**@GQDs-MnO_2-AgNPs (iv), showing the corresponding Raman intensity changes of the GQDs upon modification of the graphitic core structure. (B) Raman spectral analysis of (i) GQDs and (ii) **3**@GQDs-MnO_2-AuNPs showing peaks attributable to S-Au and MnO_2 signifying successful synthesis and chemisorption of the MnO_2 and AuNPs on the Pc/GQDs surface.

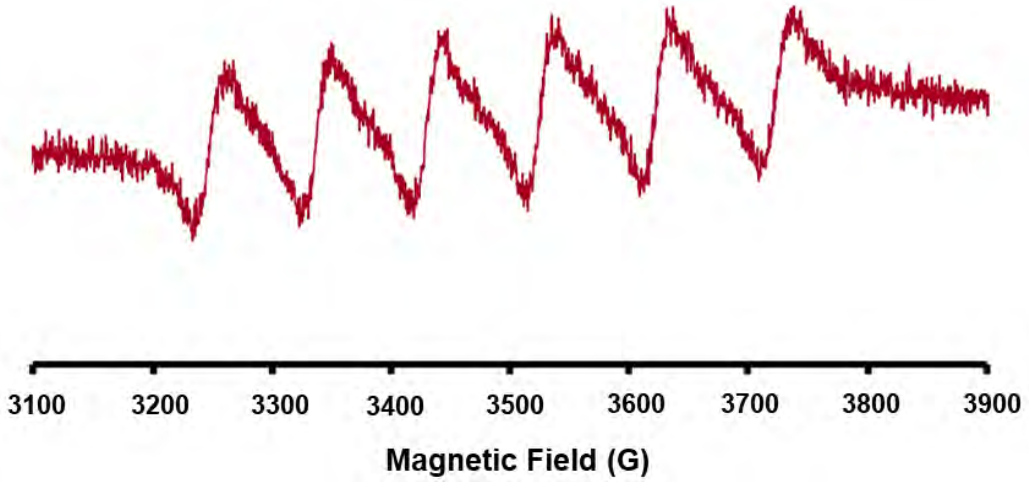

Figure 3.13: EPR Spectrum of **3**@GQDs-MnO_2-AuNPs showing six-line hyperfine splitting spectral features characteristic of manganese, registered at T = 298 K.

3.2.2.5 X-Ray Diffraction

The crystal structures of the obtained MPc composites were determined by X-ray diffraction (XRD) to show the various effects on the Bragg's reflections. This is represented using the conjugates of complex **3** as an example (**Figure 3.14**). The broad XRD pattern for **3** (**Figure 3.14** (i)) is typical of MPcs and suggests an amorphous form [211]. The GQDs feature a broad (002) peak around 25° (**Figure S6**), which is broad due to the small size of GQDs [212]. This broad amorphous XRD pattern is maintained post conjugation to complex **3** to the nanoparticles (**Figure 3.14** (ii and iii)). No clear diffraction peaks resulting from MnO_2 were observed. However, there were small sharp peaks present in the Ag and Au containing conjugates (**3**@GQDs-MnO_2-AgNPs used as an example) (**Figure 3.14** (iv)). Such peaks embedded in a broad XRD pattern suggests an increase in size after conjugation [213]. The five diffraction patterns observed in the diffractogram of the Ag-containing conjugate (used as an example) (**Figure 3.14** (iv)) correspond to the crystalline plane of the face-centred cubic structure of metallic silver with plain of 111, 200, 220, 311 and 222 (JCPDS file No. 00–004-0783) [213].

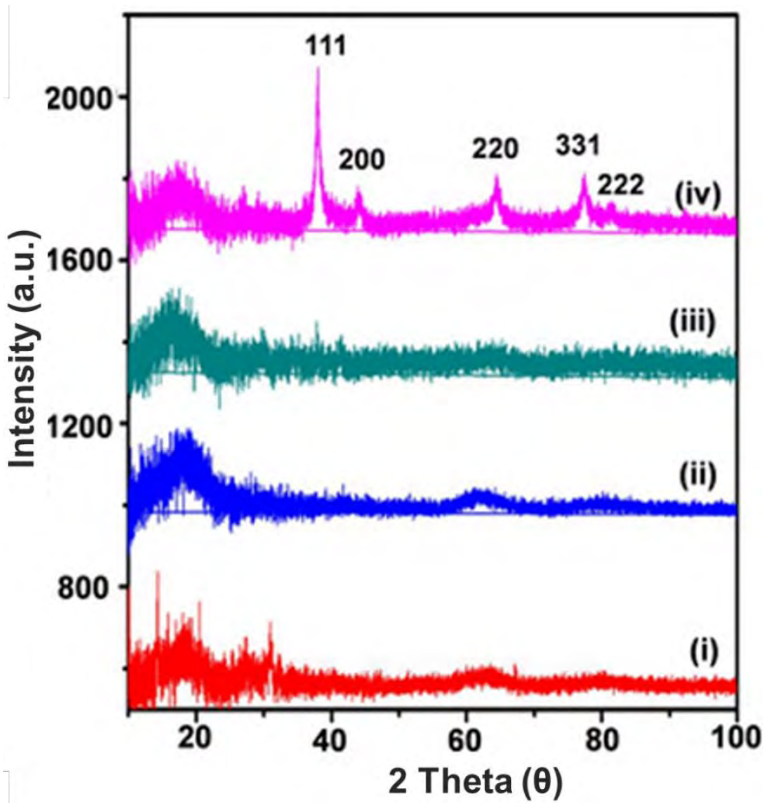

Figure 3.14: XRD patterns for complex **3** alone (i), **3**@GQDs (ii), **3**@GQDs-MnO_2 (iii), and **3**@GQDs-MnO_2-AgNPs (iv).

3.2.2.6 X-ray photoelectron spectroscopy

The successful assembly of the as-synthesized MnO_2@PtNPs onto **4**@GQDs was verified using XPS. **Figure 3.15** shows the XPS survey spectra of the **4**@GQDs-MnO_2@PtNPs, as well as the high-resolution N 1s core-level spectra of **4**@GQDs and **4**@GQDs-MnO_2@PtNPs. The XPS survey spectrum of the **4**@GQDs-MnO_2@PtNPs reveals the presence of Pt, C, O, N, Mn, and Zn (**Figure 3.15**). In **Figure 3.15**, the N 1s spectrum of **4**@GQDs was deconvoluted into three peaks at 396.0 eV (N-C), 397.4 eV (N-H), and 400.0 eV (N-C=O). The N-C and N-H peaks are attributed to the presence of GQDs (in **4**@GQDs) which contain nitrogen functional groups [214,215]. The peak at 400 eV confirms the presence of the amide bond and hence, successful anchoring of **4** to GQDs [216]. Following the adsorption of MnO_2@PtNPs onto **4**@GQDs to form **4**@GQDs-MnO_2@PtNPs, in **Figure 3.15**, the N 1s high resolution core level spectrum was deconvoluted, and four peaks were obtained at 396.3 eV (N-C), 397.6 eV (N − Pt), 397.9 eV (N-H), and 400.1 eV (N-C=O). Interestingly, N-coordinated metal peak was observed and was assigned to the presence of N-Pt in **4**@GQDs-MnO_2@PtNPs, implying exposed Pt sites in the MnO_2@PtNPs. It was noted that the position of the amine nitrogen (N-H) was found to be slightly shifted to higher binding energies (397.7 eV) in the **4**@GQDs-MnO_2@PtNPs compared to **4**@GQDs (397.4 eV). A large decrease in the intensity of the amine nitrogen (N-H) was also observed in **4**@GQDs-MnO_2@PtNPs. Both observations imply involvement of amine nitrogen in the interaction with Pt. Shifts to higher binding energies in the nitrogen species can be attributed to the presence of multiple valence electrons in the GQDs which act as electron donors facilitating metal-nitrogen binding interactions [217,218].

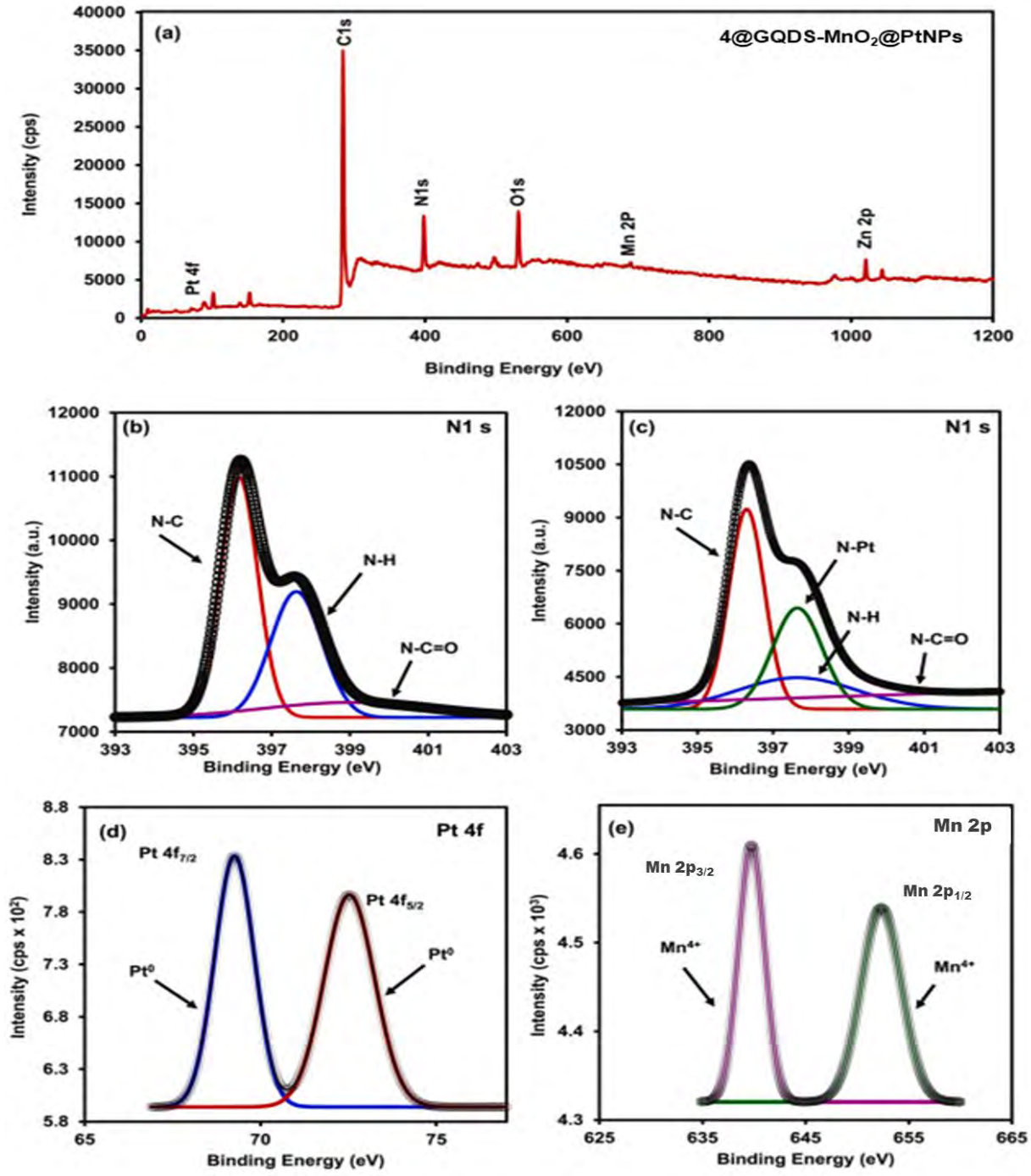

Figure 3.15: XPS survey spectra of **4**@GQDs-MnO_2@PtNPs (a). High-resolution core-level N 1s spectra of **4**@GQDs (b) and **4**@GQDs-MnO_2@PtNPs (c). High-resolution Pt 4f (d) and Mn 2p (e) core-level spectra of **4**@GQDs-MnO_2@PtNPs.

Moreover, the high-resolution Pt 4f and Mn 2p core-level spectra of the **4**@GQDs-MnO_2@PtNPs, are shown in **Figure 3.15 (d and e)**. The core-level Pt 4f deconvoluted spectrum of the **4**@GQDs-MnO_2@PtNPs contained two main peaks at 72.4 and 69.3 eV, characteristic peaks of $4f_{5/2}$ and $4f_{7/2}$, respectively (**Figure 3.15**). As discussed above, the Pt $4f_{5/2}$ and Pt $4f_{7/2}$ of the MnO_2@PtNPs before adsorption onto the **4**@GQDs were found at 74.17 eV and 70.88 eV, respectively. Shifts to lower binding energies in **4**@GQDs-MnO_2@PtNPs suggest a strong electronic interaction between MnO_2@PtNPs and **4**@GQDs. The core-level Mn 2p deconvoluted spectrum of **4**@GQDs-MnO_2@PtNPs also revealed two peaks at 639.75 eV and 652.5 eV, attributed to the $2p_{3/2}$ and $2p_{1/2}$ peaks, respectively (**Figure 3.15**). The Mn^{2+} satellite peak that was observed in the Mn 2p deconvoluted spectrum of MnO_2@PtNPs (**Figure 3.6**) was absent in **4**@GQDs-MnO_2@PtNPs. The disappearance of this Mn^{2+} suggested strong electron interaction between the MnO_2@PtNPs and **4**@GQDs. Taken together, indicate the successful synthesis of **4**@GQDs-MnO_2@PtNPs.

3.2.2.7 AFM

Atomic force microscopic (AFM) imaging revealed that the GQDs had an average topographic height of about 2nm (figure not shown), can be estimated to contain about three-four graphene layers [206]. With a surface roughness of about 2.5 nm, they can be assumed as relatively flat. However, there is a marked increase in surface roughness following modification with NPs to 68.8 nm, 164.8 nm, and 338.7 nm for **3**@GQDs-MnO_2, **3**@GQDs-MnO_2-AgNPs and **3**@GQDs-MnO_2-AuNPs, respectively (used as examples). Such increases in topographical height serve as evidence for the successful assembly of the respective NPs onto the GQDs surface. Moreover, distinct changes in 3D surface morphologies were noted for the hybrids compared to that of GQDs

alone with the presence of uneven surfaces with wrinkles and voids which are absent in GQDs alone (**Figure 3.16**).

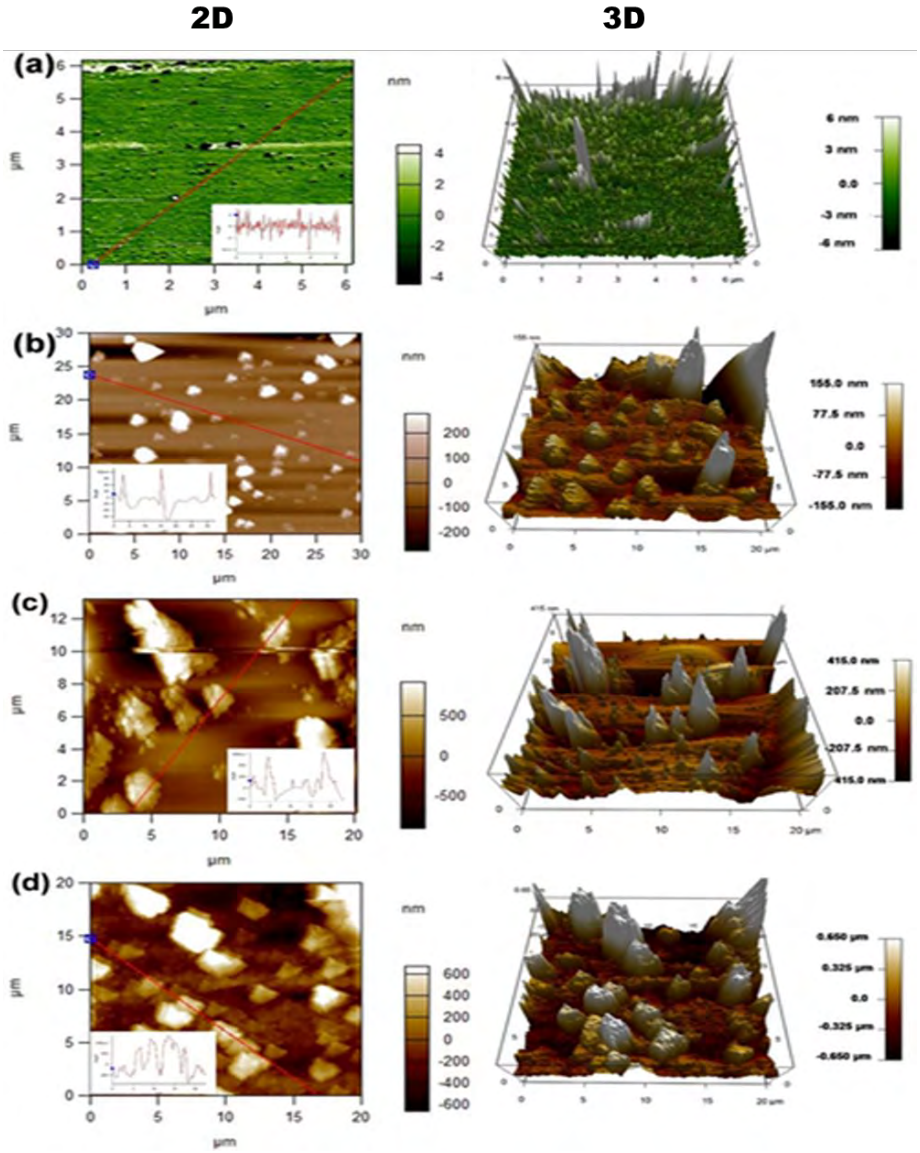

Figure 3.16: 2D and 3D AFM images of **3**@GQDs (a) and **3**@GQDs-MnO_2 (b) **3**@GQDs-MnO_2-AgNPs (c), **3**@GQDs-MnO_2-AuNPs (d) with respective height profiles.

3.2.2.8 TGA Analysis

The thermal stability of the MPcs and their respective NPs conjugates was assessed using a thermogravimetric analyser at a temperature range of 50-800 °C at a heating rate of 20 °C min^{-1}, under a steady N_2 gas flow rate of 20 mL min^{-1}. The conjugates of complex **3** are used as examples, **Figure 3.17**. **3**@GQDs-MnO_2-AgNPs (used as an example) is more stable than **3**, **3**@GQDs, **3**@GQDs-MnO_2 or GQDs alone. The GQDs start to degrade at ~ 200 °C until they are completed degraded near 800 °C. **3**@GQDs shows a degradation pattern like GQDs alone. The greater thermal stability of **3**@GQDs-MnO_2-AgNPs, **3**@GQDs-MnO_2 over GQDs or **3**@GQD implies the successful integration of metal nanoparticles on the GQDs/Pc surface.

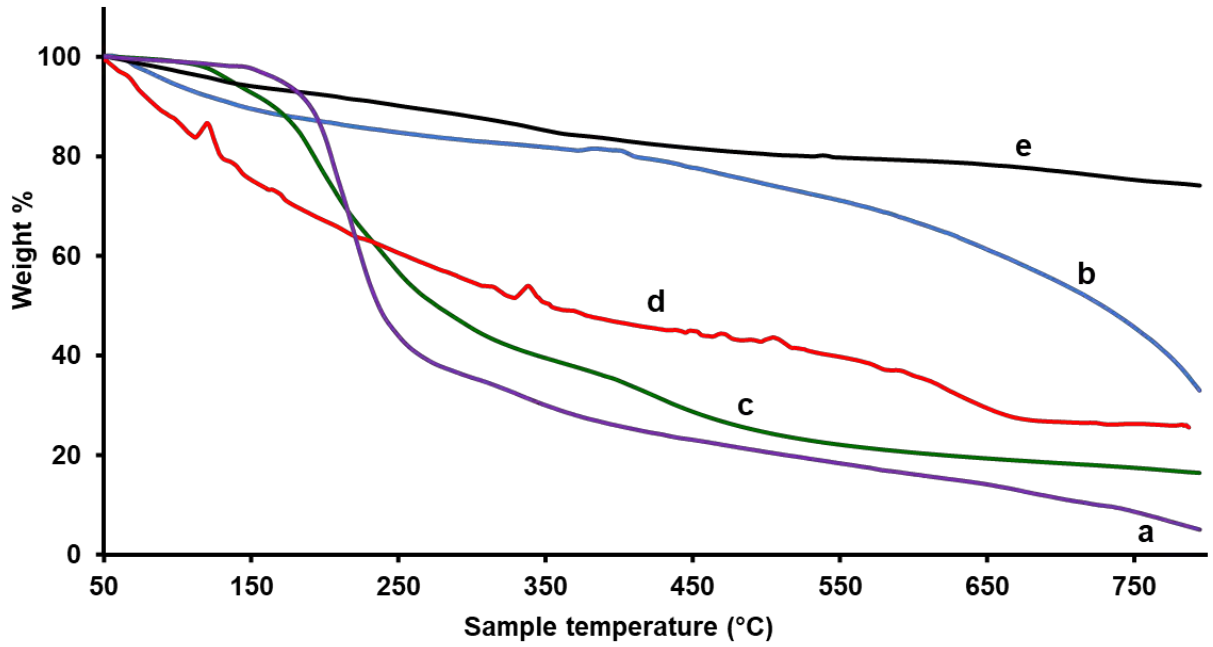

Figure 3.17: Thermogravimetric decomposition curves of GQDs alone (a), **3** (b), **3**@GQDs (c), **3**@GQDs-MnO_2(d), **3**@GQDs-MnO_2-AgNPs (e).

3.3 Summary of chapter

Novel symmetrical and asymmetrical MPcs were successfully synthesized and characterized by various microscopic and spectroscopic techniques. All the studied complexes **1**-**6** showed monomeric Q band in DMSO. The as-synthesised MPcs were conjugated to various metallic and non-metallic nanoparticles. The conjugates were characterized using a combination of spectroscopic techniques: FT-IR, TEM, SEM-EDS, XRD, UV-Vis, AFM, TGA, Raman and XPS spectroscopy which confirmed their successful fabrication.

Chapter IV

Fabrication and Characterization of fabricated Liposomes

The limited water solubility of the as-synthesized MPc complexes and MPc-nanoparticle conjugates necessitated their liposomal encapsulation. An essential premise for liposomal PS delivery is to increase the size of the pharmacological entity such that the PS passage through endothelial gaps is limited hence preferentially accumulating in tumour tissues through the enhanced permeability and retention (EPR) effect. This chapter details the synthesis and characterization of liposome formulations of MPcs, and MPc-nanoparticles reported in this work.

For all composites, liposomal formulations were obtained via thin-layer hydration using 1,2-dioleoyl-sn-glycero-3-phosphocholine (DOPC). The list of MPc-liposomes employed in this work are listed in **Table 4.1**. Details on fabrication are provided in Chapter II.

Folic acid functionalised liposomes of conjugates of complex **4** (**4**@GQDs-MnO_2@PtNPs) were used to evaluate the possibility of folate receptor targeting. **4**@GQDs-MnO_2@PtNPs-FA-liposomes were prepared using a lipid mixture of DOPC/DSPE-PEG-NH_2 and **4**@GQDs-MnO_2@PtNPs. Following this, the formed liposomes were functionalized with folic acid (FA) via EDC/NHS amide coupling reaction (**Scheme 4.1**). The conjugation of FA was possible due to the presence of amine groups on the PEG-unit as well as COOH groups on FA. Encapsulation efficiencies are listed in **Table 4.1**. The highest percentage encapsulation efficiencies were obtained for **4** and its conjugates, which may have resulted from the simpler structure which allow better packing within the liposomal bilayer.

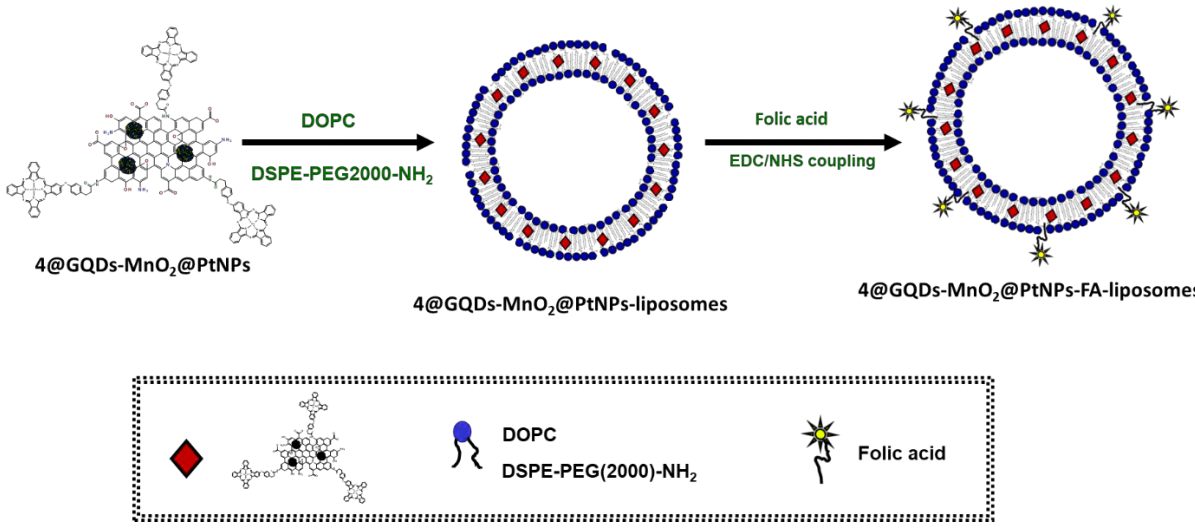

Scheme 4.1: Schematic illustration of the fabrication of the multifunctional folate-modified liposomes (**4**@GQDs-MnO_2@PtNPs-FA-liposomes) by encapsulating **4**@GQDs-MnO_2@PtNPs.

4.1 TEM/EDS

For all liposomal formulations, transmission electron microscopy (TEM) images demonstrated their successful synthesis, with liposomes appearing as spherical and monodisperse lipid vesicles (**Figure 4.1**) (complex **1**-liposomes, **2**-liposomes and **4**@GQDs-MnO_2@PtNPs-FA-liposomes used as example). Owing to the hydrophobic nature of the employed PS agents, they are preferentially incorporated into the hydrophobic bilayer of the as-prepared liposomes, better demonstrated using **4**@GQDs-MnO_2@PtNPs-FA-liposomes (**Figure 4.1C**).

The qualitative elemental mapping of the resultant liposomal nanocomposites was determined using scanning electron and X-ray energy dispersive spectroscopies (SEM-EDS). **Figure 4.2** shows the SEM image and the corresponding element mapping of **4**@GQDs-MnO_2@PtNPs-liposomes (as an example). The elements: O, C, Zn, Mn, and Pt stem from **4**@GQDs-MnO_2@PtNPs, while P originates from the DOPC lipid used in the fabrication of the liposomes.

The coexistence of these elements (distributed within the composites) implies successful liposomal incorporation of **4**@GQDs-MnO_2@PtNPs. Additionally, the results obtained were consistent with the expected elemental composition for the **4**@GQDs-MnO_2@PtNPs-liposomes (confirmed by EDS spectral analysis), **Figure 4.2**.

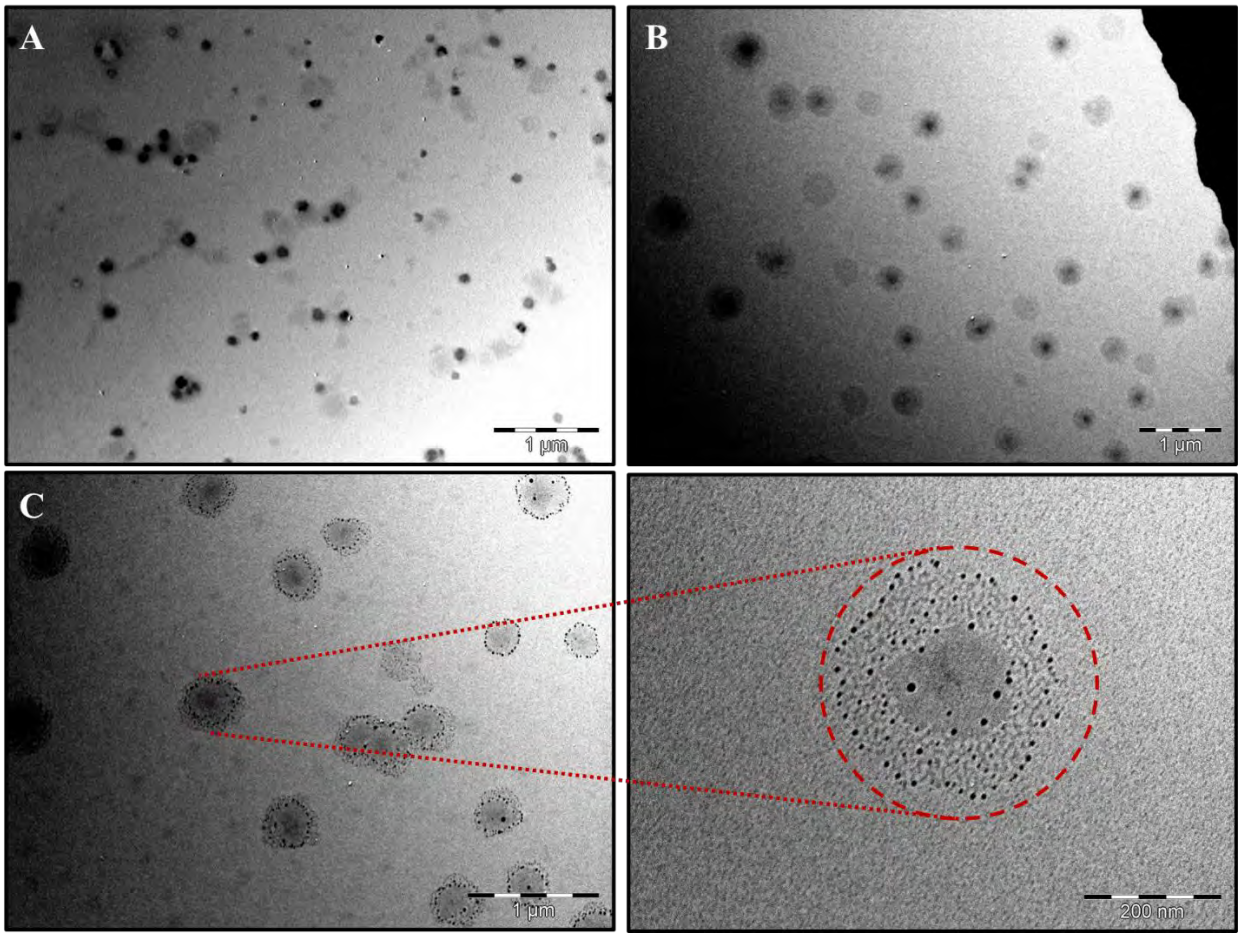

Figure 4.2: Transmission Electron Microscope (TEM) images **2**-liposomes (A), **4**@GQDs-MnO_2@PtNPs-liposomes (B) and **4**@GQDs-MnO_2@PtNPs-FA-liposomes (C).

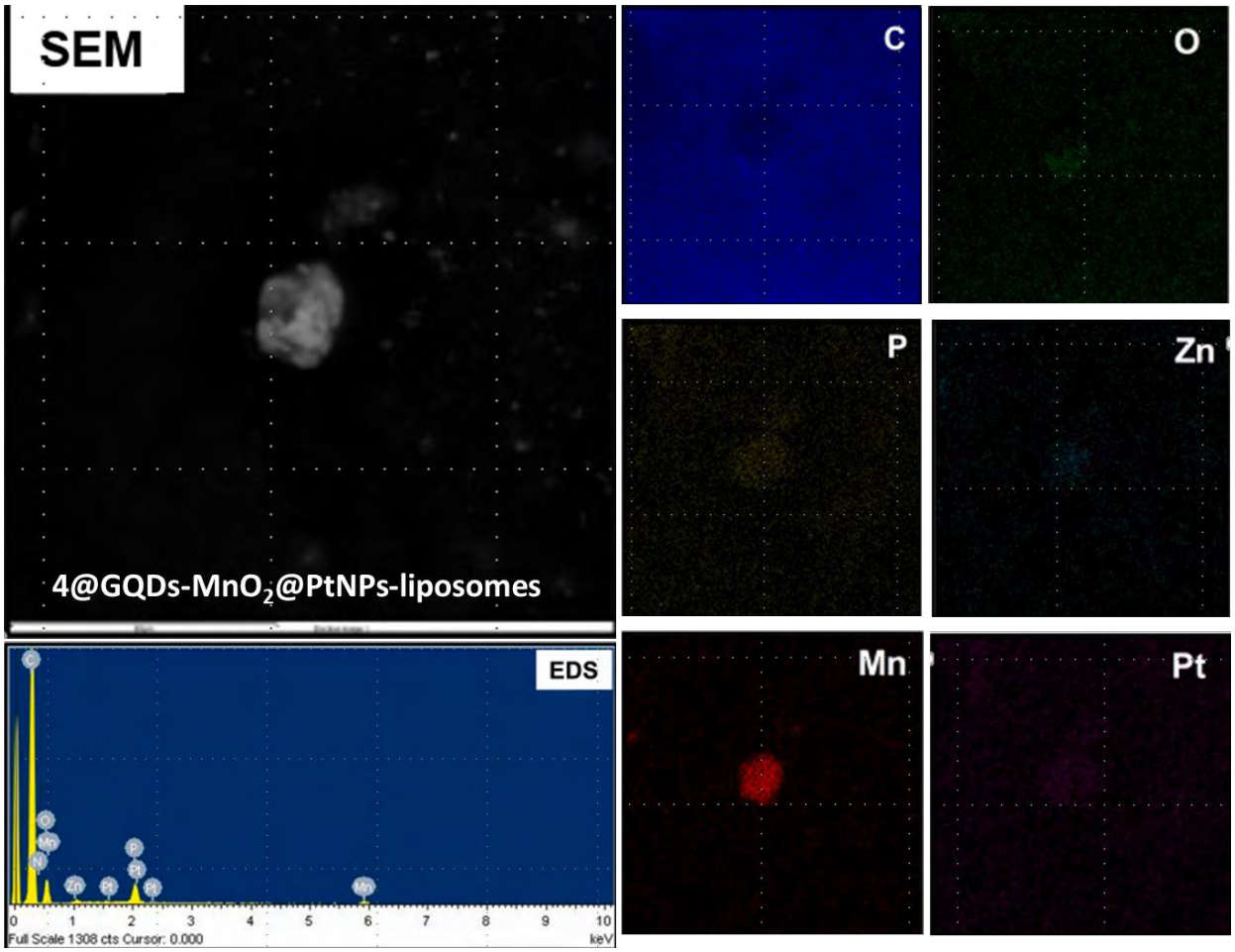

Figure 4.2: SEM images of **4**@GQDs-MnO_2@PtNPs-liposomes with corresponding SEM-EDS mapping images showing the presence of C, O, P, Pt, Mn, and Zn. The SEM image for **4**@GQDs-MnO_2@PtNPs-liposomes is also represented along with its EDS spectrum.

Table 4.1: Liposome characteristics.

Liposomes	EE (%)[a]	Particle size (nm) DLS	PDI[b]	ζ (ev)
1-liposomes	25	100	0.24	-13.1
2-liposomes	23	126	0.28	-11.2
Cl_2SiPc-liposomes	28	106	0.22	-9.4
3-liposomes	30	91	0.48	-50.1
3@GQDs-liposomes	25	142	0.44	-69.1
3@GQDs-MnO_2-liposomes	24	164	0.23	-72.7
3@GQDs-MnO_2-AuNPs-liposomes	20	190	0.28	-74.8
3@GQDs-MnO_2-AgNPs-liposomes	21	220	0.35	-73.2
4-liposomes	40	110	0.26	-18.2
4@GQDs-MnO_2@PtNPs-liposomes	33	277	0.47	-12.6
4@GQDs-MnO_2@PtNPs-FA-liposomes	62	112	0.31	-15.4
5-liposomes	24	150	0.46	-6.4
6-liposomes	28	130	0.33	-8.7

[a]EE = encapsulation efficiency. [b]PDI = Polydispersity indices.

4.2 UV-Vis

The UV-Vis spectra of the encapsulated Pc and Pc-NPs conjugates were retained in their respective liposomal formulations in PBS 7.4 with a prominent Q band (using **2**-liposomes and **4**@GQDs-MnO_2@PtNPs-FA-liposomes as examples) (**Figure 4.3**). The hydrophobic Pcs and Pc-NPs conjugates are effectively and preferentially incorporated into the bilayer of liposomes. The presence of a prominent Q band attests to the successful synthesis of the as-reported liposomes. The as-synthesized liposomes also presented the typical fluorescence features of the parent Pc or Pc-NPs, albeit with reduced fluorescence intensity (figure not shown). The weaker fluorescence of the liposomes is a testament to the successful encapsulation of Pc or Pc-NPs within the liposomal lipid bilayers.

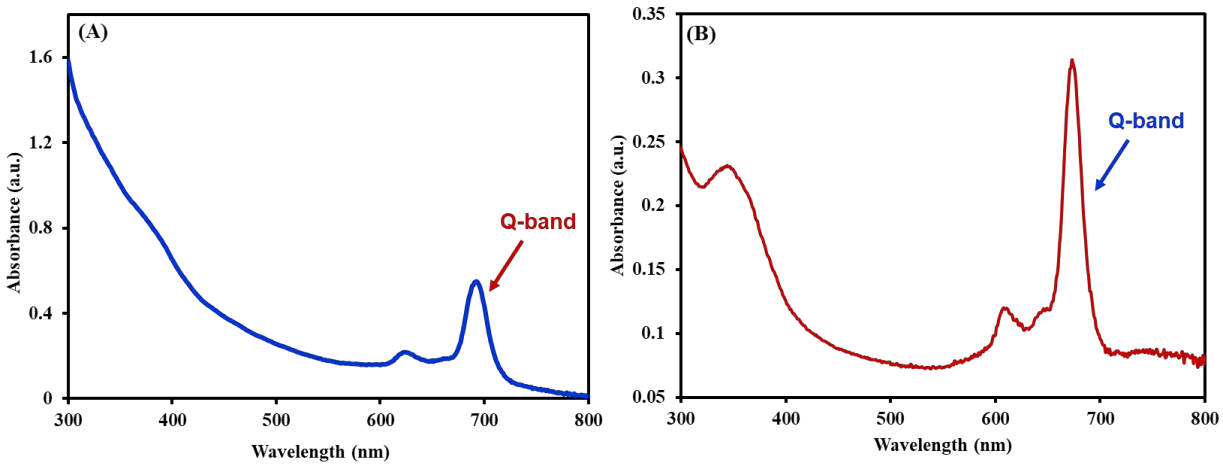

Figure 4.3: UV-Vis spectra of **2**-liposomes (A) and **4**@GQDs-MnO_2@PtNPs-FA-liposomes (B).

4.3 DLS/Zeta potential

Dynamic light scattering (DLS) measurement confirmed the nanoscale sizes for all the liposomal formulations. The obtained DLS sizes are summarized in **Table 4.1**. For the fabricated liposomes, small polydispersity index (PDI) values were obtained confirming a narrow size distribution (**Table 4.1**). The as-fabricated liposomes were nanoscale-sized and, as such, are a favourable size for PDT application. Physicochemical properties, such as size and surface charge, are critical in developing nanosized drug delivery systems. Large particles are typically subject to hepatic clearance, while particles less than 10 nm are susceptible to renal clearance [219]. Typically, nanomedicines of sizes less than 500 nm are preferred since they more readily extravasate and accumulate in tumour parenchyma via the enhanced permeability and retention (EPR) effect [220]. Larger DLS sizes were generally obtained in the presence of multiple nanoparticles.

Zeta potential (ζ) measurements were also carried out to determine the surface charges on the as-fabricated liposomes. A negative zeta ζ value was obtained for all the liposomes (**Table 4.1**). The negative surface charges may be attributed to the presence of exposed phosphate groups compared to choline groups on the outer surface of the liposomes, as is often the case for zwitterionic liposomes [221]. The phospholipid's charge significantly affects liposome's pharmacodynamics and pharmacokinetic properties. Negatively charged liposomal formulations are usually preferred since excessive positive charges are more susceptible to electrostatic interactions with serum proteins, affecting biodistribution [222]. More importantly, such nanocarriers more readily elicit an immune response and, as such, are associated with higher toxicity [223].

Larger zeta potentials were observed for **3** and its conjugates suggesting less aggregation. However, it is not understood why this is the case. The high zeta potential values of the loaded

liposomes point to higher dispersibility, signifying higher colloidal stability. The high colloidal stabilities obtained for the composites make them favourable for biological applications.

Burst release of drug cargo is often unfavourable and can result in non-specific bio-distribution of loaded drugs. An ideal drug-delivery system should only release its drug cargo in the target tissues. The tumour microenvironment, and hence extracellular tumour pH, is acidic owing to the increased production and secretion of lactate and H+ to the extracellular space [224]. As such, this work also investigated the liposomal release mechanism for the encapsulated drug. **Figure 4.4B** presents the average hydrodynamic size of the employed liposomes using **4**@GQDs-MnO_2@PtNPs-FA-liposomes (as an example) at three different pH values (7.4, 6.5, 5.5). As illustrated in **Figure 4.4B**, the rupture/bilayer disruption of liposomes is negligible at pH 7.4 and 6.5, as indicated by the negligible differences in DLS sizes. In effect, membrane destabilization and permeabilization was not observed at these pH values (pH 7.4 and 6.5) no detectable and the liposome membrane integrity is retained. The intra-micellar hydrophobic interactions maintain the liposome integrity; hence, only a negligible increase in liposomal size is observed. A slight increase in the size of the **4**@GQDs-MnO_2@PtNPs-FA-liposomes is observed as the pH is further lowered to pH 5.5. The slight increase in size is attributed to the liposome bilayer disruption due to constituent lipid's protonation which leads to membrane fusion [30]. This observation agrees with the observed decrease in ζ from -15.4 mV at pH 7.4 to +3.48 mV at pH 5.5 (**Figure 4.4A**).

The possibility of NIR triggered release was further illustrated by measuring the fluorescence before and after NIR irradiation (using **4**@GQDs-MnO_2@PtNPs-liposomes, as an example). A reduction in the fluorescence of a diluted sample of **4**@GQDs-MnO_2@PtNPs-liposomes was observed following irradiation (**Figure 4.4C**). The reduction in fluorescence intensity is attributed to loss of liposome integrity, and subsequent rupture. The encapsulated hydrophobic **4**@GQDs-

MnO_2@PtNPs are no longer perfectly maintained within the bilayer, experience enhanced aggregation which explains the observed reduction in observed fluorescence. The final solution was analyzed by transmission electron microscopy and showed the presence of lysed liposomes (**Figure 4.4C** (ii)) when compared to before irradiation, **Figure 4.4C** (i). Therefore, NIR irradiation could, in effect, trigger the release of liposome cargo and, as such, achieve a photodynamic response. The NIR-triggered release of the employed liposomes is represented in **Scheme 4.2**.

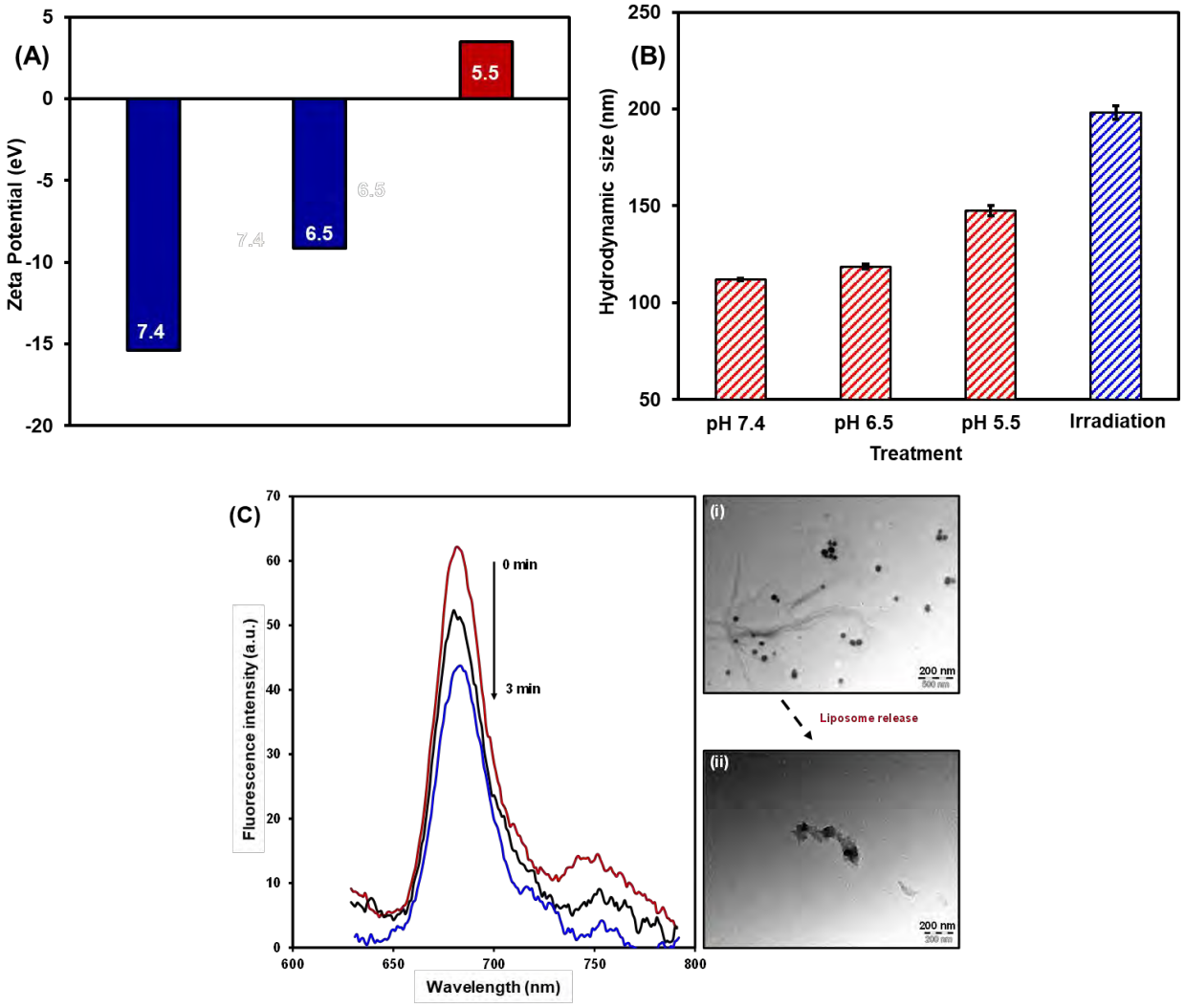

Figure 4.4: Characterizations of **4**@GQDs-MnO_2@PtNPs-FA-liposomes. Zeta potential of changes of liposomes at different pH treatments (A). Hydrodynamic sizes of liposomes in different pH treatments and following irradiation with NIR light for 2 min (B). Change in photoluminescence intensity with light irradiation (in PBS) (C). TEM images before (i) and (ii) after NIR irradiation Light triggered drug release of liposomes.

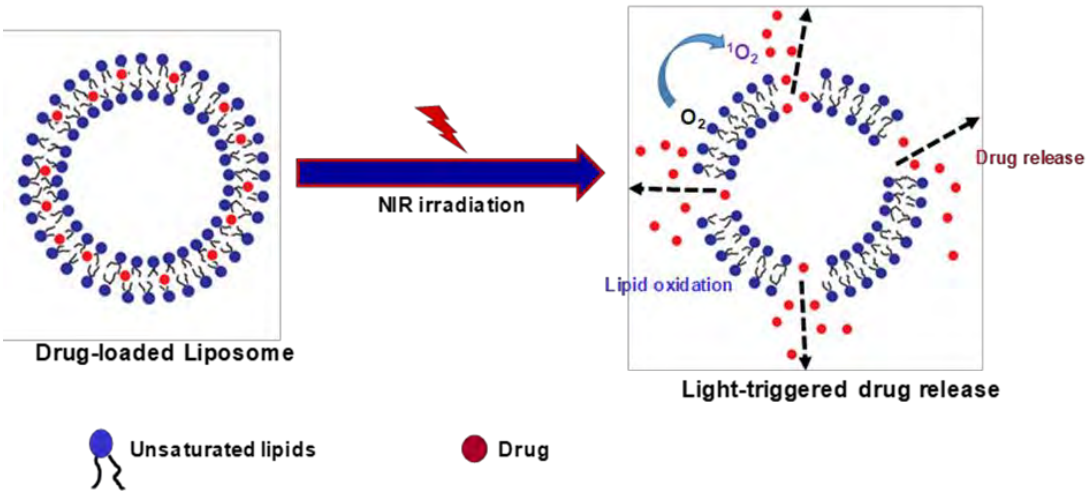

Scheme 4.2: Schematic illustration of light triggered drug release of DOPC liposomes.

4.4 XPS

X-ray photoelectron spectroscopy (XPS) was used to confirm the amide bond formation between the carboxylic acid bearing folic acid and **4**@GQDs-MnO_2@PtNPs-liposomes with amine bearing PEG units (PEG-NH_2). The XPS survey spectra of **4**@GQDs-MnO_2@PtNPs-FA-liposomes show the presence of various elements at their respective binding energies attributed to carbon (C 1s), platinum (Pt 4f), oxygen (O 1s), nitrogen (N 1s), manganese (Mn 2p), phosphorus (P 2p) and Zn (Zn 2p) (**Figure 4.5**). The deconvoluted high-resolution N1s spectra of **4**@GQDs-MnO_2@PtNPs-liposomes and **4**@GQDs-MnO_2@PtNPs-FA-liposomes are shown in **Figure 4.5**. The N 1s core-level spectra for **4**@GQDs-MnO_2@PtNPs-liposomes could be fitted into two chemically distinct components with binding energies 398.7 eV and 401.3 eV, which are attributed to the N-C and NH_2, respectively. The N 1s core-level spectra for **4**@GQDs-MnO_2@PtNPs-FA-liposomes were deconvoluted, and four chemically distinct peaks resulted. Following modification of the liposome, besides the N-C and N-H peaks at 393.0 eV and 399.4 eV, two new peaks in the peak positions 399.4 eV and 402.3 eV, attributed to the presence of the pteridine-N, and CONH, respectively. The presence of the pteridine-N (stemming from folic acid) and amide N confirms the successful attachment of folic acid and hence the synthesis of **4**@GQDs-MnO_2@PtNPs-FA-liposomes.

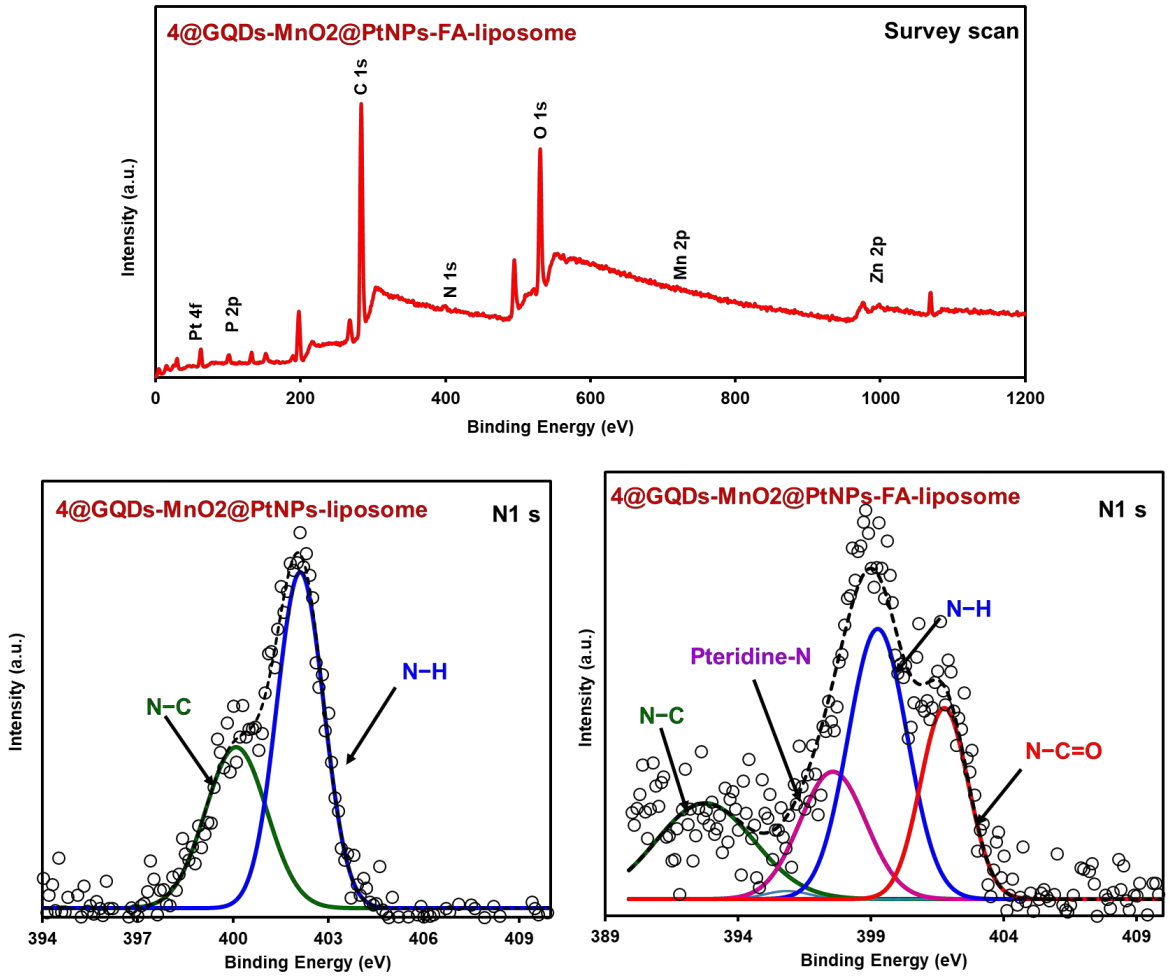

Figure 4.5: XPS survey spectra of (a) **4**@GQDs-MnO_2@PtNPs-FA-liposomes. High-resolution core-level N1 s spectra of **4**@GQDs-MnO_2@PtNPs-liposomes and **4**@GQDs-MnO_2@PtNPs-FA-liposomes.

4.5 Summary of chapter

Various Pc and Pc-NPs conjugates were successfully encapsulated into liposomes. The various drug cargos are preferentially loaded into the bi-layer of the as-synthesized liposomes owing to their hydrophobicity. The formed liposomes presented as predominantly spherical nanoscale structures with sizes between 90 and 280 nm with negative zeta potentials. The negative surface charges and favourable size ranges could benefit PDT applications. The as-synthesized liposomes displayed light responsiveness where near-infrared irradiation could effectively trigger the release of encapsulated drug cargo (Pc and Pc-NPs conjugates). This NIR response may be attributed to the oxidization of the unsaturated phospholipids upon light irradiation, owing to ROS generation by the encapsulated drug cargo.

Chapter V

Density Functional Theory, electrochemical and catalase-like properties of MPcs-NPs - Explored mechanisms for hypoxia modulation/Response

This chapter outlines the various mechanisms explored within this work employed in response to or modulating the hypoxic microenvironment using MPcs or MPc-NPs conjugates.

5. Hypoxic Response

The various methods employed are grouped into (i) Type I PDT (complex **1**), (ii) PDT coupled with oxygen -independent therapy (complex **2**) and (iii) *in-situ* oxygen generation (complexes **3** and **4**) which serves to supplement *in-vitro* oxygen concentrations.

5.1 Type I PDT

To assess hypoxic responsiveness, the redox properties and hence prodrug character of the as-synthesized complex **1** was assessed by cyclic voltammetry (CV) together with those of the Cl_2SiPc and the 2-hydroxy-1,4-naphthoquinone ligand for comparative reasons (**Figure 5.1** and **5.2**) in the aprotic solvent dimethylformamide (DMF) with tetrabutylammonium hexafluorophosphate ($TBAPF_6$) as supporting electrolyte. CV experimental details are provided in Chapter II. DMF as an aprotic solvent, mimics the nonpolar membrane environment more appropriately since the electrogenerated radicals and ion species are unstable in water and other protic solvents [225].

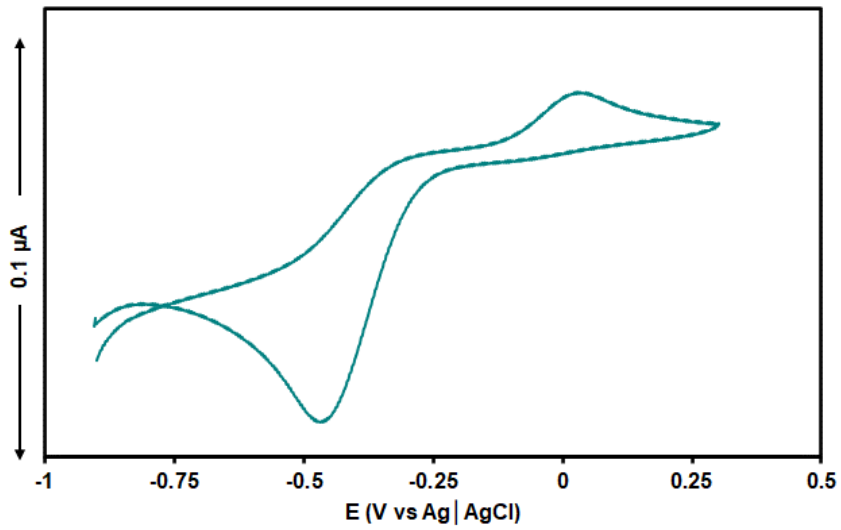

Figure 5.1: Cyclic voltammetry of 2-hydroxy-1,4-naphthoquinone (lawsone) in DMF and 0.1M tetrabutylammonium hexafluorophosphate ($TBAPF_6$) as supporting electrolyte on glassy carbon working and platinum counter electrodes. Reference: Ag/AgCl. Scan rate: 50 mVs^{-1}.

The CV spectrum of 2-hydroxy-1,4-naphthoquinone (lawsone) is shown in **Figure 5.1**. The irreversible reduction peak at −0.46 V vs Ag|AgCl for the axial 2-hydroxy-1,4-naphthoquinone (**Figure 5.1**) corresponds to the one-electron reduction of the quinone into a radical anion, in good agreement with literature values [226]. **Figure 5.2**A shows the cyclic voltammogram of the Cl_2SiPc (black) and **1** (red) in DMF solution. The electrochemical properties of both Cl_2SiPc and **1** are similar to those reported previously for other SiPcs [197]. The CV of Cl_2SiPc shows the presence of one quasi-reversible couple at −0.94 (I) and an irreversible reduction peak at −1.95 V (II) (**Figure 5.2**A), **Table 5.1**. The cyclic voltammogram of **1** shows the presence of three reduction peaks, one quasi-reversible reduction at −0.84 V (II) and two irreversible reduction peaks at −1.48 and − 1.89 V (II and III, respectively) (**Figure 5.2A**, **Table 5.1**). For Cl_2SiPc and **1**, DFT calculations point to first reduction peaks resulting from the frontier -a and -s molecular orbitals (MOs) associated with the Pc π-system (**Figure 5.2B**). For both complexes, the first reduction can

be assigned to reduction within the macrocycle. The anodic shift (by 100 mV) in the first reduction potential of complex **1** compared to that of the parent Cl_2SiPc, can be attributed to the electron-withdrawing effect of the axial naphthoquinone groups on complex **1** (**Table 5.1**). Similar trends have been observed in other SiPc complexes [197]. Electron-withdrawing substituents decrease the electron density, making it easier to reduce and harder to oxidize MPc complexes. **Figure 5.2**A shows that complex **1** is easier to reduce than Cl_2SiPc. The changes in reduction potentials may be attributed to differences in electron withdrawing behaviour of the axial ligands with naphthoquinone containing three oxygen atoms being more electron withdrawing, hence easier to reduce. The peak near 0.1 V observed for lawsone alone in **Figure 5.1**, overlaps with the peak for the SiPc in **Figure 5.2A**.

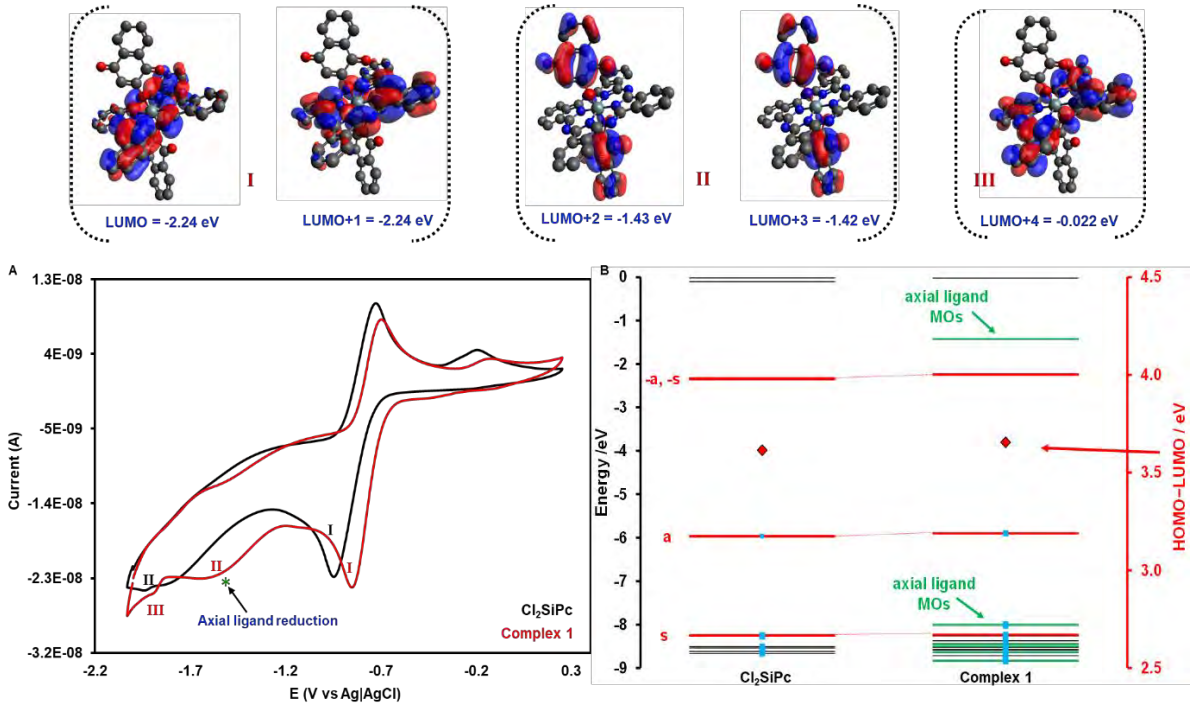

Figure 5.2: (A) Cyclic voltammograms for reductions of complex **1** (**red**) and Cl_2SiPc (**black**) in degassed dimethylformamide (DMF), Scan rate: 50 mVs^{-1}. **(**B) The MO energies of Cl_2SiPc and **1** at the CAM-B3LYP/6-31G(d) level of theory. Red lines highlight the **a**, **s**, **−a**, and **-s** MOs of Michl's perimeter model [227]. Small blue squares are used to highlight occupied MOs. Green lines denote MOs localized primarily on the axial ligands of complex **1**. HOMO–LUMO gap values are highlighted with red diamonds and are plotted against the secondary axis. **Top:** The angular nodal patterns of the orbitals of complex **1** that are responsible for the primary reduction potentials on the cyclic voltammogram of complex **1** at an iso surface of 0.02 a.u. with respective band energies.

Table 5.1. Redox data of the parent Cl_2SiPc and complex **1**.

Compound	**Reduction**[a]		
	$E_{1/2}$(I)	**$E_{1/2}$(II)**	**$E_{1/2}$(III)**
Cl_2SiPc	−0.94	–	−1.95
Complex **1**	−0.84	−1.48	−1.89

[a]Potentials are in volts (V) vs Ag|AgCl in dimethylformamide containing 0.1 M tetrabutylammonium hexafluorophosphate ($TBAPF_6$) as supporting electrolyte, recorded at room temperature at a sweep rate of 50 mV/s using glassy carbon working and platinum counter electrodes.

For Cl_2SiPc and complex **1**, no reduction peaks associated with the central silicon metal were observed since the central Si (IV) metal is redox inactive [228]. Notably, a new reduction peak of −1.48 V was observed in the cyclic voltammogram of complex **1**. This reduction peak is absent in the CV of Cl_2SiPc (**Figure 5.2B**). TD-DFT calculations provide evidence that this new peak may have resulted from the presence of the LUMO+2 and LUMO+3, primarily localized on the axial naphthoquinone moieties (**Figure 5.2B**). The reduction peak at −1.48 V in the CV of complex **1** may therefore be attributed to the reduction of the attached naphthoquinone axial ligand. The reduction of the axial naphthoquinone would result in the successful formation of the radical anion. The reduction of the naphthoquinone in complex **1** was observed at a more negative potential than the corresponding 2-hydroxy-1,4-naphthoquinone. This difference may be attributed to the introduction of the π-electron-rich phthalocyanine core. Nevertheless, CV experiments point to the successful reduction of the naphthoquinone moieties in complex **1** and suggest retention of its prodrug-like character.

Electron spin resonance was employed to gain insight into the photochemistry of the as-synthesized complex **1** to determine its ROS-producing ability ($^1O_2$, •OH, and O_2•-) (**Figure 5.3**). 2,2,6,6-Tetramethylpiperidine (TEMP) was used to probe the photogeneration of $^1O_2$. TEMP is specifically oxidized by singlet oxygen to the paramagnetic 2,2,6,6-tetramethyl piperidinyl oxy (TEMPO), detected as three hyperfine splitting signals of equal intensities.

A triplet TEMPO ESR signal was detected when a solution of the as-synthesized complex **1** was irradiated in the presence of TEMP (**Figure 5.3**). No distinct signals could be detected without irradiation. The TEMPO signal was only observed following irradiation, signifying the light-induced singlet oxygen-generating ability of **1**. 5,5-Dimethyl-1-pyrroline N-oxide (DMPO) was used to probe the generation of either •OH or O_2•- by **1**. The ESR signal of the **1** and DMPO was

silent in the absence of light (**Figure 5.3A**). However, NIR irradiation led to the emergence of an ESR signal with four hyperfine splitting signals of intensities 1:2:2:1 characteristic of the DMPO-•OH adduct, which suggested the photogeneration of hydroxyl radicals. The photochemical generation of hydroxyl radicals is known to proceed via a PS radical anion intermediate [229-231]. For comparison, the TEMP and DMPO ESR signals resulting from the photoirradiation of Cl_2SiPc is shown in **Figure 5.3B**. Both singlet oxygen and hydroxyl radicals are generated following irradiation of the Cl_2SiPc, though to a lesser degree compared to what was observed for complex **2**.

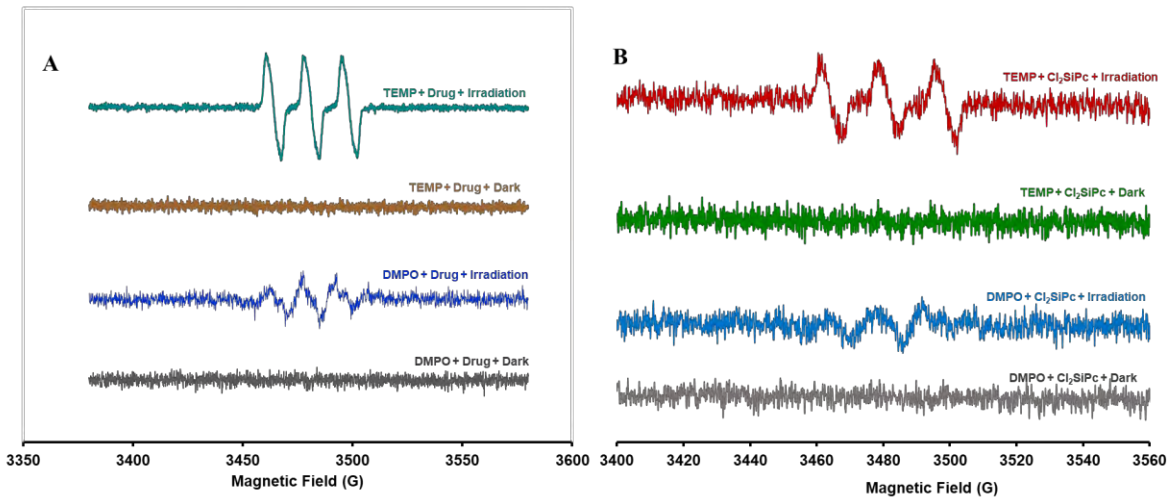

Figure 5.3: (A) Electron spin resonance spectroscopy (ESR) signal of the mixture containing either DMPO (50 µM) or TEMP (25 µM) and complex **1** under NIR light irradiation. (B) Electron spin resonance spectroscopy (ESR) signal of the mixture containing either DMPO or TEMP and Cl_2SiPc under NIR light irradiation.

While it is generally accepted that $^1O_2$ is the major cytotoxic species responsible for photodynamic lethality, recent studies have demonstrated the increasingly crucial role that hydroxyl radicals, superoxide, and other Type I species play in PDT [231,232]. However, direct comparisons between contributions of Type I and Type II photo-mechanisms are difficult owing to the relative complexity of ROS generation [233]. For the rest of the complexes, only a triplet TEMPO ESR signal was detected following irradiation in the presence of TEMP implying light-induced singlet oxygen generation. No distinct signals could be detected without irradiation. No hydroxyls radicals were also detected. The formation of hydroxyl radicals by complex **1** may be attributed to the ease of formation of the PS radical anion intermediate owing to the electron withdrawing effect of the quinoid moiety. The rest of the molecules do not experience such large changes in reduction potentials.

5.2 PDT-coupled with oxygen-independent Therapy

This work also explored the feasibility of PDT and nitric oxide release for effective tumour therapy. To achieve this, a nitroso substituted silicon phthalocyanine (complex **2**) was evaluated on its potential to release nitric oxide as a possible mechanism to hypoxic tumour therapy.

This work assessed and compared the spectral features of complex **2** against the parent Cl_2SiPc. These were explained using trends observed in DFT and TD-DFT calculations (**Figure 5.4**, **Table 5.2**) at the B3LYP/6-31G(d) and CAM-B3LYP/6-31G(d) levels of theory, respectively. The calculated TD-DFT spectrum of complex **2** is similar to what is observed experimentally. In the TD-DFT spectrum, the HOMO → LUMO and HOMO → LUMO+1 transitions provide the predominant contributions to the lower energy band, which can be assigned to the Q transition of Gouterman's 4-orbital manner [234] (**Table 5.3**). The band in the 300–400 nm region can similarly be readily assigned to the B transition.

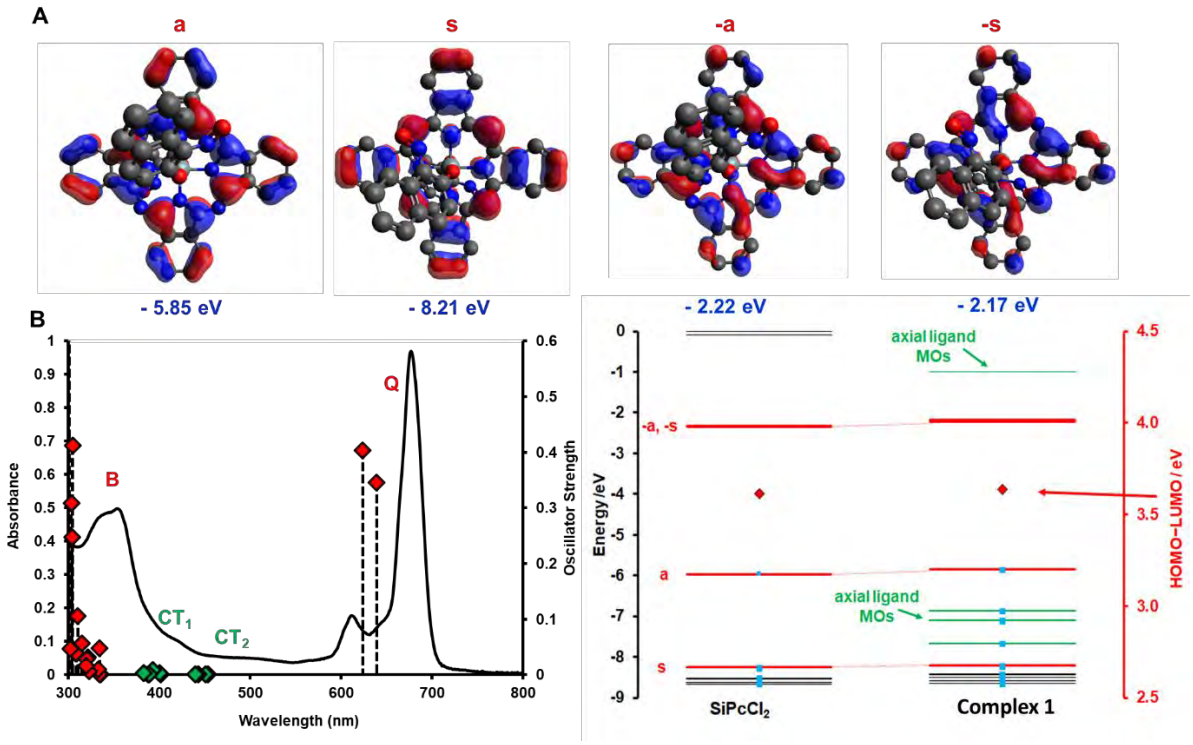

Figure 5.4: (A) The angular nodal patterns and MO energies of the a, s, -a, and -s MOs of Michl's perimeter model (corresponding to the 1a1u, 1a2u and 1eg* Mos, respectively, of Gouterman's 4-orbital model that are associated with the Q and B bands for complex **2** recorded at an isosurface of 0.02 a.u. (B) The calculated TD-DFT spectrum of the as-synthesised NO-SiPc complex at the CAM-B3LYP/6-31G(d) level of theory. The Q and B bands are highlighted with red diamonds. Green diamonds denote transitions involving occupied MOs localized on the axial ligands. These are associated with charge transfer transitions (CT_1 and CT_2) originating from the MOs localized on the axial ligands. A forbidden ligand to ligand band is predicted at 846 nm. (C) The MO energies of Cl_2SiPc and complex **2** at the CAM-B3LYP/6-31G(d) level of theory. Red lines highlight the a, s, -a and -s MOs of Michl's perimeter model. Small blue squares are used to highlight occupied MOs. Green lines denote MOs localized on the axial ligands of complex **2**. Average HOMO–LUMO gaps that take the a, s, -a and -s MOs into account are highlighted with red diamonds and are plotted against the secondary axis.

In nitroso-modified PS complexes, the photorelease of •NO is known to proceed via an electron transfer process [235]. The SiPc-core effectively acts as a photo-antennae. Therefore, it is feasible that in this case, the photorelease of •NO is initiated by photoinduced electron transfer (PET) from the nitrosonaphthalene moiety to the SiPc-core. In its excited singlet state, the nitroso moiety acts as an electron donor, facilitating electron transfer to the excited SiPc (which acts as an electron acceptor). The TD-DFT calculations reveal that the B and Q bands cannot be described as pure one-electron transitions between the main frontier π-MOs; hence, they may be affected by significant degrees of charge transfer associated with the introduction of the nitroso moieties. Evidently, the UV–Vis spectrum of complex **2** contains new, relatively weak, broad bands at ca. 410 nm and 512 nm (CT_1 and CT_2, where CT = charge transfer) (**Figure 5.4**), which are absent in the spectrum of the parent Cl_2SiPc. The TD-DFT calculations predict that the bands attributed to intramolecular charge transfer (ICT) primarily arise from electron transitions originating from molecular orbitals localized on the axial nitroso moieties.

•NO release from other PS complexes where the nitroso moiety is appended on a PS antenna has been reported to proceed through a similar mechanism [235]. Photoinduced electron transfer between two species requires close spatial proximity between the donor and acceptor moieties. The B3LYP optimized structure (**Scheme 5.1**) shows an evident bent conformation. The occupied MOs associated with the CT_1 and CT_2 bands are localized almost exclusively on the nitroso-containing axial ligand (**Scheme 5.1A**, **Table 5.3**). The B3LYP optimized geometry provides short distances between the nitroso moiety and the SiPc antenna moiety, which facilitates greater charge transfer efficiency [236]. Based on the above observations, an illustrative mechanism for the photogeneration of $^1O_2$ and •NO from complex **2** is proposed in **Scheme 5.3B**. The predicted electronic transitions observed in the NO-SiPc spectrum are summarized in **Table 5.3**.

Table 5.3. TD-DFT spectra of the B3LYP optimized geometries for complex **2** calculated with the CAM-B3LYP functional and **6-31G**(d,p) basis sets.

Band[a]	#[b]	Calculated[c]		Experimental[d]	Wavefunction=[e]	Character
		λ/nm	*f*	λ/nm		
Q	3	639	0.35	676	94 % H (**a**) →L (**-a**)	Pc(π) to Pc(π*)
	4	623	0.40		94 % H (**a**) →L+1 (**-s**)	
ICT	6	451	0.005	512	97 % H−2NO→L (**-a**)	Axial (π) to Pc(π*)
	7	443	0.003		96 % H−1NO→L+1 (**-s**)	
	11	393	0.0083	410	92 % H−3NO→L (**-a**)	
	12	389	0.0008		60 % H−4NO→L (**-a**)	
	13	387	0.0008		60 % H−3NO→L+1 (**-s**)	
B	26	305	0.41	352	54 % H−7 (**s**) →L (**-a**)	Pc(π) to Pc(π*)
	30	301	0.70		54 % H−7 (**s**) →L+1 (**-s**)	

[a]The band assignment is described in the text. [b]The number of states assigned in ascending energy within the TD-DFT calculation. [c]Calculated band energies (10^3 cm^{-1}), wavelengths (nm), and oscillator strengths (c). [d]Observed energies (10^3 cm^{-1}) and wavelengths (nm) in DMSO. [e]The wave functions based on the eigenvectors predicted by TD-DFT. H and L denote the HOMO and LUMO and Michl's [227] a, s, -a, -s notation is added in parentheses where appropriate. Only eigenvectors of 40 % or higher are reported. NO as a superscript denotes MOs largely localized on the nitrosonaphthalene axial ligand.

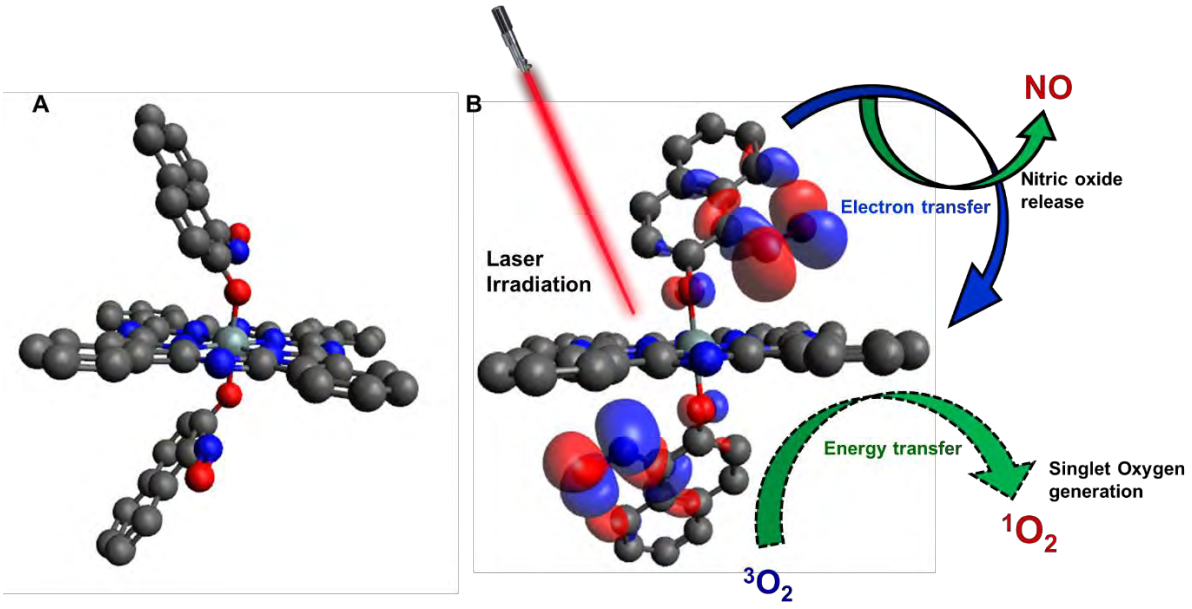

Scheme 5.1. (A) Ball and stick representation of the B3LYP optimized geometry of **2** in its ground state. (B) The HOMO−2 of complex **2** at an isosurface of 0.02 a.u.

5.3 *In-situ* oxygen generation

In this work, complexes **3** and **4** were conjugated to various nanomaterials to integrate catalase-like properties of nanomaterial hybrids with the singlet oxygen generating abilities of MPc complexes. The various nanomaterials were therefore assessed for their ability to catalyse H_2O_2 to O_2, supplementing *in-vitro* oxygen concentrations necessary for PDT. Catalase-mimicking ability was assessed using a degassed (Ar saturated) H_2O_2 solution (5×10^{-3} M) in acetate buffer (pH 5). An oxygen probe (JPBJ-608 Portable Dissolved Oxygen Meter) was used to record the dissolved O_2 in H_2O_2 solutions. Details are provided in chapter II.

For the conjugates for complex **3** (**3**@GQDs-MnO_2, **3**@GQDs-MnO_2-AgNPs, **3**@GQDs-MnO_2-AuNPs), oxygen generation was fast (bubbles were observed due to oxygen being generated from the solution). However, there were no visible bubbles (or appreciable amounts of oxygen) when complex **3** or **3**@GQDs were analysed alone. Although, **3**@GQDs-MnO_2 showed great promise for H_2O_2 catalysis, the conjugates integrating Au and AgNPs possessed higher catalase-mimicking properties (**Figure 5.5A**). The results demonstrate the advantages of incorporating the noble metals Ag and Au in increasing the oxygen generating ability of MnO_2 in acidic media which meets the requirement for hypoxic cancer therapy. Moreover, because H_2O_2 is continuously produced by tumour cells, the O_2 generation by **3**@GQDs-MnO_2-AgNPs and **3**@GQDs-MnO_2-AuNPs was examined with continuous addition of exogenous H_2O_2 (1×10^{-3} M) into the system every 15 min to simulate in vivo conditions, **Figure 5.5B**. It was found that a single dose of either **3**@GQDs-MnO_2-AgNPs or **3**@GQDs-MnO_2-AuNPs continuously generated O_2 for at least three cycles (**Figure 5.5B**) with a relatively stable production capability and a relative standard deviation (RSD) of ≈ 5.

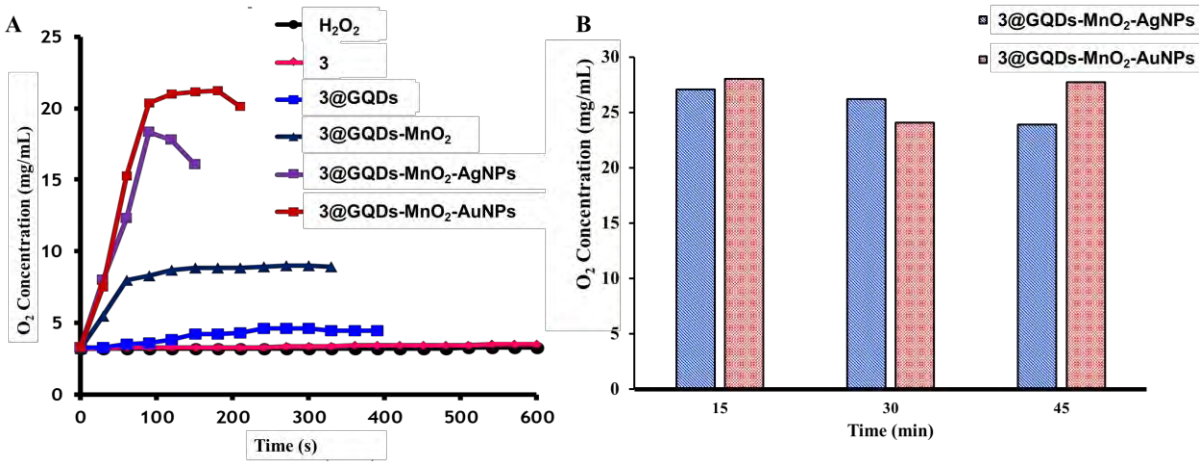

Figure 5.5: Ex vivo O_2 generation by complex 3 composites in the presence of H_2O_2. (**A**) The amount of oxygen produced in different systems (**3**, **3**@GQDs, **3**@GQDs-MnO_2, **3**@GQDs-MnO_2-AgNPs, **3**@GQDs-MnO_2-AuNPs) in the presence of H_2O_2 over time. (**B**) O_2 generation by adding H_2O_2 (1×10^{-3} M) to the nanocomposite solutions at pH 5 monitored at different times following addition of H_2O_2.

The MnO_2, PtNPs were also accessed, compared to the hybrid superstructure MnO_2@PtNPs. For the three samples probed, oxygen generation was also fast (bubbles were observed due to oxygen being generated from the solution as discussed for the conjugates). Notably, the amount of dissolved oxygen produced in the solution containing MnO_2@PtNPs was significantly higher than that observed for either MnO_2 or PtNPs, **Figure 5.6**. The breakdown of H_2O_2 using MnO_2@PtNPs was also more rapid, seen from the slope signifying fast oxygen generation (**Figure 5.6**). Indeed, these results highlight the synergistic advantages realizable by compositing MnO_2 with PtNPs as catalase mimics. In contrast, negligible responses were observed for control samples with only H_2O_2 over the same period. The as-prepared MnO_2@PtNPs, therefore, showed superior catalytic behaviour towards the catalytic conversion of H_2O_2 to O_2 which gave credence to its coupling to complex **4** for PDT experiments.

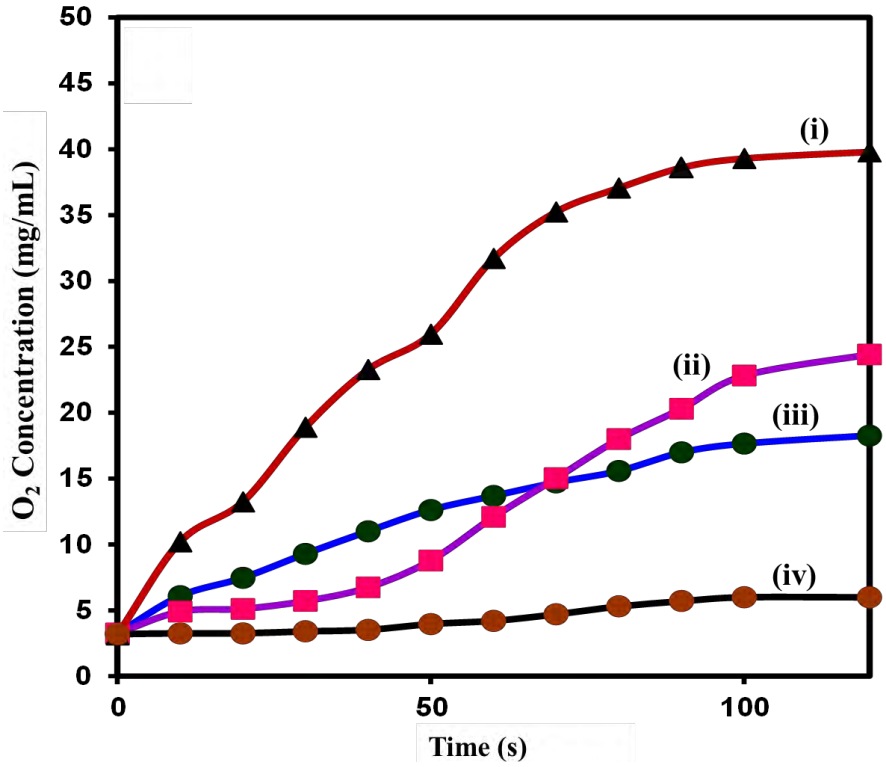

Figure 5.6: Ex vivo O_2 generation abilities of MnO_2@PtNPs (i), PtNPs (ii), MnO_2 (iii), in the presence of H_2O_2. H_2O_2 alone is used as control (iv).

5.4 Summary of Chapter

The feasibility for hypoxic response or modulation using complexes **1** and **2** as well as various NPs conjugates of complex **3** and **4** were explored in this chapter. The various mechanisms for hypoxic response included (i) Type I PDT (complex **1**), (ii) PDT coupled with oxygen - independent therapy (complex **2**) and (iii) *in-situ* oxygen generation using catalase-mimicking nanoparticles (complexes **3** and **4**) which serve to supplement *in-vitro* oxygen concentrations using MPcs or MPc-NPs conjugates were demonstrated either via computational chemistry or catalase mimicking experiments. This work shows the retention of prodrug-like character by complex **1**, and NIR responsive nitric oxide release by complex **2**. This work also highlights the synergistic advantages realizable by compositing MnO_2 with various other catalase mimics resulting in various hybrids with superior catalytic behaviour towards the catalytic conversion of H_2O_2 to O_2 and lays credence to their conjugation to MPcs complexes to afford them catalase-like character. These results therefore motivate further analysis of the PDT properties of the resulting conjugates with MPcs.

Chapter VI

Photophysical and Photochemical properties

This chapter gives details on the photophysical and photochemical behaviour; fluorescence quantum yields and lifetimes, triplet quantum yields and lifetimes, and singlet oxygen quantum yields of phthalocyanines when alone and when conjugated to nanoparticles.

6.1 Fluorescence excitation and emission spectra

The absorption, emission and excitation spectra of the employed Pcs and Pc-NP conjugates were analysed. **Figure 6.1A** shows an overlay of the absorption, excitation, and emission spectra of complex **1** in DMSO as representatives for other complexes and their conjugates. The fluorescence spectrum profile is a mirror image of the excitation and absorption spectra. The observed closeness in the position of the Q band absorption and the excitation maxima indicate that the geometry of the excited molecule does not differ from that in the ground state. In essence, the nuclear configurations of the ground and excited states are similar and are not affected by excitation and precludes aggregation in solution in DMSO. Similar fluorescence behaviour was observed for all Pc complexes alone.

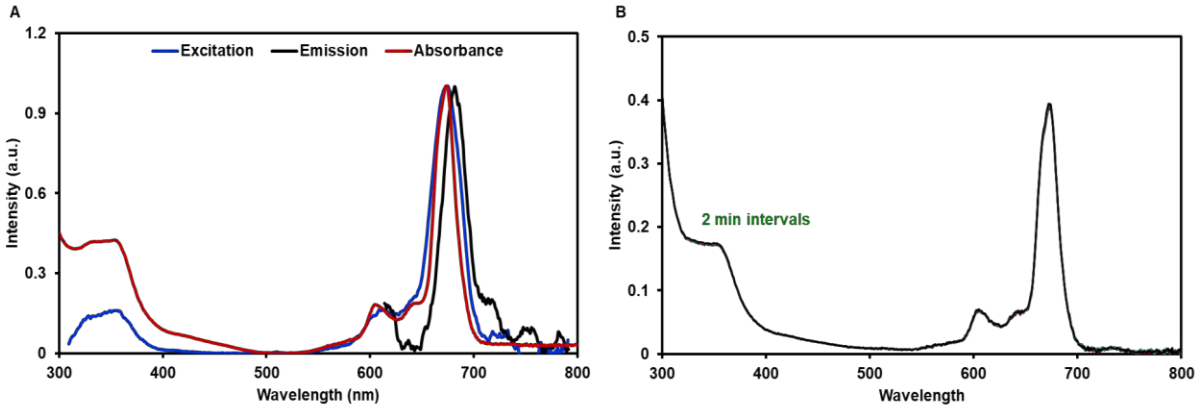

Figure 6.1: (A) Absorption, excitation, and emission spectra of complex **1** in DMSO. (B) Photostability of complex **1** in aerated DMSO solutions under irradiation at 680 nm for 10 mins using a Modulight® Medical Laser System (MLS) 7710–680 channel Turnkey laser system.

6.2 Photostability

The photostability of the as-synthesized complexes was evaluated herein and was assessed by observing the changes in its absorption features following irradiation. The ROS produced by the photosensitizers may inadvertently lead to photobleaching, severely affecting the photosensitizing ability and efficacy of PDT [237]. **Figure 6.1B** shows that the Q and B band spectra of complex **1** (as an example) maintain their original shape and intensity over the irradiation period with near infrared (NIR, 680 nm) light at 2 min intervals. The lack of significant changes in absorption features of complex **1** following light irradiation implies its stability over the studied range. Similar photostable behaviour was observed for all Pc complexes employed.

6.3 Fluorescence quantum yields (Φ_F) and lifetimes (τ_F)

In this work the fluorescence quantum yields (Φ_F) were determined by a comparative method [16] and calculated according to **Equation 1.1**. Unsubstituted ZnPc in DMSO ($\Phi_F = 0.2$) [1]. **Table 6.1** shows the Φ_F values of the complexes and their respective conjugates in DMSO.

Table 6.1: Fluorescence and triplet state parameters of the Pcs and their respective conjugates in DMSO.

Complex	[a]λabs	[b]Em	Φ_F	τ_F (ns)	Φ_T	τ_T (µs)
Complex **1**	672	680	0.37	4.58	0.36	139
Complex **2**	675	682	0.23	3.95	0.37	126
Cl_2SiPc	672	682	0.41	5.06	0.38	155
[c]Complex **3**	680	690	0.10	2.90	0.67	368
3@GQDs	680	691	0.10	2.88	0.88	249
3@GQDs-MnO_2	680	693	0.13	2.87	0.71	244
3@GQDs-MnO_2-AgNPs	680	689	0.08	2.76	0.79	224
3@GQDs-MnO_2-AuNPs	680	690	0.08	2.78	0.76	228
[d]Complex **4**	674	682	0.18	3.21	0.73	233
4@GQDs	675	683	0.16	3.20	0.68	215
4@GQDs-MnO_2@PtNPs	675	682	0.12	3.52	NS	NS
Complex **5**	678	689	0.21	2.80	0.62	138
Complex **6**	694	703	0.16	2.64	0.68	146

NS = No signal, [a]abs = absorption, [b]Em = emission, [c]data from Ref. [238], [d]data from Ref. [89].

The fluorescence quantum yield values of complexes **1** and **2** were 0.37 and 0.23, which were lower than that of the parent Cl_2SiPc (0.41) [238] (**Table 6.1**). The lower fluorescence quantum yield and lifetime value of complex **1** (in comparison to Cl_2SiPc) can be attributed to the electron-withdrawing effect of the axial naphthoquinone moiety, which acts to deactivate the excited singlet state while encouraging intersystem crossing to the triplet state [239]. The marked decrease in the fluorescence quantum yield of complex **2** (Φ_F = 0.23) may be attributed to the radical nature of nitric oxide which helps to deactivate the singlet state and may encourage intersystem crossing to the triplet state [240].

Following conjugation to NPs, an observed decrease in the Φ_F of complexes **3** and **4** was observed (**Table 6.1**). The low Φ_F of MPc-NPs conjugates can be attributed to spin orbit coupling [241]. NPs impose a heavy atom effect on the Pc, which encourages intersystem crossing to the triplet state thereby suppressing radiative relaxation of the excited photosensitisers to the ground state.

Complex **5** showed higher fluorescence quantum yield than complex **6** (**Table 6.1**). The low fluorescence quantum yield of the non-peripherally substituted complex **6** suggests quenching of the singlet state or that the substituents at the α-position enhance the intersystem crossing. The former would result in high triplet quantum yields.

The fluorescence lifetimes (τ_F) were obtained using the time correlated single photon counting (TCSPC) method. **Table 6.1** shows the τ_F values of the complexes and their respective conjugates in DMSO. Complex **1** (used as a representative example, **Figure 6.2**) exhibited a mono-exponential photoluminescence decay with a photoluminescence lifetime of 4.58 ns. The successful fitting of the fluorescence decay curve of complex **1** to a mono-exponential function ruled out aggregation effects. Mono-exponential photoluminescence decay curves were also

observed for the other MPcs or MPc-NPs conjugates. The fluorescence lifetime (τ_F) of the axially di-substituted complex **2** was determined to be 3.95 ns, **Table 6.1**, which is shortened compared to the parent Cl_2SiPc, for the same reasons provided for fluorescence quantum yields. Φ_F and τ_F values of complex **1** and complex **2** were comparable to other axially substituted SiPcs reported in the literature [242]. As expected, the reduction in the Φ_F owing to the presence of the NPs also resulted in shortened fluorescence lifetimes, except for **3**@GQDs-MnO_2 (**Table 6.1**). The fluorescence lifetime of **6** (2.64 ns) was also lower than that of **5** (2.80 ns) (**Table 6.1**) due to quenching of excited singlet states of non-peripheral substitution.

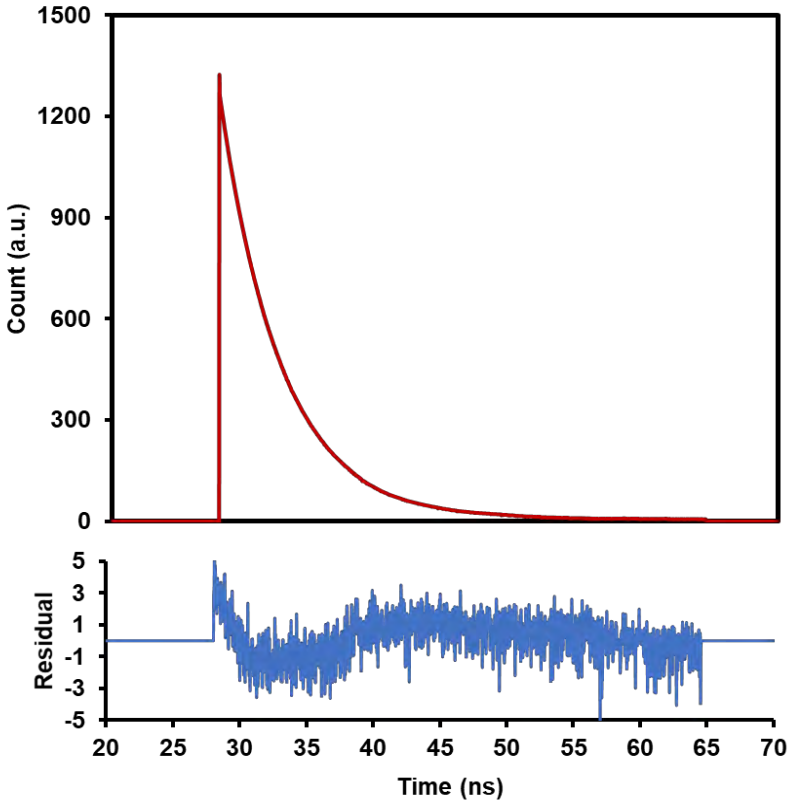

Figure 6.2: Fluorescence decay curve for complex **1** in DMSO.

6.4 Triplet Quantum yields (Φ_T) and triplet lifetimes (τ_T)

The triplet state quantum yield (Φ_T) represents the fraction of molecules that undergo intersystem crossing to the excited triplet state. A high triplet state quantum yield suggests high efficiency of intersystem crossing, which is an attractive feature for MPcs intended for PDT as photosensitizers. As such, a high triplet quantum yield is of great importance since it may inform singlet oxygen production efficiencies. The triplet state lifetime (τ_T) represents the average time taken in the excited triplet state.

In this work, the Φ_T and τ_T values were measured by laser flash photolysis system in argon saturated solutions of the complexes or their conjugates in DMSO as described in Chapter II. The Φ_T and τ_T values are summarized in **Table 6.1**. For **4**@GQDs-MnO_2@PtNPs, triplet state properties could not be determined owing to low instrumental signals. The transient differential spectrum for complex **3** (used as an example) in DMSO can be seen in **Figure 6.3** showing a triplet absorption maximum at ca. 500 nm. **Figure 6.3** (**insert**) shows the triplet decay curve for complex **3**. The triplet decay curve obeyed first-order kinetics which has been reported for MPcs-type complexes [243]. **Table 6.1** shows that introduction of either Au or Ag NPs results in sharp increases in triplet quantum yields (**Table 6.1**). This is a result of the heavy atom effect of Ag and Au. There is also a large increase in the triplet quantum yield for **3** in the presence of GQDs (Φ_T=0.88). This could be due to the electron donating ability of GQDs since electron donating groups are known to increase intersystem crossing in porphyrin-like complexes [244]. However, this was not observed for **4** and **4**@GQDs with Φ_T values of 0.73 and 0.68, respectively. In all cases, a shortening of triplet lifetime with an increase in triplet quantum yield was observed. Complex **6** had a higher triplet quantum yield and lifetime than complex **5**, a feature that may be attributed to more favourable intersystem crossing in **6** than **5**.

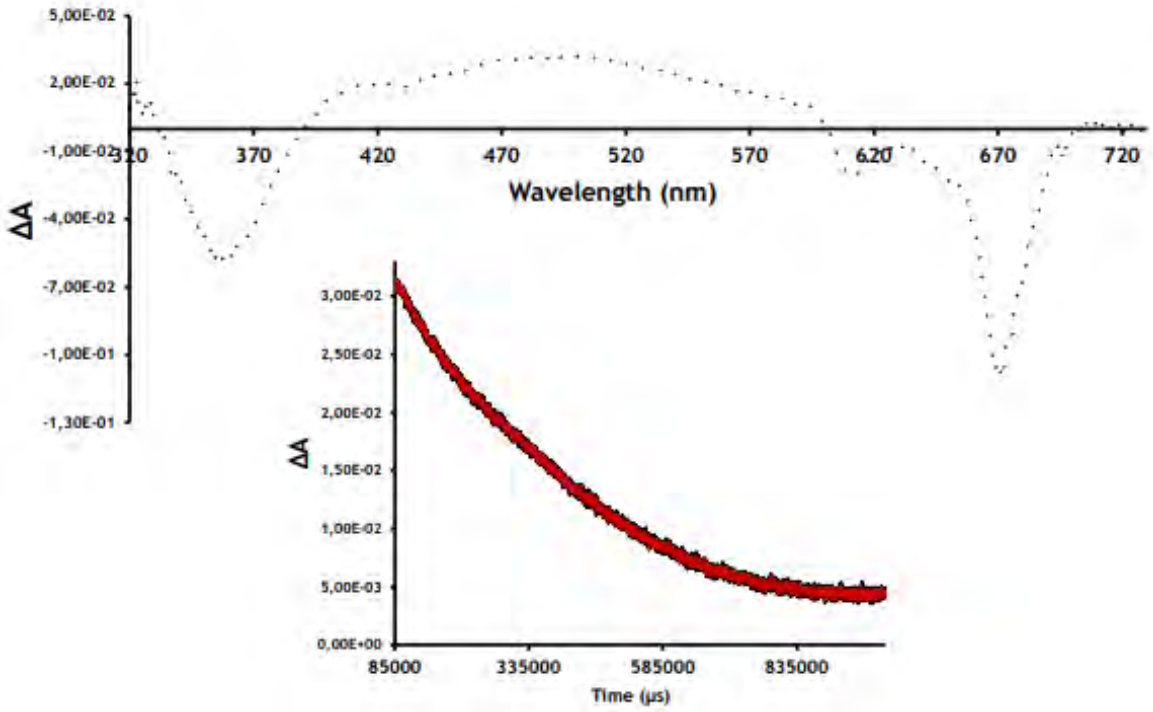

Figure 6.3. Transient differential spectrum of complex **3**, excitation wavelength at 660 nm. **Insert**: corresponding triplet decay curve in DMSO.

6.5 Singlet oxygen quantum yields (Φ_Δ)

The ability of MPcs and their conjugates to generate singlet oxygen species was evaluated using a chemical method. **Equation 1.4** was used to calculate the singlet oxygen quantum yield with unsubstituted ZnPc $\Phi_\Delta = 0.67$ in DMSO [1] as reference standard. DPBF was used as the singlet oxygen scavenger and its rate of photodegradation was monitored by UV/Vis spectroscopy. **Figure 6.4** shows the degradation of DPBF by complex **2** for illustrative purposes. A time-dependent decrease in DBPF peak was observed at the applied time intervals, indicating singlet oxygen photogeneration by the **2** (**Figure 6.4**).

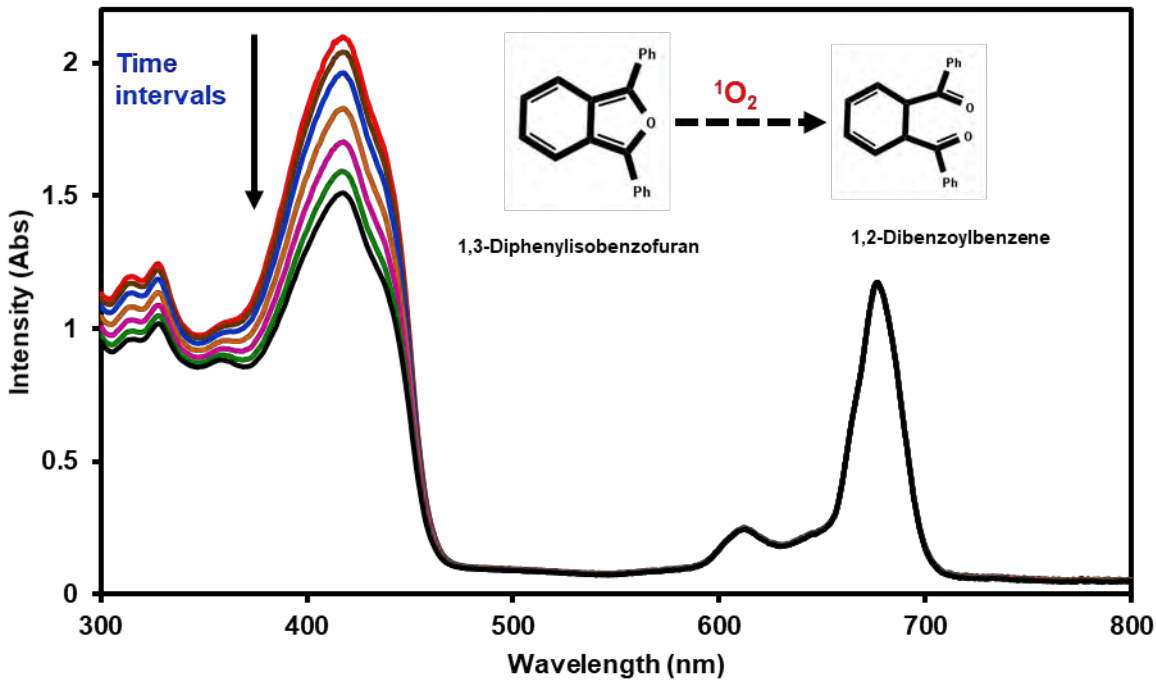

Figure 6.4: Spectral changes observed for 1,3-diphenylisobenzofuran (DPBF) degradation in the presence of **2** (**insert**: the structure of DPBF and its degradation product). All spectra were measured in DMSO.

For all MPcs and MPc-NPs conjugates, the Q band absorption did not change, suggesting their relative photostability over the irradiation period. The singlet oxygen quantum yield of **1** was determined to be 0.22 (**Table 6.2**). This obtained Φ_{Δ} was higher than that of the dichloro-substituted Cl_2SiPc (0.18). Likewise, an enhanced singlet oxygen-generating ability was observed for **2** over the parent Cl_2SiPc which may be attributed to the intramolecular electron transfer effect of the axial naphthoquinone groups. A decrease in the singlet oxygen generation of complex **3** was observed for **3**@GQDs and **3**@GQDs-MnO_2 in DMSO, yet there was a considerable increase in triplet quantum yield, from which singlet oxygen is generated. A decrease in Φ_{Δ} with increase in Φ_T may be due to the screening effects of the nanoparticles, which could have prevented the interaction of the excited triplet state of the Pc in the conjugates and the ground state molecular oxygen [245]. There were increases in Φ_{Δ} values for the rest of the conjugates of complex **3** (**Table 6.2**). The Φ_{Δ} of **4**@GQDs-MnO_2@PtNPs (0.63) was higher than that of **4** (0.55) or **4**@GQDs (0.52) in DMSO. The superior singlet oxygen quantum yield of **4**@GQDs-MnO_2@PtNPs (63%) compared to that of **4** (55%) or **4**@GQDs (52%) may be credited to the increased spin-orbital coupling effect for metals in the nanoparticles, by the heavy atom effect. A higher singlet oxygen quantum yield was observed for complex **6** (0.34) compared to complex **5** (0.25), corresponding to trends in triplet quantum yield values obtained (**Table 6.1**).

Table 6.2: Singlet oxygen quantum yields of MPcs and conjugates in DMSO.

Complex	Φ_Δ
Complex **1**	0.22
Complex **2**	0.31
[a]Cl_2SiPc	0.18
Complex **3**	0.62
3@GQDs	0.60
3@GQDs-MnO_2	0.51
3@GQDs-MnO_2-AgNPs	0.67
3@GQDs-MnO_2-AuNPs	0.65
[b]Complex **4**	0.55
4@GQDs	0.52
4@GQDs-MnO_2@PtNPs	0.63
Complex **5**	0.25
Complex **6**	0.34

[a]data from Ref. [238], [b]data from Ref. [89]

6.6 Summary of Chapter

The photophysical and photochemical properties of MPcs and their NPs conjugates were performed in DMSO using a comparative method with unsubstituted ZnPc as a standard. Fluorescence quantum yield of the employed MPcs decreased when linked to NPs due to the heavy atom effect of metal nanoparticles. The lower fluorescence quantum yield values translated to higher triplet quantum yields owing to intersystem crossing of excited molecules to the triplet state. The axial ligand exchange in Cl_2SiPc to form complexes **1** and **2** resulted in lower florescence quantum yields attributed to the electron withdrawing effects of the quinoid and nitroso substituents, respectively. Moreover, the peripherally substituted complex **5** was found to have a higher fluorescence quantum yield and lower triplet yields and triplet lifetimes than the non-peripherally substituted **6**. There are thus distinct intrinsic properties between the non-peripherally (**6**) and peripherally (**5**) substituted phthalocyanines. A higher singlet oxygen quantum yield was recorded for **6** than **5**.

Chapter VII

Cytotoxicity and photodynamic therapy activity

This chapter discusses the *in-vitro* dark cytotoxicity and photodynamic therapy activities of the employed liposomal formulations of MPcs, or MPc-NPs conjugates, reported in this work. Owing to the limited water solubility and biocompatibility of the as-synthesised MPcs and MPc-NPs conjugates, their PDT activities were analysed only following liposomal loading against MCF-7 and HeLa cell lines as *in-vitro* cancer cell models.

7 Cell culture studies

7.1 Production of Hypoxic models

In this work, two hypoxic models were used, $CoCl_2$ [92] and Oxyrase [93]. $CoCl_2$ is a well-documented hypoxia-mimicking molecule [246]. For all experiments, the cells under $CoCl_2$ or Oxyrase-induced hypoxia did not show significant morphological differences from cells cultured in normoxia (**Figure 7.1**).

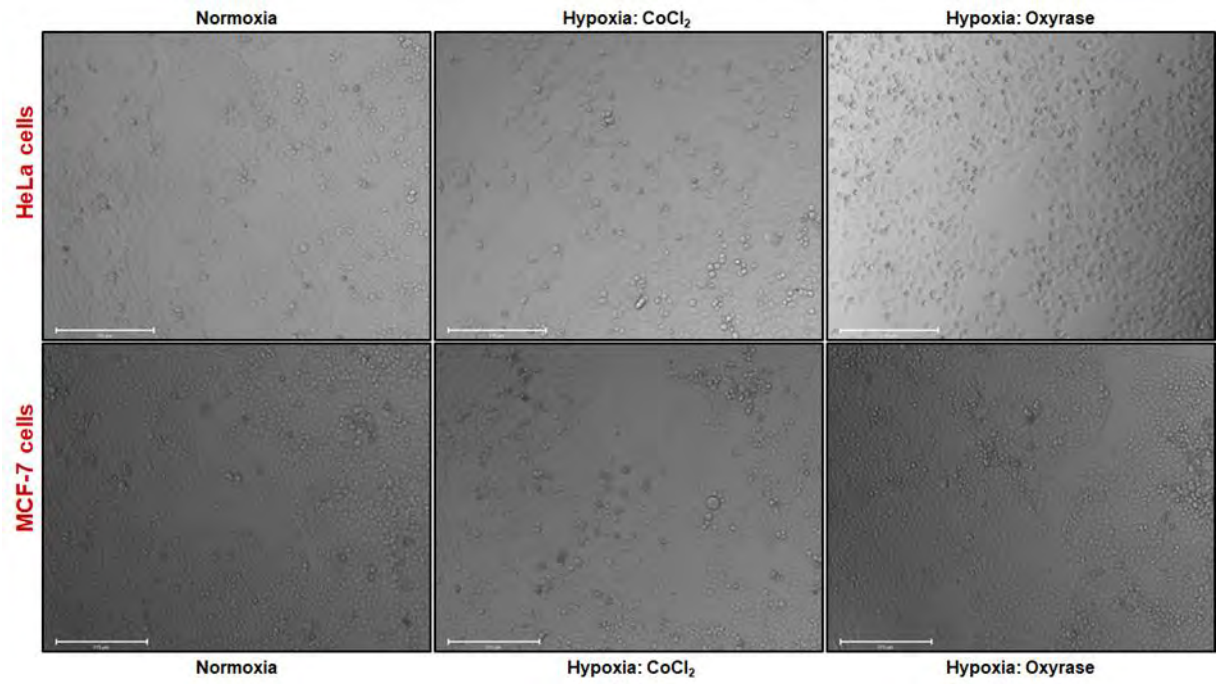

Figure 7.1: Effects of normoxia or hypoxic preconditioning on cellular morphology.

7.2 Cellular drug uptake

7.2.1 Non-FA functionalised liposomes

The relatively low diffusion distances and short half-life of ROS and reactive oxygen and nitrogen species (RONS) necessitate the intracellular localisation of potential PS drug candidates. The time-dependent uptake features of liposomal formulations of the employed Pc and Pc-NPs were determined by measuring the fluorescence intensities of the constituent Pc following excitation at 675 nm and emission at 685 nm using a Synergy 2 multi-mode microplate reader (BioTek®). Details have been provided in chapter II. The fluorescence intensities of the employed Pcs and Pc/conjugates were measured at 100 µg/mL using HeLa cells (**1**-liposomes and **2**-liposomes used as examples). Uptake features of the employed PS-liposomes were carried out at different incubation times (24 h and 48 h) to optimise the conditions. Before measuring the fluorescence, the cells were washed with phosphate-buffered saline (PBS) three times, and cells without drug treatment were used as appropriate negative controls. **Figure 7.2** shows the cellular update features of **1**-liposomes and **2**-liposomes measured at 24 h and 48 h times intervals. As can be seen in **Figure 7.2**, the cellular uptake of both drug-liposomal formulations appears to peak at 24 h. Similar drug uptake features were observed for other drug formulations. Subsequent cytotoxicity experiments were determined following 24 h incubation.

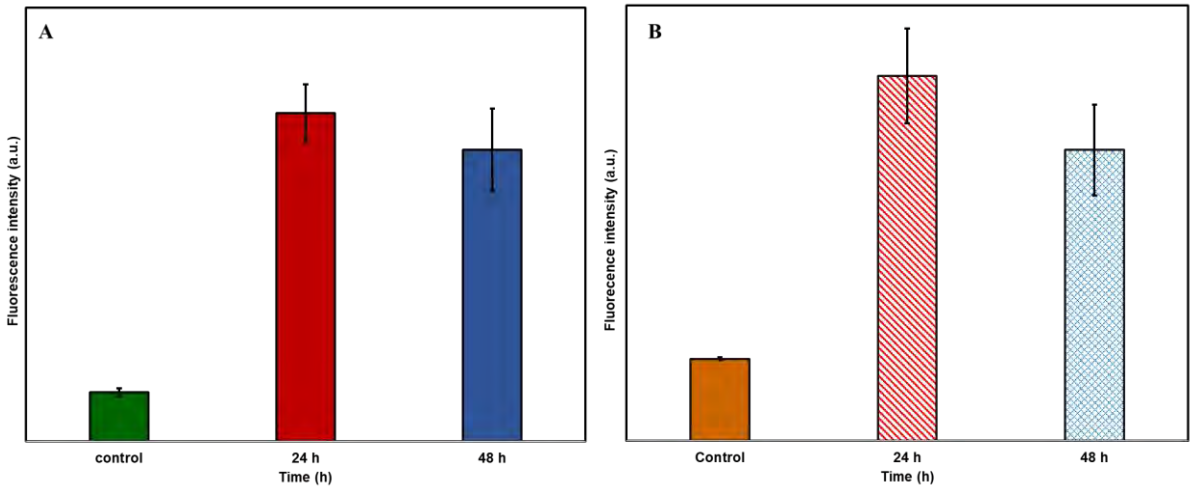

Figure 7.2: Time-dependent cellular uptake of **1**-liposomes (A) and **2**-liposomes (B) by HeLa cells at 24 h and 48 h. Control cells were measured in PBS alone without either drug-liposomal formulations.

7.2.2 FA-functionalised liposomes

This work also assessed the cellular uptake features of the FA-functionalised **4**@GQDs-MnO_2@PtNPs-FA-liposomes. Many cancer cell lines overexpress folate receptors, and as such, this work evaluated whether the as-synthesised **4**@GQDs-MnO_2@PtNPs-FA-liposomes could specifically recognise folate receptor (FR) overexpressed tumour cell lines. In this vein, the cellular uptake efficiencies of the employed **4**@GQDs-MnO_2@PtNPs-FA-liposomes were evaluated compared with **4**@GQDs-MnO_2@PtNPs-liposomes (HeLa cells were used as an example). **Figure 7.3A** shows that folic acid functionalisation led to an almost 3-fold increase in drug uptake, as evidenced by the higher fluorescence intensity resulting from **4**@GQDs-MnO_2@PtNPs-FA-liposomes than **4**@GQDs-MnO_2@PtNPs-liposomes, giving credence to folate receptor targeting. Both HeLa and MCF-7 cells overexpress the folate receptor (although to varying extents). As a result, this work also assessed whether variable uptake rates would be realised owing to differential FR expressions on HeLa and MCF-7 cell lines. Non-cancerous Mouse epithelial fibroblasts (MEF)

were used as negative controls since they do not overexpress FRs. As can be observed in **Figure 7.3B**, a 2 to 3-fold higher cellular uptake was observed for the **4**@GQDs-MnO_2@PtNPs-FA-liposomes in the cancer cell lines (HeLa and MCF-7 cells) than in the healthy MEF cell line. In all cases, control cells were measured in PBS. It is, therefore, feasible to conclude that the **4**@GQDs-MnO_2@PtNPs-FA-liposomes exploit the overexpressed FRs on the surfaces and are favourably taken up by both HeLa and MCF-7 cells over MEF cells in the order HeLa cells >MCF-7 cells > MEF cells in the order of folate-receptor expression levels [247,248].

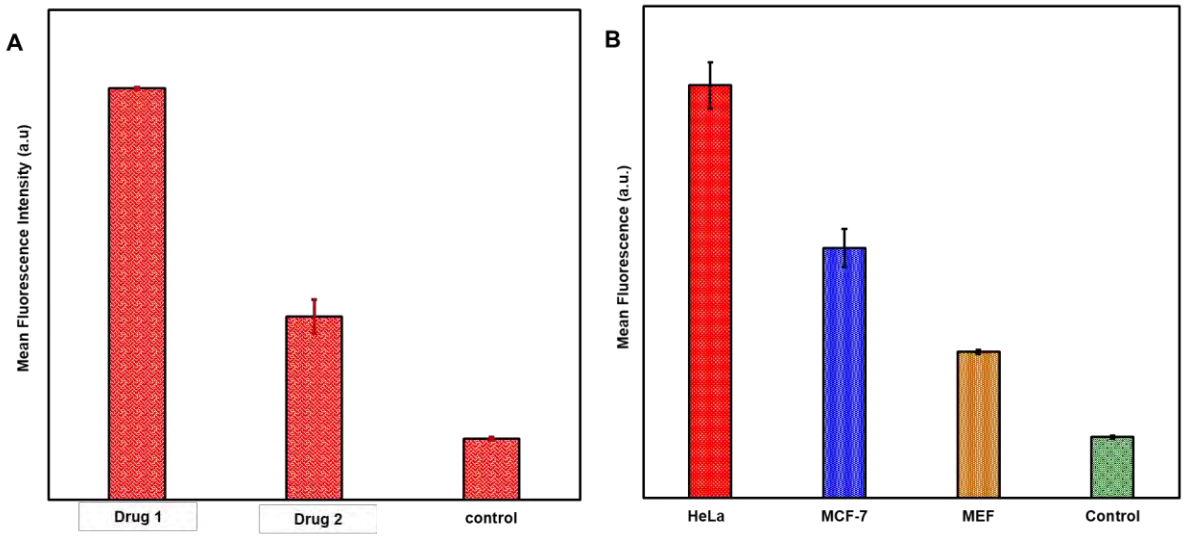

Figure 7.3. Cellular uptake. (A) Cellular uptake in HeLa cells at 24 h following incubation with **Drug 1** (**4**@GQDs-MnO_2@PtNPs-FA-liposomes) and **Drug 2** (**4**@GQDs-MnO_2@PtNPs-liposomes). (B) Cellular uptake plots for **4**@GQDs-MnO_2@PtNPs-FA-liposomes in HeLa cells, MCF-7 cells, and MEF cells at 24 h incubation. In all cases, control cells were measured in PBS.

Following this, the selectivity and intracellular localisation of the employed **4**@GQDs-MnO_2@PtNPs-FA-liposomes in cancer cells were also assessed using HeLa cells (owing to their high FR expression levels) and normal MEF cells. The internalisation of **4**@GQDs-MnO_2@PtNPs-FA-liposomes was visualised by tracing the intracellular localisation of the employed **4**@GQDs-MnO_2@PtNPs-FA-liposomes in both HeLa cells and MEF cells by fluorescence microscopy. The *in-vitro* fluorescence of the constituent complex **4** was used to track the internalisation of **4**@GQDs-MnO_2@PtNPs-FA-liposomes. Drug uptake by normal MEF cells with ultra-low expressions of FR was also assessed for comparative reasons. After washing with PBS, the cell nuclei were stained with 4',6-diamidino-2-phenylindole (DAPI) before observation. A blue fluorescence from DAPI signifies the live cells, and the constituent complex **4** in **4**@GQDs-MnO_2@PtNPs-FA-liposomes gives red fluorescence.

The fluorescence of the constituent complex **4** was sufficient to permit the intracellular visualisation of **4**@GQDs-MnO_2@PtNPs-FA-liposomes at two different time intervals, 30 min and 12 h. The increase in the fluorescence signal of complex **4** over time was observed, with 12 h incubation resulting in a higher fluorescence signal (**Figure 7.4**). At the 12 h mark, the fluorescence of the **4**@GQDs-MnO_2@PtNPs-FA-liposomes is much stronger in HeLa cells than in MEF cells. The weaker fluorescence of **4**@GQDs-MnO_2@PtNPs-FA-liposomes in MEF at the 12 h mark may be attributed to the low or passive uptake of **4**@GQDs-MnO_2@PtNPs-FA-liposomes over time in MEF. The presence of folic acid greatly facilitated the uptake of **4**@GQDs-MnO_2@PtNPs-FA-liposomes, shifting the cell population toward relatively higher fluorescence intensities in HeLa cells which over-express FRs. Since DAPI stains live cell nuclei, the lack of fluorescence overlaps between the blue DAPI and the red **4**@GQDs-MnO_2@PtNPs-FA-liposomes implies a predominantly cytoplasmic localisation of the **4**@GQDs-MnO_2@PtNPs-FA-liposomes.

The above results suggest that the uptake of **4**@GQDs-MnO_2@PtNPs-FA-liposomes may be FR-mediated. Such uptake features are favourable since receptor-mediated endocytosis can greatly reduce side effects associated with indiscriminate drug uptake and invariably facilitate better anticancer activities.

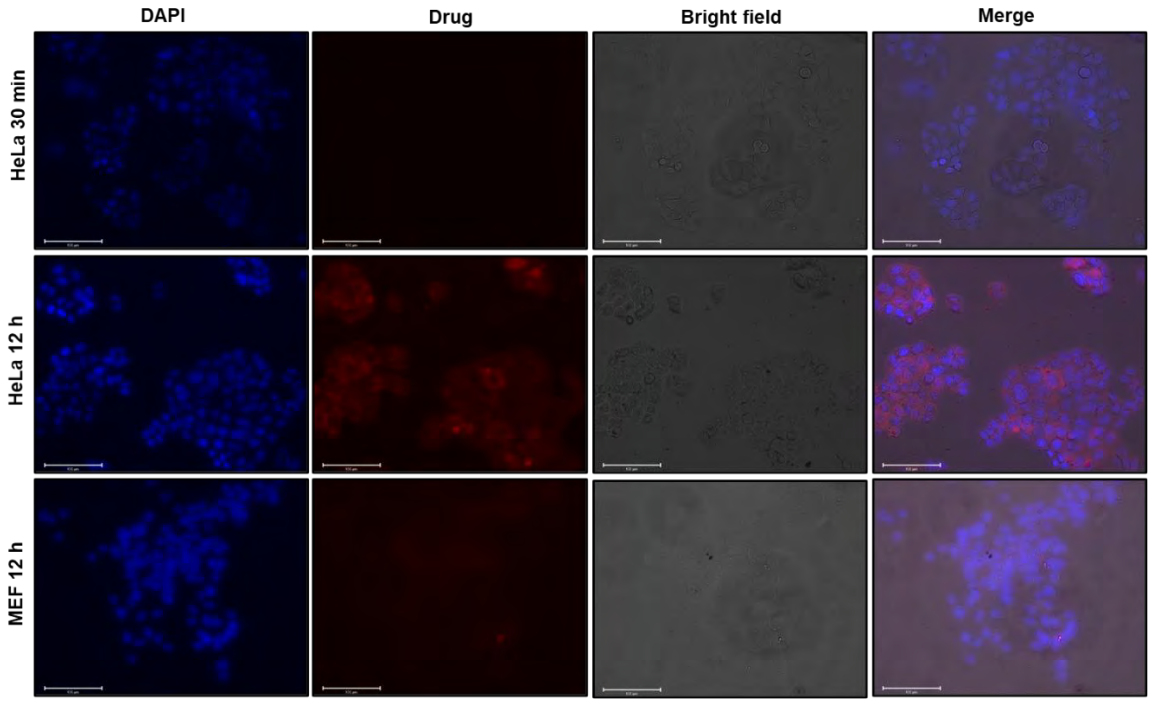

Figure 7.4. Drug cellular uptake. The intracellular distribution of **4**@GQDs-MnO_2@PtNPs-FA-liposomes (Drug, 100 µg/mL) in Hela and MEF cells. The cellular uptake in HeLa cells was imaged at different time points (30 min and 12 h) following incubation with **4**@GQDs-MnO_2@PtNPs-FA-liposomes measured by fluorescence microscopy. For comparison, MEF cells were also incubated with **4**@GQDs-MnO_2@PtNPs-FA-liposomes and imaged after 12 h. Each series can be classified into bright field, complex **4** from **4**@GQDs-MnO_2@PtNPs-FA-liposomes, blue fluorescence from nuclei of the cells stained with DAPI, and merge. Scale bar: 100 µm.

7.3 Intracellular ROS generation

Since the photocytotoxicities of the employed liposomal formulations of Pc and Pc-NPs are singlet oxygen-dependent, their capacities for light-activated intracellular ROS generation were assessed. The ROS probe 2,7-dichlorofluorescein diacetate (DCFH-DA) assay was used for semi-quantitative analysis. DCFH-DA, a cell-permeable, non-fluorescent ROS probe, is readily oxidised by intracellular ROS to the fluorescent 2′,7′-dichlorofluorescein (DCF) following hydrolysis by cellular esterase [55]. As shown in **Figure 7.5**, the corresponding fluorescent intensity in cells treated with **4**@GQDs-MnO_2@PtNPs-FA-liposomes (as an example) following irradiation was much stronger than in control groups treated with DCFH-DA alone with irradiation. The enhanced production of ROS in the cells subjected to treatment with **4**@GQDs-MnO_2@PtNPs-FA-liposomes + NIR irradiation could be ascribed to the continuous generation of singlet oxygen inside the cancer cells. The ROS-producing ability of the employed liposomes was further quantitatively analysed using a microplate analyser to measure DCF fluorescence with an excitation wavelength of 485 nm and emission of 535 nm on a Synergy 2 multi-mode microplate reader (BioTek®) using MCF-7 cells as an example. Following treatment with drug-liposomes (300 µg/mL), the cells were incubated with DCFH-DA before NIR laser irradiation (680 nm at 0.28 W/cm^2). The cells in PBS alone (negative control) showed no significant green fluorescence (**Figure 7.6**).

On the other hand, the cells exposed to H_2O_2 (positive control) or **4**-liposome and **4**@GQDs-MnO_2@PtNPs-liposomes (used as examples) with light irradiation showed a notable increase in DCF fluorescence using MCF-7 cells as an example. The elevated DCF fluorescence in response to NIR irradiation highlights light-responsive ROS production of the internalised **4**-liposomes and

4@GQDs-MnO_2@PtNPs-liposomes (compared to the DCF alone) (**Figure 7.6**). An elevated DCF fluorescence signal was observed following NIR irradiation for all studied liposomal formulations.

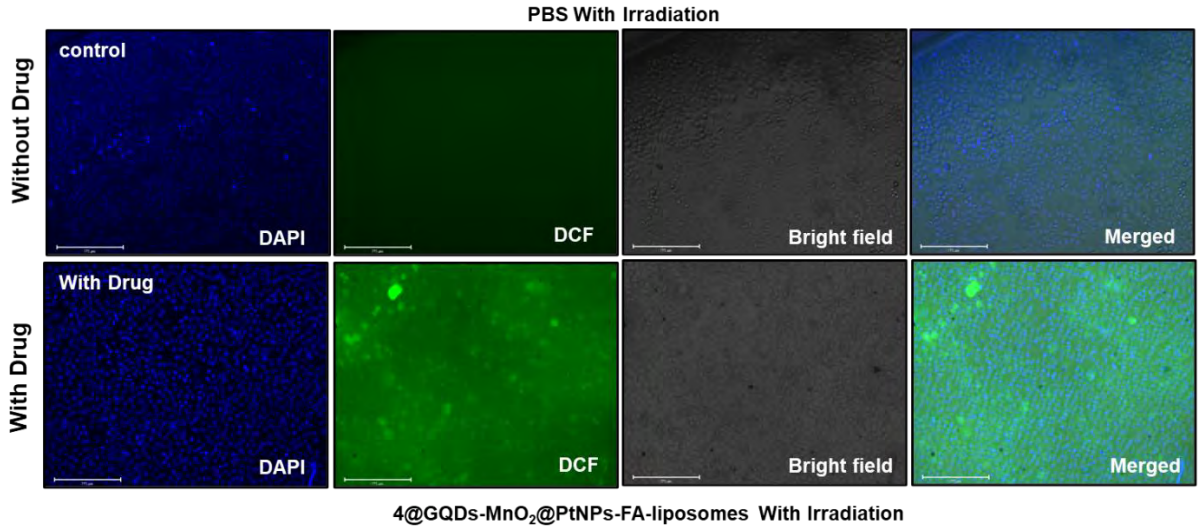

Figure 7.5. Reactive Oxygen Species (ROS) generation of light-activatable **4**@GQDs-MnO_2@PtNPs-FA-Liposomes in HeLa cells measured by DCF fluorescence. NIR laser (680 nm, 0.28 W cm^{-2}). Images were taken on Evos fluorescence microscopy. Scale: 275 µm.

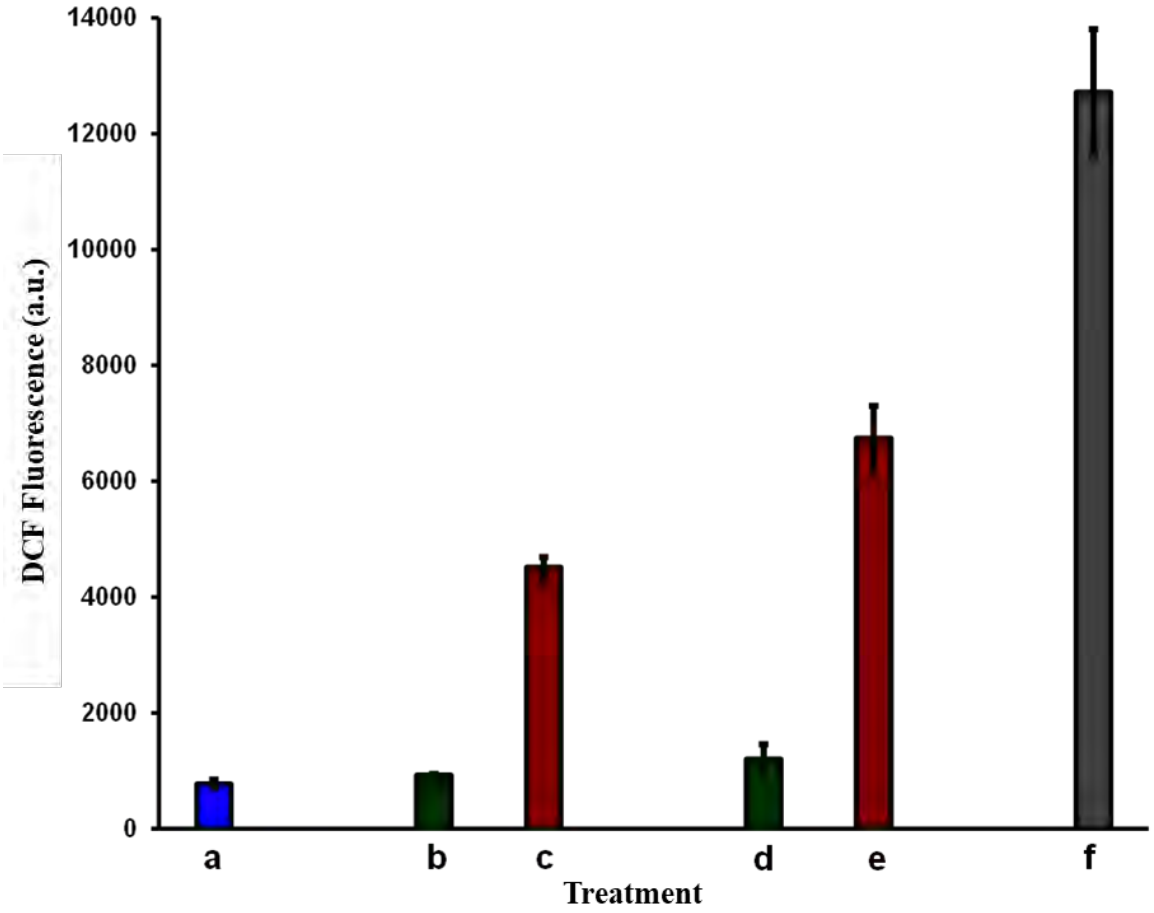

Figure 7.6: DCFH-DA fluorescence assay for the detection of ROS generation in MCF-7 cells by **4**-liposomes (**b**, **c**) and **4**@GQDs-MnO_2@PtNPs-liposomes (**d**, **e**) (100 µg/ml) after 4 h incubation in the dark (**b**, **d**) and upon irradiation for 10 min (**c**, **e**) (680 nm, 0.28 W cm^{-2}) (**red**). Cells treated with DCFH-DA alone were used as negative control (**a**), and those treated with H_2O_2 were used as the positive control (**f**). Error bars represent the standard deviation (n = 3).

7.4 Intracellular RNS generation

Since the photoactivity of the nitric oxide-releasing complex **2** is both reactive oxygen species (ROS) and reactive nitrogen species-dependent (RNS-dependent), the RNS-generating property of the liposomes loaded **2**-liposomes was assessed using diaminofluorescein-FM diacetate (DAF-FM DA) as an *in-vitro* fluorescence probe. DAF-FM DA is a cell-permeable probe that passively diffuses across cellular membranes. Upon entering the cells, DAF-FM-DA is hydrolysed to DAF-FM. DAF-FM is essentially non-fluorescent until it reacts with nitric oxide (•NO) to form a fluorescent benzotriazole. **Figure 7.7** shows the intracellular fluorescence observed in HeLa and MCF-7 cells incubated with Cl_2SiPc-liposomes or **2**-liposomes. Control experiments were performed without drug treatment (DAF-FM DA only). The •NO producing ability of **2**-liposomes was quantitatively analysed using a fluorescence microplate analyser with an excitation wavelength of 495 nm and an emission of 515 nm. As shown in **Figure 7.7**, higher fluorescent intensities were observed in cells treated with **2**-liposomes following irradiation than those in the control group (treated with DAF-FM DA alone) or with Cl_2SiPc-liposomes. The higher fluorescence in cells subjected to treatment with **2**-liposomes implies the successful *in-vitro* photorelease of cytotoxic •NO.

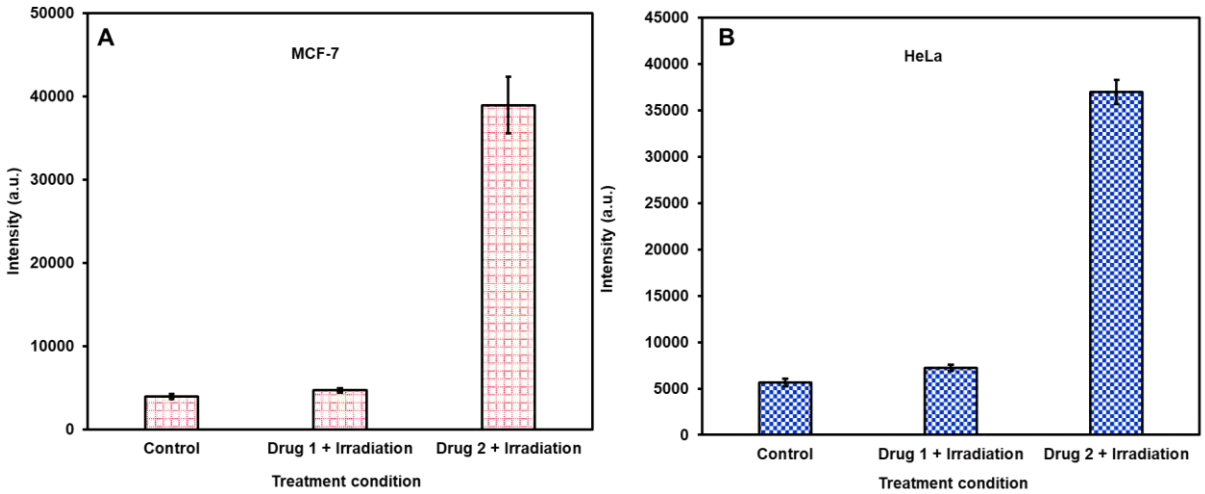

Figure 7.7: Intracellular RNS detection in MCF-7 (**A**) and HeLa cells (**B**). DAF fluorescence for the detection of •NO by **2**-liposomes following irradiation (**Drug 1** = Cl_2SiPc-liposomes, **Drug 2** = **2**-liposomes).

7.5 *In-vitro* cytotoxicity measurements

Given the promising cellular uptake features of the liposomal formulations of the employed Pc and Pc-NPs-liposomes, their feasibility to be employed as PDT agents following the drug internalization was assessed. *In-vitro* toxicities were assessed by evaluating their phototoxicities and dark cytotoxicity using *in-vitro* models with both MCF-7 cells and HeLa cells by typical colorimetric cell viability WST-1 assay with or without laser irradiation.

7.5.1 Cytotoxicity under normoxia

Prior to PDT evaluation, the intrinsic cytotoxicity of the employed encapsulated liposomes against both MCF-7 and HeLa cells as *in-vitro* models was assessed. Cytotoxicity studies were performed in the absence of light and are referred to as *in-vitro* dark toxicity. *In-vitro* dark toxicity is undesirable for photosensitizers aimed for use in PDT. Dark toxicity of the employed formulations was measured by quantifying the percentage cell survival rates using WST-1 viability assay 24 h after treatment in MCF-7 and HeLa cell lines with gradient concentration of each complex. The lower the cell viability, the higher the dark cytotoxicity. Cells in DMEM alone were used as appropriate negative controls. PDT activity of the employed formulations was measured by quantifying the percentage cell survival rates following NIR irradiation. Due to the enhanced aqueous solubility and biocompatibility afforded through liposomal loading, DMSO was not used to prepare drug concentrations. Cytotoxic features were assessed under relative normoxia, maintained in a 5% CO_2 atmosphere at 37 °C. Details are outlined in chapter II.

Under normoxia, negligible toxicity was observed in MCF-7 cells and HeLa cells for all liposomal formulations without laser irradiation representing low dark cytotoxicity. All the liposomal formulations (PS-liposomes) possessed negligible dark toxicity even at the maximal concentration used, suggesting good cytocompatibility *in-vitro* (**Figure 7.8**, **7.9** and **7.10**).

The cell viability remained above 80 % for all PS-liposomes in the dark. Since singlet oxygen generation by the Pc and Pc-NPs-liposomes is light-activated, no singlet oxygen is expected in the dark, and hence observed low cytotoxicity. The low dark cytotoxicity of the liposomal formulations suggests good biocompatibility for applications in PDT. The low dark cytotoxicity may also be attributed to the improved biocompatibility afforded to all complexes/conjugates because of liposomal encapsulation.

Before laser irradiation, the cells were washed with PBS to rule out the contribution from residual or uninternalized drug materials in media. A concentration-dependent decrease in cellular viabilities was observed when drug formulations were irradiated with NIR light complex (**Figure 7.8**, **Figure 7.9**, and **Figure 7.10**). Following NIR laser irradiation, the cell viability decreased dramatically for both cell types. For both MCF-7 cells and HeLa cells, the group exposed to irradiation alone exhibited cell viability of about 80 %, indicating that NIR irradiation alone, and hence the associated heating effect of NIR irradiation, did not contribute to the cytotoxic effect of the system. Similar drug phototoxicities were noted for the other liposomal drug formulations, with IC_{50} values summarised in **Table 7.1**. Following NIR irradiation, a concentration-dependent decrease in cell viability was observed for **1**-liposomes, **2**-liposomes (**Figure 7.8**) and both **5**-liposomes and **6**-liposomes (**Figure 7.9**).

The alpha-substituted, complex **5**-liposomes showed higher phototoxicity with IC_{50} values of 49.24 µg/mL and 56.38 µg/mL toward HeLa and MCF-7 cells, respectively. The beta-substituted complex **6** showed lower phototoxicity in both HeLa and MCF-7 cells with IC_{50} values of 60.39 µg/mL and 65.48 µg/mL (**Tables 7.1**, and **7.2**).

For the FA bearing, **4**@GQDs-MnO_2@PtNPs-FA-liposomes, HeLa cells showed much lower survival rates than MCF-7 cells (**Figure 7.10**) (**Tables 7.1** and **7.2**). The higher cell death and lower IC_{50} values of **4**@GQDs-MnO_2@PtNPs-FA-liposomes (**Table 7.1**) in HeLa cells (3.93 µg/mL) can be attributed to higher **4**@GQDs-MnO_2@PtNPs-FA-liposomes uptake by HeLa cells than MCF-7 cells (43.49 µg/mL) as demonstrated earlier owing to differential FR expression levels.

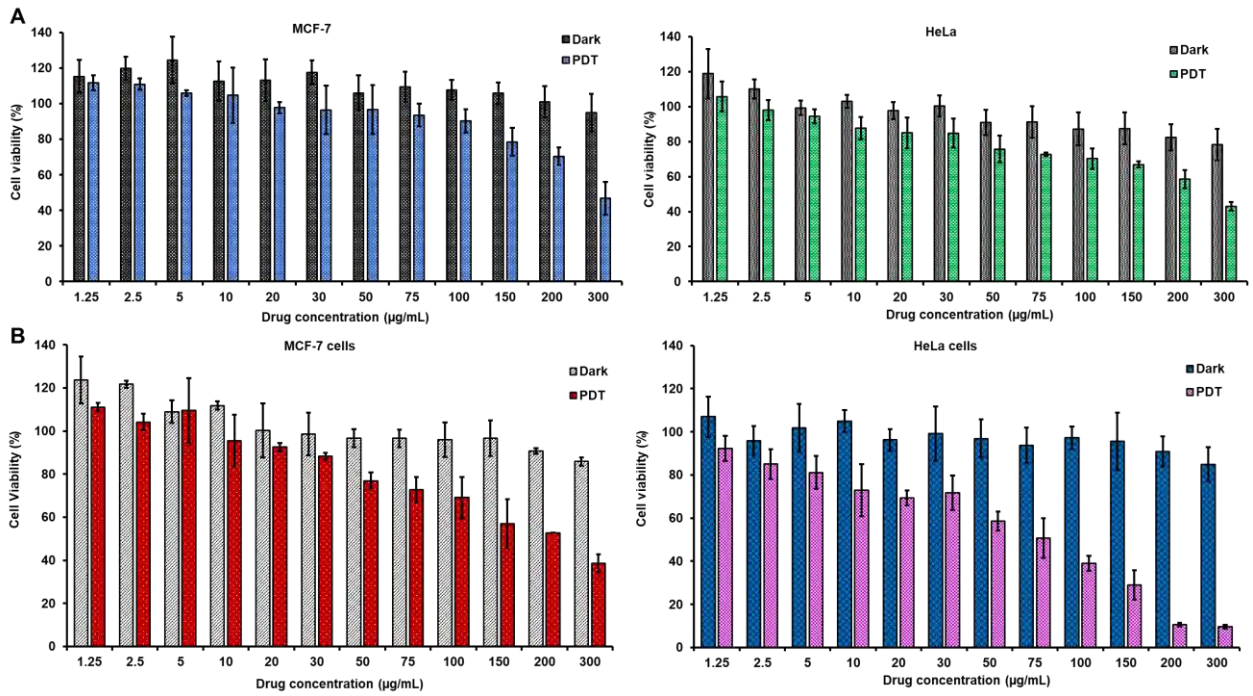

Figure 7.8: *In-vitro* cytostatic effects of **1**-liposomes (A) and **2**-liposomes (B) under normoxia with irradiation (PDT) and without NIR irradiation (Dark) against MCF-7 and HeLa cells. Cell

viabilities were recorded following 24 h incubation period (n = 3). In all cases, the photoirradiation was performed using a NIR light source, 680 nm, 0.28 W cm^{-2}.

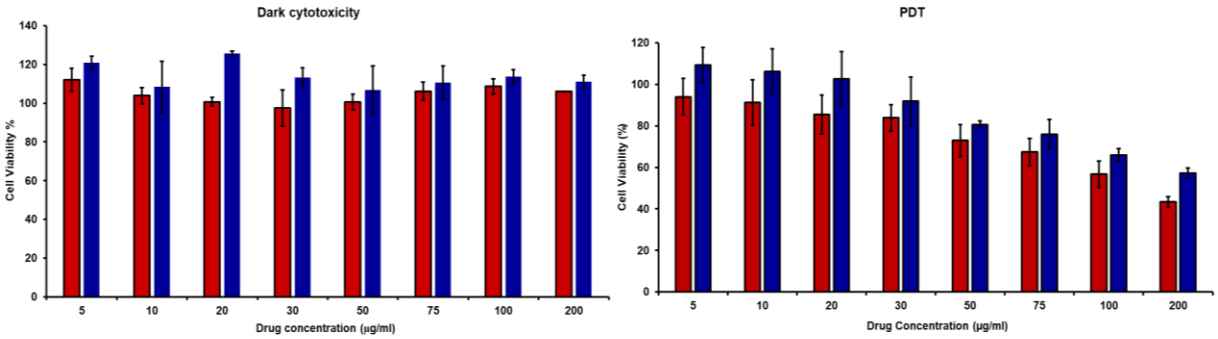

Figure 7.9. *In-vitro* dark and PDT-induced cytotoxic effects of **5**-liposomes (**blue**) and **6**-liposomes (**red**) drug formulations under normoxia without and with NIR irradiation against HeLa cells following incubation for 24 h (n = 3). In all cases, the photoirradiation was performed using a NIR light source, 680 nm, 0.28 W cm^{-2}.

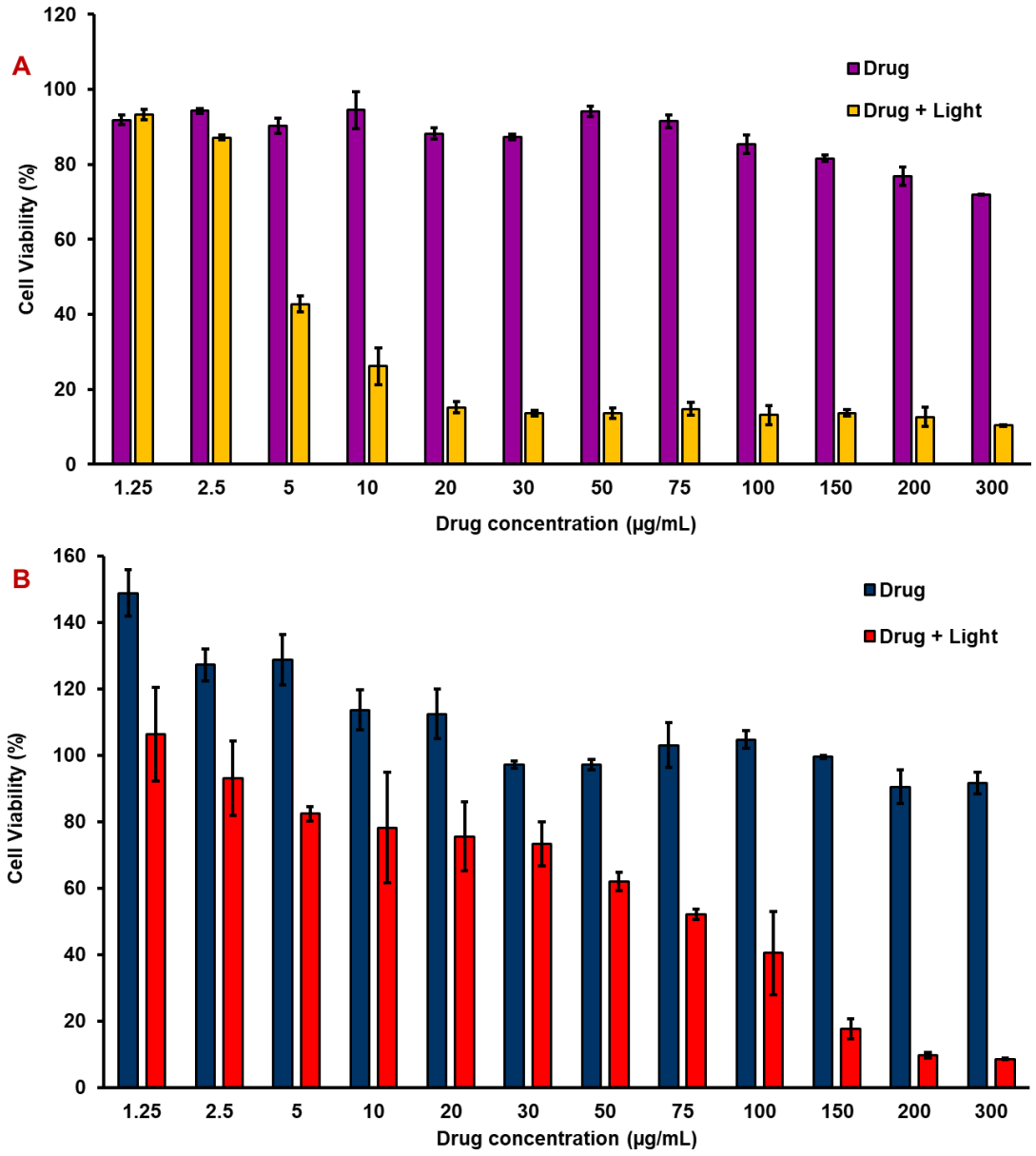

Figure 7.10. *In-vitro* dark and PDT-induced cytostatic effects of **4**@GQDs-MnO_2@PtNPs-FA-liposomes drug formulations under normoxia without and with NIR irradiation against HeLa cells (A) and MCF-7 cells (B) after incubation for 24 h (n = 3). In all cases, the photoirradiation was performed using a NIR light source, 680 nm, 0.28 W cm^{-2}. Drug = **4**@GQDs-MnO_2@PtNPs-FA-liposomes.

Table 7.1: IC_{50} values of the employed liposomes against MCF-7 cells following NIR irradiation.

Drug formulation	PDT IC_{50} (µg/mL)		
	Normoxia	**Hypoxia 1**	**Hypoxia 2**
1-liposomes	111.3	93.46	39.18
2-liposomes	50.76	99.02	73.85
3-liposomes	36.7	>100	ND
3@GQDs-liposomes	34.9	>100	ND
3@GQDs-MnO_2-liposomes	33.7	69.36	ND
3@GQDs-MnO_2-AuNPs-liposomes	31.6	58.15	ND
3@GQDs-MnO_2-AgNPs-liposomes	26.8	54.36	ND
4-liposomes	65.42	>100	ND
4@GQDs-MnO_2@PtNPs-liposomes	56.28	73.5	ND
4@GQDs-MnO_2@PtNPs-FA-liposomes	43.49	133.1	46.54
5-liposomes	56.38		
6-liposomes	65.48		

Hypoxia 1 = $CoCl_2$-induced, Hypoxia 2 = Oxyrase-induced. ND = not determined

Table 7.2: IC_{50} values of the employed liposomes against HeLa cells following NIR irradiation.

Drug formulation	PDT IC_{50} (µg/mL)		
	Normoxia	**Hypoxia 1**	**Hypoxia 2**
1-liposomes	52.62	55.56	52.81
2-liposomes	56.59	90.45	86.85
3-liposomes	ND	ND	ND
3@GQDs-liposomes	ND	ND	ND
3@GQDs-MnO_2-liposomes	ND	ND	ND
3@GQDs-MnO_2-AuNPs-liposomes	ND	ND	ND
3@GQDs-MnO_2-AgNPs-liposomes	ND	ND	ND
4-liposomes	58.35	>100	ND
4@GQDs-MnO_2@PtNPs-liposomes	42.84	70.96	ND
4@GQDs-MnO_2@PtNPs-FA-liposomes	3.93	9.17	3.94
5-liposomes	49.24		
6-liposomes	60.39		

Hypoxia 1 = $CoCl_2$-induced, Hypoxia 2 = Oxyrase-induced. ND = not determined

7.5.2 Cytotoxicity under hypoxia

WST cell viability assay assessed the cytotoxicity of the employed Pc-liposomes and Pc-NPs-liposomes under hypoxia in breast and cervical (MCF-7 and HeLa) cancer cells. It is important to note that besides the hypoxic preconditioning employed herein, hypoxia is also potentiated by PDT treatment through NIR-actuated oxygen consumption by the various photosensitizers employed in this work

7.5.2.1 Dark cytotoxicity

The *in-vitro* dark cytotoxicity of all the liposomal formulations was evaluated at gradient concentrations under hypoxia using both MCF-7 and HeLa cell lines. In each case, Pc-liposomes and Pc-NPs-liposomes resulted in around 80% viable cells, even at the maximal concentrations used (**Figure 7.11**). No significant cytotoxicity was found in all cell groups without laser radiation, indicating low dark cytotoxicity and the outstanding biocompatibility of the liposome-loaded drug candidates.

7.5.2.2 PDT-induced cytotoxicity

This work further explored the PDT-induced cytotoxicity of the employed complexes following NIR irradiation under hypoxia. For simplicity, complexes with similar mechanisms are grouped. As such, three groups are discussed herein: (i) type I PDT (complex **1**), (ii) PDT-coupled with oxygen-independent therapy (complex **2**), and (iii) *in-situ* oxygen generation (conjugates of complexes **3** and **4**). In each case, before laser irradiation, the cells were washed with PBS to rule out the contribution from residual or uninternalized drug materials in media. Cells incubated in cell media alone and subjected to laser irradiation served as appropriate negative controls.

7.5.2.2.1 Type I PDT

This work studied the concentration-dependent phototoxicity of **1**-liposomes as a hypoxia-responsive PDT agent. For both MCF-7 and HeLa cells, comparable phototoxicities were observed under hypoxia. Under hypoxic conditions with photoirradiation, the cell viability of **1**-liposomes-treated cells decreased to about 55% for both cell types at 300 µg/mL. Phototoxicities under hypoxia may be attributed to the cooperative therapeutic effect of the Pc and the constituent quinoid moiety, **Figure 7.11**.

This work also compared the PDT effect of the as-synthesized **1**-liposomes and Cl_2SiPc-liposomes using HeLa cells, **Figure 7.12**. Lawsone alone, **Figure 7.12**, did not show PDT activity as expected since it does not generate ROS to the same extent as SiPc with a singlet oxygen quantum yield of only 0.010 in aqueous media [249]. A notable decrease in cell viability was observed in the cell groups treated with Cl_2SiPc-liposomes following NIR irradiation under normoxia. However, a reduced PDT effect was observed under hypoxic conditions for Cl_2SiPc-liposomes (**Figure 7.12**). For **1**-liposomes, there is a clearly improved PDT activity when using $CoCl_2$ to induce hypoxia, **Figure 7.12**. It is believed that the photodynamic action of **1**-liposomes consumed the intracellular oxygen in generating ROS. Although the efficacy of PDT is limited in hypoxia, the potential reduction and hence activation of complex **1** may have acted to induce a chemotherapeutic effect which ultimately compensated for the otherwise attenuation of PDT activity under hypoxia. The above results confirmed the anticancer efficacy of the employed **1**-liposomes, and the presence of the naphthoquinone moiety, preferentially activated under hypoxic conditions, may have resulted in an amplified therapeutic effect in either normoxia or hypoxia.

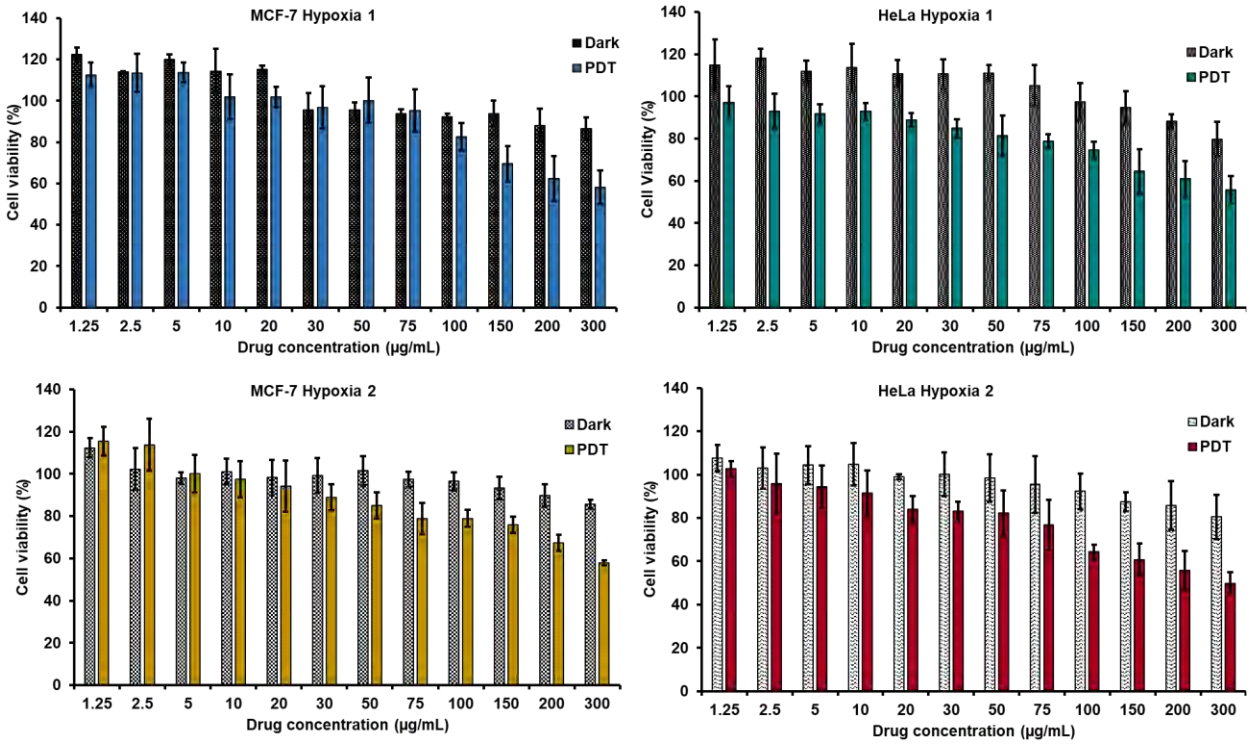

Figure 7.11: *In-vitro* phototoxicities of the **1**-liposomes: cytostatic effects of **1**-liposomes under the employed hypoxia with NIR irradiation against MCF-7 cells and HeLa cells following incubation for 24 h (n = 3). $CoCl_2$-induced hypoxia (Hypoxia 1), Oxyrase-induced hypoxia (Hypoxia 2). All measurements were obtained using WST-1 viability assays 24 h post-treatment. (In all cases, the photoirradiation was performed using a NIR light source, 680 nm at 0.28 W cm^{-2}).

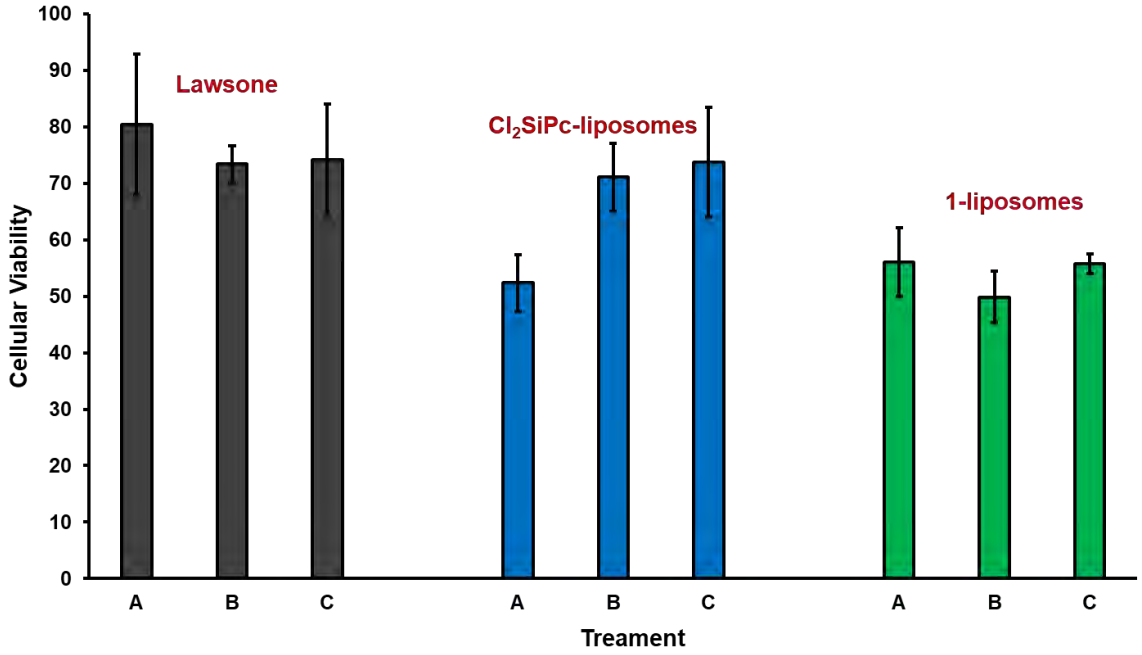

Figure 7.12: *In-vitro* cell cytotoxicity of lawsone (2-hydroxy,1,4-naphthoquinone) (black, 50 µg/mL), Cl_2SiPc-liposomes (blue, 300 µg/mL) and **1**-liposomes (green, 300 µg/mL) against HeLa cells after incubation for 24 h under normoxia (A), and hypoxia (B and C – $CoCl_2$ and Oxyrase, respectively) following NIR light irradiation (680 nm, 0.28 Wcm^{-2}).

7.5.2.2.2 PDT-coupled with oxygen-independent Therapy

The as-synthesized nitric oxide and singlet oxygen-generating **2**-liposomes were also assessed under hypoxic models employed in this work using WST-1 cell viability assay and MCF-7 and HeLa cancer cells. Following laser irradiation, the **2**-liposomes displayed PDT activity (**Figure 7.13**). Compared to the observed phototoxicity under normoxia (**Figure 7.8B**), the milder phototoxicity of **2**-liposomes under hypoxia may be attributed to insufficient O_2 supply since both oxygen-dependent, and oxygen-independent mechanisms persist under normoxia. In contrast, under hypoxia, these mechanisms would be more subdued. Both MCF-7 and HeLa displayed similar sensitivity to the phototoxicity of **2**-liposomes with about 50 % and 55% cell death, respectively, at the maximal concentration (300 μg/mL) (**Figure 7.13**). For both cell types, the PDT-induced lethality was observed to be lower in cells pre-treated with $CoCl_2$ compared to Oxyrase-induced hypoxia. The reason for this trend is not understood. However, the difference in sensitivity may be associated with differential expression of redox regulatory transcription factors and cytoprotective proteins [250-252]. Although the PDT effect of the employed **2**-liposomes was more favoured under normoxia than hypoxia, because of the dual effects of singlet oxygen and nitric oxide release, the photoactivity of **2**-liposomes remained reasonable even under hypoxia where singlet oxygen generation is subdued.

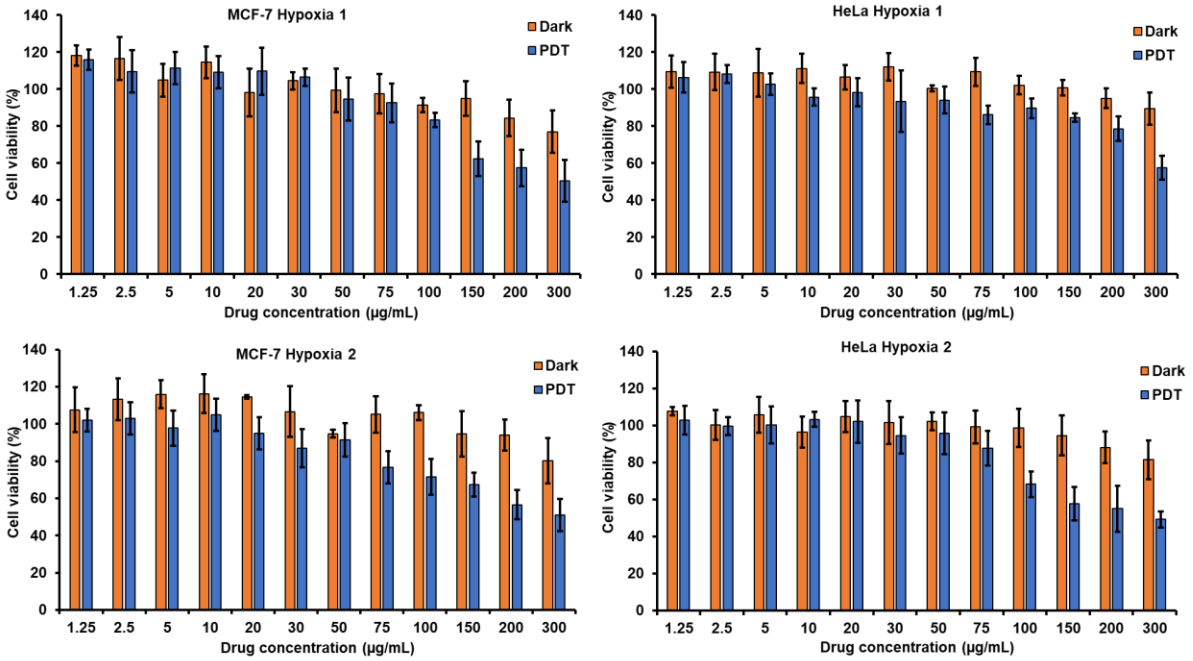

Figure 7.13. *In-vitro* PDT efficacy of **2**-liposomes. Relative cellular viabilities of the employed HeLa and MCF-7 cells under hypoxia; $CoCl_2$-induced hypoxia (Hypoxia 1), Oxyrase-induced hypoxia (Hypoxia 2). All measurements were obtained using WST-1 viability assays 24 h post-treatment.

7.5.2.2.3 *In-situ* oxygen generation

IC_{50} values are summarized in **Table 7.1**. Higher PDT efficacies against MCF-7 cells were observed for MnO_2-containing composites of **3** (**3**@GQDs-MnO_2, **3**@GQDs-MnO_2-AgNPs and **3**@GQDs-MnO_2-AuNPs) vs those lacking MnO_2 (complex **3** and **3**@GQDs). Similar phototoxicities were observed for conjugates for MnO_2 and folic acid containing **4**@GQDs-MnO_2@PtNPs-FA-liposomes (as an example) (**Figure 7.14**) (**Tables 7.1, 7.2**). The photoinduced toxicities of these catalase-mimicking hybrids under hypoxia were not comparable to what was observed in normoxia (**Table 7.1**). The observed phototoxicities under hypoxia were attributed to their ability to supplement intracellular oxygen, a feature not shared by **3**-liposomes or **4**-liposomes.

The observed heightened PDT activities of catalase-mimicking hybrids imply the successful *in-situ* decomposition of the endogenous hydrogen peroxide in hypoxic cancer cells to produce oxygen for PDT. PDT activity under hypoxia was highest for nanozyme (catalase-mimicking nanoparticle hybrids) containing PS hybrids. These results confirm that in view of oxygen-generating ability, the phthalocyanine-based nano platforms loaded with MnO_2 alone, MnO_2-AgNPs, and MnO_2-AuNPs or MnO_2@PtNPs can remarkably enhance the PDT efficacy in the hypoxic models presented here.

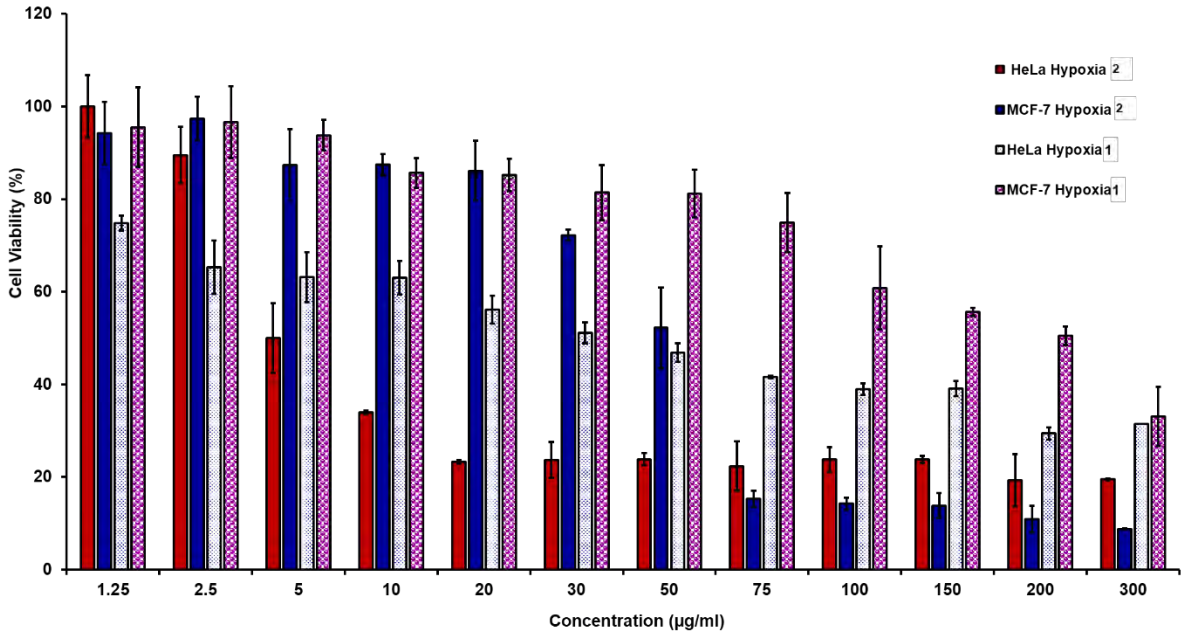

Figure 7.14: *In-vitro* PDT efficacy of **4**@GQDs-MnO_2@PtNPs-FA-liposomes. Relative cell viabilities of HeLa cells and MCF-7 cells under hypoxia; $CoCl_2$-induced hypoxia (Hypoxia 1), Oxyrase-induced hypoxia (Hypoxia 2) and All measurements were obtained using WST viability assays at 24 h post-treatment.

7.5.3 Live/Dead cell staining and cell morphology

The cellular morphology changes of the PS-liposomes incubated HeLa cells were also noted following NIR (680 nm) irradiation. Apoptotic cell-death characteristics, including cell shrinkage and plasma membrane blebbing (typical apoptotic features), were observed in cells subjected to drug treatment with subsequent irradiation (**Figure 7.15**) and corroborated well with the observed WST-1 *in-vitro* PDT assay results. No significant morphological changes were observed for control cells (without drug treatment).

Live/Dead cell staining assay verified the PDT effect of PS-liposomes under hypoxia (**Figure 7.16**) (**2**-liposomes are used here as an example). The low and sparse green fluorescence of control group cells reveal minimal cytotoxicity in the absence of irradiation, **Figure 7.16**. In contrast, NIR laser irradiation (680 nm, 0.28 W cm^{-2}) of the cells treated with **2**-liposomes triggered significantly high cytotoxicity. The sustained PDT activity (high number of dead cells as revealed by the green fluorescence) of **2**-liposomes even under hypoxia may be attributed to the contribution of hypoxic response, which supplements its anticancer activity even under low oxygen partial pressures. These results indicate that greater anticancer synergy can be achieved by coupling singlet oxygen and nitric oxide photogeneration (in this case), which are especially important under hypoxia. Similar results were observed for the other liposomal hybrids employed.

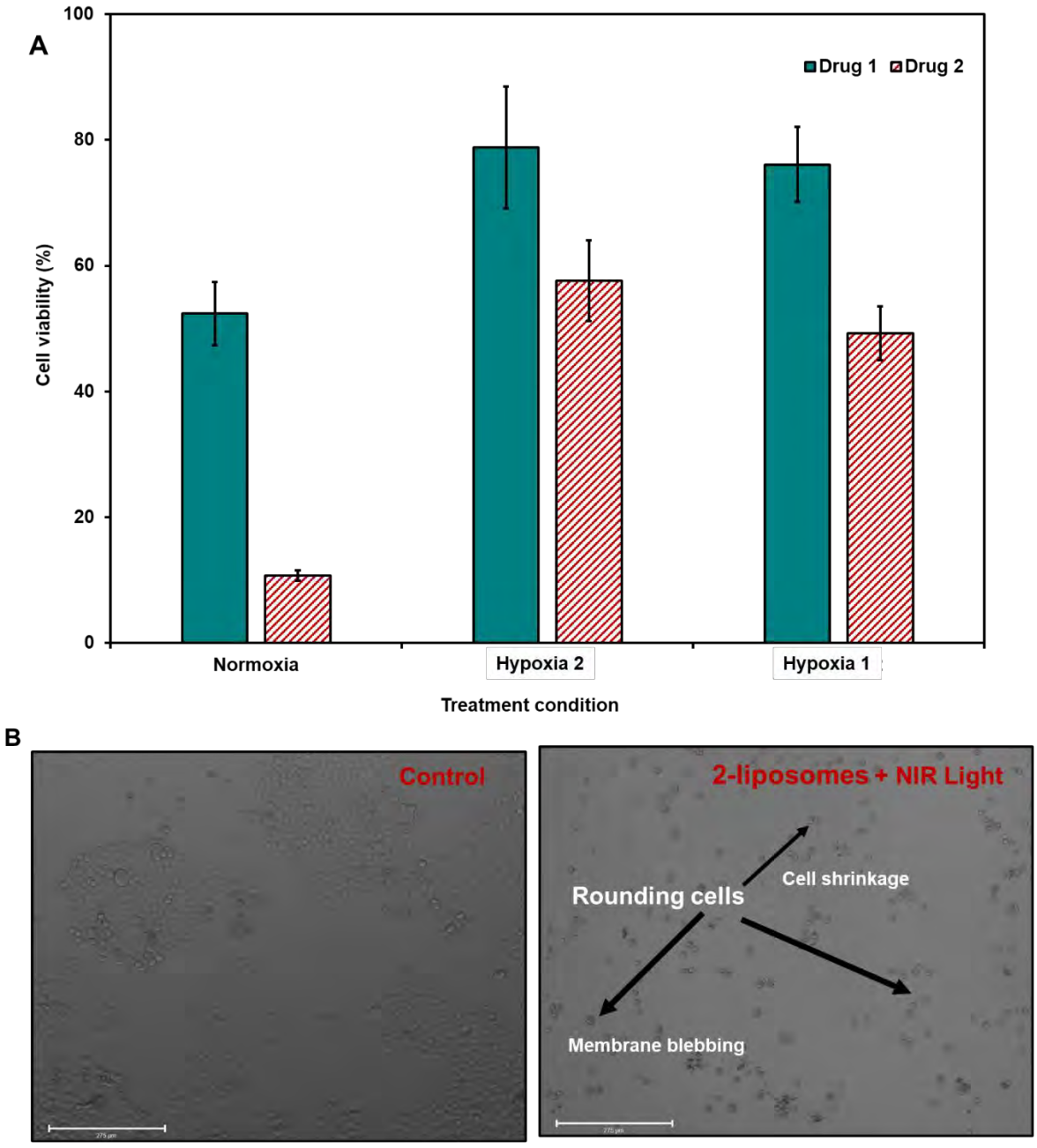

Figure 7.15: (A) *In-vitro* cell cytotoxicity of Cl_2SiPc-liposomes (**Drug 1**) and **2**-liposomes (**Drug 2**) against HeLa cells after incubation for 24 h under normoxia and Hypoxia 1 and Hypoxia 2 (Hypoxia 1 - $CoCl_2$-induced), Hypoxia 2 – Oxyrase-induced) following NIR light irradiation (0.28 Wcm^{-2}). (B) Changes in the morphology of HeLa cells treated with 300 µg/mL of **2**-liposomes following NIR irradiation.

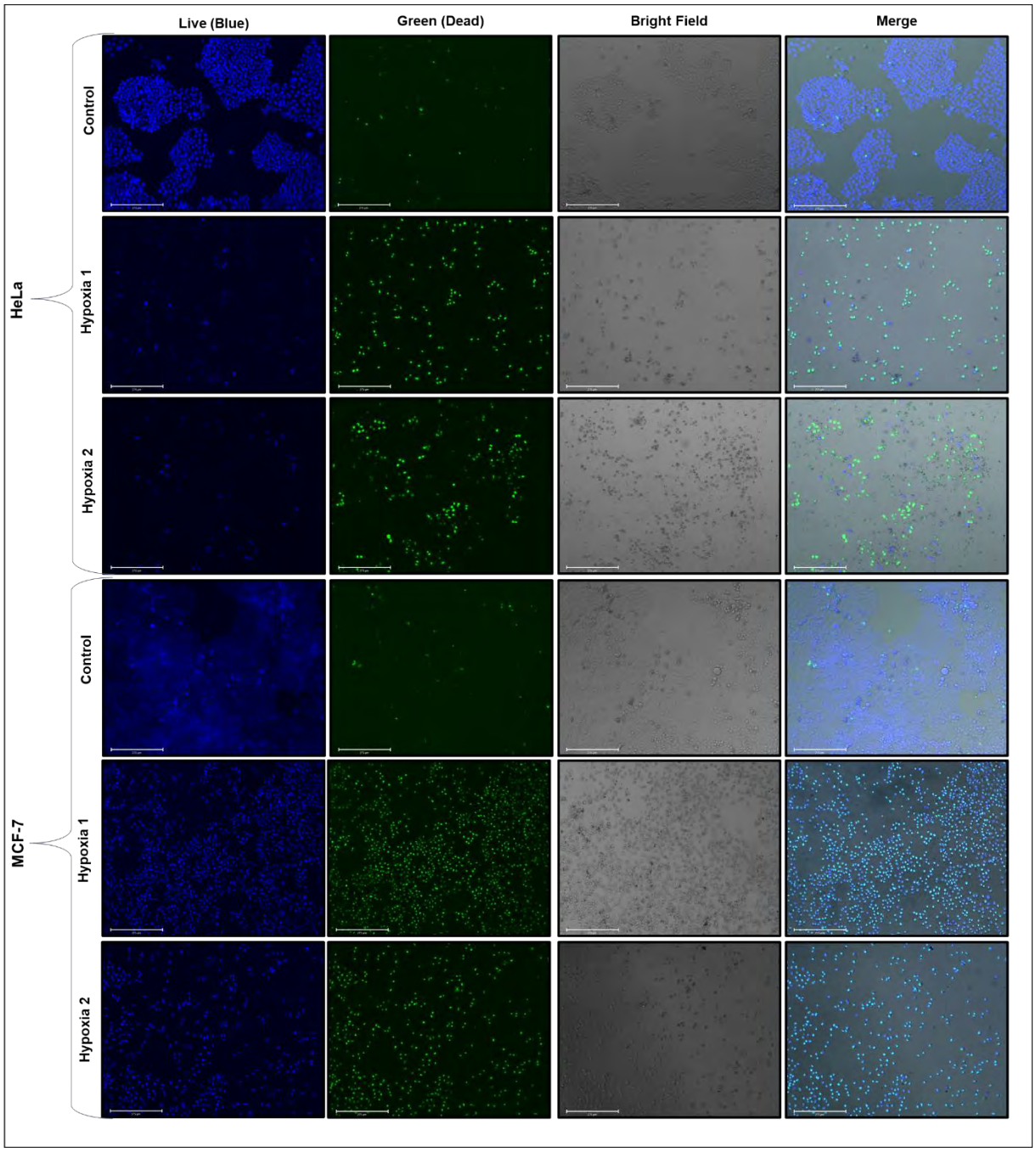

Figure 7.16. *In-vitro* live/dead staining of HeLa and MCF-7 cells incubated with **2**-liposomes (300 µg/mL) with NIR irradiation. Two hypoxic models are used: $CoCl_2$ pre-conditioning (Hypoxia 1) and incubation with Oxyrase enzyme (Hypoxia 2). Control cells were only subjected to NIR irradiation without drug treatment. Scale: 275 µm.

To access the long-term phototoxicity of the employed PS-liposomes, HeLa and MCF-7 cells were subjected to treatment with PS-liposomal formulations. **2**-liposomes (500 μg/mL, used as an example) were accessed over 72 h. The results obtained with the WST-1 cell viability assays in both cell lines were determined together with resultant changes in cell morphologies following irradiation. **Figure 7.17** shows the viability of HeLa and MCF-7 cells over 72 h at 24 h intervals with and without irradiation. There was minimal dark toxicity as cell viabilities remained above 75 % in the dark. For both cell types, treated cells (with drug and irradiation) resulted in about 90% cell death. There was no further growth of cells post-PDT treatment implying that both cancer cell types could not recover from the PDT-induced damage effects 48 or 72 h after treatment.

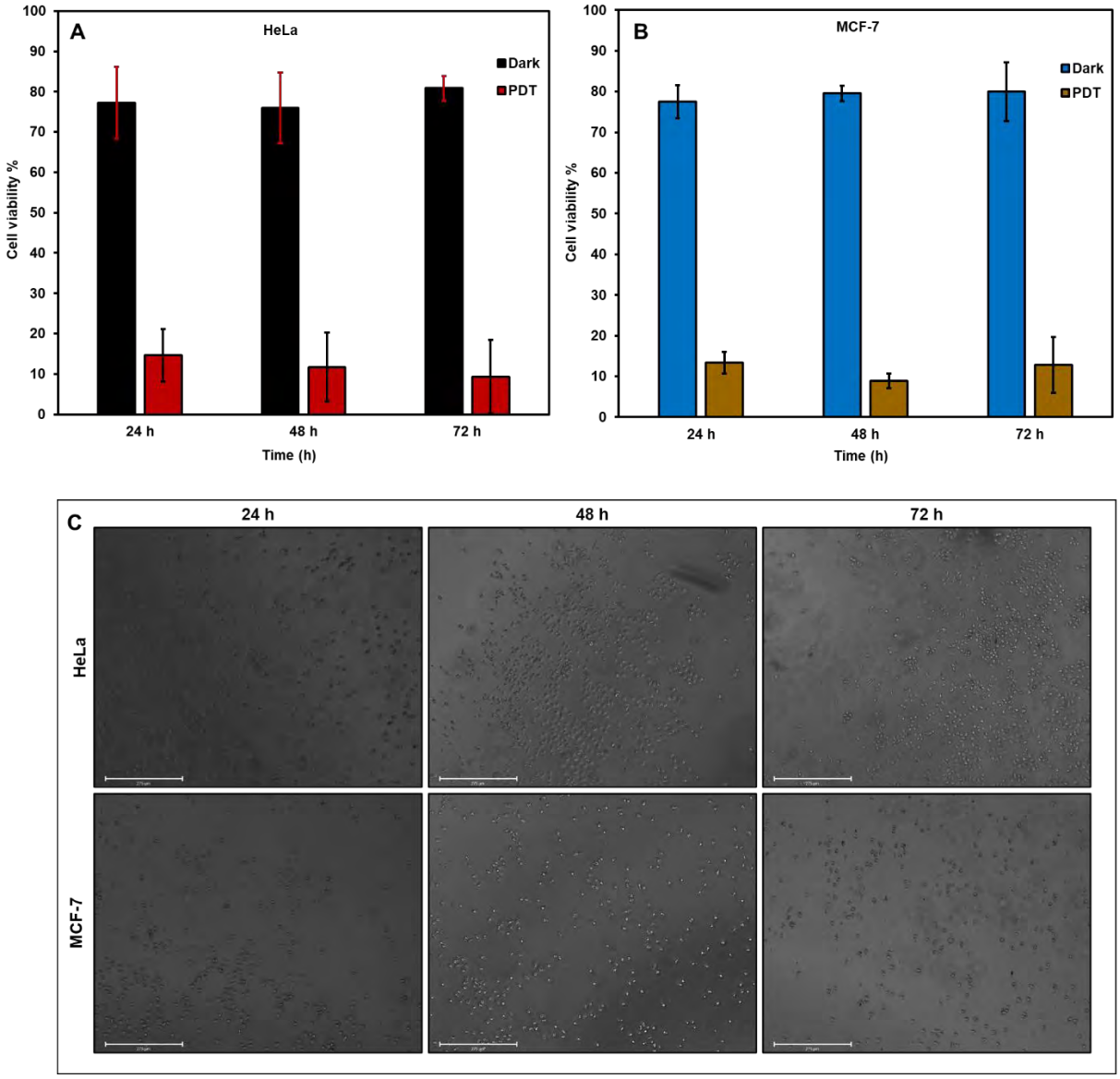

Figure 7.17: *In-vitro* phototoxicity effects of **2**-liposomes. Relative cellular viabilities of the employed HeLa (A) and MCF-7 (B) cells assessed at 24 h, 48 h and 72 h. Growth inhibitory effects of **2**-liposomes (500 µg/mL) resulted in a time-dependent decrease in cell viability. Control cells were only subjected to NIR irradiation without drug treatment. Cell morphologies of HeLa and MCF-7 cells treated with **2**-liposomes and subjected to NIR irradiation recorded at 24 h, 48 h and 72 h post PDT treatment (C). Scale: 275 µm.

7.6 Summary of Chapter

The *in-vitro* dark cytotoxicity test and photodynamic therapy activities of some Pc-liposomes and Pc/NPs-liposomes on either HeLa cells or MCF-7 breast cancer cells are presented herein. This work showed that liposome-loaded Pc or Pc/NPs could effectively undergo passive up-take by the employed cell lines. Moreover, this work showed that folic acid functionalization of liposomes could be exploited for active drug delivery and herein led to an almost 3-fold increase in drug uptake vs non-FA functionalised liposomes in accordance with FR expression levels between HeLa and MCF-7 cells, giving credence to folate receptor targeting.

Low *in-vitro* cytocidal effects were observed for all liposomal formulations with maximal concentrations resulting in less than 20 % cell death under both normoxia and hypoxia in the dark. The low cytocidal effects imply that the employed formulations were non-toxic to both cell lines when incubated in the dark. However, high PDT activities were observed following NIR laser irradiation. This work related the phototoxicities to NIR-responsive ROS generation. For **5**-liposomes and **6**-liposomes, the reported phototoxicity results were consistent with their singlet oxygen quantum yields.

For all formulations applied under hypoxia, milder phototoxicity was observed than under normoxia and may be attributed to insufficient O_2 supply since both oxygen-dependent, and oxygen-independent mechanisms persist under normoxia, whereas under hypoxia, these mechanisms would be more subdued. For **1**-liposomes, although the efficacy of PDT is limited in hypoxia, the potential reduction and hence activation of the quinoid may have acted to induce a chemotherapeutic effect which ultimately compensated for the otherwise attenuation of PDT activity under hypoxia. The above results confirmed the anticancer efficacy of the employed **1**-liposomes, and the presence of the naphthoquinone moiety, preferentially activated under hypoxic

conditions, may have resulted in an amplified therapeutic effect in either normoxia or hypoxia. Following laser irradiation, **2**-liposomes also displayed enhanced PDT activity. Both MCF-7 and HeLa displayed similar sensitivity to the phototoxicity of **2**-liposomes. Although the PDT effect of the employed **2**-liposomes was more favoured under normoxia than hypoxia because of the dual effects of oxygen-dependent singlet oxygen and nitric oxide release, the photoactivity of **2**-liposomes remained reasonable even under hypoxia where singlet oxygen generation is subdued.

The results indicate that the Pc/NPs-liposomes incorporating catalase-mimicking NPs exhibited lethality post-laser irradiation in both normoxia and hypoxia. Their sustained phototoxicity under hypoxia was attributed to their ability to supplement oxygen *in-vitro* through the breakdown of endogenous hydrogen peroxide. For all formulations, the high PDT lethality under normoxia lays credence to the remarkable synergistic and concentration-dependent phototoxic effects of the employed liposomes, which may be attributed to photoinduced ROS generation.

Chapter VIII

Photoelectrocatalytic degradation of orange G pollutant

This chapter outlines the fabrication of a visible light-responsive TiO_2-graphene oxide nanosheets – complex **4** (TiO_2@GONS@**4**) ternary structure for the photoelectrochemical degradation of Orange G azo dye as a side application. The contribution and effects of various parameters such as pH, persulfate concentration, as well as applied potential bias on degradation, are herein assessed.

8.1 Synthesis and characterization of TiO_2@GONS@4

The synthesis of the TiO_2@GONS@**4** photocatalyst is represented in **Scheme 8.1A** and it involved the adsorption of TiO_2 onto GONS followed by subsequent adsorption of complex **4**. Full details are outlined in chapter II.

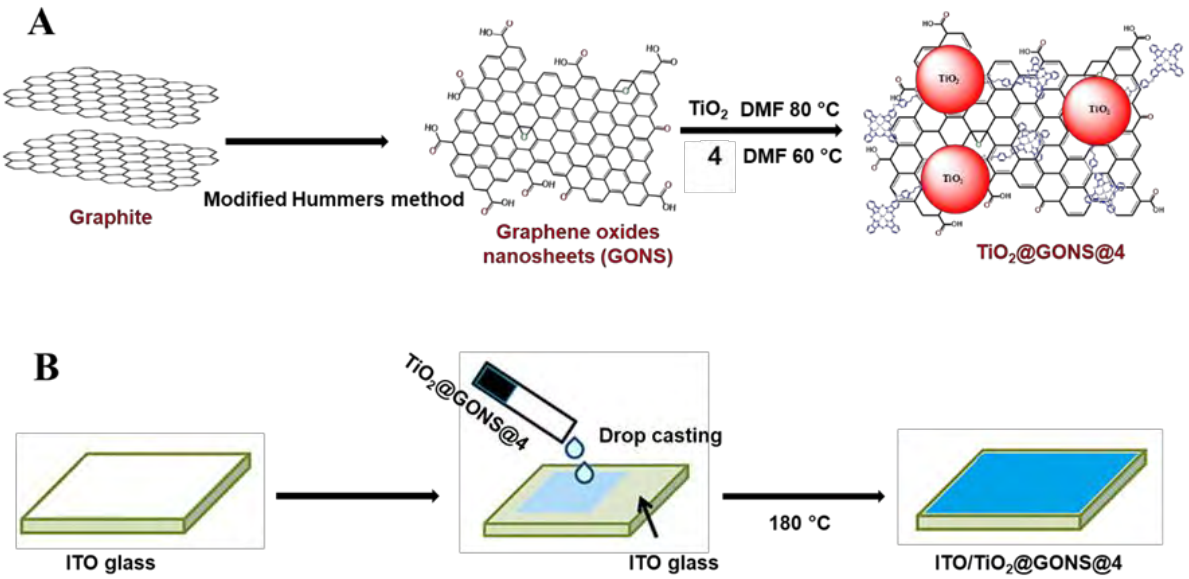

Scheme 8.1: Schematic representation of the synthesis of the TiO_2@GONS@**4** photocatalyst (A) and the fabrication of the ITO/TiO_2@GONS@**4** photoelectrode (B).

Transmission electron microscopy (TEM) was used to assess the morphologies of the respective composites. **Figure 8.1** shows the TEM micrograph of (a) GONS, (b) TiO_2, (c) TiO_2@GONS and (d) TiO_2@GONS@**4**. The TEM micrograph of the as-synthesized GONS shows the nanosheets-like morphology with folds along the surface, which is often attributed to defect sites within the structure [253,254]. The TEM image of TiO_2 in **Figure 8.1** (b) shows the largely spherical morphology of the TiO_2 with an average size of about 20 nm. The TEM image of TiO_2@GONS in **Figure 8.1** (**c**) shows that TiO_2 is adsorbed onto the surface of GONS to form the TiO_2@GONS nanocomposite. There were no observable changes in either the sizes or morphology of the TiO_2 post assembly onto the GONS surface. The large surface area of GONS allows for the introduction of complex **4** onto the TiO_2@GONS. There were no observable differences between TiO_2@GONS and TiO_2@GONS@**4** (**Figure 8.1** (d).

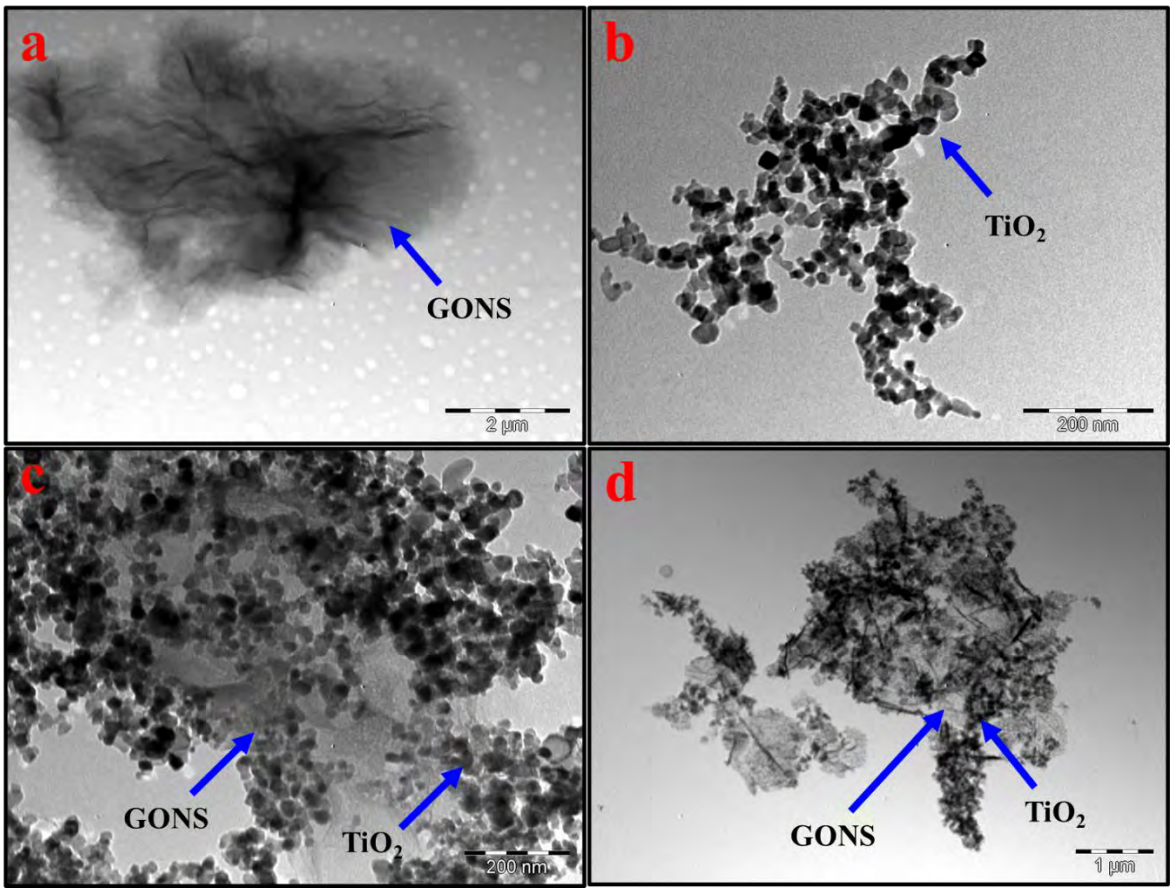

Figure 8.1: Transmission electron micrographs of (**a**) GONS, (**b**) TiO2, (**c**) TiO_2@GONS, and (d) TiO_2@GONS@**4**.

The Raman spectrum for TiO_2 in **Figure 8.2A(i)** exhibited peaks at 395 cm^{-1}, 519 cm^{-1}, and 638 cm^{-1}, which are characteristic of the $B_{1g(1)}$, A_{1g} + $B_{1g(2)}$, and $E_{g(2)}$ modes of anatase phase of TiO_2, respectively [255]. Graphene-based materials such as GONS like GQDS are known to display characteristic Raman peaks termed the G-band (sp^2) tangential mode and the D-disorder band (breathing mode, sp^3). The D and G bands are observed at 1283 cm^{-1} and 1601 cm^{-1}, respectively, for GONS alone (not shown). The Raman spectra of the TiO_2@GONS and TiO_2@GONS@**4** nanocomposites showed Raman bands attributable to the presence of TiO_2 and the GONS. The Raman peaks were observed at 1292 cm^{-1} (D band) and 1591 cm^{-1} (G band) for TiO_2@GONS and 1264 cm^{-1} (D band) and 1596 cm^{-1} (G band) for TiO_2@GONS@**4**, shifted compared to GONS alone. Moreover, the changes in the I_D/I_G from 0.88 for GONS alone to 1.05 for (TiO_2@GONS) and 1.15 for the (TiO_2@GONS@**4**) is indicative of increase in defects and the successful fabrication of the TiO_2@GONS@**4** composite.

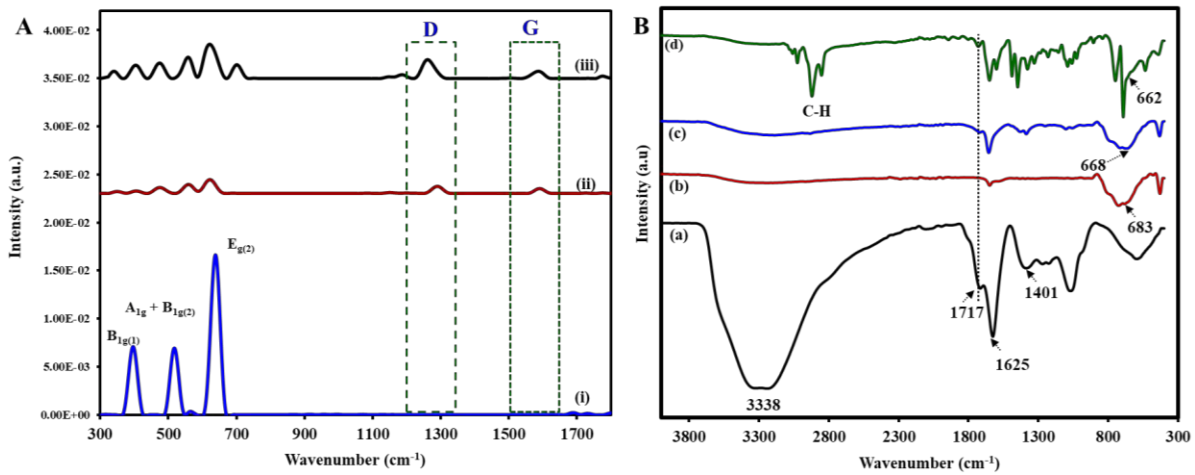

Figure 8.2: (A) Raman spectra of TiO_2 (i), TiO_2@GONS (ii) and TiO_2@GONS@**4** (iii). FT-IR spectra of GONS (a), TiO_2 (b), TiO_2@GONS (c), and TiO_2@GONS@**4** (d).

The FT-IR spectra of GONS, TiO_2, TiO_2@GONS, and TiO_2@GONS@**4** are shown in **Figure 8.2**. The FT-IR spectrum of GONS shows a broad absorption peak around at 3338 cm^{-1}, attributable to the stretching vibration of O-H, while the carbonyl C=O stretching vibration was observed at about 1717 cm^{-1}, **Figure 8.2** (a). The peaks at around 1401 cm^{-1} are credited to the skeletal C=C vibration and C–H bending vibration [256]. The broad peak in **Figure 8.2** (b) at 683 cm^{-1} was attributable to the Ti-O-Ti in TiO_2. The Ti-O-Ti was observed at 668 cm^{-1} in the TiO_2@GONS. Both the presence and shifts in this peak in the TiO_2@GONS composite confirm their successful formation. For the TiO_2@GONS@**4** conjugate, both the C=O stretching vibration and the Ti-O-Ti vibration were observed. However, in TiO_2@GONS@**4**, the Ti-O-Ti peak was observed at 662 cm^{-1}. The alkyl C–H stretch vibration emanating from complex **4** was also observed in TiO_2@GONS@**4**.

Figure 8.3 shows (a) the XPS survey spectra of TiO_2@GONS@**4** nanocomposite, and the high-resolution core level Ti 2p spectra of (b) TiO_2, (c) TiO_2@GONS, and (d) TiO_2@GONS@**4** nanocomposite and the high-resolution core level O 1s spectra of (e) TiO_2, (f) TiO_2@GONS, and (g) TiO_2@GONS@**4**. The XPS survey spectrum shows typical C 1s, Ti 2p, O 1s, and Zn 2p of the TiO_2@GONS@**4**, indicating the presence of the individual components. The high-resolution XPS analysis was used to study the chemical states of the prepared samples, using the deconvoluted Ti 2p peaks of TiO_2, TiO_2@GONS, and TiO_2@GONS@**4**. For all the samples, the Ti 2p peak was deconvoluted into two peaks, which can be ascribed to the Ti $2p_{½}$ and Ti $2p_{3/2}$ of TiO_2. The Ti $2p_{½}$ and Ti $2p_{3/2}$ peak positions for TiO_2 were observed at 459.5 eV and 465.3 eV, respectively, **Figure 8.3** (**b**). The Ti $2p_{½}$ and Ti $2p_{3/2}$ peak positions were observed at 459.3 eV and 465.1 eV for TiO_2@GONS, and 457.5 eV and 453.0 eV for TiO_2@GONS@**4**, respectively. The lowered binding energy of Ti 2p in the TiO_2@GONS and TiO_2@GONS@**4** composite demonstrates electron transfer from the GONS to the TiO_2 and represents an interaction between the constituent

assemblies. Moreover, such shifts in the binding energy of the Ti 2p peak have been attributed to the formation of oxygen vacancies in composites of TiO_2 and carbon nanomaterials [257]. Oxygen vacancies are known to act as electron traps and inhibit electron-hole recombination processes [258]. The core level O1 s XPS spectra of TiO_2 were resolved into two peaks (**Figure 8.3** (**e**)). These peaks were located at 530.6 eV (Ti-O-Ti, lattice oxygen) and 533.7 eV (surface oxygen, Ti-OH) [259] for TiO_2. The O1 s XPS spectra of TiO_2@GONS and TiO_2@GONS@**4** were both deconvoluted into four peaks (**Figure 8.3** (f and g). For TiO_2@GONS, these peaks were located at 529.9 eV, 530.8 eV, 532.1 eV, and 533.8 eV and were assigned to the Ti-O-Ti bonding of the semiconductor lattice, Ti-O-C, Ti−OH, and O-C, respectively [260]. For TiO_2@GONS@**4**, these same peaks were located at 529.6 eV, 529.9 eV, 531.1 eV, and 531.7 eV, respectively. For TiO_2@GONS and TiO_2@GONS@**4**, the existence of the peaks assigned to the Ti-O-C serves as evidence for the incorporation of TiO_2 and shows the existence of the interaction between the oxygen atoms present in the functional groups in the graphene sheet and **4** with TiO_2, hence confirms the successful synthesis of TiO_2@GONS and TiO_2@GONS@**4** composites.

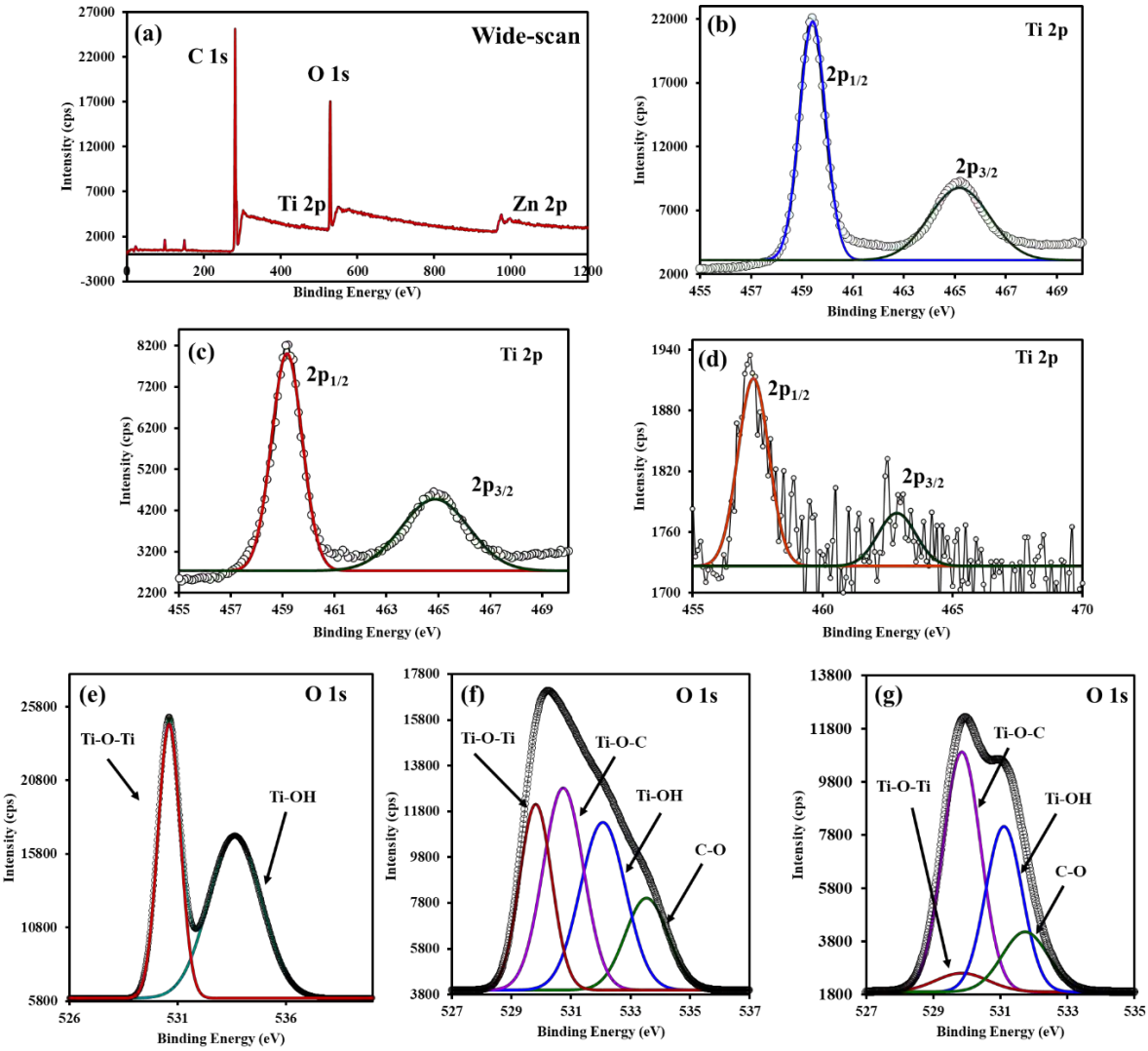

Figure 8.3: (a) XPS survey spectra of TiO_2@GONS@**4** composite. High resolution core level Ti 2p spectra of (b) TiO_2, (c) TiO_2@GONS, and (d) TiO_2@GONS@**4** composite. High resolution core level O 1s spectra of TiO_2 (e), TiO_2@GONS (f), and TiO_2@GONS@**4** composite (g).

Figure 8.4 shows the UV-Vis spectra of (**a**) TiO_2, (**b**) GONS, (**c**) TiO_2@GONS, (**d**) TiO_2@GONS@**4**. The UV-Vis of TiO_2 presents the characteristic broad absorption below 400 nm. The UV-Vis of TiO_2@GONS also shows a broad absorption band below 400 nm (**Figure 8.4** (**b**)). There were no observable shifts observed in the UV-Vis spectrum of TiO_2@GONS, implying that the compositing of GONS and TiO_2 did not significantly affect the absorption spectrum of TiO_2. The absorption spectra of the TiO_2@GONS@**4** retained the characteristics monomeric Q-band attributable to the presence of **4**. Moreover, a consequence of the conjugation of TiO_2@GONS and **4** was the enhancement in the B-band region, as highlighted in **Figure 8.4** (**d**). Such a broad band below 500 nm has been attributed to strong electronic interactions between TiO_2 and **4**. The bandgap energies were obtained from the ground state absorption spectra using the Tauc **equation 8.1** [130].

$$h\nu\alpha^{1/n} = A(h\nu - E_g) \qquad \textbf{(8.1)}$$

where α is the absorption coefficient, h is the Planck's constant, ν light frequency, A is a proportionality constant for the disorder of the material, and E_g is the bandgap energy. The value of n is governed by the nature of transition in the semiconductor. The value of n is determined from the optical transition characteristics. For direct transitions, n = ½ and n = 2 for indirect transitions. Firstly, to establish the type of band-to-band transition in the employed TiO_2, the absorption data were fitted to equations for both indirect and direct bandgap transitions. The band gaps were extrapolated from the x-axis of the Tauc plots $(h\nu\alpha)^{1/n}$ $vs. h\nu$). TiO_2 was more accurately fitted using a direct transition and the extrapolation yields an E_g value of 3.2 eV which agrees with the known bandgap of commercial titania [261] and an n value of ½ was retained.

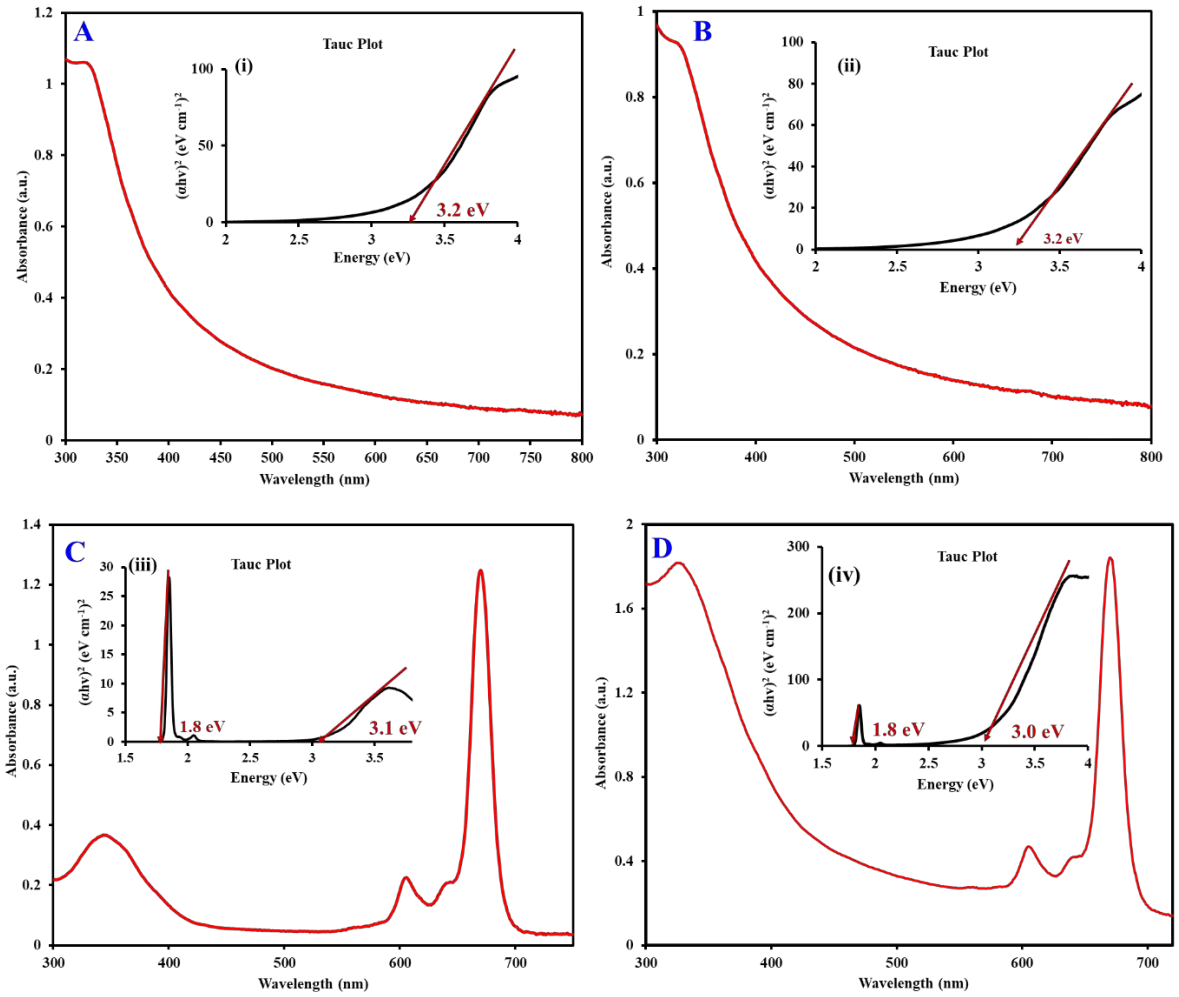

Figure 8.4: UV–vis absorption of TiO_2 alone (A), TiO_2@GONS (B), complex **4** (C), and TiO_2@GONS@**4** composites (D). Inserts: Corresponding Tauc plots. All measurements were taken in DMF. Bandgaps (E_g) are obtained by extrapolation to $\alpha = 0$.

Figure 8.4 show the respective Tauc plot of the (i) TiO_2, (ii) TiO_2@GONS, (iii) **4**, and (iv) TiO_2@GONS@**4**, as inserts. From the Tauc plot, the bandgap of TiO_2 and TiO_2@GONS were estimated as 3.2 eV, which implies that the introduction of GONS did not alter the bandgap of TiO_2. Such negligible bandgap differences between TiO_2 and carbon materials have been reported in their composites [262,263]. A significant reduction in the bandgap of TiO_2@GONS to 3.0 eV was obtained for the TiO_2@GONS@**4** composite (**Figure 8.4** (D) insert). There were no differences in the bandgap value of the **4** (1.8 eV) following the introduction of the TiO_2@GONS in terms of Q band absorbance. Despite this fact, what is most welcome in the TiO_2@GONS@**4** composite (in addition to the reduced bandgap value of 3.0 eV) is the presence of a Q-band absorbance stemming from the **4**. Indeed, owing to the presence of several absorption maxima as well as reduced bandgap, one can infer that such a ternary composite would more adequately absorb light, well into the visible light spectrum.

Charge transfer rates and electron-hole recombination rates were assessed by studying the photoluminescence (PL) quenching effect. Low PL intensity is often indicative of enhanced separation of photoinduced electrons and holes [264,265]. To this effect, the PL quenching was used to determine the effect of GONS and **4** on the separation of photogenerated electrons. **Figure 8.5** shows the photoluminescence spectra of TiO_2, TiO_2@GONS and TiO_2@GONS@**4**, which indicate the excited states of the respective materials. As shown in **Figure 8.5**, a broad luminescence peak could be observed in the region of 350-400 nm for all samples. The peak at around 380 nm, could be attributed to the band-band PL phenomenon with the energy of light approximately equal to the band-gap energy of TiO_2. The PL intensity of TiO_2 decreased following its deposition on the GONS surface. A similar effect was observed upon addition of complex **4**.

Therefore, both GONS and the **4** act as electron carriers for TiO_2 to hinder charge recombination. This enhanced charge separation efficiency in the TiO_2@GONS@**4** could serve to improve the overall efficiency in a photoelectrocatalytic process.

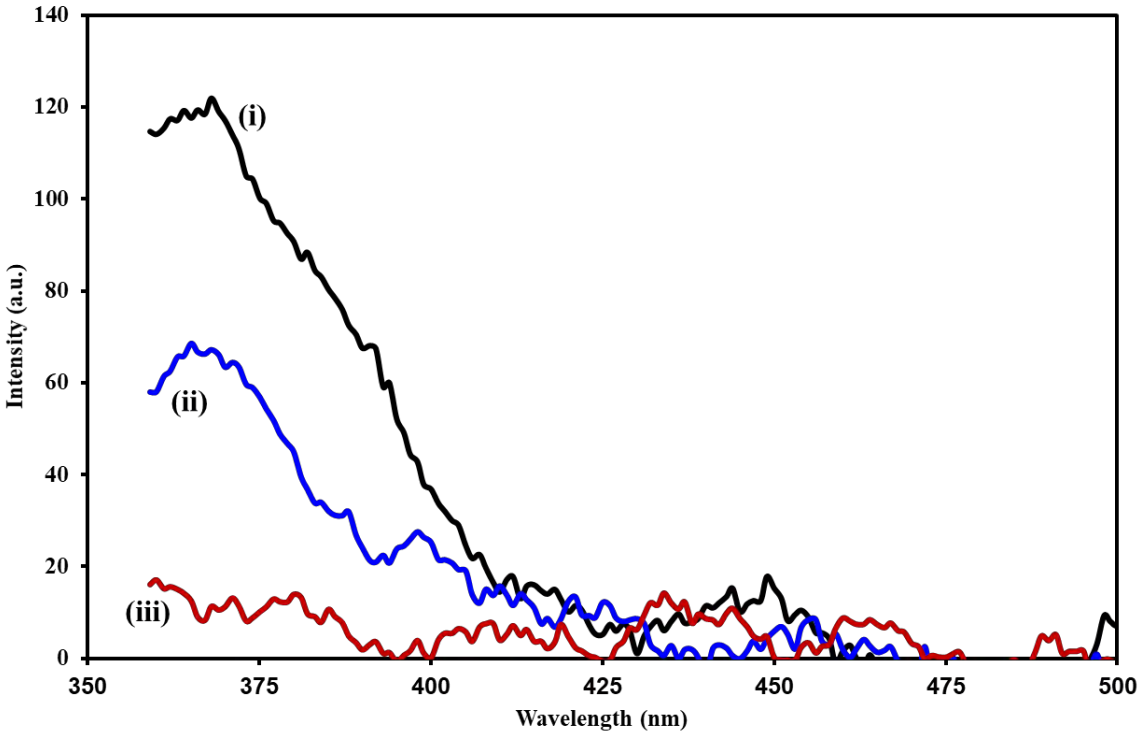

Figure 8.5: Photoluminescence spectra of (i) TiO_2, (ii) TiO_2@GONS and (iii) TiO2@GONS@**4** showing reduction in luminescence intensity with modification of TiO_2 with excitation at 350 nm in DMF.

The time-resolved fluorescence decays were also obtained to determine photoluminescence lifetimes of charge carriers of the respective samples. The photoluminescence lifetimes of TiO_2, TiO_2@GONS and TiO_2@GONS@**4** were determined to be 0.15 ns, 0.18 ns, and 0.41 ns, respectively. The prolonged lifetimes upon introduction of both GONS and **4** further illustrates that resultant photogenerated charge carriers have prolonged lifetime. Increased lifetimes of charge carriers are associated with slower recombination processes [266,267]. Therefore, the recombination of electrons is more greatly inhibited following introduction of the GONS and **4** to the TiO_2.

8.2 ITO/TiO_2@GONS@4 photoelectrode

The TiO_2@GONS@**4** photoelectrodes were prepared by drop-casting method, as illustrated in **Scheme 8.1B**. The fabricated ITO/TiO_2@GONS@**4** photoelectrode surface was analysed by atomic force microscopy (AFM) to study film surface topography. **Figure 8.6** shows the 2D AFM images of (a) unmodified ITO glass and (b) ITO/TiO_2@GONS@**4** surfaces. Their corresponding 3D AFM profiles are also shown. The unmodified ITO had a much smoother surface than the ITO/TiO_2@GONS@**4**. A marked change in surface morphology was noted for ITO/TiO_2@GONS@**4** with evidence of a more uneven surface with wrinkles and voids, compared to that of ITO alone, as can be seen in the 3D AFM plots. Such changes in surface morphology and roughness signify successful modification of the ITO surface. The higher surface area in the ITO/TiO_2@GONS@**4** could result in better pollutant adsorption and therefore may result in improved surface kinetics for degradation. Unmodified ITO surface alone showed a mean square roughness (RMS) value of 6.0 nm. The modified ITO/TiO_2@GONS@**4** photoelectrode in **Figure 8.6** (b) had an RMS of 37.2 nm.

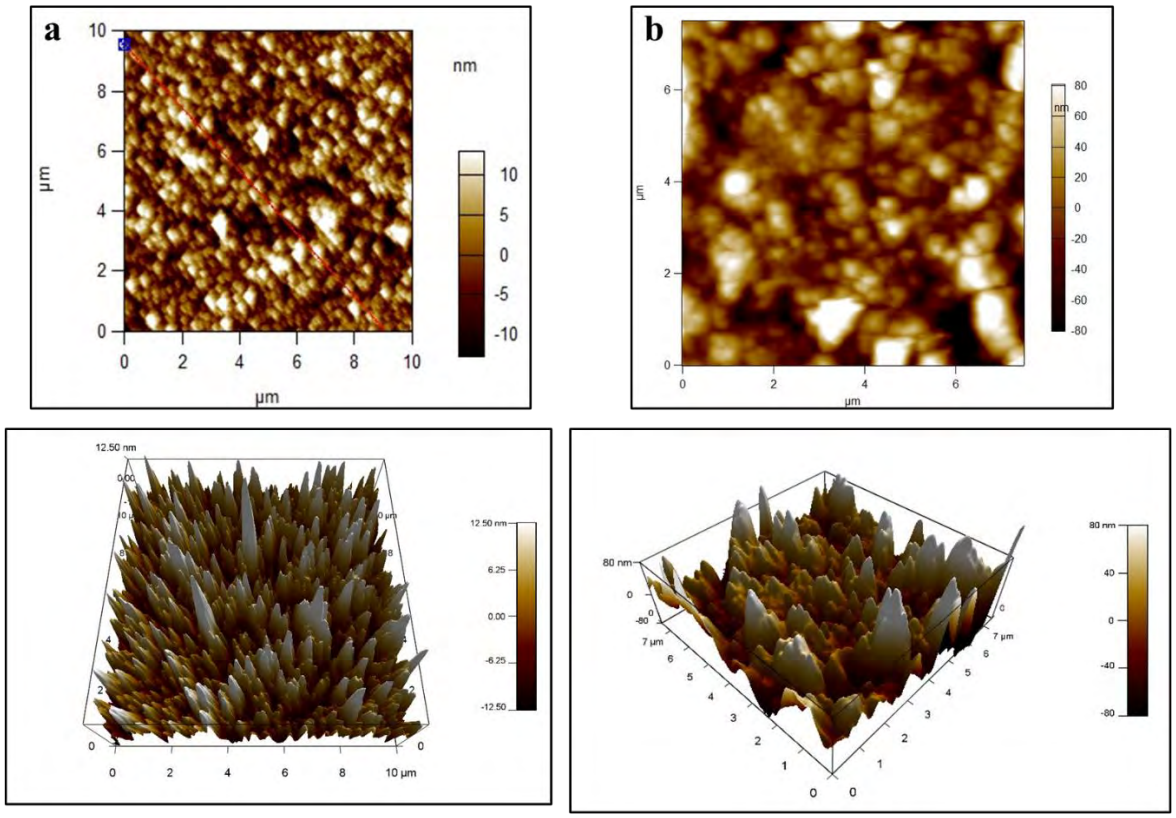

Figure 8.6: AFM images of (**a**) ITO glass and (**b**) ITO/TiO_2@GONS@**4**. Top = 2D and bottom = 3D images.

The conductivity characteristics of the heterojunction-structured TiO_2@GONS@**4** composite were elucidated by the Mott–Schottky electrochemical analysis and interpreted through the mathematical model described by **Equation 8.2** [268], results shown in **Figure 8.7**.

$$\frac{1}{C^2} = \frac{2}{e\varepsilon\varepsilon_0 A^2 N_D}\left(V - V_{fb} - \frac{k_B T}{e}\right) \qquad (\mathbf{8.2})$$

where C, A, N_D, V, V_{fb}, k_B, T, ε, ε_0 and e are the space charge capacitance, area of the electrode, donor density, the applied voltage, flat band potential, Boltzmann's constant, the absolute temperature, the dielectric constant of the semiconductor in use, the vacuum permittivity (8.85×10^{-12} C^2/Nm^2) and elementary charge (1.6×10^{-19} C), respectively.

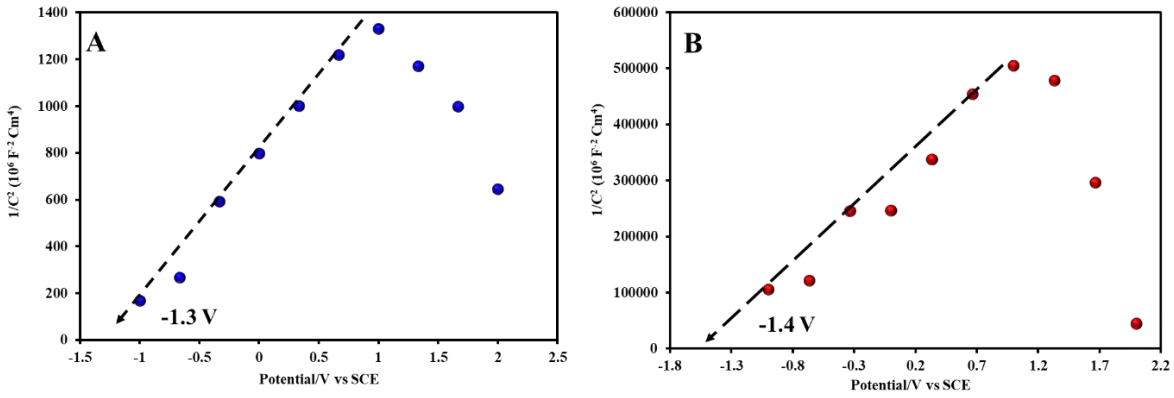

Figure 8.7: Mott-Schottky (MS) plots of ITO/TiO_2 nanospheres (**A**) and ITO/TiO_2@GONS@**4** composites (**B**).

As can be seen in **Figure 8.7** (A and B), both TiO_2 alone and TiO_2@GONS@**4** composite show n-type semiconductor behaviours, as highlighted by the positive slope [269], measured at a bias frequency of 1000 Hz. The respective values of V_{fb} (flat band potential) were estimated to be -1.3 and -1.4 for TiO_2 and TiO_2@GONS@**4**, respectively. This negative shift in the flat band potential of TiO_2@GONS@**4** compared to TiO_2 alone is attributed to the inhibition of recombination of the photogenerated electron-hole pairs and reflects improved electron transport in TiO_2@GONS@**4** composite [270].

Following this, the ITO/TiO_2@GONS@**4** photocurrent response was evaluated using chronoamperometry and electrochemical impedance spectroscopy (EIS) in the absence and presence of light irradiation. The photocurrent response tests were carried out under visible light irradiation. **Figure 8.8A** shows the transient photocurrent responses and **Figure 8.8B** the Nyquist plot of the ITO/TiO_2@GONS@**4** photoelectrode at the different applied potentials in the dark and under visible light illumination. TiO_2@GONS@**4** catalyst is responsive to ON-and OFF light

illumination with an observed current response the light source is turned on. ITO/TiO_2@GONS@**4** photoelectrode exhibits an efficient, and reasonably stable visible light photoelectric response for 0 – 1.5 V, thereafter the current was not stable for 2.0 eV. Thus, 1.5 eV was selected to conduct the photochemical and degradation studies. The tailing current response at 1.5 eV resulted from slightly higher background noise observed at this bias potential. It could be inferred that the visible light illumination and an applied potential induced an electric field between the photoanode and the Pt counter electrode [271]. The electric field results in accelerated charge separation and reduction in electron-hole/pair recombination, which is detected directly as a photocurrent response. **Figure 8.8A** clearly shows that the applied potential has a significant effect on the photocurrent response. The low photocurrent response at lower potentials is attributed to a low rate of charge separation (high rate of recombination) coupled with high transfer resistance. As the applied potential increased, faster rates of electron transfer result. Also, such high potentials reduce the back flow of electrons such that turning on the light results in higher photocurrent responses [272]. The high-charge mobility and electroconductivity of GONS and the visible light responsiveness of complex **4** are fully utilized in the ITO/TiO_2@GONS@**4** photoelectrode to promote the separation of electron-hole pairs and improve the photocurrent response.

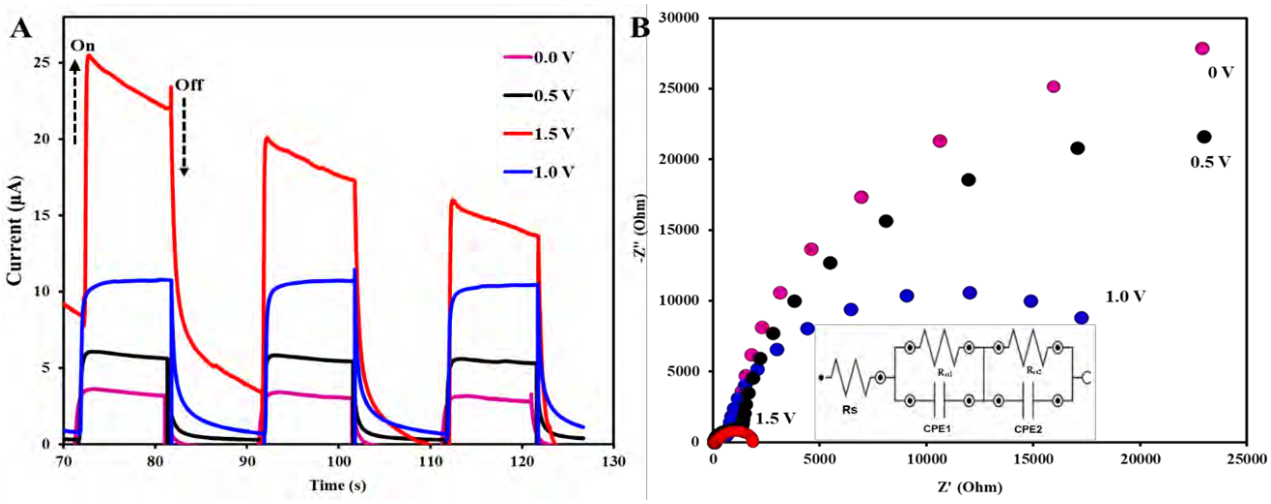

Figure 8.8: (**A**) Amperometric photocurrent responses of ITO/TiO_2@GONS@**4** at 0, 0.5, 1, and 1.5 V. (**B**) The influence of photo-irradiation and bias potential on the EIS spectra of TiO_2@GONS@**4**. All measurements were made in 0.5 M Na_2SO_4.

The above conclusions were further confirmed by electrochemical impedance spectroscopy (EIS) analysis under the dc bias range of 0 V to +1.5 V, in steps of 0.5 V at room temperature. **Figure 8.8B** shows the Nyquist plots of EIS data for the fabricated ITO/TiO_2@GONS@**4**. The impedance data (Nyquist plot) were fitted with a Randles equivalent circuit shown in **Figure 8.8B (insert)**. The impedance spectra were best interpreted by the equivalent circuit consisting of two parallel RC circuits connected in series. The data from the fitted circuit parameters are summarized in **Table 8.1**. At higher frequency regions, a semicircle was observed, indicative of an electron transfer limiting processes (**Figure 8.8B**). In each case, the diameter of the semicircles decreased with an increase in the applied positive potential bias which implies potential bias-dependence. Subsequently, two interfaces, i) ITO/photoanode and ii) photoanode/electrolyte interface, were considered. The two interfaces were fitted by the Randles-Sevcik equivalent circuit with series resistance R_s, charge transfer resistance at the ITO/photoanode (R_{ct1}) and charge transfer resistance

at the photoanode/electrolyte interface (R_{ct2}). For the potential bias range studied, the Rs values were relatively unchanged. However, both R_{ct1} and R_{ct2} values change with variations in applied potential bias (**Table 8.1**). For all potential readings, R_{ct2} gave a higher value than R_{ct1}. Moreover, R_{ct2} was more responsive to increasing applied bias potential than Rct1. Such observations imply the presence of a Schottky junction in the photoanode/electrolyte interface (R_{ct2}) [273]. Schottky junctions are usually associated with semiconductor/electrolyte interfaces (in this case photoanode/electrolyte interface). Schottky junctions influence the electron hole separation kinetics. They form when a semiconductor material is in contact with a secondary phase with a different Fermi level or redox potential (in this case redox potential since an electrolyte solution is involved) and result in band-bending (the change in the electrochemical potential) of the semiconductor to reach an equilibrium at the interface [274]. As can be seen in **Table 8.1**, the greater responsiveness in R_{ct2} in response to potential changes illustrate the effect of applied bias potential on band-bending within a semiconductor. In essence, the increase in applied bias potential improves charge transfer characteristics within the TiO_2@GONS@**4** catalyst. This is reflected by the improved current responses with increasing bias potential observed in **Figure 8.8A**. Taken together, these results highlight the interfacial charge transfer and the separation of photoexcited carriers achievable with the TiO_2@GONS@**4** composite.

Table 8.1: Nyquist fitted parameter values for the fabricated ITO/TiO_2@GONS@ZnPc.

Potential Bias/V	**R_s/Ω**	**R_{ct1}/kΩ**	**R_{ct2}/kΩ**
0	58.2	1.07	57.5
0.5	49.9	1.33	43.2
1.0	50.9	0.66	21.2
1.5	48.9	0.24	1.58

8.2.1 Evaluation of the photocatalytic, electrocatalytic, and photoelectrochemical performance

The degradation of orange G using the as-fabricated ITO/TiO_2@GONS@**4** was investigated under different conditions including light irradiation in the presence of the photoelectrode solely (photocatalysis, PC), applied electrochemical potential to the photoelectrode solely (electrocatalysis, EC), and light-irradiation with an applied potential to the photoelectrode (photoelectrocatalytic, PEC). Details on the experimental setup and procedure are outlined in chapter II. For all experiments, the ITO/TiO_2@GONS@**4** photoelectrode was equilibrated in the orange G solution for 30 min under stirring before initial measurements were taken to compensate for the effect of physical adsorption.

The catalytic performance of the ITO/TiO_2@GONS@**4** photoelectrode for the degradation of azo dyes was investigated using the degradation of Orange G dye. The degradation experiments were monitored using a UV-Vis spectrophotometer. Four characteristics absorbance peaks are observed at 475 nm (π* systems of the -N = N-), 420 nm (π -π* transition of -N = N- linked naphthalene), 330 nm (π- π* transition of the naphthalene ring), and 254 nm (π- π* transition of the benzoic ring) [275, 276]. **Figure 8.9** shows the UV-Vis absorption spectra of orange G degradation for PEC and PEC + persulfate system. The characteristic absorption peak at 475 nm, 420 nm, and 330 nm decreased with time. In the PEC system alone, an increase in the absorbance of the peak at 254 nm attributed to the π- π* transition of the benzoic ring increases with time. This increase suggests the possible formation of benzoic intermediate products [151]. Moreover, a new peak was observed at around 290 nm. The intensity of this new peak was observed to increase with treatment time, which suggests the formation of a phenolic by-product of aniline-type. Indeed, aniline and naphthol amine are common degradation intermediates in the degradation of Orange G [277]. The

characteristic absorption of the azo group of the orange G at 475 nm was monitored by taking aliquots at 10 min intervals, **Figure 8.9**.

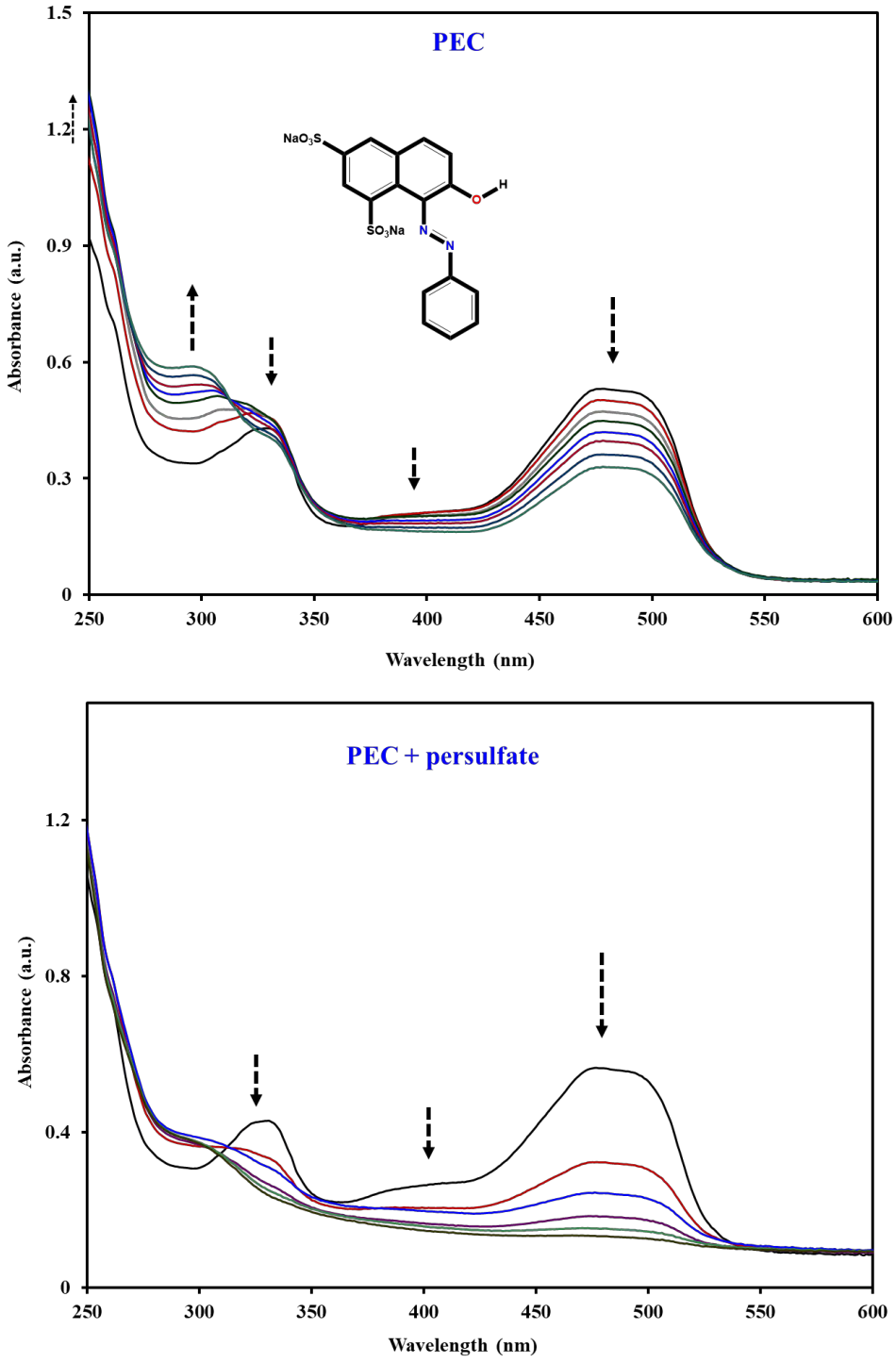

Figure 8.9: Changes in the absorbance with time in the PEC system and PEC + persulfate system. Aliquots were taken every 10 min for the PEC system and at 2 min intervals for the PEC + persulfate system. **Insert**: Structure of Orange G.

The degradation of orange G under different conditions (PC, EC, and PEC) were tested in 30 µM Orange G solution containing 0.5 M Na_2SO_4 supporting electrolyte (**Figure 8.10**). The values of k_{obs} were obtained from the slope of the plot of ln (C_0/C_t) vs. time. **Figure 8.10A** shows the changes in the Orange G concentrations with time and **Figure 8.10B** shows the pseudo first-order kinetic plots of the (i) PC, (ii) EC and (iii) PEC systems. The PC and EC experiments had 5 and 13 % degradation efficiencies, respectively, while the PEC experiment had 55 % degradation efficiency over a period of 100 min. The linearity of the plots ln (C_0/C_t) vs. time indicated that the degradation of orange G followed pseudo-first-order kinetics [278] for all the methods, **Figure 8.10B**. The apparent rate constants (k_{obs}) for the degradation of orange G using the PC system were 0.5×10^{-3} min^{-1}, which is lower than 1.4×10^{-3} min^{-1} for the EC systems, **Table 8.2**. However, the PEC-system exhibited the highest rate constant (2.5×10^{-3} min^{-1}) in unbuffered solution and a correlation coefficient of 0.97, demonstrating a high efficiency of the TiO_2@GONS@**4**-based PEC system for the degradation of the Orange G. The results demonstrate the synergistic advantage of combined PC and EC in PEC on the catalytic degradation efficiency, where the efficiency of PEC is greater than the sum of the PC and EC systems alone.

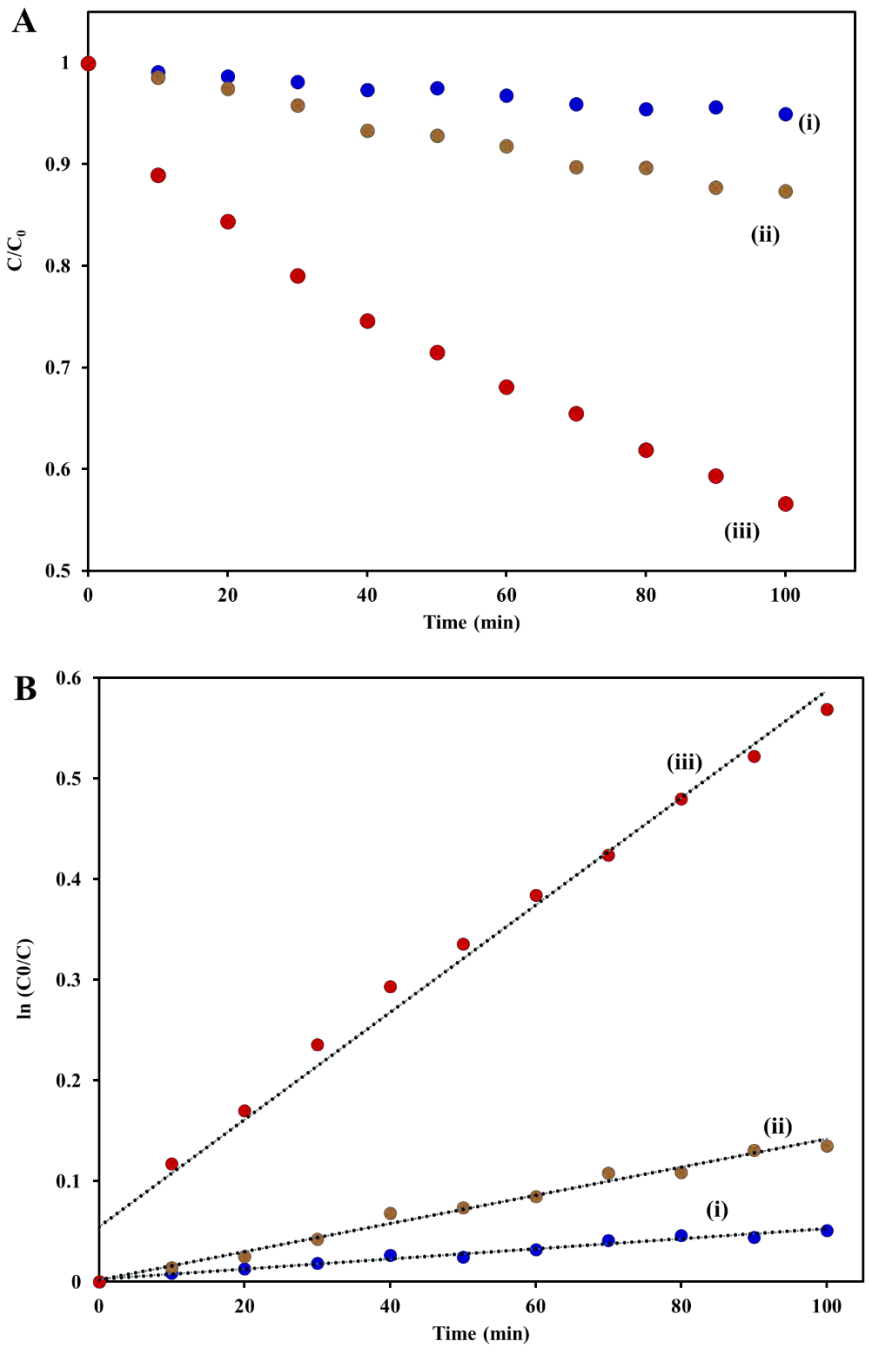

Figure 8.10: Comparison of PC (i), EC (ii), and PEC (iii) activity of the ITO/TiO_2@GONS@**4** electrode for the decomposition of OG (A) and the corresponding degradation kinetic plots (B). Experimental conditions: pH = unadjusted, and 0.1 M Na_2SO_4 electrolyte solution.

Table 8.2: Orange G (30 μM) degradation kinetics for TiO_2@GONS@**4**. pH 3 was employed unless otherwise stated.

Parameter		k_{obs} ($\times 10^{-3}$)	The correlation coefficient (R^2)	Initial rate ($\times 10^{-7}$ mol L^{-1} min^{-1})
PC*		0.5	0.98	0.27
EC*		1.4	0.99	0.45
PEC	**Unbuffered***	2.5	0.97	1.17
	pH 3	5.3	0.99	3.46
	pH 5	2.4	0.99	1.14
	pH 8	1.1	0.97	0. 72
	pH 11	0.3	0.74	0.19
Persulfate concentration	**1 mM**	53.1	0.95	4.21
	5 mM	90.8	0.99	30.56
	10 mM	139.4	0.89	70.85

*pH unadjusted.

The effect of pH on the PEC degradation of orange G was assessed. pH is known to affect the degradation of azo dyes since pH not only affects how easily the dye is oxidized, but also influences the surface interactions at the catalyst-pollutant interface [276]. For this, all other parameters, such as solution concentration, were kept constant. Four pH values (3, 5, 8, and 11) were evaluated and shown in **Table 8.2**. The observed initial rates of degradation of Orange G were 3.46, 1.14, 0.72, and 0.19 ($\times 10^{-7}$ mol L^{-1} min^{-1}) for pH values of 3, 5, 8, and 11, respectively. The initial rates of degradation increased with decreasing pH from basic to mildly acidic conditions possibly due to more favourable surface dynamics that helped to encourage pollutant interaction with the catalyst at lower pH values. This is ascribed to the strong electrostatic interaction between TiO_2@GONS@**4** and protonated groups in orange G molecules. For further experiments, pH 3 was employed in this work.

8.2.2 Persulfate assisted photoelectrocatalytic degradation

To achieve superior degradation efficiencies and complete mineralization of pollutants, this work explored combining PEC and activated persulfate chemistry. Indeed, few accounts exist in literature where a visible light-responsive catalyst is combined with an electro-assisted persulfate activation system [279].

Unlike for PEC alone, in the PEC + persulfate system, no new peaks attributable to the formation of by products were observed. Furthermore, the PEC + persulfate systems achieved the complete degradation of orange G in less than 10 min, while the PEC system (without persulfate) could only achieve about 12 % degradation within the same time limit.

8.2.2.1 Effect of persulfate concentration

The effect of persulfate concentration on the degradation performance was evaluated. **Figure 8.11A** shows changes in the absorbance with time and (B) pseudo-first-order kinetic plot of orange G at 475 nm for persulfate concentrations for (i) 1 mM, (ii) 5 mM, and (iii) 10 mM, **Figure 8.11B**. The rate of orange G degradation was found to increase with increasing concentrations of persulfate with initial rates of 4.21, 30.56, and 70.85 ($\times 10^{-7}$ mol L^{-1} min^{-1}), **Table 8.2**, for persulfate concentrations of 1 mM, 5 mM, and 10 mM, respectively. An almost 60-fold increase in the initial rate and k_{obs} of Orange G degradation is realized with a persulfate concentration of 10 mM when compared to what was achievable without persulfate addition (unbuffered solution). Indeed, the presence of the persulfate led to the greater oxidative degradation of orange G.

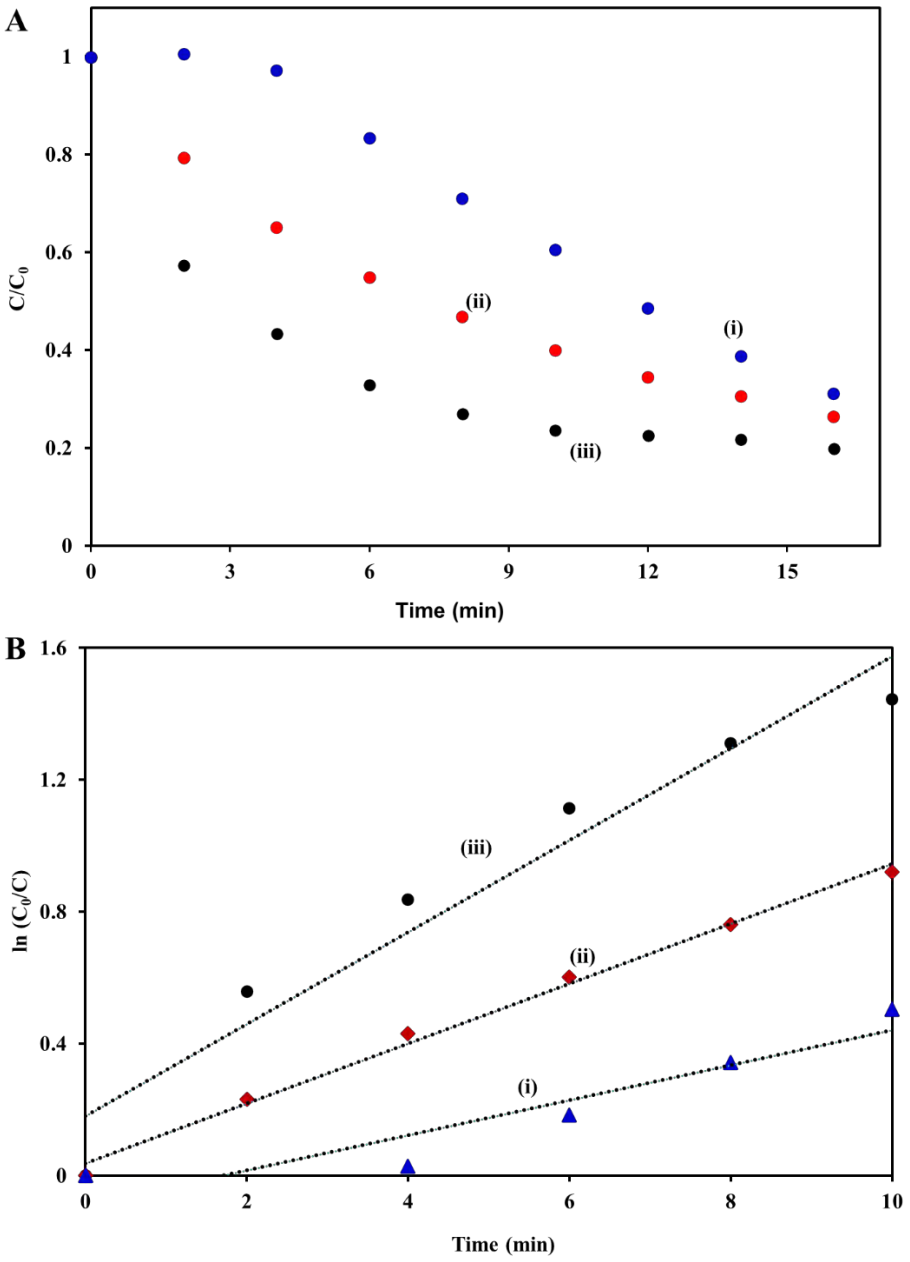

Figure 8.11: Effect of persulfate concentration on the degradation of OG (A). The pseudo-first-order reaction kinetics for Orange G in the presence of different persulfate concentrations (B). In both instances (A) and (B), three different persulfate concentrations were used: 1 mM (i), 5 mM (ii), and 10 mM (iii).

8.2.2.2 Effect of applied bias potential

The effect of the applied bias potential to ITO/TiO_2@GONS@**4** on the photoelectrocatalytic degradation of Orange G was also investigated. Three potential biases of 1.0 V, 1.5 V, and 2 V vs. Ag|AgCl were applied for the degradation of 30 µM of Orange G with the addition of 5 mM of persulfate. **Figure 8.12A** shows that the degradation efficiencies were 30 %, 48 %, and 50 %, for 1.0 V, 1.5 V and 2.0 V vs. Ag|AgCl, respectively. This indicated that an increase in the applied potential lead to an increase in the rate of persulfate activation and hence enhanced degradation.

The long-term stability and consequent reusability of the ITO/TiO_2@GONS@**4** electrodes was also evaluated. The ITO/TiO_2@GONS@**4** showed good stability and reusability as can be observed from the cycling experiments (**Figure 8.12B**). In each case, the ITO/TiO_2@GONS@**4** electrode was purged with deionized water and air dried at room temperature after each cycle run. At the third application cycle, the percentage degradation of OG was approximately 76 % suggesting minimal fluctuations in the performance of the employed ITO/TiO_2@GONS@**4** electrode even after the three cycles.

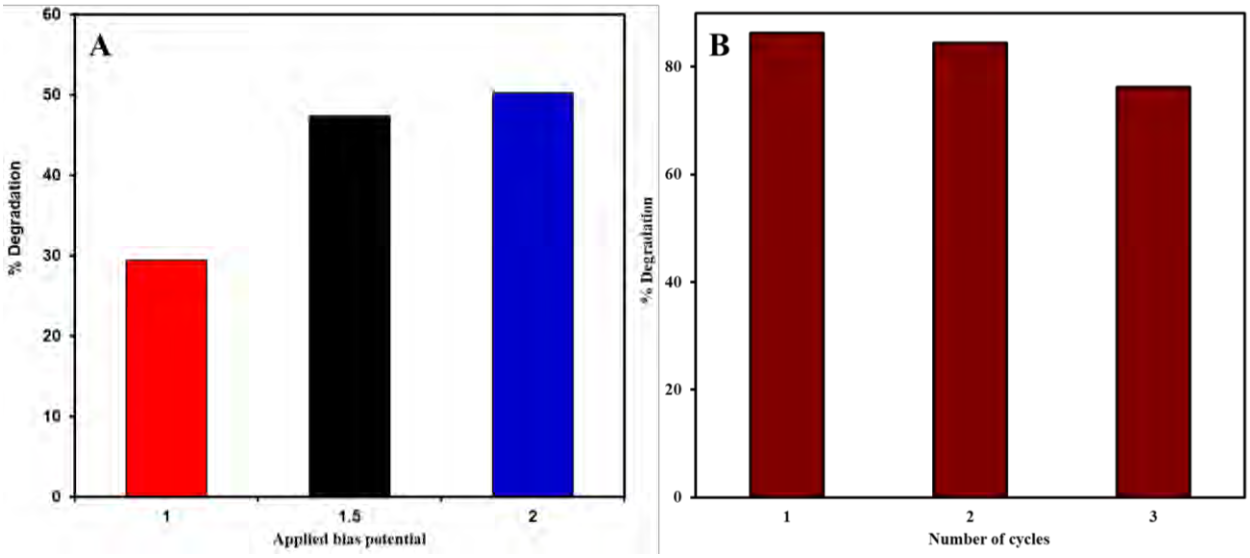

Figure 8.12: (A) Effect of bias potential on the degradation of Orange G (30 µM). (B) Cycle experiments for the degradation of Orange G on the ITO/TiO_2@GONS@**4** electrode. All with 5 mM persulfate.

8.2.3 Catalytic mechanism

The catalytic mechanism for the degradation of orange G by the ITO/TiO_2@GONS@**4** was investigated. It has been generally recognized that the photocatalytic and photoelectrocatalytic degradation proceed via the generation of reactive oxygen species (ROS) including, hydroxyl radical (·OH), superoxide ($O_2^{\cdot-}$), singlet oxygen ($^1O_2$), and sulfate radical (·$SO4^-$) (the latter, if persulfate is present). Electron spin resonance (ESR) spectroscopy was employed to identify the possible ROS generated during the ITO/TiO_2@GONS@**4** mediated PEC and PEC + persulfate systems. 5,5-Dimethyl-1-pyrroline N-oxide (DMPO) was used to probe the existence of hydroxyl radicals, superoxide radicals, or persulfate radicals (in the case of persulfate addition), and 2,2,6,6-tetramethylpiperidine (TEMP) was used to probe the generation of singlet oxygen ($^1O_2$). **Figure 8.13** (A) shows the DMPO/·OH/·SO_4^- electron spin resonance spectra of (ii) ITO/TiO_2, (iii) ITO/TiO_2@GONS, and (iv) ITO/TiO_2@GONS@**4**. **Figure 8.13** (A)(ii) shows the mixed signal of DMPO−·OH and DMPO-·SO_4^- adduct produced in the ITO/TiO_2 system. An additional single symmetrical signal, which is attributed to the carbon-centered radical generated at the edges of the π electron systems [280], was observed at 3482 G in the ITO/TiO_2@GONS systems (**Figure 8.13** (A)(iii)).

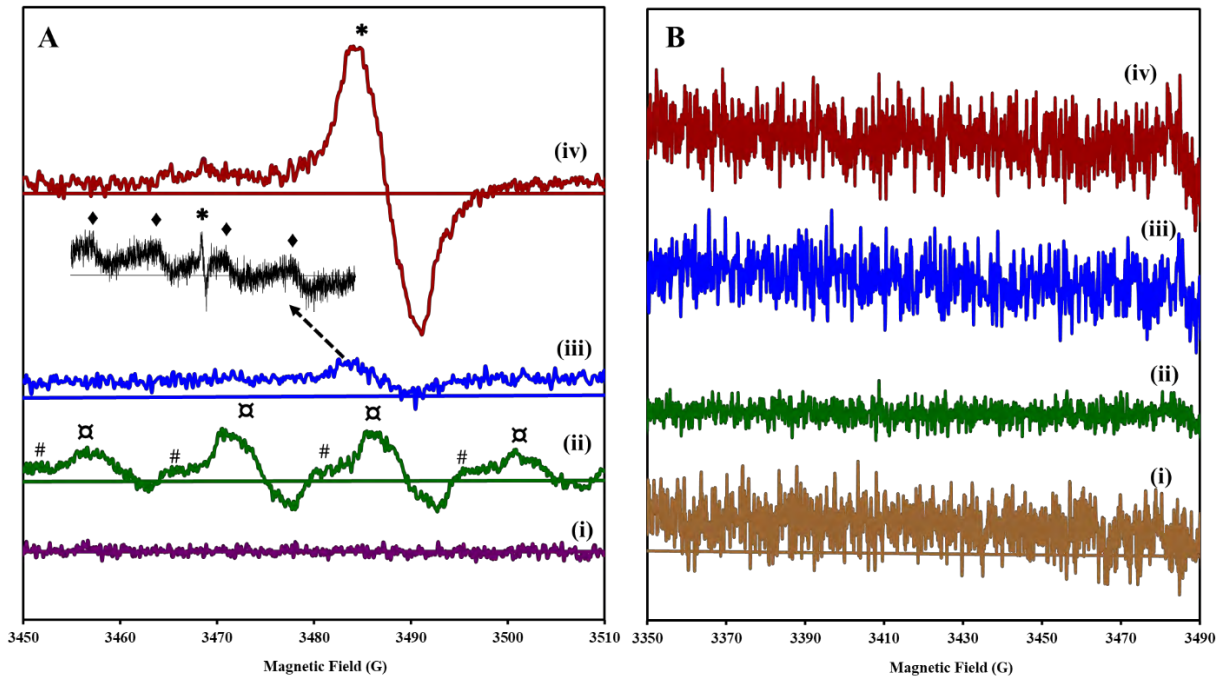

Figure 8.13: (A) DMPO and (B) TEMP ESR spectra of (i) DMPO/TEMP alone, or with (ii) TiO_2, (iii) TiO_2@GONS, and (iv) TiO_2@GONS@**4**. Experiments were performed in the presence of persulfate (10 mM). ["♦" represents the presence of DMPO-OH adducts, "#" represents the presence of DMPO-SO_4 adducts, and "*" represents the presence of carbon-centered radicals].

There were no distinguishable signal peaks attributable to either DMPO−·OH or DMPO-·SO_4^- radical adduct in the ESR spectrum of the ITO/TiO_2@GONS@**4** system (**Figure 8.13** (A) (iv). Instead, the spectrum was dominated by the presence of the carbon-centered radical signal of π electron systems which suggested that the presence of the highly conjugated π system of GONS and **4** in the ITO/TiO_2@GONS@**4** system may have modulated the catalytic mechanism to a charge transfer mediated persulfate activation. Furthermore, the singlet oxygen driven catalytic mechanism was investigated. The ESR result in **Figure 8.13** (B) did not show the typical three-line ESR spectrum with equal intensities attributable to the TEMPO for ITO/TiO_2, ITO/TiO_2@GONS and ITO/TiO_2@GONS@**4**. This suggests that the TiO_2@GONS@**4** did not produce singlet oxygen, and hence singlet oxygen was not responsible for the degradation of Orange G in the PS system.

Although scarce, reports of non-radical activation of persulfates have been reported [281]. This is believed to proceed through an electron transfer mechanism from an organic material that serves as an electron donor to persulfate (electron acceptor) [282]. This usually involves the use of a conductive catalyst that serves to mediate the charge transfer mechanism. In this case, complex **4** and GONS adequately modulate this process, as demonstrated earlier by the Mott-Schottky analysis. A proposed mechanism of Orange G degradation following persulfate (PS) activation via a non-radical route using the as-reported system is as follows: (i) firstly, PS and Orange G azo dye within the electrolyte solution transfer from the electrolyte to the surface of the ITO/TiO_2@GONS@**4** photoanode, (ii) PS molecules adsorbed on the surface of the photoanode are subsequently activated, (iii) oxidation of Orange G molecules occurs on the surface of the photoanode through electron transfer to the PS, facilitated by the carbon framework of the TiO_2@GONS@**4** catalyst (**Scheme 8.2**).

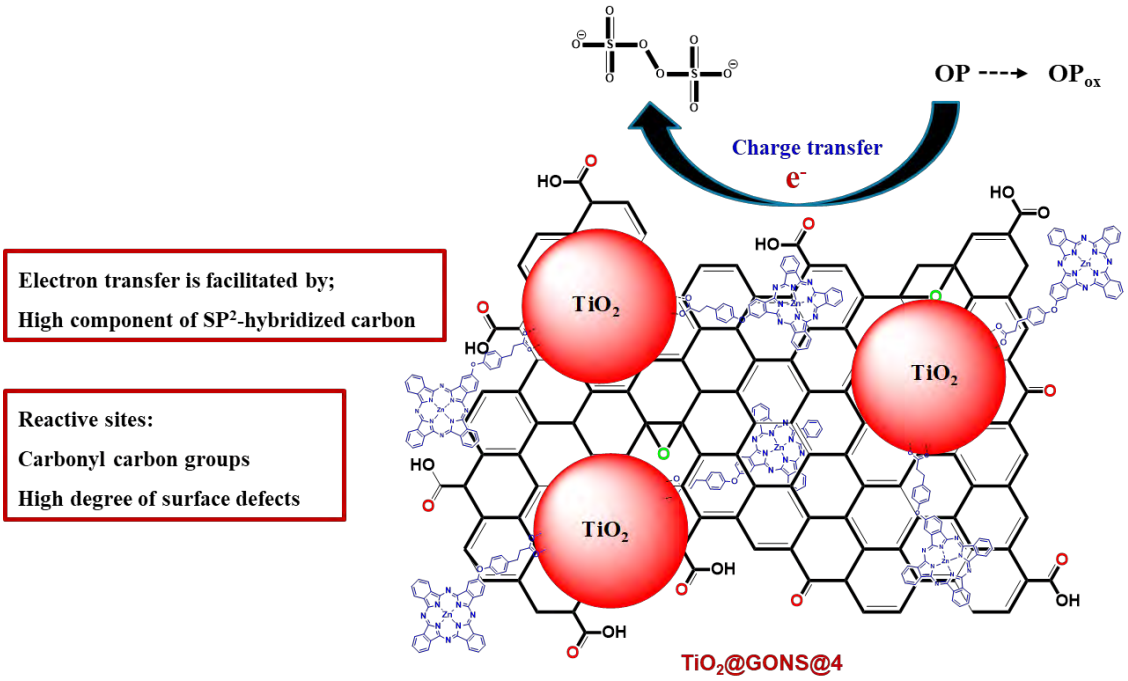

Scheme 8.2: Proposed pathways for the carbocatalytic non-radical activation of persulfate in the TiO_2@GONS@**4** system. OP and OPox stand for organic pollutants and oxidation products, respectively.

This works serves as the first report of persulfate activation by such MPc complexes where radical intermediates such as sulfate radical anion and hydroxyl radical are not responsible for this persulfate-driven oxidation of an organic pollutant. This is important because non-radical pathways are highly selective systems. Their substrate-dependent oxidizing capacity allows for better targeting of the priority pollutants present at trace levels in the complicated water matrices. Non-selective radicals (such as sulfate and hydroxyl radicals) would be fruitlessly consumed through the reactions with background organic and inorganic substrates [283,284].

8.3 Summary of chapter

The excellent visible-light harvesting properties of MPcs were exploited in the fabrication of MPc-NPs ternary structure using complex **4** (TiO_2@GONS@**4**). The compositing of such a hybrid heterojunction promotes charge separation and electron migration, significantly improving the degradation efficiency with an applied potential. The degradation kinetics were found to follow pseudo first order kinetics. Electron spin resonance analyses suggested that neither hydroxyl radicals nor sulfate radicals were produced for TiO_2@GONS@**4**, and therefore were not responsible for the persulfate-driven oxidation of the OG dye. These findings suggest that MPcs can play a critical role in mediating the eventual charge transfer mediated PS activation.

Chapter IX

General conclusions and recommendations

This chapter summarizes the results obtained from the studies conducted and reported in this thesis. It also gives recommendations on future work that could be conducted to enhance the reported studies.

9.1 General conclusions

This study reported on the successful synthesis of novel asymmetric and symmetrical zinc phthalocyanine complexes as well as silicon metal-based phthalocyanine complexes. The structures of MPcs were confirmed by various techniques, including, FT-IR, NMR, MALDI-TOF mass spectrometry and elemental analysis.

The MPcs were further conjugated to various NPs and techniques such as FT-IR and X–ray photoelectron spectroscopy was used to confirm the successful compositing of the individual components. Generally, the presence of nanoparticles resulted in enhanced triplet and singlet oxygen quantum yields of Pcs and this was attributed to the heavy atom effect of the nanoparticles. The employed MPcs and MPc-NPs conjugates were successfully encapsulated into unmodified as well as FA-functionalized liposomes to improve biocompatibility and aqueous solubility. The formed liposomes presented as predominantly spherical nanoscale structures with sizes between 90 and 280 nm with negative zeta potentials.

The liposome-loaded MPcs and MPc-NPs were successfully applied in PDT using MCF-7 and HeLa cells as *in-vitro* cancer models. This work showed that liposome-loaded Pc or Pc/NPs could effectively undergo passive up-take by the employed cell lines. Folic acid functionalization of liposomes could be exploited for active drug delivery and herein led to an almost 3-fold increase in drug uptake vs non-FA functionalized liposomes in accordance with FR expression levels between HeLa and MCF-7 cells, giving credence to folate receptor targeting. The employed liposomal formulations displayed low cytotoxicity in the dark. However, high PDT activities were

observed following NIR laser irradiation. This work related the phototoxicities to NIR-responsive ROS generation.

For **1**-liposomes, although the efficacy of PDT is limited in hypoxia, the potential reduction and hence activation of the quinoid may have acted to induce a chemotherapeutic effect which ultimately compensated for the otherwise attenuation of PDT activity under hypoxia. The PDT effect of the employed **2**-liposomes under hypoxia benefited from dual effects of oxygen-dependent singlet oxygen and nitric oxide release. This work also demonstrated that incorporating catalase-mimicking NPs with MPcs afforded the MPcs with the ability to supplement oxygen *in-vitro* through the breakdown of endogenous hydrogen peroxide which ultimately translated into sustained phototoxicity under hypoxia.

A simplified lab-scale fabrication and photoelectrocatalytic evaluation of a TiO_2-GONS-MPcs heterojunction resulted in an NIR-responsive photocatalyst which cooperative properties for the degradation of Orange G as a sample industrial pollutant. The resultant composite exhibited great potential for advanced water treatment technology.

9.2 Future recommendations

For future work and direction, it would be interesting to evaluate newer classes of MPcs with more tunable hypoxia-activated response. Computational chemistry would play a huge role in this case isolating compounds of favourable reduction potentials to the applied in hypoxic PDT. Also, in line with this, the possibility of carbon monoxide (CO) releasing MPcs complexes would pose an interesting addition to the host MPcs that can be applied in hypoxic PDT.

Based on the promising activities of the photoelectrocatalytic composite reported herein, future work could entail applying them for other water related problems such as the photoreduction of heavy metals and desulfurization of crude oils as well as a host of other toxic aqueous pollutants.

References

[1] A. Ogunsipe, J.Y. Chen, T. Nyokong, Photophysical and photochemical studies of zinc(II) phthalocyanine derivatives - Effects of substituents and solvents, New J. Chem. 28 (2004) 822–827. https://doi.org/10.1039/b315319c.

[2] M. Özçeşmeci, I.B. Özçeşmeci, E. Hamuryudan, Synthesis and characterization of new polyfluorinated dendrimeric phthalocyanines, Polyhedron. 29 (2010) 2710–2715. https://doi.org/10.1016/j.poly.2010.06.023.

[3] K. Sanusi, E. Antunes, T. Nyokong, Optical nonlinearities in non-peripherally substituted pyridyloxy phthalocyanines: A combined effect of symmetry, ring-strain and demetallation, Dalt. Trans. 43 (2014) 999–1010. https://doi.org/10.1039/c3dt52462k.

[4] M. Hanack, T. Schneider, M. Barthel, J.S. Shirk, S.R. Flom, R.G.S. Pong, Indium phthalocyanines and naphthalocyanines for optical limiting, Coord. Chem. Rev. 219–221 (2001) 235–258. https://doi.org/10.1016/S0010-8545(01)00327-7.

[5] D. Dini, M. Barthel, M. Hanack, Phthalocyanines as active materials for optical limiting, European J. Org. Chem. (2001) 3759–3769. https://doi.org/10.1002/1099-0690(200110)2001:20<3759::AID-EJOC3759>3.0.CO;2-U.

[6] S. Khene, D.A. Geraldo, C.A. Togo, J. Limson, T. Nyokong, Synthesis, electrochemical characterization of tetra- and octa-substituted dodecyl-mercapto tin phthalocyanines in solution and as self-assembled monolayers, Electrochim. Acta. 54 (2008) 183–191. https://doi.org/10.1016/j.electacta.2008.08.018.

[7] P. Mashazi, T. Nyokong, Electrocatalytic studies of covalently immobilized metal tetra-amino phthalocyanines onto derivatized screen-printed gold electrodes, Microchim. Acta. 171 (2010) 321–332. https://doi.org/10.1007/s00604-010-0438-6.

[8] X. Li, K. Jeong, Y. Lee, T. Guo, D. Lee, J. Park, N. Kwon, J.H. Na, S.K. Hong, S.S. Cha, J.D. Huang, S. Choi, S. Kim, J. Yoon, Water-soluble phthalocyanines selectively bind to albumin dimers: A green approach toward enhancing tumor-targeted photodynamic therapy, Theranostics. 9 (2019) 6412–6423. https://doi.org/10.7150/thno.35210.

[9] X. Li, B. De Zheng, X.H. Peng, S.Z. Li, J.W. Ying, Y. Zhao, J.D. Huang, J. Yoon, Phthalocyanines as medicinal photosensitizers: Developments in the last five years, Coord. Chem. Rev. 379 (2019) 147–160. https://doi.org/10.1016/j.ccr.2017.08.003.

[10] X. Li, D. Lee, J.D. Huang, J. Yoon, Phthalocyanine-Assembled Nanodots as Photosensitizers for Highly Efficient Type I Photoreactions in Photodynamic Therapy, Angew. Chemie - Int. Ed. 57 (2018) 9885–9890. https://doi.org/10.1002/anie.201806551.

[11] B. O'Regan, M. Grätzel, A low-cost, high-efficiency solar cell based on dye-sensitized colloidal TiO2 films, Nature. 353 (1991) 737–740. https://doi.org/10.1038/353737a0.

[12] K. Guilard, Roger. Caemelbecke, Eric. Tabard, Alain. Kadish, The Porphyrin Handbook: Inorganic, organometallic and coordination chemistry, Academic Press/World Scientific, San Diego, 2003.

[13] R.D. Joyner, M.E. Kenney, Phthalocyaninosilicon Compounds, Inorg. Chem. 1 (1962) 236–238. https://doi.org/10.1021/ic50002a008.

[14] J.W. Hofman, F. Van Zeeland, S. Turker, H. Talsma, S.A.G. Lambrechts, D. V. Sakharov, W.E. Hennink, C.F. Van Nostrum, Peripheral and axial substitution of phthalocyanines with solketal groups: Synthesis and in vitro evaluation for photodynamic therapy, J. Med. Chem. 50 (2007) 1485–1494. https://doi.org/10.1021/jm061136w.

[15] H. Li, T.J. Jensen, F.R. Fronczek, M.G.H. Vicente, Syntheses and properties of a series of cationic water-soluble phthalocyanines, J. Med. Chem. 51 (2008) 502–511. https://doi.org/10.1021/jm070781f.

[16] K. Mitra, M.C.T. Hartman, Silicon phthalocyanines: synthesis and resurgent applications, Org. Biomol. Chem. 19 (2021) 1168–1190. https://doi.org/10.1039/d0ob02299c.

[17] G. De La Torre, C.G. Claessens, T. Torres, Phthalocyanines: Old dyes, new materials. Putting color in nanotechnology, Chem. Commun. (2007) 2000–2015. https://doi.org/10.1039/b614234f.

[18] A.M. Paoletti, G. Pennesi, G. Rossi, A. Generosi, B. Paci, V.R. Albertini, Titanium and ruthenium phthalocyanines for NO2 sensors: A mini-review, Sensors. 9 (2009) 5277–5297. https://doi.org/10.3390/s90705277.

[19] L. Edwards, M. Gouterman, Porphyrins. XV. Vapor absorption spectra and stability: Phthalocyanines, J. Mol. Spectrosc. 33 (1970) 292–310. https://doi.org/10.1016/0022-2852(70)90040-8.

[20] J. Mack, M.J. Stillman, Assignment of the optical spectra of metal phthalocyanines through spectral band deconvolution analysis and ZINDO calculations, Coord. Chem. Rev. 219–221 (2001) 993–1032. https://doi.org/10.1016/S0010-8545(01)00394-0.

[21] M. Gouterman, Spectra of porphyrins, J. Mol. Spectrosc. 6 (1961) 138–163. https://doi.org/10.1016/0022-2852(61)90236-3.

[22] M. Gouterman, G.H. Wagnière, L.C. Snyder, Spectra of porphyrins. Part II. Four orbital model, J. Mol. Spectrosc. 11 (1963) 108–127. https://doi.org/10.1016/0022-2852(63)90011-0.

[23] C.G. Claessens, U. Hahn, T. Torres, Phthalocyanines: From outstanding electronic properties to emerging applications, Chem. Rec. 8 (2008) 75–97. https://doi.org/10.1002/tcr.20139.

[24] R.M. Szeimies, C.A. Morton, A. Sidoroff, L.R. Braathen, Photodynamic therapy for non-melanoma skin cancer, Acta Derm. Venereol. 85 (2005) 483–490. https://doi.org/10.1080/00015550510044136.

[25] B.J. Qumseya, W. David, H.C. Wolfsen, Photodynamic therapy for Barrett's esophagus and esophageal carcinoma, Clin. Endosc. 46 (2013) 30–37. https://doi.org/10.5946/ce.2013.46.1.30.

[26] K. Moghissi, K. Dixon, Update on the current indications, practice and results of photodynamic therapy (PDT) in early central lung cancer (ECLC), Photodiagnosis Photodyn. Ther. 5 (2008) 10–18. https://doi.org/10.1016/j.pdpdt.2007.11.001.

[27] L.B. Josefsen, R.W. Boyle, Unique diagnostic and therapeutic roles of porphyrins and phthalocyanines in photodynamic therapy, imaging and theranostics, Theranostics. 2 (2012) 916–966. https://doi.org/10.7150/thno.4571.

[28] D.P. Valenzeno, Photomodification of Biological Membranes With Emphasis on Singlet Oxygen Mechanisms, Photochem. Photobiol. 46 (1987) 147–160. https://doi.org/10.1111/j.1751-1097.1987.tb04749.x.

[29] J.N. Silva, P. Filipe, P. Morlière, J.C. Mazière, J.P. Freitas, J.L. Cirne De Castro, R. Santus, Photodynamic therapies: Principles and present medical applications, Biomed. Mater. Eng. 16 (2006) S147–S154.

[30] S. Pervaiz, M. Olivo, Art and science of photodynamic therapy, Clin. Exp. Pharmacol. Physiol. 33 (2006) 551–556. https://doi.org/10.1111/j.1440-1681.2006.04406.x.

[31] M.A. Calin, S. V. Parasca, Photodynamic therapy in oncology, J. Optoelectron. Adv. Mater. 8 (2006) 1173–1179. https://doi.org/10.1634/theoncologist.11-9-1034.

[32] M. Ochsner, Light scattering of human skin: A comparison between zinc(II)-phthalocyanine and photofrin II®, J. Photochem. Photobiol. B Biol. 32 (1996) 3–9. https://doi.org/10.1016/1011-1344(95)07209-8.

[33] T.J. Dougherty, Photodynamic Therapy, Photochem. Photobiol. 58 (1993) 895–900. https://doi.org/10.1111/j.1751-1097.1993.tb04990.x.

[34] B. Aru, A. Günay, E. Şenkuytu, G. Yanlkkaya Demirel, A.G. Gürek, D. Atilla, A Translational Study of a Silicon Phthalocyanine Substituted with a Histone Deacetylase Inhibitor for Photodynamic Therapy, ACS Omega. 5 (2020) 25854–25867. https://doi.org/10.1021/acsomega.0c03180.

[35] K. Sato, K. Ando, S. Okuyama, S. Moriguchi, T. Ogura, S. Totoki, H. Hanaoka, T. Nagaya, R. Kokawa, H. Takakura, M. Nishimura, Y. Hasegawa, P.L. Choyke, M. Ogawa, H. Kobayashi,

Photoinduced Ligand Release from a Silicon Phthalocyanine Dye Conjugated with Monoclonal Antibodies: A Mechanism of Cancer Cell Cytotoxicity after Near-Infrared Photoimmunotherapy, ACS Cent. Sci. 4 (2018) 1559–1569. https://doi.org/10.1021/acscentsci.8b00565.

[36] E.D. Baron, C.L. Malbasa, D. Santo-Domingo, P. Fu, J.D. Miller, K.K. Hanneman, A.H. Hsia, N.L. Oleinick, V.C. Colussi, K.D. Cooper, Silicon phthalocyanine (pc 4) photodynamic therapy is a safe modality for cutaneous neoplasms: Results of a phase 1 clinical trial, Lasers Surg. Med. 42 (2010) 888–895. https://doi.org/10.1002/lsm.20984.

[37] P. Agostinis, K. Berg, K.A. Cengel, T.H. Foster, A.W. Girotti, S.O. Gollnick, S.M. Hahn, M.R. Hamblin, A. Juzeniene, D. Kessel, M. Korbelik, J. Moan, P. Mroz, D. Nowis, J. Piette, B.C. Wilson, J. Golab, Photodynamic therapy of cancer: An update, CA. Cancer J. Clin. 61 (2011) 250–281. https://doi.org/10.3322/caac.20114.

[38] H. He, A.L. Nieminen, P. Xu, A bioactivatable self-quenched nanogel for targeted photodynamic therapy, Biomater. Sci. 7 (2019) 5143–5149. https://doi.org/10.1039/c9bm01237k.

[39] K. Jeong, C.S. Kang, Y. Kim, Y.D. Lee, I.C. Kwon, S. Kim, Development of highly efficient nanocarrier-mediated delivery approaches for cancer therapy, Cancer Lett. 374 (2016) 31–43. https://doi.org/10.1016/j.canlet.2016.01.050.

[40] F. Moret, E. Reddi, Strategies for optimizing the delivery to tumors of macrocyclic photosensitizers used in photodynamic therapy (PDT), J. Porphyr. Phthalocyanines. 21 (2017) 239–256. https://doi.org/10.1142/S1088424617300014.

[41] W.S. Kuo, H.H. Chen, S.Y. Chen, C.Y. Chang, P.C. Chen, Y.I. Hou, Y.T. Shao, H.F. Kao, C.L. Lilian Hsu, Y.C. Chen, S.J. Chen, S.R. Wu, J.Y. Wang, Graphene quantum dots with nitrogen-doped content dependence for highly efficient dual-modality photodynamic antimicrobial

therapy and bioimaging, Biomaterials. 120 (2017) 185–194. https://doi.org/10.1016/j.biomaterials.2016.12.022.

[42] C. Qian, P. Yan, G. Wan, S. Liang, Y. Dong, J. Wang, Facile synthetic Photoluminescent Graphene Quantum dots encapsulated β-cyclodextrin drug carrier system for the management of macular degeneration: Detailed analytical and biological investigations, J. Photochem. Photobiol. B Biol. 189 (2018) 244–249. https://doi.org/10.1016/j.jphotobiol.2018.10.019.

[43] E. Masoudipour, S. Kashanian, N. Maleki, A targeted drug delivery system based on dopamine functionalized nano graphene oxide, Chem. Phys. Lett. 668 (2017) 56–63. https://doi.org/10.1016/j.cplett.2016.12.019.

[44] X. Zeng, J. Sun, S. Li, J. Shi, H. Gao, W. Sun Leong, Y. Wu, M. Li, C. Liu, P. Li, J. Kong, Y.Z. Wu, G. Nie, Y. Fu, G. Zhang, Blood-triggered generation of platinum nanoparticle functions as an anti-cancer agent, Nat. Commun. 11 (2020) 567–579. https://doi.org/10.1038/s41467-019-14131-z.

[45] P.H. Yang, X. Sun, J.F. Chiu, H. Sun, Q.Y. He, Transferrin-mediated gold nanoparticle cellular uptake, Bioconjug. Chem. 16 (2005) 494–496. https://doi.org/10.1021/bc049775d.

[46] A.G. Tkachenko, H. Xie, D. Coleman, W. Glomm, J. Ryan, M.F. Anderson, S. Franzen, D.L. Feldheim, Multifunctional gold nanoparticle-peptide complexes for nuclear targeting, J. Am. Chem. Soc. 125 (2003) 4700–4701. https://doi.org/10.1021/ja0296935.

[47] P.K. Brown, A.T. Qureshi, A.N. Moll, D.J. Hayes, W.T. Monroe, Silver nanoscale antisense drug delivery system for photoactivated gene silencing, ACS Nano. 7 (2013) 2948–2959. https://doi.org/10.1021/nn304868y.

[48] V.P. Torchilin, Recent advances with liposomes as pharmaceutical carriers, Nat. Rev. Drug Discov. 4 (2005) 145–160. https://doi.org/10.1038/nrd1632.

[49] M. Mezei, V. Gulasekharam, Liposomes—A selective drug delivery system for the topical route of administration: gel dosage form, J. Pharm. Pharmacol. 34 (1982) 473–474. https://doi.org/10.1111/j.2042-7158.1982.tb04767.x.

[50] X. Damoiseau, H.J. Schuitmaker, J.W.M. Lagerberg, M. Hoebeke, Increase of the photosensitizing efficiency of the Bacteriochlorin a by liposome-incorporation, J. Photochem. Photobiol. B Biol. 60 (2001) 50–60. https://doi.org/10.1016/S1011-1344(01)00118-X.

[51] S. Dhami, D. Phillips, Comparison of the photophysics of an aggregating and non-aggregating aluminium phthalocyanine system incorporated into unilamellar vesicles, J. Photochem. Photobiol. A Chem. 100 (1996) 77–84. https://doi.org/10.1016/S1010-6030(96)04438-3.

[52] A.M. Garcia, E. Alarcon, M. Muñoz, J.C. Scaiano, A.M. Edwards, E. Lissi, Photophysical behaviour and photodynamic activity of zinc phthalocyanines associated to liposomes, Photochem. Photobiol. Sci. 10 (2011) 507–514. https://doi.org/10.1039/c0pp00289e.

[53] M. Sadasivam, P. Avci, G.K. Gupta, S. Lakshmanan, R. Chandran, Y.Y. Huang, R. Kumar, M.R. Hamblin, Self-assembled liposomal nanoparticles in photodynamic therapy, Eur. J. Nanomedicine. 5 (2013) 115–129. https://doi.org/10.1515/ejnm-2013-0010.

[54] H.I. Chang, M.K. Yeh, Clinical development of liposome-based drugs: Formulation, characterization, and therapeutic efficacy, Int. J. Nanomedicine. 7 (2012) 49–60. https://doi.org/10.2147/ijn.s26766.

[55] M.L. Immordino, F. Dosio, L. Cattel, Stealth liposomes: Review of the basic science, rationale, and clinical applications, existing and potential, Int. J. Nanomedicine. 1 (2006) 297–315. https://doi.org/10.2217/17435889.1.3.297.

[56] A.S.L. Derycke, P.A.M. De Witte, Liposomes for photodynamic therapy, Adv. Drug Deliv. Rev. 56 (2004) 17–30. https://doi.org/10.1016/j.addr.2003.07.014.

[57] M. Srinivasarao, C. V. Galliford, P.S. Low, Principles in the design of ligand-targeted cancer therapeutics and imaging agents, Nat. Rev. Drug Discov. 14 (2015) 203–219. https://doi.org/10.1038/nrd4519.

[58] A. Wicki, D. Witzigmann, V. Balasubramanian, J. Huwyler, Nanomedicine in cancer therapy: Challenges, opportunities, and clinical applications, J. Control. Release. 200 (2015) 138–157. https://doi.org/10.1016/j.jconrel.2014.12.030.

[59] M. Fenech, The role of folic acid and Vitamin B12 in genomic stability of human cells, Mutat. Res. - Fundam. Mol. Mech. Mutagen. 475 (2001) 57–67. https://doi.org/10.1016/S0027-5107(01)00079-3.

[60] N. Parker, M.J. Turk, E. Westrick, J.D. Lewis, P.S. Low, C.P. Leamon, Folate receptor expression in carcinomas and normal tissues determined by a quantitative radioligand binding assay, Anal. Biochem. 338 (2005) 284–293. https://doi.org/10.1016/j.ab.2004.12.026.

[61] E.I. Sega, P.S. Low, Tumor detection using folate receptor-targeted imaging agents, Cancer Metastasis Rev. 27 (2008) 655–664. https://doi.org/10.1007/s10555-008-9155-6.

[62] J. Sudimack, R.J. Lee, Targeted drug delivery via the folate receptor, Adv. Drug Deliv. Rev. 41 (2000) 147–162. https://doi.org/10.1016/S0169-409X(99)00062-9.

[63] A.R. Hilgenbrink, P.S. Low, Folate receptor-mediated drug targeting: From therapeutics to diagnostics, J. Pharm. Sci. 94 (2005) 2135–2146. https://doi.org/10.1002/jps.20457.

[64] R.J. Lee, P.S. Low, Delivery of liposomes into cultured KB cells via folate receptor-mediated endocytosis, J. Biol. Chem. 269 (1994) 3198–3204. https://doi.org/10.1016/s0021-9258(17)41848-5.

[65] M.M. Qualls, D.H. Thompson, Chloroaluminum phthalocyanine tetrasulfonate delivered via acid-labile diplasmenylcholine-folate liposomes: Intracellular localization and synergistic phototoxicity, Int. J. Cancer. 93 (2001) 384–392. https://doi.org/10.1002/ijc.1339.

[66] G. De Simone, R.M. Vitale, A. Di Fiore, C. Pedone, A. Scozzafava, J.L. Montero, J.Y. Winum, C.T. Supuran, Carbonic anhydrase inhibitors: Hypoxia-activatable sulfonamides incorporating disulfide bonds that target the tumor-associated isoform IX, J. Med. Chem. 49 (2006) 5544–5551. https://doi.org/10.1021/jm060531j.

[67] P. Vaupel, O. Thews, M. Hoeckel, Treatment resistance of solid tumors: Role of hypoxia and anemia, Med. Oncol. 18 (2001) 243–259. https://doi.org/10.1385/MO:18:4:243.

[68] G. Melillo, Targeting hypoxia cell signaling for cancer therapy, Cancer Metastasis Rev. 26 (2007) 341–352. https://doi.org/10.1007/s10555-007-9059-x.

[69] Z. Shen, Q. Ma, X. Zhou, G. Zhang, G. Hao, Y. Sun, J. Cao, Strategies to improve photodynamic therapy efficacy by relieving the tumor hypoxia environment, NPG Asia Mater. 13 (2021) 39–57. https://doi.org/10.1038/s41427-021-00303-1.

[70] M. Camerin, M. Magaraggia, M. Soncin, G. Jori, M. Moreno, I. Chambrier, M.J. Cook, D.A. Russell, The in vivo efficacy of phthalocyanine-nanoparticle conjugates for the

photodynamic therapy of amelanotic melanoma, Eur. J. Cancer. 46 (2010) 1910–1918. https://doi.org/10.1016/j.ejca.2010.02.037.

[71] N. Nombona, K. Maduray, E. Antunes, A. Karsten, T. Nyokong, Synthesis of phthalocyanine conjugates with gold nanoparticles and liposomes for photodynamic therapy, J. Photochem. Photobiol. B Biol. 107 (2012) 35–44. https://doi.org/10.1016/j.jphotobiol.2011.11.007.

[72] T. Mthethwa, T. Nyokong, Fluorescence behavior and singlet oxygen generating abilities of aluminum phthalocyanine in the presence of anisotropic gold nanoparticles, J. Lumin. 157 (2015) 207–214. https://doi.org/10.1016/j.jlumin.2014.09.005.

[73] M. Miretti, T.C. Tempesti, C.G. Prucca, M.T. Baumgartner, Zn phthalocyanines loaded into liposomes: Characterization and enhanced performance of photodynamic activity on glioblastoma cells, Bioorganic Med. Chem. 28 (2020) 115355. https://doi.org/10.1016/j.bmc.2020.115355.

[74] P.E. Feuser, A.P. Cordeiro, G. de Bem Silveira, M.E.A. Borges Corrêa, P.C. Lock Silveira, C. Sayer, P.H.H. de Araújo, R.A. Machado-de-Ávila, A.G. Dal Bó, Co-encapsulation of sodium diethyldithiocarbamate (DETC) and zinc phthalocyanine (ZnPc) in liposomes promotes increases phototoxic activity against (MDA-MB 231) human breast cancer cells, Colloids Surfaces B Biointerfaces. 197 (2021) 111434. https://doi.org/10.1016/j.colsurfb.2020.111434.

[75] Ö. Çoban, B. Barut, C.Ö. Yalçın, A. Özel, Z. Bıyıklıoğlu, Development and in vitro evaluation of BSA-coated liposomes containing Zn (II) phthalocyanine-containing ferrocene groups for photodynamic therapy of lung cancer, J. Organomet. Chem. 925 (2020) 121469. https://doi.org/10.1016/j.jorganchem.2020.121469.

[76] E. Antunes, N. Rapulenyane, M. Ledwaba, C. Litwinski, W. Chidawanyika, T. Nyokong, The synthesis and characterisation of magnetic nanoparticles and their interaction with a zinc phthalocyanine, Inorg. Chem. Commun. 29 (2013) 60–64. https://doi.org/10.1016/j.inoche.2012.12.010.

[77] L.C. Nene, M. Managa, T. Nyokong, Photo-physicochemical properties and in vitro photodynamic therapy activity of morpholine-substituted Zinc(II)-Phthalocyanines π-π stacked on biotinylated graphene quantum dots, Dye. Pigment. 165 (2019) 488–498. https://doi.org/10.1016/j.dyepig.2019.03.002.

[78] R. Matshitse, M. Managa, T. Nyokong, The modulation of the photophysical and photodynamic therapy activities of a phthalocyanine by detonation nanodiamonds: Comparison with graphene quantum dots and carbon nanodots, Diam. Relat. Mater. 101 (2020) 107617. https://doi.org/10.1016/j.diamond.2019.107617.

[79] D.O. Oluwole, E. Prinsloo, T. Nyokong, Photophysicochemical properties of nanoconjugates of zinc(II) 2(3)-mono-2-(4-oxy)phenoxy)acetic acid phthalocyanine with cysteamine capped silver and silver–gold nanoparticles, Polyhedron. 119 (2016) 434–444. https://doi.org/10.1016/j.poly.2016.09.034.

[80] A.L. Lin, P.P. Fan, S.F. Liu, J.H. Chen, Y.Y. Zhao, B.Y. Zheng, M.R. Ke, J.D. Huang, A phthalocyanine-based liposomal nanophotosensitizer with highly efficient tumor-targeting and photodynamic activity, Dye. Pigment. 180 (2020) 108455. https://doi.org/10.1016/j.dyepig.2020.108455.

[81] P. García Calavia, I. Chambrier, M.J. Cook, A.H. Haines, R.A. Field, D.A. Russell, Targeted photodynamic therapy of breast cancer cells using lactose-phthalocyanine functionalized

gold nanoparticles, J. Colloid Interface Sci. 512 (2018) 249–259. https://doi.org/10.1016/j.jcis.2017.10.030.

[82] D. Wang, R. Shi, J. Zhou, S. Shi, H. Wu, P. Xu, H. Wang, G. Xia, T.E. Barnhart, W. Cai, Z. Guo, Q. Chen, Photo-Enhanced Singlet Oxygen Generation of Prussian Blue-Based Nanocatalyst for Augmented Photodynamic Therapy, IScience. 9 (2018) 14–26. https://doi.org/10.1016/j.isci.2018.10.005.

[83] M. Broekgaarden, R. Weijer, M. Krekorian, B. van den IJssel, M. Kos, L.K. Alles, A.C. van Wijk, Z. Bikadi, E. Hazai, T.M. van Gulik, M. Heger, Inhibition of hypoxia-inducible factor 1 with acriflavine sensitizes hypoxic tumor cells to photodynamic therapy with zinc phthalocyanine-encapsulating cationic liposomes, Nano Res. 9 (2016) 1639–1662. https://doi.org/10.1007/s12274-016-1059-0.

[84] R. Weijer, M. Broekgaarden, M. Krekorian, L.K. Alles, A.C. van Wijk, C. Mackaaij, J. Verheij, A.C. van der Wal, T.M. van Gulik, G. Storm, M. Heger, Inhibition of hypoxia inducible factor 1 and topoisomerase with acriflavine sensitizes perihilar cholangiocarcinomas to photodynamic therapy, Oncotarget. 7 (2016) 3341–3356. https://doi.org/10.18632/oncotarget.6490.

[85] M. Broekgaarden, R. Weijer, A.C. Van Wijk, R.C. Cox, M.R. Egmond, R. Hoebe, T.M. Van Gulik, M. Heger, Photodynamic therapy with liposomal zinc phthalocyanine and tirapazamine increases tumor cell death via DNA damage, J. Biomed. Nanotechnol. 13 (2017) 204–220. https://doi.org/10.1166/jbn.2017.2327.

[86] A. Borgatti-Jeffreys, S.B. Hooser, M.A. Miller, M.D. Lucroy, Phase I clinica trial of the use of zinc phthalocyanine tetrasulfonate as a photosensitizer for photodynamic therapy in dogs, Am. J. Vet. Res. 68 (2007) 399–404. https://doi.org/10.2460/ajvr.68.4.399.

[87] H.L.L.M. van Leengoed, V. Cuomo, A.A.C. Versteeg, N. van der Veen, G. Jori, W.M. Star, In vivo fluorescence and photodynamic activity of zinc phthalocyanine administered in liposomes, Br. J. Cancer. 69 (1994) 840–845. https://doi.org/10.1038/bjc.1994.163.

[88] R.R. Allison, G.H. Downie, R. Cuenca, X.H. Hu, C.J.H. Childs, C.H. Sibata, Photosensitizers in clinical PDT, Photodiagnosis Photodyn. Ther. 1 (2004) 27–42. https://doi.org/10.1016/S1572-1000(04)00007-9.

[89] E. Dube, N. Nwaji, D.O. Oluwole, J. Mack, T. Nyokong, Investigation of photophysicochemical properties of zinc phthalocyanines conjugated to metallic nanoparticles, J. Photochem. Photobiol. A Chem. 349 (2017) 148–161. https://doi.org/10.1016/j.jphotochem.2017.09.020.

[90] I. Papandreou, R.A. Cairns, L. Fontana, A.L. Lim, N.C. Denko, HIF-1 mediates adaptation to hypoxia by actively downregulating mitochondrial oxygen consumption, Cell Metab. 3 (2006) 187–197. https://doi.org/10.1016/j.cmet.2006.01.012.

[91] T. Hagen, Oxygen versus reactive oxygen in the regulation of HIF-1 α: the balance tips, Biochem. Res. Int. (2012). https://doi.org/10.1155/2012/436981.

[92] S. Li, J. Zhang, H. Yang, C. Wu, X. Dang, Y. Liu, Copper depletion inhibits CoCl2 -induced aggressive phenotype of MCF-7 cells via downregulation of HIF-1 and inhibition of Snail/Twist-mediated epithelial-mesenchymal transition, Sci. Rep. 5 (2015) 12410. https://doi.org/10.1038/srep12410.

[93] Z. Dong, M.A. Venkatachalam, J. Wang, Y. Patel, P. Saikumar, G.L. Semenza, T. Force, J. Nishiyama, Up-regulation of apoptosis inhibitory protein IAP-2 by hypoxia: HIF-1-independent mechanisms, J. Biol. Chem. 276 (2001) 18702–18709. https://doi.org/10.1074/jbc.M011774200.

[94] S.T. Halpin, D.M. Spence, Direct plate-reader measurement of nitric oxide released from hypoxic erythrocytes flowing through a microfluidic device, Anal. Chem. 82 (2010) 7492–7497. https://doi.org/10.1021/ac101130s.

[95] S. Koch, F. Mayer, F. Honecker, M. Schittenhelm, C. Bokemeyer, Efficacy of cytotoxic agents used in the treatment of testicular germ cell tumours under normoxic and hypoxic conditions in vitro, Br. J. Cancer. 89 (2003) 2133–2139. https://doi.org/10.1038/sj.bjc.6601375.

[96] Y. Wang, Y. Xie, J. Li, Z.H. Peng, Y. Sheinin, J. Zhou, D. Oupický, Tumor-Penetrating Nanoparticles for Enhanced Anticancer Activity of Combined Photodynamic and Hypoxia-Activated Therapy, ACS Nano. 11 (2017) 2227–2238. https://doi.org/10.1021/acsnano.6b08731.

[97] L. Feng, L. Cheng, Z. Dong, D. Tao, T.E. Barnhart, W. Cai, M. Chen, Z. Liu, Theranostic Liposomes with Hypoxia-Activated Prodrug to Effectively Destruct Hypoxic Tumors Post-Photodynamic Therapy, ACS Nano. 11 (2017) 927–937. https://doi.org/10.1021/acsnano.6b07525.

[98] Y. Liu, Y. Liu, W. Bu, C. Cheng, C. Zuo, Q. Xiao, Y. Sun, D. Ni, C. Zhang, J. Liu, J. Shi, Hypoxia Induced by Upconversion-Based Photodynamic Therapy: Towards Highly Effective Synergistic Bioreductive Therapy in Tumors, Angew. Chemie - Int. Ed. 54 (2015) 8105–8109. https://doi.org/10.1002/anie.201500478.

[99] X. Li, Y.H. Jeon, N. Kwon, J.G. Park, T. Guo, H.R. Kim, J.D. Huang, D.S. Lee, J. Yoon, In Vivo-assembled phthalocyanine/albumin supramolecular complexes combined with a hypoxia-

activated prodrug for enhanced photodynamic immunotherapy of cancer, Biomaterials. 266 (2021) 120430. https://doi.org/10.1016/j.biomaterials.2020.120430.

[100] L.J. Ignarro, B.A. Freeman, Nitric Oxide: Biology and Pathobiology: Third Edition, Academic Press, London, 2017.

[101] A. Fraix, S. Sortino, Combination of PDT photosensitizers with NO photodononors, Photochem. Photobiol. Sci. 17 (2018) 1709–1727. https://doi.org/10.1039/c8pp00272j.

[102] Q. Xiang, B. Qiao, Y. Luo, J. Cao, K. Fan, X. Hu, L. Hao, Y. Cao, Q. Zhang, Z. Wang, Increased photodynamic therapy sensitization in tumors using a nitric oxide-based nanoplatform with ATP-production blocking capability, Theranostics. 11 (2021) 1953–1969. https://doi.org/10.7150/thno.52997.

[103] D.A. Wink, J.B. Mitchell, Chemical biology of nitric oxide: Insights into regulatory, cytotoxic, and cytoprotective mechanisms of nitric oxide, Free Radic. Biol. Med. 25 (1998) 434–456. https://doi.org/10.1016/S0891-5849(98)00092-6.

[104] W.A. Pryor, G.L. Squadrito, The chemistry of peroxynitrite: A product from the reaction of nitric oxide with superoxide, Am. J. Physiol. - Lung Cell. Mol. Physiol. 268 (1995) L699–L722. https://doi.org/10.1152/ajplung.1995.268.5.l699.

[105] D.A. Wink, Y. Vodovotz, J. Laval, F. Laval, M.W. Dewhirst, J.B. Mitchell, The multifaceted roles of nitric oxide in cancer, Carcinogenesis. 19 (1998) 711–721. https://doi.org/10.1093/carcin/19.5.711.

[106] H.J. Xiang, Q. Deng, L. An, M. Guo, S.P. Yang, J.G. Liu, Tumor cell specific and lysosome-targeted delivery of nitric oxide for enhanced photodynamic therapy triggered by 808 nm near-infrared light, Chem. Commun. 52 (2016) 148–151. https://doi.org/10.1039/c5cc07006f.

[107] L.B. Negri, T.J. Martins, R.S. da Silva, M.R. Hamblin, Photobiomodulation combined with photodynamic therapy using ruthenium phthalocyanine complexes in A375 melanoma cells: Effects of nitric oxide generation and ATP production, J. Photochem. Photobiol. B Biol. 198 (2019) 111564. https://doi.org/10.1016/j.jphotobiol.2019.111564.

[108] A.R. Lippert, G.C. Van De Bittner, C.J. Chang, Boronate oxidation as a bioorthogonal reaction approach for studying the chemistry of hydrogen peroxide in living systems, Acc. Chem. Res. 44 (2011) 793–804. https://doi.org/10.1021/ar200126t.

[109] T.P. Szatrowski, C.F. Nathan, Production of Large Amounts of Hydrogen Peroxide by Human Tumor Cells, Cancer Res. 51 (1991) 794–798.

[110] M. López-Lázaro, Dual role of hydrogen peroxide in cancer: Possible relevance to cancer chemoprevention and therapy, Cancer Lett. 252 (2007) 1–8. https://doi.org/10.1016/j.canlet.2006.10.029.

[111] S. Qin, Y. Xu, H. Li, H. Chen, Z. Yuan, Recent advances in in situ oxygen-generating and oxygen-replenishing strategies for hypoxic-enhanced photodynamic therapy, Biomater. Sci. 10 (2022) 51–84. https://doi.org/10.1039/d1bm00317h.

[112] H. Chen, J. Tian, W. He, Z. Guo, H2O2-activatable and O2-evolving nanoparticles for highly efficient and selective photodynamic therapy against hypoxic tumor cells, J. Am. Chem. Soc. 137 (2015) 1539–1547. https://doi.org/10.1021/ja511420n.

[113] X. Cheng, L. He, J. Xu, Q. Fang, L. Yang, Y. Xue, X. Wang, R. Tang, Oxygen-producing catalase-based prodrug nanoparticles overcoming resistance in hypoxia-mediated chemo-photodynamic therapy, Acta Biomater. 112 (2020) 234–249. https://doi.org/10.1016/j.actbio.2020.05.035.

[114] H. Chen, C. He, T. Chen, X. Xue, New strategy for precise cancer therapy: Tumor-specific delivery of mitochondria-targeting photodynamic therapy agents and: In situ O2-generation in hypoxic tumors, Biomater. Sci. 8 (2020) 3994–4002. https://doi.org/10.1039/d0bm00500b.

[115] J. Liu, T. Liu, P. Du, L. Zhang, J. Lei, Metal–Organic Framework (MOF) Hybrid as a Tandem Catalyst for Enhanced Therapy against Hypoxic Tumor Cells, Angew. Chemie - Int. Ed. 58 (2019) 7808–7812. https://doi.org/10.1002/anie.201903475.

[116] C. Shi, M. Li, Z. Zhang, Q. Yao, K. Shao, F. Xu, N. Xu, H. Li, J. Fan, W. Sun, J. Du, S. Long, J. Wang, X. Peng, Catalase-based liposomal for reversing immunosuppressive tumor microenvironment and enhanced cancer chemo-photodynamic therapy, Biomaterials. 233 (2020) 119755. https://doi.org/10.1016/j.biomaterials.2020.119755.

[117] Y. Lin, J. Ren, X. Qu, Catalytically active nanomaterials: A promising candidate for artificial enzymes, Acc. Chem. Res. 47 (2014) 1097–1105. https://doi.org/10.1021/ar400250z.

[118] X. Lian, Y. Fang, E. Joseph, Q. Wang, J. Li, S. Banerjee, C. Lollar, X. Wang, H.C. Zhou, Enzyme-MOF (metal-organic framework) composites, Chem. Soc. Rev. 46 (2017) 3386–3401. https://doi.org/10.1039/c7cs00058h.

[119] W. Luo, C. Zhu, S. Su, D. Li, Y. He, Q. Huang, C. Fan, Self-catalyzed, self-limiting growth of glucose oxidase-mimicking gold nanoparticles, ACS Nano. 4 (2010) 7451–7458. https://doi.org/10.1021/nn102592h.

[120] G.L. Wang, L.Y. Jin, Y.M. Dong, X.M. Wu, Z.J. Li, Intrinsic enzyme mimicking activity of gold nanoclusters upon visible light triggering and its application for colorimetric trypsin detection, Biosens. Bioelectron. 64 (2015) 523–529. https://doi.org/10.1016/j.bios.2014.09.071.

[121] C.L. Hsu, C.W. Lien, C.W. Wang, S.G. Harroun, C.C. Huang, H.T. Chang, Immobilization of aptamer-modified gold nanoparticles on BiOCl nanosheets: Tunable peroxidase-like activity by protein recognition, Biosens. Bioelectron. 75 (2016) 181–187. https://doi.org/10.1016/j.bios.2015.08.049.

[122] W. Zhen, Y. Liu, L. Lin, J. Bai, X. Jia, H. Tian, X. Jiang, BSA-IrO2: Catalase-like Nanoparticles with High Photothermal Conversion Efficiency and a High X-ray Absorption Coefficient for Anti-inflammation and Antitumor Theranostics, Angew. Chemie - Int. Ed. 57 (2018) 10309–10313. https://doi.org/10.1002/anie.201804466.

[123] F. Wang, E. Ju, Y. Guan, J. Ren, X. Qu, Light-Mediated Reversible Modulation of ROS Level in Living Cells by Using an Activity-Controllable Nanozyme, Small. 13 (2017). https://doi.org/10.1002/smll.201603051.

[124] M. Liang, X. Yan, Nanozymes: From New Concepts, Mechanisms, and Standards to Applications, Acc. Chem. Res. 52 (2019) 2190–2200. https://doi.org/10.1021/acs.accounts.9b00140.

[125] W. Fan, W. Bu, B. Shen, Q. He, Z. Cui, Y. Liu, X. Zheng, K. Zhao, J. Shi, Intelligent MnO2 Nanosheets Anchored with Upconversion Nanoprobes for Concurrent pH-/H2O2-Responsive UCL Imaging and Oxygen-Elevated Synergetic Therapy, Adv. Mater. 27 (2015) 4155–4161. https://doi.org/10.1002/adma.201405141.

[126] P. Kannan, G. Maduraiveeran, Bimetallic Nanomaterials-Based Electrochemical Biosensor Platforms for Clinical Applications, Micromachines. 13 (2022) 76. https://doi.org/10.3390/mi13010076.

[127] M. Solís, A. Solís, H.I. Pérez, N. Manjarrez, M. Flores, Microbial decolouration of azo dyes: A review, Process Biochem. 47 (2012) 1723–1748. https://doi.org/10.1016/j.procbio.2012.08.014.

[128] Y.M. Slokar, A. Majcen Le Marechal, Methods of decoloration of textile wastewaters, Dye. Pigment. 37 (1998) 335–356. https://doi.org/10.1016/S0143-7208(97)00075-2.

[129] C. Galindo, P. Jacques, A. Kalt, Photooxidation of the phenylazonaphthol AO20 on TIO2: Kinetic and mechanistic investigations, Chemosphere. 45 (2001) 997–1005. https://doi.org/10.1016/S0045-6535(01)00118-7.

[130] P.J. Mafa, A.T. Kuvarega, B.B. Mamba, B. Ntsendwana, Photoelectrocatalytic degradation of sulfamethoxazole on g-C 3 N 4 /BiOI/EG p-n heterojunction photoanode under visible light irradiation, Appl. Surf. Sci. 483 (2019) 506–520. https://doi.org/10.1016/j.apsusc.2019.03.281.

[131] M.G. Peleyeju, O.A. Arotiba, Recent trend in visible-light photoelectrocatalytic systems for degradation of organic contaminants in water/wastewater, Environ. Sci. Water Res. Technol. 4 (2018) 1389–1411. https://doi.org/10.1039/c8ew00276b.

[132] A. Di Paola, M. Bellardita, L. Palmisano, Brookite, the least known TiO2 photocatalyst, Catalysts. 3 (2013) 36–73. https://doi.org/10.3390/catal3010036.

[133] N.A. Ramos-Delgado, L. Hinojosa-Reyes, I.L. Guzman-Mar, M.A. Gracia-Pinilla, A. Hernández-Ramírez, Synthesis by sol-gel of WO3/TiO2 for solar photocatalytic degradation of

malathion pesticide, Catal. Today. 209 (2013) 35–40. https://doi.org/10.1016/j.cattod.2012.11.011.

[134] S. Yamazaki, K. Kozasa, K. Okimura, K. Honda, Visible light responsive TiO2photocatalysts for degradation of indoor acetaldehyde, RSC Adv. 10 (2020) 41393–41402. https://doi.org/10.1039/d0ra07567a.

[135] A.A. Murashkina, P.D. Murzin, A. V. Rudakova, V.K. Ryabchuk, A. V. Emeline, D.W. Bahnemann, Influence of the Dopant Concentration on the Photocatalytic Activity: Al-Doped TiO2, J. Phys. Chem. C. 119 (2015) 24695–24703. https://doi.org/10.1021/acs.jpcc.5b06252.

[136] J.C. Kim, J. Choi, Y.B. Lee, J.H. Hong, J.I. Lee, J.W. Yang, W.I. Lee, N.H. Hur, Enhanced photocatalytic activity in composites of TiO2 nanotubes and CdS nanoparticles, Chem. Commun. (2006) 5024–5026. https://doi.org/10.1039/b612572g.

[137] D.R. Pernik, K. Tvrdy, J.G. Radich, P. V. Kamat, Tracking the adsorption and electron injection rates of CdSe quantum dots on TiO2: Linked versus direct attachment, J. Phys. Chem. C. 115 (2011) 13511–13519. https://doi.org/10.1021/jp203055d.

[138] C. Liu, Y. Li, Q. Duan, Preparation of magnetic and thermal dual-responsive zinc-tetracarboxyl-phthalocyanine-g-Fe3O4@SiO2@TiO2-g-poly(N-isopropyl acrylamide) core-shell green photocatalyst, Appl. Surf. Sci. 503 (2020). https://doi.org/10.1016/j.apsusc.2019.144111.

[139] A.E.H. Machado, M.D. França, V. Velani, G.A. Magnino, H.M.M. Velani, F.S. Freitas, P.S. Müller, C. Sattler, M. Schmücker, Characterization and Evaluation of the Efficiency of TiO 2 /Zinc Phthalocyanine Nanocomposites as Photocatalysts for Wastewater Treatment Using Solar Irradiation, Int. J. Photoenergy. 2008 (2008). https://doi.org/10.1155/2008/482373.

[140] K.P. Priyanka, S. Sankararaman, K.M. Balakrishna, T. Varghese, Enhanced visible light photocatalysis using TiO2/phthalocyanine nanocomposites for the degradation of selected industrial dyes, J. Alloys Compd. 720 (2017) 541–549. https://doi.org/10.1016/j.jallcom.2017.05.308.

[141] J.D. Huang, Y.F. Zhang, J.Q. Li, Ab initio study on some metal phthalocyanines, Jiegou Huaxue. 21 (2002) 214–217.

[142] J.O. Morley, M.H. Charlton, Theoretical investigation of the structure and spectra of zinc phthalocyanines, J. Phys. Chem. 99 (1995) 1928–1934. https://doi.org/10.1021/j100007a023.

[143] E. Vargas, R. Vargas, O. Núñez, A TiO2 surface modified with copper(II) phthalocyanine-tetrasulfonic acid tetrasodium salt as a catalyst during photoinduced dichlorvos mineralization by visible solar light, Appl. Catal. B Environ. 156–157 (2014) 8–14. https://doi.org/10.1016/j.apcatb.2014.02.045.

[144] A. Ebrahimian, M.A. Zanjanchi, H. Noei, M. Arvand, Y. Wang, TiO2 nanoparticles containing sulphonated cobalt phthalocyanine: Preparation, characterization and photocatalytic performance, J. Environ. Chem. Eng. 2 (2014) 484–494. https://doi.org/10.1016/j.jece.2014.01.022.

[145] İ. Altın, M. Sökmen, Z. Bıyıklıoğlu, Quaternized zinc(II) phthalocyanine-sensitized TiO2: surfactant-modified sol–gel synthesis, characterization and photocatalytic applications, Desalin. Water Treat. 57 (2016) 16196–16207. https://doi.org/10.1080/19443994.2015.1084535.

[146] Y. Liu, Synthesis of iron(III) tetracarboxyl-phthalocyauine sensitized nano TiO2 composite as photoelectrochemical hydroquinone sensor, Int. J. Electrochem. Sci. 15 (2020) 7575–7584. https://doi.org/10.20964/2020.08.29.

[147] J. Zheng, X. Li, Y. Qin, S. Zhang, M. Sun, X. Duan, H. Sun, P. Li, S. Wang, Zn phthalocyanine/carbon nitride heterojunction for visible light photoelectrocatalytic conversion of CO2 to methanol, J. Catal. 371 (2019) 214–223. https://doi.org/10.1016/j.jcat.2019.01.022.

[148] Y. Kawashima, K. Ohkubo, V.M. Blas-Ferrando, H. Sakai, E. Font-Sanchis, J. Ortíz, F. Fernández-Lázaro, T. Hasobe, Á. Sastre-Santos, S. Fukuzumi, Near-Infrared Photoelectrochemical Conversion via Photoinduced Charge Separation in Supramolecular Complexes of Anionic Phthalocyanines with Li+@C60, J. Phys. Chem. B. 119 (2015) 7690–7697. https://doi.org/10.1021/jp5123163.

[149] Q. Sun, Y. Xu, Sensitization of tiO2with aluminum phthalocyanine: factors influencing the efficiency for chlorophenol degradation in water under visible light, J. Phys. Chem. C. 113 (2009) 12387–12394. https://doi.org/10.1021/jp9016882.

[150] M. Wu, K. Fu, H. Deng, J. Shi, Cobalt tetracarboxyl phthalocyanine-manganese octahedral molecular sieve (OMS-2) as a heterogeneous catalyst of peroxymonosulfate for degradation of diclofenac, Chemosphere. 219 (2019) 756–765. https://doi.org/10.1016/j.chemosphere.2018.12.030.

[151] W. Minhui, S. Jun, D. Chao, D. Huiping, Binuclear cobalt phthalocyanine supported on manganese octahedral molecular sieve: High-efficiency catalyzer of peroxymonosulfate decomposition for degrading propranolol, Sci. Total Environ. 686 (2019) 97–106. https://doi.org/10.1016/j.scitotenv.2019.05.474.

[152] E. Roduner, Size matters: Why nanomaterials are different, Chem. Soc. Rev. 35 (2006) 583–592. https://doi.org/10.1039/b502142c.

[153] J. Peng, W. Gao, B.K. Gupta, Z. Liu, R. Romero-Aburto, L. Ge, L. Song, L.B. Alemany, X. Zhan, G. Gao, S.A. Vithayathil, B.A. Kaipparettu, A.A. Marti, T. Hayashi, J.J. Zhu, P.M. Ajayan, Graphene quantum dots derived from carbon fibers, Nano Lett. 12 (2012) 844–849. https://doi.org/10.1021/nl2038979.

[154] D. Pan, C. Xi, Z. Li, L. Wang, Z. Chen, B. Lu, M. Wu, Electrophoretic fabrication of highly robust, efficient, and benign heterojunction photoelectrocatalysts based on graphene-quantum-dot sensitized TiO2 nanotube arrays, J. Mater. Chem. A. 1 (2013) 3551–3555. https://doi.org/10.1039/c3ta00059a.

[155] X. Yan, X. Cui, B. Li, L.S. Li, Large, solution-processable graphene quantum dots as light absorbers for photovoltaics, Nano Lett. 10 (2010) 1869–1873. https://doi.org/10.1021/nl101060h.

[156] J. Zhao, G. Chen, L. Zhu, G. Li, Graphene quantum dots-based platform for the fabrication of electrochemical biosensors, Electrochem. Commun. 13 (2011) 31–33. https://doi.org/10.1016/j.elecom.2010.11.005.

[157] H. Razmi, R. Mohammad-Rezaei, Graphene quantum dots as a new substrate for immobilization and direct electrochemistry of glucose oxidase: Application to sensitive glucose determination, Biosens. Bioelectron. 41 (2013) 498–504. https://doi.org/10.1016/j.bios.2012.09.009.

[158] D. Du, K. Wang, Y. Wen, Y. Li, Y.Y. Li, Photodynamic Graphene Quantum Dot: Reduction Condition Regulated Photoactivity and Size Dependent Efficacy, ACS Appl. Mater. Interfaces. 8 (2016) 3287–3294. https://doi.org/10.1021/acsami.5b11154.

[159] F. Wo, R. Xu, Y. Shao, Z. Zhang, M. Chu, D. Shi, S. Liu, A multimodal system with synergistic effects of magneto-mechanical, photothermal, photodynamic and chemo therapies of

cancer in graphene-quantum dot-coated hollow magnetic nanospheres, Theranostics. 6 (2016) 485–500. https://doi.org/10.7150/thno.13411.

[160] S. Stankovich, D.A. Dikin, R.D. Piner, K.A. Kohlhaas, A. Kleinhammes, Y. Jia, Y. Wu, S.B.T. Nguyen, R.S. Ruoff, Synthesis of graphene-based nanosheets via chemical reduction of exfoliated graphite oxide, Carbon N. Y. 45 (2007) 1558–1565. https://doi.org/10.1016/j.carbon.2007.02.034.

[161] J.S. Yeo, R. Kang, S. Lee, Y.J. Jeon, N.S. Myoung, C.L. Lee, D.Y. Kim, J.M. Yun, Y.H. Seo, S.S. Kim, S.I. Na, Highly efficient and stable planar perovskite solar cells with reduced graphene oxide nanosheets as electrode interlayer, Nano Energy. 12 (2015) 96–104. https://doi.org/10.1016/j.nanoen.2014.12.022.

[162] R. Eivazzadeh-Keihan, R. Taheri-Ledari, N. Khosropour, S. Dalvand, A. Maleki, S.M. Mousavi-Khoshdel, H. Sohrabi, Fe3O4/GO@melamine-ZnO nanocomposite: A promising versatile tool for organic catalysis and electrical capacitance, Colloids Surfaces A Physicochem. Eng. Asp. 587 (2020) 124335. https://doi.org/10.1016/j.colsurfa.2019.124335.

[163] X. Zhang, X. Sun, H. Zhang, D. Zhang, Y. Ma, Microwave-assisted reflux rapid synthesis of MnO2 nanostructures and their application in supercapacitors, Electrochim. Acta. 87 (2013) 637–644. https://doi.org/10.1016/j.electacta.2012.10.022.

[164] L. Tian, Q. Chen, X. Yi, J. Chen, C. Liang, Y. Chao, K. Yang, Z. Liu, Albumin-Templated Manganese Dioxide Nanoparticles for Enhanced Radioisotope Therapy, Small. 13 (2017) 1700640. https://doi.org/10.1002/smll.201700640.

[165] T.N. Lambert, J.A. Vigil, S.E. White, C.J. Delker, D.J. Davis, M. Kelly, M.T. Brumbach, M.A. Rodriguez, B.S. Swartzentruber, Understanding the Effects of Cationic Dopants on α-MnO2

Oxygen Reduction Reaction Electrocatalysis, J. Phys. Chem. C. 121 (2017) 2789–2797. https://doi.org/10.1021/acs.jpcc.6b11252.

[166] W. Zhu, Z. Dong, T. Fu, J. Liu, Q. Chen, Y. Li, R. Zhu, L. Xu, Z. Liu, Modulation of Hypoxia in Solid Tumor Microenvironment with MnO2 Nanoparticles to Enhance Photodynamic Therapy, Adv. Funct. Mater. 26 (2016) 5490–5498. https://doi.org/10.1002/adfm.201600676.

[167] Y. Tao, L. Zhu, Y. Zhao, X. Yi, L. Zhu, F. Ge, X. Mou, L. Chen, L. Sun, K. Yang, Nano-graphene oxide-manganese dioxide nanocomposites for overcoming tumor hypoxia and enhancing cancer radioisotope therapy, Nanoscale. 10 (2018) 5114–5123. https://doi.org/10.1039/c7nr08747k.

[168] J. Liu, L. Meng, Z. Fei, P.J. Dyson, L. Zhang, On the origin of the synergy between the Pt nanoparticles and MnO2 nanosheets in Wonton-like 3D nanozyme oxidase mimics, Biosens. Bioelectron. 121 (2018) 159–165. https://doi.org/10.1016/j.bios.2018.08.004.

[169] B. Duncan, C. Kim, V.M. Rotello, Gold nanoparticle platforms as drug and biomacromolecule delivery systems, J. Control. Release. 148 (2010) 122–127. https://doi.org/10.1016/j.jconrel.2010.06.004.

[170] A. El-Hussein, I. Mfouo-Tynga, M. Abdel-Harith, H. Abrahamse, Comparative study between the photodynamic ability of gold and silver nanoparticles in mediating cell death in breast and lung cancer cell lines, J. Photochem. Photobiol. B Biol. 153 (2015) 67–75. https://doi.org/10.1016/j.jphotobiol.2015.08.028.

[171] J. Yu, X. He, Z. Wang, S. Liu, D. Hao, X. Li, Y. Huang, Combination of starvation therapy and Pt-NP based chemotherapy for synergistic cancer treatment, J. Mater. Chem. B. 9 (2021) 6406–6411. https://doi.org/10.1039/d1tb01222c.

[172] Z. Bao, M. He, H. Quan, D. Jiang, Y. Zheng, W. Qin, Y. Zhou, F. Ren, M. Guo, C. Jiang, FePt nanoparticles: A novel nanoprobe for enhanced HeLa cells sensitivity to chemoradiotherapy, RSC Adv. 6 (2016) 35124–35134. https://doi.org/10.1039/c6ra03990a.

[173] L. Fan, X. Ji, G. Lin, K. Liu, S. Chen, G. Ma, W. Xue, X. Zhang, L. Wang, Green synthesis of stable platinum nanoclusters with enhanced peroxidase-like activity for sensitive detection of glucose and glutathione, Microchem. J. 166 (2021) 106202. https://doi.org/10.1016/j.microc.2021.106202.

[174] H. Wei, E. Wang, Nanomaterials with enzyme-like characteristics (nanozymes): Next-generation artificial enzymes, Chem. Soc. Rev. 42 (2013) 6060–6093. https://doi.org/10.1039/c3cs35486e.

[175] B. Liu, J. Liu, Surface modification of nanozymes, Nano Res. 10 (2017) 1125–1148. https://doi.org/10.1007/s12274-017-1426-5.

[176] M. Zhang, T. Chen, Y. Wang, Insights into TiO2 polymorphs: Highly selective synthesis, phase transition, and their polymorph-dependent properties, RSC Adv. 7 (2017) 52755–52761. https://doi.org/10.1039/c7ra11515f.

[177] A. Jabłoński, Über den Mechanismus der Photolumineszenz von Farbstoffphosphoren, Zeitschrift Für Phys. 94 (1935) 38–46. https://doi.org/10.1007/BF01330795.

[178] S. Fery-Forgues, D. Lavabre, Are fluorescence quantum yields so tricky to measure? A demonstration using familiar stationery products, J. Chem. Educ. 76 (1999) 1260–1264. https://doi.org/10.1021/ed076p1260.

[179] A.M. Brouwer, Standards for photoluminescence quantum yield measurements in solution (IUPAC technical report), Pure Appl. Chem. 83 (2011) 2213–2228. https://doi.org/10.1351/PAC-REP-10-09-31.

[180] J.W. Boag, Techniques of Flash Photolysis, Photochem. Photobiol. 8 (1968) 565–577. https://doi.org/10.1111/j.1751-1097.1968.tb05899.x.

[181] T.H. Tran-Thi, C. Desforge, C. Thiec, S. Gaspard, Singlet-singlet and triplet-triplet intramolecular transfer processes in a covalently linked porphyrin-phthalocyanine heterodimer, J. Phys. Chem. 93 (1989) 1226–1233. https://doi.org/10.1021/j100341a013.

[182] A. Nas, H. Kantekin, A. Koca, Novel 4-(2-(benzo[d]thiazol-2-yl)phenoxy) substituted phthalocyanine derivatives: Synthesis, electrochemical and in situ spectroelectrochemical characterization, J. Organomet. Chem. 757 (2014) 62–71. https://doi.org/10.1016/j.jorganchem.2014.01.012.

[183] Z. Huang, L. Huang, Y. Huang, Y. He, X. Sun, X. Fu, X. Xu, G. Wei, D. Chen, C. Zhao, Phthalocyanine-based coordination polymer nanoparticles for enhanced photodynamic therapy, Nanoscale. 9 (2017) 15883–15894. https://doi.org/10.1039/c7nr05402e.

[184] S. Mgidlana, P. Sen, T. Nyokong, Photodegradation of tetracycline by asymmetrical zinc(II)phthalocyanines conjugated to cobalt tungstate nanoparticles, J. Mol. Struct. 1261 (2022) 132938. https://doi.org/10.1016/j.molstruc.2022.132938.

[185] N. Nwahara, R. Nkhahle, B.P. Ngoy, J. Mack, T. Nyokong, Synthesis and photophysical properties of BODIPY-decorated graphene quantum dot-phthalocyanine conjugates, New J. Chem. 42 (2018). https://doi.org/10.1039/c8nj00758f.

[186] O.J. Achadu, I. Uddin, T. Nyokong, The interaction between graphene quantum dots grafted with polyethyleneimine and Au@Ag nanoparticles: Application as a fluorescence “turn-on” nanoprobe, J. Photochem. Photobiol. A Chem. 324 (2016) 96–105. https://doi.org/10.1016/j.jphotochem.2016.03.016.

[187] G.Y. Atmaca, C. Dizman, T. Eren, A. Erdoɨmuş, Novel axially carborane-cage substituted silicon phthalocyanine photosensitizer; Synthesis, characterization and photophysicochemical properties, Spectrochim. Acta - Part A Mol. Biomol. Spectrosc. 137 (2015) 244–249. https://doi.org/10.1016/j.saa.2014.08.035.

[188] Y. Liang, C. Li, S. Li, B. Su, M.Z. Hu, X. Gao, C. Gao, Graphene quantum dots (GQDs)-polyethyleneimine as interlayer for the fabrication of high performance organic solvent nanofiltration (OSN) membranes, Chem. Eng. J. 380 (2020) 122462. https://doi.org/10.1016/j.cej.2019.122462.

[189] C. Wang, Z. Xu, C. Zhang, Polyethyleneimine-Functionalized Fluorescent Carbon Dots: Water Stability, pH Sensing, and Cellular Imaging, Chem. Nano Mat. 1 (2015) 122–127. https://doi.org/10.1002/cnma.201500009.

[190] S.N. Alam, N. Sharma, L. Kumar, Synthesis of Graphene Oxide (GO) by Modified Hummers Method and Its Thermal Reduction to Obtain Reduced Graphene Oxide (rGO)*, Graphene. 06 (2017) 1–18. https://doi.org/10.4236/graphene.2017.61001.

[191] H. Elsana, T.O.B. Olusanya, J. Carr-wilkinson, S. Darby, A. Faheem, A.A. Elkordy, Evaluation of novel cationic gene based liposomes with cyclodextrin prepared by thin film hydration and microfluidic systems, Sci. Rep. 9 (2019) 15120. https://doi.org/10.1038/s41598-019-51065-4.

[192] M. Miroshnikov, K. Kato, G. Babu, K.P. Divya, L.M. Reddy Arava, P.M. Ajayan, G. John, A common tattoo chemical for energy storage: Henna plant-derived naphthoquinone dimer as a green and sustainable cathode material for Li-ion batteries, RSC Adv. 8 (2018) 1576–1582. https://doi.org/10.1039/c7ra12357d.

[193] Z. Huang, H. Chen, L. Zhao, W. Fang, X. He, W. Li, P. Tian, In suit inducing electron-donating and electron-withdrawing groups in carbon nitride by one-step NH4Cl-assisted route: A strategy for high solar hydrogen production efficiency, Environ. Int. 126 (2019) 289–297. https://doi.org/10.1016/j.envint.2019.02.030.

[194] D. Jiang, Y. Chen, N. Li, W. Li, Z. Wang, J. Zhu, H. Zhang, B. Liu, S. Xu, Synthesis of luminescent graphene quantum dots with high quantum yield and their toxicity study, PLoS One. 10 (2015) e0144906. https://doi.org/10.1371/journal.pone.0144906.

[195] O.K. Adeniyi, P.N. Mashazi, Stable thin films of human P53 antigen on gold surface for the detection of tumour associated anti-P53 autoantibodies, Electrochim. Acta. 331 (2020) 135272. https://doi.org/10.1016/j.electacta.2019.135272.

[196] J.Y.Y. Loh, N.P. Kherani, X-ray photospectroscopy and electronic studies of reactor parameters on photocatalytic hydrogenation of carbon dioxide by defect-laden indium oxide hydroxide nanorods, Molecules. 24 (2019) 3818. https://doi.org/10.3390/molecules24213818.

[197] A.K. Pal, S. Varghese, D.B. Cordes, A.M.Z. Slawin, I.D.W. Samuel, E. Zysman-Colman, Near-Infrared Fluorescence of Silicon Phthalocyanine Carboxylate Esters, Sci. Rep. 7 (2017) 12282. https://doi.org/10.1038/s41598-017-12374-8.

[198] Y.Y. Zhao, J.Y. Chen, J.Q. Hu, L. Zhang, A.L. Lin, R. Wang, B.Y. Zheng, M.R. Ke, X. Li, J.D. Huang, The substituted zinc(II) phthalocyanines using “sulfur bridge” as the linkages.

Synthesis, red-shifted spectroscopic properties and structure-inherent targeted photodynamic activities, Dye. Pigment. 189 (2021) 109270. https://doi.org/10.1016/j.dyepig.2021.109270.

[199] A.G. Martynov, J. Mack, A.K. May, T. Nyokong, Y.G. Gorbunova, A.Y. Tsivadze, Methodological Survey of Simplified TD-DFT Methods for Fast and Accurate Interpretation of UV-Vis-NIR Spectra of Phthalocyanines, ACS Omega. 4 (2019) 7265–7284. https://doi.org/10.1021/acsomega.8b03500.

[200] J. Mack, M.J. Stillman, Photochemical Formation of the Anion Radical of Zinc Phthalocyanine and Analysis of the Absorption and Magnetic Circular Dichroism Spectral Data. Assignment of the Optical Spectrum of [ZnPc(-3)]-, J. Am. Chem. Soc. 116 (1994) 1292–1304. https://doi.org/10.1021/ja00083a015.

[201] M. Oku, K. Hirokawa, S. Ikeda, X-ray photoelectron spectroscopy of manganese-oxygen systems, J. Electron Spectros. Relat. Phenomena. 7 (1975) 465–473. https://doi.org/10.1016/0368-2048(75)85010-9.

[202] F. Zeng, Y. Pan, Y. Yang, Q. Li, G. Li, Z. Hou, G. Gu, Facile construction of Mn3O4-MnO2 hetero-nanorods/graphene nanocomposite for highly sensitive electrochemical detection of hydrogen peroxide, Electrochim. Acta. 196 (2016) 587–596. https://doi.org/10.1016/j.electacta.2016.03.031.

[203] C. Wang, H. Daimon, S. Sun, Dumbbell-like Pt - Fe 3O 4 nanoparticles and their enhanced catalysis for oxygen reduction reaction, Nano Lett. 9 (2009) 1493–1496. https://doi.org/10.1021/nl8034724.

[204] W. Yuan, Y. Zhang, N. Zhang, C. Yin, X. Zhang, X. Liu, Carbon riveted Pt-MnO2/reduced graphene oxide anode catalyst for DMFC, Catal. Commun. 100 (2017) 66–70. https://doi.org/10.1016/j.catcom.2017.06.030.

[205] Y. Zhu, C. Su, X. Xu, W. Zhou, R. Ran, Z. Shao, A universal and facile way for the development of superior bifunctional electrocatalysts for oxygen reduction and evolution reactions utilizing the synergistic effect, Chem. - A Eur. J. 20 (2014) 15533–15542. https://doi.org/10.1002/chem.201403192.

[206] R. Ye, C. Xiang, J. Lin, Z. Peng, K. Huang, Z. Yan, N.P. Cook, E.L.G. Samuel, C.C. Hwang, G. Ruan, G. Ceriotti, A.R.O. Raji, A.A. Martí, J.M. Tour, Coal as an abundant source of graphene quantum dots, Nat. Commun. 4 (2013) 2943. https://doi.org/10.1038/ncomms3943.

[207] A. Chakravarty, D. Sengupta, B. Basu, A. Mukherjee, G. De, MnO2 nanowires anchored on amine functionalized graphite nanosheets: Highly active and reusable catalyst for organic oxidation reactions, RSC Adv. 5 (2015) 92585–92595. https://doi.org/10.1039/c5ra17777d.

[208] B. Varnholt, P. Oulevey, S. Luber, C. Kumara, A. Dass, T. Bürgi, Structural information on the Au-S interface of thiolate-protected gold clusters: A raman spectroscopy study, J. Phys. Chem. C. 118 (2014) 9604–9611. https://doi.org/10.1021/jp502453q.

[209] S. Liang, F. Teng, G. Bulgan, R. Zong, Y. Zhu, Effect of phase structure of MnO2 nanorod catalyst on the activity for CO oxidation, J. Phys. Chem. C. 112 (2008) 5307–5315. https://doi.org/10.1021/jp0774995.

[210] S.J. Abbas, P.V.R.K. Ramacharyulu, S.C. Ke, MnO2/TiO2 catalyzed synthesis of coenzyme pyridoxamine-5′-phosphate analogues: 3-deoxypyridoxamine-5′-phosphate, RSC Adv. 6 (2016) 10242–10248. https://doi.org/10.1039/c5ra25779d.

[211] R. Prabakaran, R. Kesavamoorthy, G.L.N. Reddy, F.P. Xavier, Structural investigation of copper phthalocyanine thin films using X-ray diffraction, Raman scattering and optical absorption measurements, Phys. Status Solidi Basic Res. 229 (2002) 1175–1186. https://doi.org/10.1002/1521-3951(200202)229:3<1175::AID-PSSB1175>3.0.CO;2-K.

[212] M. Zhang, L. Bai, W. Shang, W. Xie, H. Ma, Y. Fu, D. Fang, H. Sun, L. Fan, M. Han, C. Liu, S. Yang, Facile synthesis of water-soluble, highly fluorescent graphene quantum dots as a robust biological label for stem cells, J. Mater. Chem. 22 (2012) 7461–7467. https://doi.org/10.1039/c2jm16835a.

[213] I. Uddin, P. Poddar, N. Phogat, Novel Green Hemoglobin-Mediated Biosynthesis of Gold Nanoparticles, Mater. Focus. 2 (2013) 80–85. https://doi.org/10.1166/mat.2013.1055.

[214] A. Xu, P. He, T. Huang, J. Li, X. Hu, P. Xiang, D. Chen, S. Yang, G. Wang, G. Ding, Selective supramolecular interaction of ethylenediamine functionalized graphene quantum dots: Ultra-sensitive photoluminescence detection for nickel ion in vitro, Synth. Met. 244 (2018) 106–112. https://doi.org/10.1016/j.synthmet.2018.05.013.

[215] J. Ederer, P. Janoš, P. Ecorchard, J. Tolasz, V. Štengl, H. Beneš, M. Perchacz, O. Pop-Georgievski, Determination of amino groups on functionalized graphene oxide for polyurethane nanomaterials: XPS quantitation vs. functional speciation, RSC Adv. 7 (2017) 12464–12473. https://doi.org/10.1039/c6ra28745j.

[216] O.M. Bankole, O.J. Achadu, T. Nyokong, Nonlinear Interactions of Zinc Phthalocyanine-Graphene Quantum Dots Nanocomposites: Investigation of Effects of Surface Functionalization with Heteroatoms, J. Fluoresc. 27 (2017) 755–766. https://doi.org/10.1007/s10895-016-2008-8.

[217] L. Bin Zhao, R. Huang, M.X. Bai, D.Y. Wu, Z.Q. Tian, Effect of aromatic amine-metal interaction on surface vibrational Raman spectroscopy of adsorbed molecules investigated by density functional theory, J. Phys. Chem. C. 115 (2011) 4174–4183. https://doi.org/10.1021/jp1117135.

[218] A. Adenier, M.M. Chehimi, I. Gallardo, J. Pinson, N. Vilà, Electrochemical oxidation of aliphatic amines and their attachment to carbon and metal surfaces, Langmuir. 20 (2004) 8243–8253. https://doi.org/10.1021/la049194c.

[219] P. Yuan, Z. Ruan, W. Jiang, L. Liu, J. Dou, T. Li, L. Yan, Oxygen self-sufficient fluorinated polypeptide nanoparticles for NIR imaging-guided enhanced photodynamic therapy, J. Mater. Chem. B. 6 (2018) 2323–2331. https://doi.org/10.1039/c8tb00493e.

[220] P. Decuzzi, B. Godin, T. Tanaka, S.Y. Lee, C. Chiappini, X. Liu, M. Ferrari, Size and shape effects in the biodistribution of intravascularly injected particles, J. Control. Release. 141 (2010) 320–327. https://doi.org/10.1016/j.jconrel.2009.10.014.

[221] A. Salvati, S. Ristori, D. Pietrangeli, J. Oberdisse, L. Calamai, G. Martini, G. Ricciardi, Insertion of a magnesium(II)-octacarboranyl(hexylsulfanyl) porphyrazine into liposomes: A physico-chemical study, Biophys. Chem. 131 (2007) 43–51. https://doi.org/10.1016/j.bpc.2007.09.002.

[222] O. Taratula, O.B. Garbuzenko, A.M. Chen, T. Minko, Innovative strategy for treatment of lung cancer: Targeted nanotechnology-based inhalation co-delivery of anticancer drugs and siRNA, J. Drug Target. 19 (2011) 900–914. https://doi.org/10.3109/1061186X.2011.622404.

[223] R.B. Campbell, D. Fukumura, E.B. Brown, L.M. Mazzola, Y. Izumi, R.K. Jain, V.P. Torchilin, L.L. Munn, Cationic charge determines the distribution of liposomes between the vascular and extravascular compartments of tumors, Cancer Res. 62 (2002) 6831–6836.

[224] H. Wu, L. Zhu, V.P. Torchilin, PH-sensitive poly(histidine)-PEG/DSPE-PEG co-polymer micelles for cytosolic drug delivery, Biomaterials. 34 (2013) 1213–1222. https://doi.org/10.1016/j.biomaterials.2012.08.072.

[225] L.S. Hernández-Muñoz, M. Gómez, F.J. González, I. González, C. Frontana, Towards a molecular-level understanding of the reactivity differences for radical anions of juglone and plumbagin: An electrochemical and spectroelectrochemical approach, Org. Biomol. Chem. 7 (2009) 1896–1903. https://doi.org/10.1039/b822684a.

[226] Y.M. Hijji, B. Barare, Y. Zhang, Lawsone (2-hydroxy-1,4-naphthoquinone) as a sensitive cyanide and acetate sensor, Sensors Actuators, B Chem. 169 (2012) 106–112. https://doi.org/10.1016/j.snb.2012.03.067.

[227] J. Michl, Magnetic circular dichroism of aromatic molecules, Tetrahedron. 40 (1984) 3845–3934. https://doi.org/10.1016/s0040-4020(01)99999-5.

[228] Z. Biyiklioglu, H. Alp, Electropolymerizable peripherally tetra-{2-[3-(diethylamino)phenoxy]ethoxy} substituted as well as axially (4-phenylpiperazin-1-yl)propanoxy-disubstituted silicon phthalocyanines and their electrochemistry, Dalt. Trans. 44 (2015) 18993–18999. https://doi.org/10.1039/c5dt03421c.

[229] A.B.P. Lever, J.P. Wilshire, Redox potentials of metal phthalocyanines in non-aqueous media, Can. J. Chem. 54 (1976) 2514–2516. https://doi.org/10.1139/v76-356.

[230] E.F.F. Silva, C. Serpa, J.M. Dąbrowski, C.J.P. Monteiro, S.J. Formosinho, G. Stochel, K. Urbanska, S. Simões, M.M. Pereira, L.G. Arnaut, Mechanisms of singlet-oxygen and superoxide-ion generation by porphyrins and bacteriochlorins and their implications in photodynamic therapy, Chem. - A Eur. J. 16 (2010) 9273–9286. https://doi.org/10.1002/chem.201000111.

[231] X. Liu, G. Li, M. Xie, S. Guo, W. Zhao, F. Li, S. Liu, Q. Zhao, Rational design of type I photosensitizers based on Ru(ii) complexes for effective photodynamic therapy under hypoxia, Dalt. Trans. 49 (2020) 11192–11200. https://doi.org/10.1039/d0dt01684e.

[232] Z. Lv, H. Wei, Q. Li, X. Su, S. Liu, K.Y. Zhang, W. Lv, Q. Zhao, X. Li, W. Huang, Achieving efficient photodynamic therapy under both normoxia and hypoxia using cyclometalated Ru(II) photosensitizer through type i photochemical process, Chem. Sci. 9 (2018) 502–512. https://doi.org/10.1039/c7sc03765a.

[233] H. Ding, H. Yu, Y. Dong, R. Tian, G. Huang, D.A. Boothman, B.D. Sumer, J. Gao, Photoactivation switch from type II to type i reactions by electron-rich micelles for improved photodynamic therapy of cancer cells under hypoxia, J. Control. Release. 156 (2011) 276–280. https://doi.org/10.1016/j.jconrel.2011.08.019.

[234] M. Gouterman, Optical Spectra and Electronic Structure of Porphyrins and Related Rings, in: The Porphyrins, 1978: pp. 1–165. https://doi.org/10.1016/b978-0-12-220103-5.50008-8.

[235] C. Parisi, M. Failla, A. Fraix, A. Rescifina, B. Rolando, L. Lazzarato, V. Cardile, A.C.E. Graziano, R. Fruttero, A. Gasco, S. Sortino, A molecular hybrid producing simultaneously singlet oxygen and nitric oxide by single photon excitation with green light, Bioorg. Chem. 85 (2019) 18–22. https://doi.org/10.1016/j.bioorg.2018.12.027.

[236] T. Matsumoto, Y. Urano, T. Shoda, H. Kojima, T. Nagano, A thiol-reactive fluorescence probe based on donor-excited photoinduced electron transfer: Key role of ortho substitution, Org. Lett. 9 (2007) 3375–3377. https://doi.org/10.1021/ol071352e.

[237] D. Çakir, M. Göksel, V. Çakir, M. Durmuş, Z. Biyiklioglu, H. Kantekin, Amphiphilic zinc phthalocyanine photosensitizers: Synthesis, photophysicochemical properties and in vitro studies for photodynamic therapy, Dalt. Trans. 44 (2015) 9646–9658. https://doi.org/10.1039/c5dt00747j.

[238] P. Sen, T. Nyokong, A novel axially palladium(II)-Schiff base complex substituted silicon(IV) phthalocyanine: Synthesis, characterization, photophysicochemical properties and photodynamic antimicrobial chemotherapy activity against Staphylococcus aureus, Polyhedron. 173 (2019) 114135. https://doi.org/10.1016/j.poly.2019.114135.

[239] J. Huang, Y. Wu, D. Wang, Y. Ma, Z. Yue, Y. Lu, M. Zhang, Z. Zhang, P. Yang, Silicon phthalocyanine covalently functionalized N-doped ultrasmall reduced graphene oxide decorated with Pt nanoparticles for hydrogen evolution from water, ACS Appl. Mater. Interfaces. 7 (2015) 3732–3741. https://doi.org/10.1021/am508476d.

[240] Z. Wang, J. Zhao, A. Barbon, A. Toffoletti, Y. Liu, Y. An, L. Xu, A. Karatay, H.G. Yaglioglu, E.A. Yildiz, M. Hayvali, Radical-Enhanced Intersystem Crossing in New Bodipy Derivatives and Application for Efficient Triplet-Triplet Annihilation Upconversion, J. Am. Chem. Soc. 139 (2017) 7831–7842. https://doi.org/10.1021/jacs.7b02063.

[241] A. Drzewiecka-Matuszek, A. Kania, A. Karocki, G. Stochel, L. Fiedor, Effects of heavy central metal on the ground and excited states of chlorophyll, J. Biol. Inorg. Chem. 10 (2005) 453–462. https://doi.org/10.1007/s00775-005-0652-6.

[242] İ. Ömeroğlu, E.N. Kaya, M. Göksel, V. Kussovski, V. Mantareva, M. Durmuş, Axially substituted silicon(IV) phthalocyanine and its quaternized derivative as photosensitizers towards tumor cells and bacterial pathogens, Bioorganic Med. Chem. 25 (2017) 5415–5422. https://doi.org/10.1016/j.bmc.2017.07.065.

[243] J. Chen, S. Li, F. Gong, Z. Yang, S. Wang, H. Xu, Y. Li, M. Jin Shi, G. Yang, Photophysics and triplet-triplet annihilation analysis for axially substituted gallium phthalocyanine doped in solid matrix, J. Phys. Chem. C. 113 (2009) 11943–11951. https://doi.org/10.1021/jp902723h.

[244] T.G.B. De Souza, M.G. Vivas, C.R. Mendonça, S. Plunkett, M.A. Filatov, M.O. Senge, L. De Boni, Studying the intersystem crossing rate and triplet quantum yield of meso-substituted porphyrins by means of pulse train fluorescence technique, J. Porphyr. Phthalocyanines. 20 (2016) 282–291. https://doi.org/10.1142/S1088424616500048.

[245] E.I. Sagun, E.I. Zenkevich, V.N. Knyukshto, A.M. Shulga, D.A. Starukhin, C. Von Borczyskowski, Interaction of multiporphyrin systems with molecular oxygen in liquid solutions: Extra-ligation and screening effects, Chem. Phys. 275 (2002) 211–230. https://doi.org/10.1016/S0301-0104(01)00517-1.

[246] Q. Li, R. Ma, M. Zhang, CoCl2 increases the expression of hypoxic markers HIF-1α, VEGF and CXCR4 in breast cancer MCF-7 cells, Oncol. Lett. 15 (2018) 1119–1124. https://doi.org/10.3892/ol.2017.7369.

[247] F. Sonvico, C. Dubernet, V. Marsaud, M. Appel, H. Chacun, B. Stella, M. Renoir, P. Colombo, P. Couvreur, Establishment of an in vitro model expressing the folate receptor for the investigation of targeted delivery systems, J. Drug Deliv. Sci. Technol. 15 (2005) 407–410. https://doi.org/10.1016/s1773-2247(05)50080-7.

[248] F. Sonvico, S. Mornet, S. Vasseur, C. Dubernet, D. Jaillard, J. Degrouard, J. Hoebeke, E. Duguet, P. Colombo, P. Couvreur, Folate-conjugated iron oxide nanoparticles for solid tumor targeting as potential specific magnetic hyperthermia mediators: Synthesis, physicochemical characterization, and in vitro experiments, Bioconjug. Chem. 16 (2005) 1181–1188. https://doi.org/10.1021/bc050050z.

[249] N. Singh, E.S. Aazam, U. Riaz, Synthesis and characterization of lawsone incorporated singlet oxygen generating conjugated polymers: Experimental and computational studies, J. Mol. Struct. 1240 (2021). https://doi.org/10.1016/j.molstruc.2021.130533.

[250] B. Singh, R.S. Patwardhan, S. Jayakumar, D. Sharma, S.K. Sandur, Oxidative stress associated metabolic adaptations regulate radioresistance in human lung cancer cells, J. Photochem. Photobiol. B Biol. 213 (2020) 112080. https://doi.org/10.1016/j.jphotobiol.2020.112080.

[251] T. Zaidieh, J.R. Smith, K.E. Ball, Q. An, ROS as a novel indicator to predict anticancer drug efficacy, BMC Cancer. 19 (2019) 1224. https://doi.org/10.1186/s12885-019-6438-y.

[252] Q. Cui, J.Q. Wang, Y.G. Assaraf, L. Ren, P. Gupta, L. Wei, C.R. Ashby, D.H. Yang, Z.S. Chen, Modulating ROS to overcome multidrug resistance in cancer, Drug Resist. Updat. 41 (2018) 1–25. https://doi.org/10.1016/j.drup.2018.11.001.

[253] J. Guo, J.R. Morris, Y. Ihm, C.I. Contescu, N.C. Gallego, G. Duscher, S.J. Pennycook, M.F. Chisholm, Topological defects: Origin of nanopores and enhanced adsorption performance in nanoporous carbon, Small. 8 (2012) 3283–3288. https://doi.org/10.1002/smll.201200894.

[254] J. Wang, B. Chen, B. Xing, Wrinkles and Folds of Activated Graphene Nanosheets as Fast and Efficient Adsorptive Sites for Hydrophobic Organic Contaminants, Environ. Sci. Technol. 50 (2016) 3798–3808. https://doi.org/10.1021/acs.est.5b04865.

[255] X. Bai, X. Zhang, Z. Hua, W. Ma, Z. Dai, X. Huang, H. Gu, Uniformly distributed anatase TiO2 nanoparticles on graphene: Synthesis, characterization, and photocatalytic application, J. Alloys Compd. 599 (2014) 10–18. https://doi.org/10.1016/j.jallcom.2014.02.049.

[256] Y. Zhang, W. Cui, W. An, L. Liu, Y. Liang, Y. Zhu, Combination of photoelectrocatalysis and adsorption for removal of bisphenol A over TiO2-graphene hydrogel with 3D network structure, Appl. Catal. B Environ. 221 (2018) 36–46. https://doi.org/10.1016/j.apcatb.2017.08.076.

[257] Q. Zhang, N. Bao, X. Wang, X. Hu, X. Miao, M. Chaker, D. Ma, Advanced Fabrication of Chemically Bonded Graphene/TiO2 Continuous Fibers with Enhanced Broadband Photocatalytic Properties and Involved Mechanisms Exploration, Sci. Rep. 6 (2016). https://doi.org/10.1038/srep38066.

[258] H. Rasoulnezhad, G. Hosseinzadeh, R. Hosseinzadeh, N. Ghasemian, Preparation of transparent nanostructured N-doped TiO2 thin films by combination of sonochemical and CVD methods with visible light photocatalytic activity, J. Adv. Ceram. 7 (2018) 185–196. https://doi.org/10.1007/s40145-018-0270-8.

[259] M. Shaban, J. Poostforooshan, A.P. Weber, Surface-initiated polymerization on unmodified inorganic semiconductor nanoparticles: Via surfactant-free aerosol-based synthesis toward core-shell nanohybrids with a tunable shell thickness, J. Mater. Chem. A. 5 (2017) 18651–18663. https://doi.org/10.1039/c7ta04985d.

[260] G. Jiang, Z. Lin, C. Chen, L. Zhu, Q. Chang, N. Wang, W. Wei, H. Tang, TiO2 nanoparticles assembled on graphene oxide nanosheets with high photocatalytic activity for removal of pollutants, Carbon N. Y. 49 (2011) 2693–2701. https://doi.org/10.1016/j.carbon.2011.02.059.

[261] K.M. Reddy, S. V. Manorama, A.R. Reddy, Bandgap studies on anatase titanium dioxide nanoparticles, Mater. Chem. Phys. 78 (2003) 239–245. https://doi.org/10.1016/S0254-0584(02)00343-7.

[262] A. Morais, C. Longo, J.R. Araujo, M. Barroso, J.R. Durrant, A.F. Nogueira, Nanocrystalline anatase TiO2/reduced graphene oxide composite films as photoanodes for photoelectrochemical water splitting studies: The role of reduced graphene oxide, Phys. Chem. Chem. Phys. 18 (2016) 2608–2616. https://doi.org/10.1039/c5cp06707c.

[263] M. Minella, F. Sordello, C. Minero, Photocatalytic process in TiO2/graphene hybrid materials. Evidence of charge separation by electron transfer from reduced graphene oxide to TiO2, Catal. Today. 281 (2017) 29–37. https://doi.org/10.1016/j.cattod.2016.03.040.

[264] M. Khenfouch, O. Bajjou, M. Baïtoul, N. Mongwaketsi, M. Maaza, J. Wery Venturini, Optical properties and dynamics excitation relaxation in reduced graphene oxide functionalized with nanostructured porphyrins, Opt. Mater. (Amst). 42 (2015) 479–483. https://doi.org/10.1016/j.optmat.2015.02.006.

[265] S.R. Kim, I. Ali, J.O. Kim, Phenol degradation using an anodized graphene-doped TiO 2 nanotube composite under visible light, Appl. Surf. Sci. 477 (2019) 71–78. https://doi.org/10.1016/j.apsusc.2017.12.024.

[266] Q. Zou, Z. Zhang, H. Li, W. Pei, M. Ding, Z. Xie, Y. Huo, H. Li, Synergistic removal of organic pollutant and metal ions in photocatalysis-membrane distillation system, Appl. Catal. B Environ. 264 (2020). https://doi.org/10.1016/j.apcatb.2019.118463.

[267] Y. Li, P. Li, J. Wang, Y. Yang, W. Yao, Z. Wei, J. Wu, X. Yan, X. Xu, Y. Liu, Y. Zhu, Water soluble graphitic carbon nitride with tunable fluorescence for boosting broad-response photocatalysis, Appl. Catal. B Environ. 225 (2018) 519–529. https://doi.org/10.1016/j.apcatb.2017.12.017.

[268] B.O. Orimolade, O.A. Arotiba, Towards visible light driven photoelectrocatalysis for water treatment: Application of a FTO/BiVO4/Ag2S heterojunction anode for the removal of emerging pharmaceutical pollutants, Sci. Rep. 10 (2020). https://doi.org/10.1038/s41598-020-62425-w.

[269] J. Wang, C. Xue, W. Yao, J. Liu, X. Gao, R. Zong, Z. Yang, W. Jin, D. Tao, MOF-derived hollow TiO2@C/FeTiO3 nanoparticles as photoanodes with enhanced full spectrum light PEC activities, Appl. Catal. B Environ. 250 (2019) 369–381. https://doi.org/10.1016/j.apcatb.2019.03.002.

[270] E. Aguilera-Ruiz, M. De La Garza-Galván, P. Zambrano-Robledo, J.C. Ballesteros-Pacheco, J. Vazquez-Arenas, J. Peral, U.M. García-Pérez, Facile synthesis of visible-light-driven Cu2O/BiVO4 composites for the photomineralization of recalcitrant pesticides, RSC Adv. 7 (2017) 45885–45895. https://doi.org/10.1039/c7ra08513c.

[271] Z. Wei, F. Liang, Y. Liu, W. Luo, J. Wang, W. Yao, Y. Zhu, Photoelectrocatalytic degradation of phenol-containing wastewater by TiO2/g-C3N4 hybrid heterostructure thin film, Appl. Catal. B Environ. 201 (2017) 600–606. https://doi.org/10.1016/j.apcatb.2016.09.003.

[272] J.W. Moir, E. V. Sackville, U. Hintermair, G.A. Ozin, Kinetics versus Charge Separation: Improving the Activity of Stoichiometric and Non-Stoichiometric Hematite Photoanodes Using a Molecular Iridium Water Oxidation Catalyst, J. Phys. Chem. C. 120 (2016) 12999–13012. https://doi.org/10.1021/acs.jpcc.6b00735.

[273] G.G. Bessegato, T.T. Guaraldo, J.F. de Brito, M.F. Brugnera, M.V.B. Zanoni, Achievements and Trends in Photoelectrocatalysis: from Environmental to Energy Applications, Electrocatalysis. 6 (2015) 415–441. https://doi.org/10.1007/s12678-015-0259-9.

[274] I. Paramasivam, H. Jha, N. Liu, P. Schmuki, A review of photocatalysis using self-organized TiO 2 nanotubes and other ordered oxide nanostructures, Small. 8 (2012) 3073–3103. https://doi.org/10.1002/smll.201200564.

[275] C.F. Liu, C.P. Huang, C.C. Hu, C. Huang, A dual TiO2/Ti-stainless steel anode for the degradation of orange G in a coupling photoelectrochemical and photo-electro-Fenton system, Sci. Total Environ. 659 (2019) 221–229. https://doi.org/10.1016/j.scitotenv.2018.12.224.

[276] C. Galindo, P. Jacques, A. Kalt, Photodegradation of the aminoazobenzene acid orange 52 by three advanced oxidation processes: UV/H2O2, UV/TiO2 and VIS/TiO2. Comparative mechanistic and kinetic investigations, J. Photochem. Photobiol. A Chem. 130 (2000) 35–47. https://doi.org/10.1016/S1010-6030(99)00199-9.

[277] A.D. Bokare, R.C. Chikate, C. V. Rode, K.M. Paknikar, Iron-nickel bimetallic nanoparticles for reductive degradation of azo dye Orange G in aqueous solution, Appl. Catal. B Environ. 79 (2008) 270–278. https://doi.org/10.1016/j.apcatb.2007.10.033.

[278] S. Garcia-Segura, E. Brillas, Applied photoelectrocatalysis on the degradation of organic pollutants in wastewaters, J. Photochem. Photobiol. C Photochem. Rev. 31 (2017) 1–35. https://doi.org/10.1016/j.jphotochemrev.2017.01.005.

[279] S. Yan, Y. Shi, Y. Tao, H. Zhang, Enhanced persulfate-mediated photocatalytic oxidation of bisphenol A using bioelectricity and a g-C3N4/Fe2O3 heterojunction, Chem. Eng. J. 359 (2019) 933–943. https://doi.org/10.1016/j.cej.2018.11.093.

[280] S. Lettieri, V. Gargiulo, D.K. Pallotti, G. Vitiello, P. Maddalena, M. Alfè, R. Marotta, Evidencing opposite charge-transfer processes at TiO2/graphene-related materials interface through combined EPR, photoluminescence and photocatalysis assessment, Catal. Today. 315 (2018) 19–30. https://doi.org/10.1016/j.cattod.2018.01.022.

[281] T. Zhang, Y. Chen, Y. Wang, J. Le Roux, Y. Yang, J.P. Croué, Efficient peroxydisulfate activation process not relying on sulfate radical generation for water pollutant degradation, Environ. Sci. Technol. 48 (2014) 5868–5875. https://doi.org/10.1021/es501218f.

[282] X. Duan, H. Sun, S. Wang, Metal-Free Carbocatalysis in Advanced Oxidation Reactions, Acc. Chem. Res. 51 (2018) 678–687. https://doi.org/10.1021/acs.accounts.7b00535.

[283] S. Zhu, C. Jin, X. Duan, S. Wang, S.H. Ho, Nonradical oxidation in persulfate activation by graphene-like nanosheets (GNS): Differentiating the contributions of singlet oxygen (1O2) and sorption-dependent electron transfer, Chem. Eng. J. 393 (2020) 124725. https://doi.org/10.1016/j.cej.2020.124725.

[284] E.T. Yun, J.H. Lee, J. Kim, H.D. Park, J. Lee, Identifying the Nonradical Mechanism in the Peroxymonosulfate Activation Process: Singlet Oxygenation Versus Mediated Electron Transfer, Environ. Sci. Technol. 52 (2018) 7032–7042. https://doi.org/10.1021/acs.est.8b00959.

Supporting Information

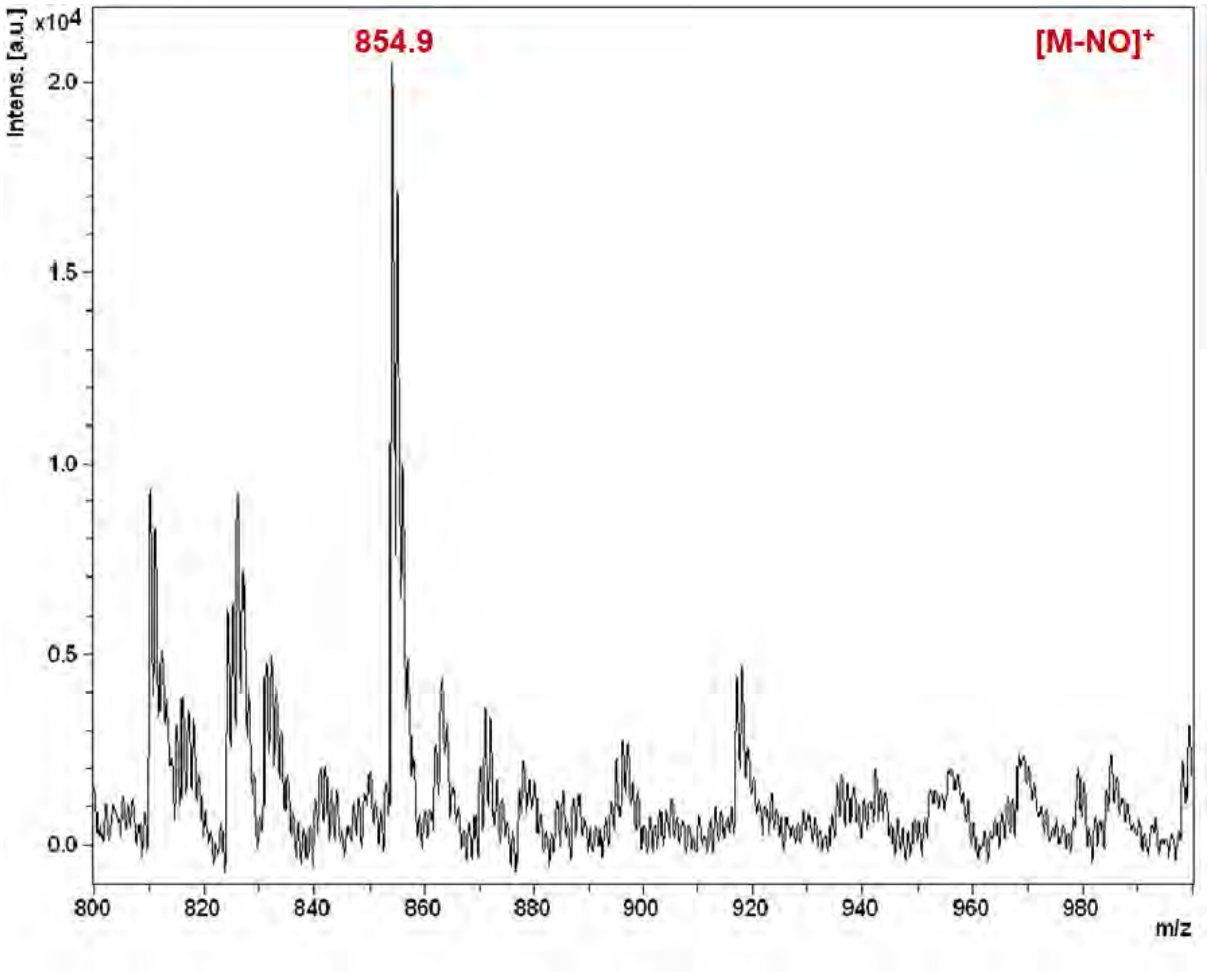

Figure S1: MALDI-TOF mass spectrum of the as-synthesized complex **2**.

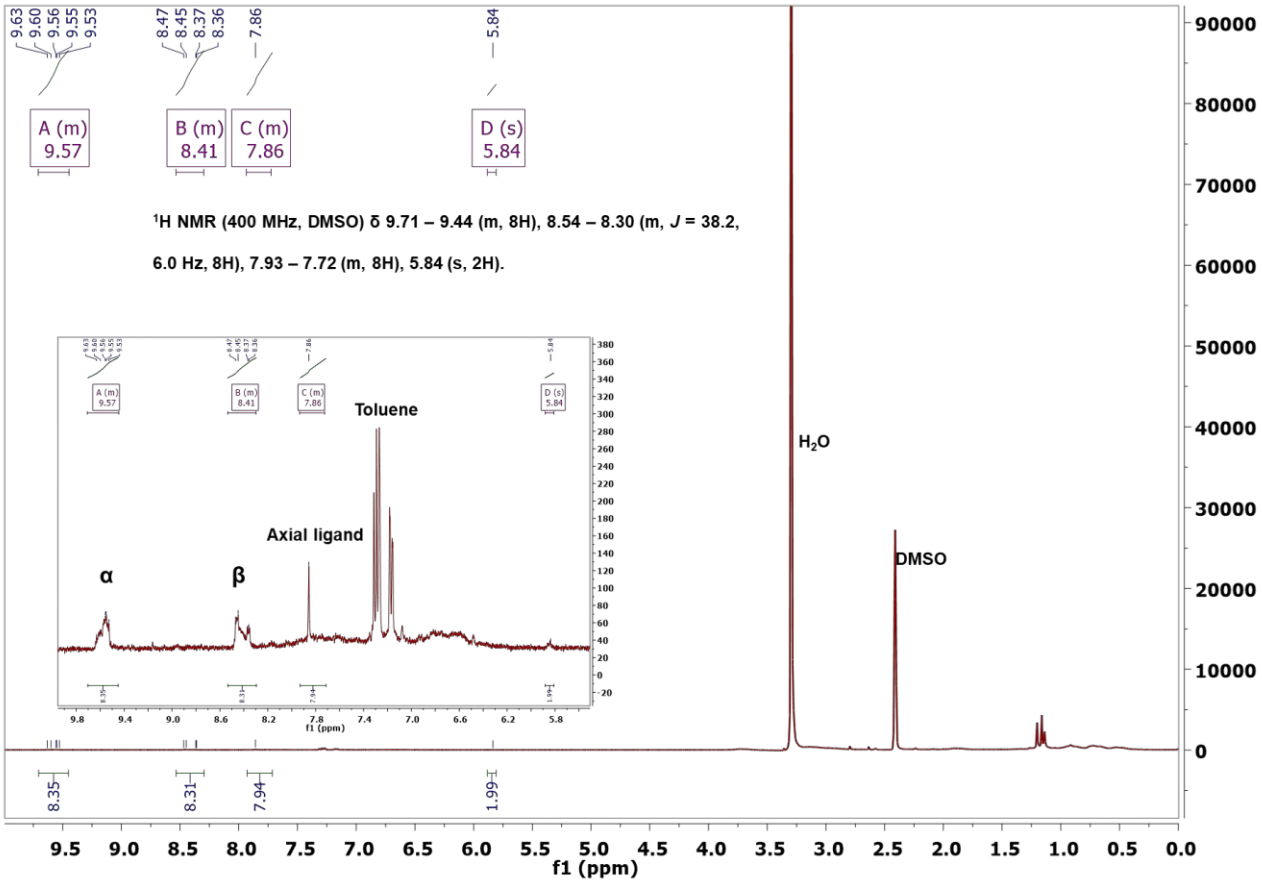

Figure S2: ^{1}H NMR spectrum of complex **1** in DMSO-d_6

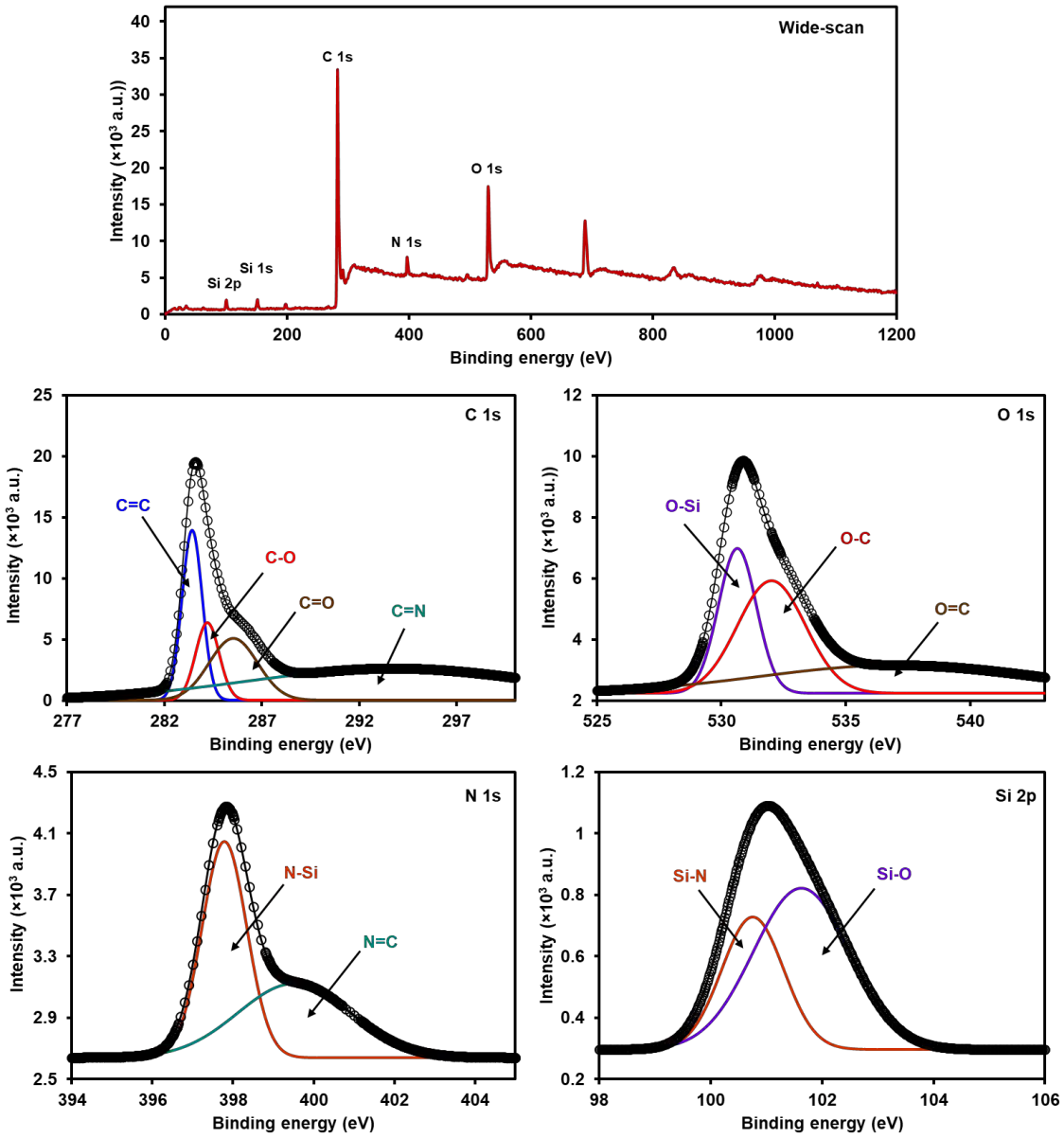

Figure S3: XPS wide-scan survey and high-resolution C 1s, O 1s, C 1s, and Si 2p spectra of **1**.

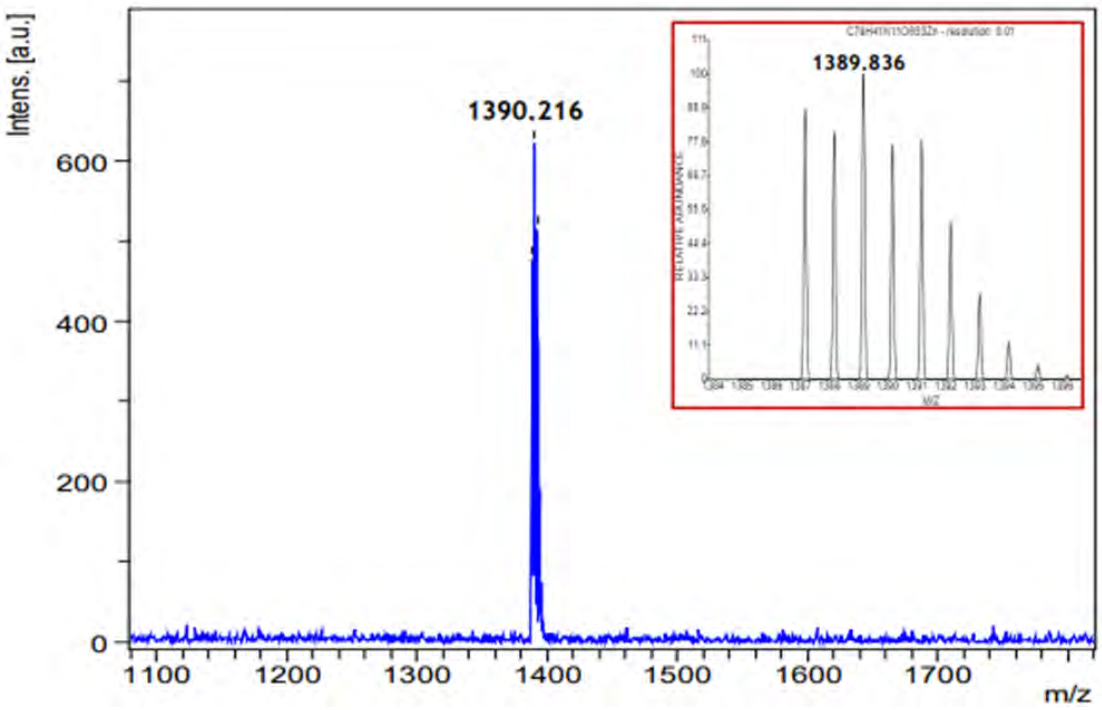

Figure S4: Maldi-TOF spectra of complex **3**. Insert = simulated isotopic mass distribution for complex **3**.

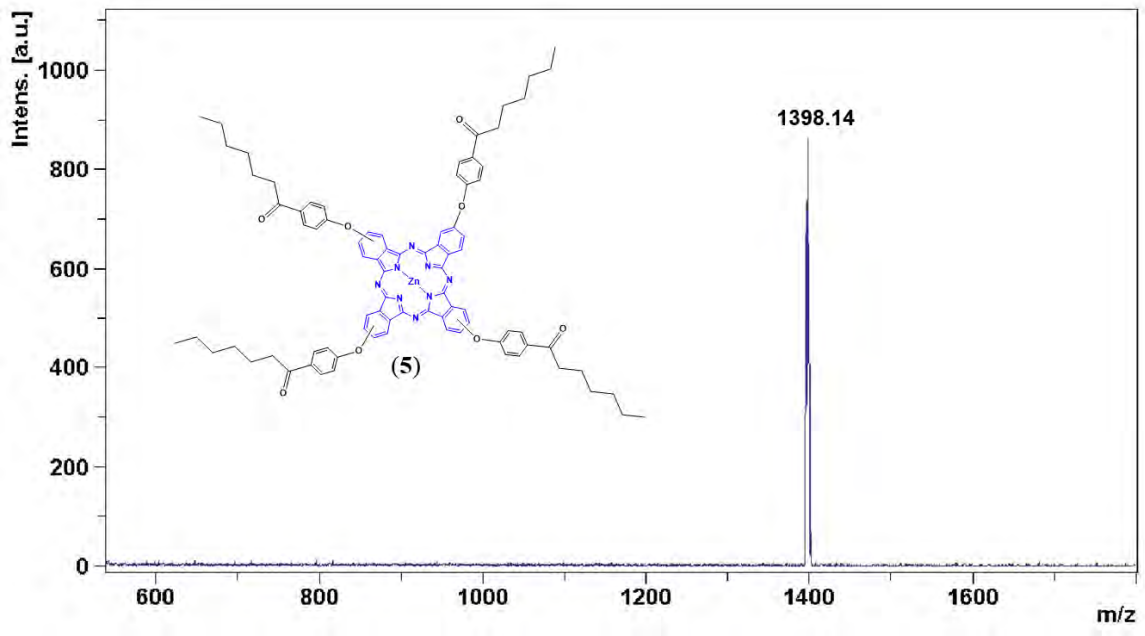

Figure S5: Maldi-TOF mass spectrum of **5**.

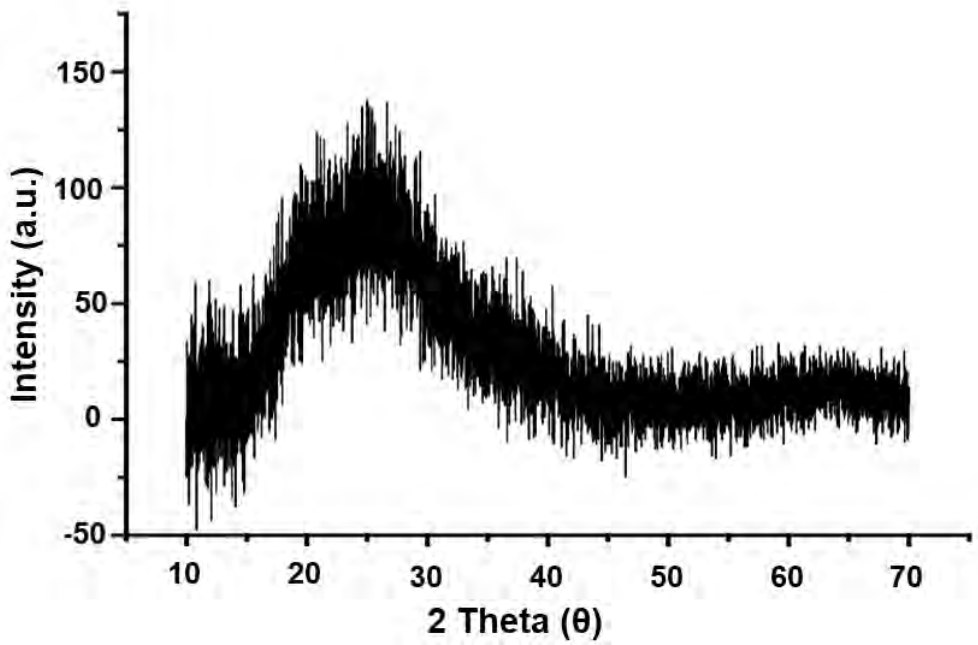

Figure S6: XRD diffraction patterns of GQDs alone